



# VERS UNE SIGNATURE DES SYSTEMES BINAIRES COMPORTANT UN TROU NOIR ...

Philippe Laurent

## ► To cite this version:

Philippe Laurent. VERS UNE SIGNATURE DES SYSTEMES BINAIRES COMPORTANT UN TROU NOIR .... Phénomènes cosmiques de haute energie [astro-ph.HE]. Université Paris-Diderot - Paris VII, 2009. tel-00683273

HAL Id: tel-00683273

<https://theses.hal.science/tel-00683273>

Submitted on 28 Mar 2012

**HAL** is a multi-disciplinary open access archive for the deposit and dissemination of scientific research documents, whether they are published or not. The documents may come from teaching and research institutions in France or abroad, or from public or private research centers.

L'archive ouverte pluridisciplinaire **HAL**, est destinée au dépôt et à la diffusion de documents scientifiques de niveau recherche, publiés ou non, émanant des établissements d'enseignement et de recherche français ou étrangers, des laboratoires publics ou privés.

# **VERS UNE SIGNATURE DES SYSTEMES BINAIRES COMPORTANT UN TROU NOIR ...**

**Philippe Laurent**

**Unité Mixte de Recherche 7164 AstroParticule et Cosmologie (APC) – Paris,**

**Service d’Astrophysique / IRFU / DSM – CEA Saclay,**

**France**

**Habilitation à diriger des recherches**

**présentée à l’Université Paris 7 - Denis Diderot**

*Dossier soumis aux rapporteurs le 01/10/2008*

*Soutenue le 20/01/2009 devant le jury composé de:*

Pierre Binetruy	Président
Gilles Henri	Rapporteur
Sandip Chakrabarti	Rapporteur
Marcello Fulchignoni	Rapporteur
Andréa Goldwurm	Examinateur



*à Nathalie ...*



## **Table des matières**

<b>Introduction .....</b>	<b>6</b>
<b>Curriculum vitae.....</b>	<b>7</b>
<b>Résumé des activités de recherche .....</b>	<b>9</b>
<b>Activités d'encadrement.....</b>	<b>11</b>
<b>Responsabilités scientifiques et administratives .....</b>	<b>11</b>
<b>Activités internationales.....</b>	<b>12</b>
<b>Travaux et publications.....</b>	<b>13</b>
<b>Publications principales .....</b>	<b>14</b>
<b>Vers une signature des systèmes binaires comportant un trou noir .....</b>	<b>17</b>

# **Introduction**

Ce mémoire présente mon dossier pour l'obtention du diplôme d'habilitation à diriger des recherches à l'université *Denis Diderot* de Paris 7.

Les premières sept sections contiennent les documents suivantes : un bref curriculum vitae (section I), un résumé chronologique des mes activités de recherche (section II), la liste des mes activités d'encadrement tant au niveau scientifique qu'au niveau manageriel (section III), mes responsabilités scientifiques et administratives, notamment dans les projets d'astronomie gamma auxquels j'ai participé (section IV). En section V je liste mes activités scientifiques internationales, comme l'organisation de conférences et les présentations invitées à des colloques, je donne ensuite les statistiques sur mes publications (section VI), la liste complète des mes travaux étant reportée en Annexe.

# **Curriculum vitae**

Nom : Laurent Prénom : Philippe  
Date de naissance : 17 juin 1962 Lieu de naissance: Paris  
Nationalité : Française Marié, 3 enfants

**Ingénieur Chercheur au**  
Commissariat à l'Énergie Atomique de Saclay (CEA-Saclay)  
Direction Sciences de la Matière (DSM)  
Institut de Recherche sur les lois Fondamentales de l'Univers (IRFU)  
Service d'Astrophysique (SAp)  
Laboratoire Phénomènes Cosmiques à Haute Energie (LPCHE)

Date d'arrivée dans l'unité (CFR) : septembre 1988  
Début CDI (ingénieur chercheur) : 1<sup>er</sup> août 1992  
Classement actuel : E4 depuis le 1<sup>er</sup> octobre 1999

**Membre de**  
Groupement de Recherche Phénomènes Cosmiques à Haute Energie (GDR PCHE)  
Groupe LISA France

## **Etudes et expérience professionnelle**

Juin 1986 Paris	Diplôme d'ingénieur de l'Ecole Centrale des Arts et Manufactures,
Juin 1988	DEA Astrophysique Paris VII/Meudon
Sept. 88 – Mars 92	Thésard au Service d'Astrophysique CEA-Saclay
24 mars 1992	Soutenance de thèse : «Calcul de la réponse spectrale du télescope spatial SIGMA, application à l'étude des binaires X dans le domaine des rayons gamma de basse énergie »
Juillet 92 à ce jour	Ingénieur chercheur au SAp-CEA Saclay, dans le groupe d'astronomie gamma puis au Laboratoire Phénomènes Cosmiques de Haute Energie.

### **Domaines de recherche**

- Instrumentation et méthodes d'analyse des données d'astronomie X et gamma
- Simulation de transfert de rayonnement
- Astronomie X , gamma, et ondes gravitationnelles
- Astrophysique des objets compacts

### **Projets et sujets de recherche**

- Astronomie X : analyse et interprétation des données de télescopes X de sources galactiques.
- Théorie du transfert de rayonnement dans l'environnement proche d'un trou noir. Simulation de transfert de rayonnement en Relativité Générale.
- Télescope gamma spatial SIGMA : étude de la réponse en énergie, analyse et interprétation des données des sources compactes galactiques (trous noirs ou étoiles à neutrons)
- Observatoire gamma spatial Integral/Ibis : simulations des performances, simulation détaillée du télescope, calcul des matrices de réponse Ibis, coordination des étalonnages du satellite, contribution aux phases opérationnelles et aux étalonnages en vol. Développement du logiciel d'analyse du mode Compton d'Ibis. Analyse et interprétation des données. Observations HESS des sources Integral.
- Projet Simbol-X : Définition du plan focal, développement de l'anti-coïncidence

### **Transfert de technologie**

- Co-inventeur avec O. Limousin de la caméra gamma 3D, utilisable pour la détection de risques nucléaires ou la médecine nucléaire. (Brevet BD 1688 déposé le 20 juin 2006).

### **Responsabilités**

1990 – 1995	Participation aux opérations de contrôle SIGMA à la station de réception.
Depuis 1995	Instrument Scientist du télescope Integral/Ibis.
Depuis 1996	Responsable du groupe de simulation Ibis. Responsable du calcul des matrices de réponse Ibis.
1999-2002	Responsable Scientifique des étalonnages « end to end » Integral à l'ESA/ESTEC.
Depuis 2004	membre de LISA France
Depuis 2005	Instrument Scientist du plan focal Simbol-X
	Responsable Scientifique du développement de l'anti-coïncidence du plan focal du projet Simbol-X
Depuis 2006	Project Scientist de Simbol-X

### **Encadrements**

- Encadrement scientifique de 3 stages de DEA, d'une thèse, et 2 stages post doctoraux.
- Coordination du travail du SAp et de 4 laboratoires Ibis (2 italiens, un polonais et un anglais) pour le développement du simulateur Ibis.

## **Publications**

173 publications, dont 86 sur des revues à comité de lecture, 80 dans de comptes rendus de conférences, 7 circulaires.

## **Langues**

Français, Anglais, Espagnol

## **Résumé des activités de recherche**

**1986 – Ecole Centrale des Arts et Manufactures, Paris** – Stage de 3<sup>ème</sup> année sous la direction de M. Cassé :

- « Discussions sur différentes acceptations du Temps en Physique »

**1986-1987 – Service militaire au CEA/DAM ( Limeil - Brévannes ) :**

- « Etude de la diffusion du plutonium dans un plasma d'hydrogène »

**1987-1988 – DEA d'astrophysique, Paris, Meudon.**

**1988-1992 – Service d'Astrophysique du CEA, Saclay (France) – Contrat de thèse CFR :**

- Calcul de la matrice de réponse en énergie du télescope gamma à masque codé GRANAT/SIGMA.
- Etude des binaires X détectées avec SIGMA : les candidats « trou noir » Cygnus X-1 et GX 339-4, et les pulsars accrétaux 4U 1700-377, et GX1+4.

**1992-1999 – SAp/CEA-Saclay (France) – Ingénieur Chercheur**

- Etude détaillé des données SIGMA des binaires X contenant un trou noir (1E1740.7-2942, GRS 1758-258, Cygnus X-1, GX 339-4, nova Muscae) ou une étoile à neutrons (4U 1700-377, GX 1+4, Vela X-1, SLX 1735-235, KS 1731-260). Mise au point du critère spectral pour discriminer les systèmes à trou noir vs système à étoile à neutrons. Etude des données SIGMA sur les pulsars isolés (Crabe, PSR 1509-58, PSR J0437-4715)

**1995-2002**

- Participation à la définition du télescope à masque codé Ibis du projet Integral. Simulations des différents projets d'instrument Ibis.
- Réalisation de logiciels d'analyse des données ISGRI pendant le développement de la caméra.
- Participation au projet Integral (consortium Ibis), notamment pour la conception et la réalisation du simulateur d'Ibis, et la définition du plan de calibration.
- Campagne de calibration au sol, et de recette en vol d'Integral/Ibis/ISGRI.

**1999-2002**

- Définition des étalonnages « end to end » d'Integral à l'ESA/ESTEC. Conception du plan de calibration.
- Réalisation du dispositif d'étalonnage (générateur X + sources gamma)

- Coordination, en binôme avec l'ESA, des étalonnages sur trois semaines regroupant plus de quarante chercheurs venant de huit pays différents.

### **Depuis 1998**

- Simulation par méthode Monte-Carlo des processus de « Comptonisation »
- Etude théorique de l'émission de la matière tombant dans un trou noir par méthode Monte-Carlo
- Etude du transfert de rayonnement dans la métrique de Schwartzchild
- Etude des propriétés spectrales et temporelles de ces émissions
- Modélisation de l'élargissement de la raie du Fer observée en provenance des candidats trou noir.
- Etude de la création de paires près de l'horizon d'un trou noir.

### **2002-2006**

- Analyse et publication des résultats des étalonnages en vol d'Integral/Ibis.
- Création et mise à disposition de la communauté des matrices de réponse Ibis.
- Participation à la mise au point de la barycentrisation des données temporelles Integral.
- Analyse des données de Cygnus X-1, 4U 1700-377, OAO 1657-415, PSR 1509-58, et du Crabe.
- Conception du logiciel d'analyse du mode Compton d'Ibis.
- Etude de la polarisation du Crabe mesurée par Ibis.
- Etude des sursauts gamma observés loin de l'axe du télescope par le mode Compton d'Ibis.
- Etude simultanée radio-gamma du pulsar du Crabe, en collaboration avec l'Université de Gallway (Irlande).

### **Depuis 2004**

- Participation à LISA France ; étude des systèmes binaires trou noir stellaire – trou noir super-massif.

### **Depuis 2005**

- Définition du plan focal du projet spatial Simbol-X.
- Conception de l'anti-coïncidence du plan focal Simbol-X.
- Détermination des paramètres système de la mission en fonction des exigences scientifiques de la mission Simbol-X (« flow-down document »).

## Activités d'encadrement

- Responsable CEA pour la thèse doctorale (Ecole doctorale d'astrophysique d'Ile de France, Université Paris 7) de **Michaël Forot** sur l'analyse du mode Compton du télescope Integral/Ibis, l'étude Integral/HESS du plérion MSH 15-52 et de la polarisation du Crabe (octobre 2003 – décembre 2006).
- Contribution au suivie de la thèse de **Marion Cadolle-Bel** sur l'analyse des données Integral de la source Cygnus X-1 (octobre 2003 – septembre 2006).
- Contribution au suivie du stage post-doctoral (contrat CDD INSU/CNES) de **Maurizio Falanga** sur l'analyse des données Integral des binaires X de basse masse et des pulsars X accrétaux (depuis 2002).
- Participation au jury de thèse de **Julien Malzac** au CESR, Toulouse.
- Contribution au suivie du stage post-doctoral (contrat CTE du CEA) de **Pedro David** sur l'analyse des données X ASCA du système binaire avec étoile à neutrons SLX 1735-265 (1996).

## Responsabilités scientifiques et administratives

- **Responsable du développement du simulateur Ibis**
  - Coordination du travail des équipes Ibis du SAP/CEA Saclay, IASF/CNR Bologne, IASF/CNR Rome (Italie), Université de Southampton (UK), et du CBK (Varsovie) pour le développement du simulateur Ibis.
  - Conception du site Web interfaçant le simulateur Collaboration SAp, CBK (Varsovie).
  - Calcul des matrices de réponses d'Ibis.
- **Instrument Scientist du projet Integral/Ibis**
  - Contribution à la définition de l'instrument Ibis.
  - Contribution à la définition et à la réalisation des étalonnages au sol Ibis.
  - Responsable des étalonnages « end to end » d'Integral à l'ESA/ESTEC.
  - Contribution à l'étalonnage en vol d'Ibis.
  - Développement du logiciel d'analyse des données Compton d'Ibis.
- **Responsable Scientifique du projet APC Anti-coïncidence Simbol-X**
  - Définition de l'Anti-Coïncidence (AC).
  - Definition et suivi des tests de concept d'AC.
  - Suivi des ressources financières et humaines APC à ce projet.

- **Project Scientist de la mission Symbol-X**

- Définition de l'instrument.
- Coordination du groupe simulation (France, Allemagne).
- Coordination du groupe «Etude du bruit de fond » (France, Allemagne, Italie)
- Détermination des paramètres système de la mission (« flow-down document »).

- **Membre du Conseil de laboratoire du laboratoire APC**

- **Coordination de collaborations ou réseaux**

- Collaboration GDR PCHE sur le thème : *Modelisation de l'émission gamma produite au voisinage d'un trou noir*. 5 chercheurs de 2 instituts français et un américain (année 2000, 2001 et 2002).
- Collaboration avec des laboratoires polonais, dans le cadre du programme européen ECONET, sur le thème : *Etude des sursauts gamma avec Integral dans la région du MeV* (année 2006 et 2007).

## **Activités internationales**

- **Contributions lors de conférences**

**SIGMA observations of bright X-ray binaries**

Conférence "Recent Advances in High Energy Astronomy", 17-20 Mars 1992, Toulouse, France.

**Hard X-Ray Observations of Black Holes and Neutron Stars**

The 7<sup>th</sup> Marcel Grossman Meeting on Relativistic Astrophysics, 24-30 Juillet 1994, Stanford University, USA.

**Monte-Carlo simulations of Comptonization on free-falling electrons**

The 9<sup>th</sup> Marcel Grossman Meeting on Relativistic Astrophysics, 2-8 juillet 2000, Université de Rome "La Sapienza", Italie.

**Integral/Ibis observations of persistent black hole spectral states during the Core Program**

The 4<sup>th</sup> Integral Workshop, "Exploring the Gamma-Ray Universe", 4-8 Sep 2001, Alicante, Espagne.

**The Symbol-X focal plane**

Workshop Symbol-X, "The hard X-ray Universe in focus", 14-16 mai 2007, Bologne, Italie

- **Contributions à écoles et ateliers**

**"Integral out of the FOV imaging and spectral capabilities"**

Atelier Integral, ESA, ESTEC, 18-21 janvier 2005

**"Radiative processes around black hole horizons in X-ray binaries"**

Cours pour l'International Relativistic Astrophysics Ph.D., ICRA, Nice Sophia Antipolis, 6 – 17 février 2006

**“Le plan focal Simbol-X”**

Atelier Simbol-X, 4 mai 2006, CNES Paris, France

**“Etude des pulsars avec Simbol-X”**

Atelier Simbol-X, 4 mai 2006, CNES Paris, France

• **Organisation d'écoles et conférences**

**Membre du comité d'organisation des :**

**Rencontres de Blois**, 16-22 juin 2002, château de Blois, France.

**Journée « Objets Compacts »**, Journées de l'APC, 21 janvier 2003, Paris/Jussieu, France.

**Black Holes in the Universe**, École de Cargèse, 12-24 mai 2003, Cargèse, Corse, France.

**Journées Jeunes Chercheurs**, La Roche en Ardennes, Belgique, 30 novembre – 5 décembre 2003.

**Journées Jeunes Chercheurs**, Ile de Berder, Bretagne, 28 novembre - 3 décembre 2004.

**6<sup>ème</sup> Rencontres du Vietnam**, Hanoï, 6-12 août 2006.

**Ecole des Houches**, Les Houches, 12-23 mars 2007.

• **Conférences et séminaires**

Participation à plus de 10 conférences internationales avec contribution orale ou poster et invité à plus de 5 séminaires à Saclay, en France et à l'étranger.

• **Référé**

A plusieurs reprises pour **The Astrophysical Journal** et **Astronomy and Astrophysics**.

• **Formation**

Stage **CAMARI**, option X et gamma, chez InterContrôle, 24-28 septembre 2001

## **Travaux et publications**

Nombre total de publications scientifiques : 173

**86 articles publiés (ou en cours de publication) dans des revues à comité de lecture**

**80 articles publiés dans des comptes-rendus de conférences**

**7 circulaires à l'Union Astronomique Internationale**

Le site ADS ([http://adsabs.harvard.edu/abstract\\_service.html](http://adsabs.harvard.edu/abstract_service.html)) fait apparaître (en septembre 2008) 180 publications à mon nom (voir section VII).

**Editions de livres et articles de divulgation scientifique :**

- livre « **L’Astronomie Gamma Spatiale** » (J. Paul & P. Laurent) destiné aux étudiants à partir de la maîtrise de physique, Gordon & Breach edition, 1997.
- Participation au **livre « Concepts in Space Science »** ed. R.R. Daniel (chapitre sur l’astronomie à haute énergie), 2002.
- **3 articles** publiés dans des revues de divulgation scientifique (La Recherche, Europhysics News, Pour la Science).
- Participation à **l’exposition APC « l’Histoire du proton »** à la Bibliothèque François Mitterrand (BNF), Paris, 2006.
- Participation à un **livre** pour les astronomes amateurs **sur le phénomène des « lobes de Roche »** (chapitre sur le débordement du lobe de Roche dans les binaires X), 2007.
- **Article** sur l’astronomie gamma dans **l’encyclopédie Mc Graw and Hill**, 2007.

La **liste complète des publications**, classées en publications a comite de lecture (code A), publications dans des comptes rendu de conférences (code C), télégrammes ou circulaires à l’IAU (code T) est reportée en **Annexe**.

## Publications principales

### LES INSTRUMENTS : SIMULATIONS DE TELESCOPES X DURS ET $\gamma$ , CALCUL DES MATRICES DE REONSE ET ETALONNAGES (VIII-2)

1. **Calibration of detectors for soft gamma-ray astronomy: the Monte Carlo approach applied to the SIGMA telescope**  
D. Barret, P. Laurent,  
1991, *Nuclear Instruments and Methods in Physics Research*, A 307, 512
2. **Status of the Integral/Ibis telescope modeling and of the response matrices generation**  
P. Laurent, O. Limousin, M. Cadolle-Bel, P. Goldoni, G. Malaguti, E. Caroli, G. De Cesare, M. Del Santo, A.J. Bird, J. Grygorczuk, J.M. Torrejon  
2003, *Astronomy & Astrophysics*, 411, L185
3. **Compton Telescope with a Coded Aperture Mask: Imaging with the Integral/Ibis Compton Mode**  
M. Forot, P. Laurent, F. Lebrun et O. Limousin  
2007, *Astrophysical Journal*, 668, 1259
4. **Monte Carlo simulations of stacked X-ray detectors as designed for SIMBOL-X**  
C. Tenzer, E. Kendziorra, A. Santangelo, M. Kuster, P. Ferrando, P. Laurent, A. Claret, R. Chipaux,  
2006, *SPIE*, 6266, 78

## **LES OBJETS : LES SYSTEMES BINAIRES X DANS LA GALAXIE (VIII-3)**

5. **SIGMA observations of the soft gamma-ray source GRS 1758-258**  
P. Laurent, B. Cordier, A. Goldwurm, J. Paul, J.-P. Roques, L. Bouchet, M. Denis, P. Mandrou, R. Sunyaev, E. Churazov,  
1993, *Advances in Space Research*, 13, (12)751
6. **Spectral distinction between black holes and neutron stars: the contribution of the SIGMA telescope**  
P. Laurent, P David  
1997, *Advances in Space Research*, Volume 19, Issue 1, 45
7. **The broad-band spectrum of Cygnus X-1 measured by Integral**  
M. Cadolle Bel, P. Sizun, A. Goldwurm, J. Rodriguez, P. Laurent, A. Zdziarski, L. Foschini, P. Goldoni, C. Gouiffès, J. Malzac, E. Jourdain & J.-P. Roques  
2006, *Astronomy & Astrophysics*, 446, 591

## **VERS UNE SIGNATURE DES SYSTEMES A TROUS NOIRS ... (VIII-4)**

8. **The Converging Inflow Spectrum Is an Intrinsic Signature for a Black Hole: Monte Carlo Simulations of Comptonization on Free-falling Electrons**  
P. Laurent, L. Titarchuk.  
1999, *ApJ*, 511, 289
9. **Timing and Spectral Properties of X-Ray Emission from the Converging Flows onto a Black Hole: Monte Carlo Simulations**  
P. Laurent, L. Titarchuk.  
2001, *ApJ*, 562, 67
10. **Effects of Downscattering on the Continuum and Line Spectra in Powerful Wind Environment. II Monte Carlo Simulations, Analytical Results and Data Analysis**  
P. Laurent, L. Titarchuk.  
2007, *ApJ*, 656, 1056



## VIII

**Vers une signature des systèmes binaires  
comportant un trou noir ...**



<b>1. INTRODUCTION</b>	<b>21</b>
<i>La recherche des trous noirs.....</i>	<b>21</b>
<b>2. LES INSTRUMENTS : SIMULATIONS DE TELESCOPES X DURS ET <math>\gamma</math>, CALCUL DES MATRICES DE REPONSE ET ETALONNAGES</b>	<b>23</b>
<i>Une réponse instrumentale particulièrement intriquée.....</i>	<b>23</b>
Le cas particulier de la réponse en énergie	23
Les étalonnages au sol	24
L'influence de l'environnement lors des étalonnages	25
Les étalonnages auprès d'accélérateurs de particules	25
L'apport des simulations numériques	26
L'apport des étalonnages en orbite	27
<i>Le télescope Sigma .....</i>	28
<i>Calcul de la matrice de réponse de Sigma.....</i>	29
<i>L'observatoire Integral .....</i>	30
<i>Simulations et étalonnages du télescope Integral/Ibis .....</i>	33
Simulations des configurations d'Ibis	33
Les étalonnages au sol	33
Les étalonnages en vol	34
<i>Création des matrices de réponse Ibis .....</i>	34
<i>Développement de l'analyse de données du mode Compton d'Ibis.....</i>	34
<i>Le projet Simbol-X .....</i>	35
<i>Définition du projet Simbol-X et conception de l'anticoïncidence .....</i>	36
<i>Bibliographie .....</i>	38
<i>Publications principales afférentes à ce chapitre .....</i>	39
<b>3. LES OBJETS : LES SYSTEMES BINAIRES X DANS LA GALAXIE</b>	<b>41</b>
<i>Qu'est-ce qu'une binaire X ?.....</i>	<b>41</b>
Les binaires de faible masse (LMXB)	43
Les binaires massives (HMXB)	45
<i>L'émission des binaires X .....</i>	<b>46</b>
La luminosité d'Eddington	46
L'influence du champ magnétique induit par l'astre accrétant	47
Le modèle standard des disques d'accrétion	48
Emettre des rayons X durs/ $\gamma$ ?	49
Evolution récentes des modèles de disque	50
<i>Observations Sigma des binaires X .....</i>	<b>50</b>
Les binaires X observées par Sigma	50
Observations Sigma des trous noirs accrétants	50
<i>Observations Integral des binaires X à trou noir.....</i>	<b>51</b>
<i>Bibliographie .....</i>	<b>52</b>
<i>Publications principales afférentes à ce chapitre .....</i>	<b>53</b>
<b>4. VERS UNE SIGNATURE DES SYSTÈMES A TROU NOIR ...</b>	<b>55</b>
<i>Les différents états spectraux des systèmes binaires comportant un trou noir.....</i>	<b>55</b>
L'état dur	55

<b>L'état mou</b>	<b>55</b>
<i>Le modèle générique de l'émission X des binaires à trous noirs .....</i>	55
Rayonnement émis par un disque d'accrétion	56
Rayonnement émis par la région interne : la comptonisation	57
<i>Modèle simple de l'émission X dur et <math>\gamma</math>de l'environnement immédiat du trou noir..</i>	57
L'énergie disponible dans la région proche du trou noir	58
Un mécanisme de chauffage	58
Deux mécanismes de refroidissement	59
Bilan énergétique	60
Binaires X à trous noirs dans l'état mou	62
Binaires X à trous noirs dans l'état dur	62
<i>Simulation Monte-Carlo de la « bulk motion Comptonization (BMC) ».....</i>	62
La simulation Monte-Carlo en relativité générale	63
Etude de l'émission X dur des systèmes à trou noir dans l'état dur	63
Etude de l'émission X dur des systèmes à trou noir dans l'état mou	64
Etude des variations temporelles des systèmes à trou noir.	64
<i>Une signature contreversée : l'élargissement de la raie du Fer.....</i>	64
<i>Bibliographie .....</i>	66
<i>Publications principales afférentes à ce chapitre .....</i>	67
<b>5. PROJET DE RECHERCHE ET PERSPECTIVES</b>	<b>69</b>
<i>Les perspectives instrumentales.....</i>	69
Le projet Simbol-X	69
Le projet IXO	69
D'autres projets en perspectives ...	70
<i>Les perspectives observationnelles.....</i>	70
Observations jusqu'à plusieurs MeV de Cygnus X-1 grâce à Integral	70
Observation de la polarisation en provenance des systèmes à trous noirs	70
<i>Les perspectives théoriques .....</i>	70
Etude de l'état « ultrasoft »	70
Création de paires au voisinage d'un trou noir	71
Les trous noirs de Kerr : accélérateur de particules ?	71

# 1. INTRODUCTION

## *La recherche des trous noirs*

Les trous noirs sont un phénomène maintenant bien connu du grand public, et dont la théorie découle directement de la théorie de la Relativité Générale d'Einstein. Un trou noir est une région de l'espace-temps à l'intérieur de laquelle le champ gravitationnel est si intense qu'il empêche toute matière et tout rayonnement de s'échapper. Une preuve directe de leur existence n'existe pas encore, mais, néanmoins, quelques preuves indirectes existent. La plus connue est liée à la notion de fonction de masse. Ce paramètre découle directement de la troisième loi de Kepler qui fournit la relation entre la période orbitale  $P$  d'un système double d'étoile, la masse  $M_1$  de la première étoile, suspectée d'être un trou noir, la masse  $M_2$  de l'étoile compagnon et la séparation orbitale  $a$  du système :

$$P^2 = \frac{4\pi^2}{G(M_1 + M_2)} a^3$$

Dans un système double, les deux corps ont des orbites elliptiques de demi grand-axe  $a_1$  et  $a_2$  dépendant du demi grand-axe  $a$  et des masses  $M_1$  et  $M_2$  selon :

$$a_1 = \frac{M_2}{M_1 + M_2} a \quad a_2 = \frac{M_1}{M_1 + M_2} a$$

La vitesse  $V$  du compagnon le long de son orbite s'exprime alors de la manière suivante :

$$V = \frac{2\pi a_2}{P} = \frac{2\pi M_1 a}{P (M_1 + M_2)}$$

À partir du décalage Doppler affectant les raies d'émission produites par le compagnon, des observations menées dans le visible permettent d'estimer la projection de la vitesse  $V$  le long de la ligne de visée, soit  $V_0 = V \sin(i)$ , où  $i$  mesure l'inclinaison du système ( $i = 0$  lorsque la ligne de visée est perpendiculaire au plan orbital du système). On définit alors la fonction de masse  $f$  par la relation suivante :

$$f = \frac{PV_0^3}{2\pi G} = \frac{PV^3 \sin(i)^3}{2\pi G} = \frac{4\pi^2 M_1^3 a^3 \sin(i)^3}{P^2 G (M_1 + M_2)^3} = \frac{M_1^3}{(M_1 + M_2)^2} \sin(i)^3$$

où  $G$  est la constante de la gravitation. Au vu de cette équation, on constate que la fonction de masse  $f$ , déterminée à partir de deux grandeurs observables,  $V_0$  et  $P$ , nous donne une relation sur les masses  $M_1$  et  $M_2$ , sans nécessiter les autres paramètres du système. À la limite, si on suppose en plus que la masse du compagnon est nulle ( $M_2 = 0$ ) et que l'observateur se situe dans le plan orbital du système ( $\sin i = 1$ ), la fonction de masse  $f$  est alors égale à la masse  $M_1$  de l'astre compact. En pratique,  $M_2 > 0$  et  $\sin i < 1$ ;  $f$  est donc toujours plus petite que la masse  $M_1$  de l'étoile effondrée et la fonction de masse fournit alors une limite inférieure de la masse de l'astre compact. Il est d'autre part généralement admis sur la base de travaux théoriques portant sur la matière ultra-condensée que la masse d'une étoile à neutrons ne peut pas dépasser trois fois la masse du Soleil. Tout système double d'étoiles présentant une fonction de masse  $f > 3 M_\odot$  est donc réputée abriter un authentique trou noir.

Si on connaît les propriétés de l'étoile compagnon, la fonction de masse permet donc d'identifier un trou noir. Dans le cas le plus connu, Cygnus X-1, un système double d'étoile où la présence d'un trou noir est fortement pressentie, l'étoile compagnon est une supergéante bleue de masse comprise entre 25 et 40 masses solaires. Le calcul de la fonction de masse nous donne donc que la masse minimale du compagnon serait supérieure à 7 fois la masse du soleil, soit bien au delà de la limite des astres compacts plus classiques.

Mes recherches ont donc eu pour but principal de trouver d'autres signatures de système comprenant un trou noir. Comme nous le verrons au chapitre 4, les astronomies X et gamma semblent bien adaptées pour ces recherches. J'ai donc participé à la définition d'instruments pour l'astronomie X et gamma (chapitre 2), puis j'ai analysé les données, une fois ces instruments lancés dans l'espace (chapitre 3). Enfin, j'ai essayé de modéliser quelques signatures X-durs des trous noirs, comme nous le verrons au chapitre 4. Mes perspectives de recherche seront enfin résumées au chapitre 5.

## **2. LES INSTRUMENTS : SIMULATIONS DE TELESCOPES X DURS ET $\gamma$ , CALCUL DES MATRICES DE REONSE ET ETALONNAGES**

### ***Une réponse instrumentale particulièrement intriquée***

La manière dont les télescopes  $\gamma$  répondent aux sources célestes est en général une fonction complexe de l'énergie et de l'angle d'incidence des photons qui sollicitent l'appareil. Pour connaître la réponse de leurs télescopes, les astronomes  $\gamma$  sont alors conduits à estimer les deux grandeurs suivantes :

1. La fonction d'appareil du télescope, pour savoir comment le dispositif expérimental répond à un faisceau parallèle de rayons  $\gamma$  issus d'une source ponctuelle supposée à l'infini.
2. La réponse en énergie, pour savoir comment le dispositif expérimental en question répond à une source de photons  $\gamma$  mono-énergétiques.

Contrairement à une pratique d'usage courant dans d'autres domaines spectraux, on ne peut pas se contenter d'estimer la réponse instrumentale des télescopes  $\gamma$  avec les seuls photons émis par les sites cosmiques eux-mêmes. Les sources  $\gamma$  célestes émettent en effet beaucoup trop peu de photons et sont pour la plupart d'entre elles beaucoup trop variables pour garantir un étalonnage satisfaisant des télescopes. Sans oublier qu'un photon  $\gamma$  aborde le plus souvent le plan détecteur d'un télescope  $\gamma$  après avoir traversé au préalable divers milieux matériels, comme ceux qui enveloppent les détecteurs eux-mêmes. Il en résulte une absorption du rayonnement incident qu'il convient d'estimer avec soin. Avant la mise en orbite, il est donc nécessaire de mesurer la réponse instrumentale d'un appareil en l'exposant à des faisceaux de rayons  $\gamma$  produits au sol, tout en développant un programme de simulation numérique afin de modéliser le plus précisément possible cette même réponse instrumentale.

### **Le cas particulier de la réponse en énergie**

Quand un astronome  $\gamma$  observe une source, le spectre de coups qu'il recueille présente souvent un rapport plus ou moins lointain avec le spectre de photons de la source en question. Un télescope  $\gamma$  fournit en effet un spectre de coups assez complexe en réponse à une source mono-énergétique. On peut néanmoins tenter de qualifier la réponse en énergie de l'appareil par le truchement de la résolution en énergie, un paramètre que l'on peut définir comme la largeur à mi-hauteur du pic correspondant à l'absorption totale des photons  $\gamma$ .

La complexité de la réponse en énergie, surtout dans le régime où la diffusion Compton est le mécanisme interactif dominant, est cependant telle qu'il serait illusoire de vouloir reconstituer

le spectre effectif d'une source de photons  $\gamma$  active dans ce régime en se contentant de diviser le taux de comptage mesuré dans l'intervalle par la surface efficace du télescope à cette même énergie  $E$ .

Dans tout le domaine  $\gamma$ , en particulier dans la bande des photons  $\gamma$  de basse énergie, la relation entre le spectre de coups  $S_T$  que fournit le télescope et le spectre de photons  $S_E$  de la source s'obtient plutôt par le truchement de la matrice de la réponse en énergie de l'instrument. Cette matrice, notée  $M$ , est définie par la relation matricielle suivante :

$$S_T = M * S_E$$

Il suffit donc d'inverser  $M$  pour obtenir  $S_E$  connaissant  $S_T$ . Cette procédure n'est pas sans poser de sérieux problèmes, la matrice  $M$  n'étant généralement pas assez régulière pour être inversée à l'aide de méthodes numériques simples. Dans la pratique, un étalonnage du télescope avant la mise en orbite permet d'estimer la réponse en énergie du télescope, à condition toutefois que la matrice  $M$  telle que mesurée au sol soit identique à celle qui prévaut une fois le télescope mis en orbite, ce qui n'est pas toujours le cas.

## Les étalonnages au sol

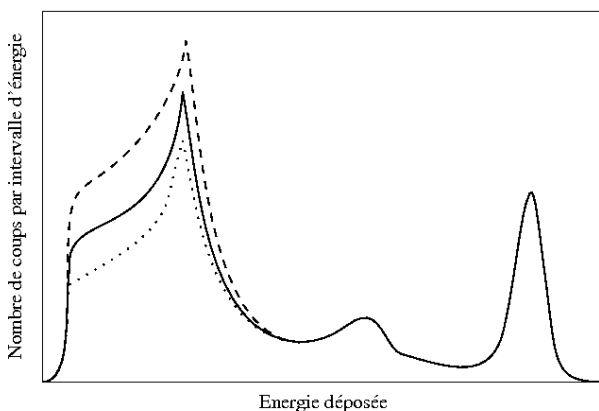
Les sources de rayons  $\gamma$  à base d'isotopes radioactifs ne sont pas en mesure de produire des photons dont l'énergie dépasse quelques mégaélectronvolts. L'étalonnage des télescopes  $\gamma$  au moyen de sources radioactives n'est donc envisageable que pour des appareils opérant dans la bande des photons  $\gamma$  de basse énergie. On expose le télescope à diverses sources étalon. Mais les sources radioactives ne permettent pas de fournir tous les spectres étalon qu'il faut réunir pour élaborer la matrice de la réponse en énergie de l'instrument. On est donc amené à produire une série de spectres intermédiaires en interpolant les spectres enregistrés avec les sources étalon.

Il faut alors tenir compte du fait que les différentes composantes de la réponse en énergie du télescope à une source mono-énergétique n'évoluent pas de la même manière en fonction de l'énergie des photons incidents. C'est ainsi que l'énergie à laquelle le front Compton apparaît s'accroît en fonction de l'énergie des photons incidents, tandis que le pic de rétrodiffusion se situe toujours aux mêmes énergies. Une interpolation directe des spectres étalon fournit alors un résultat peu satisfaisant, il faut envisager des méthodes plus complexes, en découplant le spectre en différentes zones et en interpolant différemment dans chaque zone, par exemple.

Quand il s'agit d'estimer la fonction d'appareil des télescopes  $\gamma$ , les étalonnages pratiqués au moyen de sources radioactives sont loin d'offrir des conditions satisfaisantes. Sauf à mettre en œuvre des sources très intenses, que l'on peut donc disposer à grande distance de l'instrument, les faisceaux de rayons  $\gamma$  émis par les sources radioactives sont beaucoup trop divergents pour simuler l'effet d'une source cosmique située à l'infini. Ce type d'étalonnages permet cependant de préciser la réponse angulaire d'appareils dotés de dispositifs optiques simplistes, comme les collimateurs, ainsi que d'estimer l'effet des rayonnements que les télescopes sont susceptibles de collecter en dehors de leur champ de vue nominal.

## L'influence de l'environnement lors des étalonnages

Elle se fait d'autant plus sentir que l'on étalonne un télescope opérant dans le secteur où la diffusion Compton peut être l'effet dominant. Outre les photons  $\gamma$  émis par la source, le télescope recueille en effet tous ceux ayant diffusé un peu partout dans la salle d'étalonnage (sol, murs et plafond) et dans les matériaux qui constituent le conditionnement même de la source. Tous ces milieux plus ou moins diffusifs perturbent les spectres enregistrés lors des phases d'étalonnage du télescope et des principaux sous-systèmes scientifiques. À titre d'exemple, la figure ci-dessous montre comment évolue l'amplitude du pic de rétrodiffusion des spectres enregistrés par la caméra à scintigraphie du télescope Sigma en fonction de la distance entre la source étalon et le plafond de la salle d'étalonnage.



L'amplitude du pic de rétrodiffusion, l'une des composantes majeures du spectre, dépend donc au premier chef des conditions de mesure. Il n'est donc pas possible d'utiliser tels quels les spectres enregistrés lors des phases d'étalonnage pour estimer la réponse en énergie de l'appareil une fois en orbite. On peut certes pallier cette dépendance à l'égard des conditions de mesure en pratiquant les étalonnages dans des salles aussi vastes que possible. Une autre approche consiste à entreprendre une modélisation numérique précise des phases d'étalonnage afin de bien séparer les composantes induites par l'environnement. On peut ainsi disposer de spectres étalon corrigés d'où l'on a soustrait les diverses contributions dues à l'environnement du télescope.

## Les étalonnages auprès d'accélérateurs de particules

Les sources radioactives n'étant pas en mesure d'émettre des photons  $\gamma$  d'énergie supérieure à quelques mégaélectronvolts, l'étalonnage des télescopes opérant au delà de cette limite impose donc de produire des rayons  $\gamma$  en bombardant une cible avec des particules fournies par des accélérateurs. Ce procédé, relativement lourd à mettre en œuvre, est le seul utilisable au delà de quelques mégaélectronvolts pour obtenir la réponse des télescopes  $\gamma$  à des photons  $\gamma$  mono-énergétiques. Ainsi, en bombardant une cible mince faite d'un matériau donné avec des protons accélérés à des énergies judicieusement ajustées, on parvient à exciter les noyaux du matériau cible. Par retour à l'état fondamental, ces noyaux émettent alors par désexcitation nucléaire des photons  $\gamma$  mono-énergétiques dont l'énergie peut atteindre une vingtaine de

mégaélectronvolts. C'est ainsi que la partie haute énergie du télescope *Integral/SPI* a été étalonnée à Bruyères le Châtel.

A basse énergie, des faisceaux plus intenses que les sources radioactives, peuvent être obtenus grâce à des accélérateurs d'électrons. En effet, en bombardant une cible mince avec des électrons relativistes d'énergie  $E_0$  fournis par un accélérateur de particules, on engendre par Bremsstrahlung un spectre continu de photons  $\gamma$ . Puis, on sélectionne parmi les électrons émergeant de la cible ceux d'énergie  $E_1$ . On est alors en mesure de produire un signal électronique chaque fois que la cible rayonne un photon X d'énergie donnée. On désigne les photons en question par le terme de "photons étiquetés". Ce procédé sera utilisé pour l'étalonnage de la future mission spatiale Simbol-X, dont nous reparlerons plus loin.

Les photons  $\gamma$  rayonnés par désexcitation de noyaux bombardés par des protons émergent des cibles sous les angles les plus variés. Les photons produits par freinage d'électrons relativistes constituent au contraire un faisceau quasiment parallèle de photons X étiquetés dont l'énergie n'a pas d'autre limite que celle des électrons produits par l'accélérateur. Les faisceaux de photons étiquetés sont donc aussi largement utilisés pour étalonner aussi bien la réponse en énergie que la fonction d'appareil des télescopes.

## L'apport des simulations numériques

Aussi complets qu'ils soient, les étalonnages au sol ne permettent donc pas de fournir dans toute sa diversité la réponse instrumentale d'un télescope  $\gamma$  en orbite. Pour ne pas accroître la durée des phases d'étalonnage au sol et pour des raisons de disponibilité de sources étalon, il n'est pas possible de mesurer au sol la réponse instrumentale à toutes les énergies et sous tous les angles d'incidence possibles. Comme précisé plus haut, il faut aussi tenir compte du fait que la réponse d'un télescope opérant dans la bande des photons  $\gamma$  de basse énergie est fortement affectée par tout ce qui constitue son environnement lors des phases d'étalonnage.

Pour compléter les résultats d'étalonnage des télescopes  $\gamma$  aux énergies où il n'y a pas de source disponible, ainsi que pour préciser la contribution de l'environnement, j'ai été conduit à entreprendre une modélisation numérique aussi précise que possible des télescopes et de tous les matériaux situés à proximité (y compris ceux qui constituent la salle de mesure), toujours dans le but d'identifier les composantes rayonnées par l'entourage. Cette modélisation s'appuie sur les données collectées lors des étalonnages, y compris ceux pratiqués au niveau des sous-systèmes du télescope. Pour des raisons évidentes de complexité des logiciels et de temps calcul, les simulations ne peuvent fournir qu'une vision approchée de la réalité.

Tout au long d'une simulation numérique de type "Monte-Carlo", on suit pas à pas le parcours d'un photon se propageant dans le dispositif expérimental et/ou son proche environnement jusqu'à son absorption dans le milieu ou son échappement du système considéré. On suit également le parcours des particules secondaires éventuellement créées par le photon en question. Chaque fois qu'un photon  $\gamma$  se présente face à une couche de matériau où il doit effectuer un parcours de longueur  $l_T$ , on détermine la distance  $l_I$  que le photon parcourt effectivement avant de subir une interaction. Dans le but d'estimer cette longueur  $l_I$ , on

pratique un tirage aléatoire selon la loi de probabilité exprimée par l'équation suivante (où  $\lambda$  est le libre parcours moyen dans le milieu considéré) :

$$P(l_I) = \frac{1}{\lambda} e^{-\frac{l_I}{\lambda}}$$

Si  $l_I$  est supérieure à  $l_T$ , le photon s'échappe. Dans le cas contraire, il y a une interaction dont on détermine la nature (effet photoélectrique, effet Compton ou effet de paire) en pratiquant un tirage uniforme entre 0 et 1, chaque interaction de nature  $i$  ayant une probabilité  $\sigma_i / \sigma_{\text{tot}}$  de se produire,  $\sigma_i$  étant la section efficace de l'interaction de type  $i$  et  $\sigma_{\text{tot}}$  la somme des sections efficaces de toute nature. À partir des caractéristiques de l'interaction, on détermine alors l'énergie et la direction des particules secondaires issues du mécanisme interactif, particules que l'on suit jusqu'à leur absorption, leur annihilation ou leur échappement.

Contrairement aux photons, les particules secondaires, quand elles sont chargées électriquement, interagissent de très nombreuses fois avant de s'arrêter, de s'annihiler ou de s'échapper. C'est ainsi qu'un électron d'énergie  $E_e \sim 1$  MeV subit près de 10 000 diffusions coulombiennes quand il se propage sur un centimètre au sein d'un milieu détecteur. Un traitement statistique s'avère alors nécessaire, car il serait totalement illusoire de vouloir comptabiliser chaque diffusion comme dans le cas des photons. Ce traitement s'effectue à partir d'abaques qui fournissent pour une interaction donnée l'énergie perdue en moyenne par une particule d'énergie initiale  $E_i$  ayant parcouru une distance donnée.

Si on effectue le tirage d'un grand nombre de photons incidents d'énergie donnée selon des directions aléatoires dans un angle solide donné, on obtient au bout du compte une estimation de la réponse du dispositif expérimental à une source mono-énergétique. Les progrès de l'informatique permettant aujourd'hui de faire des calculs complexes sur des systèmes souples et autonomes, on peut refaire un nouveau tirage en quelques heures à peine après avoir modifié les paramètres des algorithmes de simulation. En raison de la nécessité de prendre en compte l'environnement lors des phases d'étalonnage des télescopes  $\gamma$ , les méthodes numériques sont devenues désormais incontournables pour la mise au point et de l'estimation des performances des dispositifs expérimentaux opérant dans ce domaine.

## L'apport des étalonnages en orbite

Les étalonnages en orbite complètent ceux menés au sol en fournissant le moyen de vérifier que la réponse en énergie et la fonction d'appareil d'un télescope  $\gamma$  sont compatibles avec les estimations qui résultent des séances d'étalonnages et des simulations numériques évoquées ci-dessus. Ces phases de vérification s'effectuent en pointant l'instrument en direction d'une source  $\gamma$  brillante dont l'éclat varie le moins possible, dont le spectre de photons est assez bien connu et dont on connaît la position sur la voûte céleste. Une seule source répond à cette triple contrainte : la nébuleuse du Crabe, active surtout à basse énergie, et le pulsar radio qu'elle renferme, dont l'émission s'étend jusqu'aux  $\gamma$  de haute énergie.

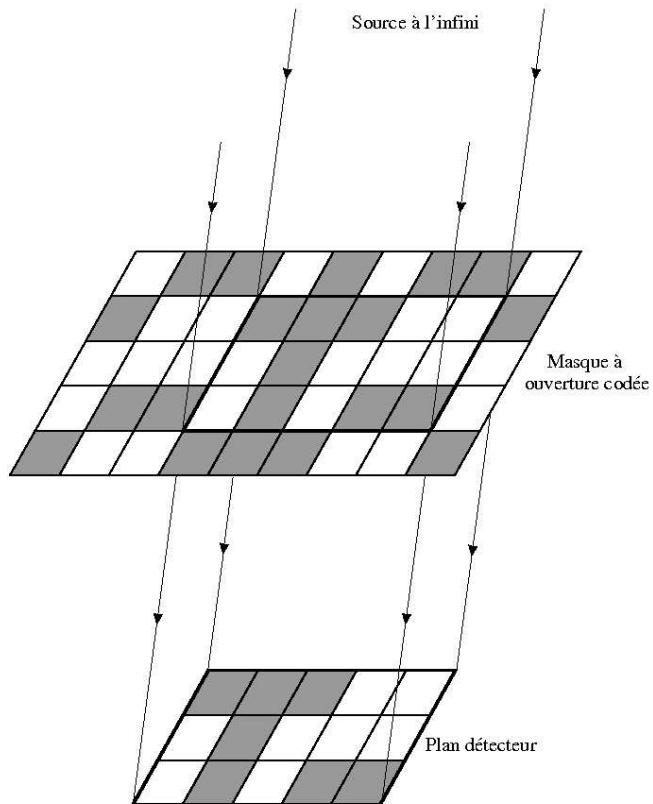
L'apport essentiel des étalonnages en orbite concerne la mesure *in situ* du bruit de fond du télescope afin de prévoir les temps de pose qui seront nécessaires pour détecter une source  $\gamma$  donnée. Même si on peut tenter de l'estimer par le truchement de modélisations numériques du type de celles évoquées ci-dessus, le bruit de fond en question reste très difficile à prédire avant le lancement. A basse énergie, les raies  $\gamma$  que l'on identifie dans le spectre du bruit de fond contribuent également à affiner l'estimation de la réponse en énergie du télescope et de son évolution dans le temps, complétant ainsi les données fournies par les sources radioactives d'étalonnage en vol que l'on dispose parfois à bord du dispositif expérimental.

## ***Le télescope Sigma***

Le télescope Sigma (*Système d'Imagerie Gamma à Masque Aléatoire*) fut la première expérience spatiale à ouverture codée opérant dans le domaine gamma. Fruit d'une collaboration entre deux laboratoires français<sup>1</sup>, le télescope Sigma, d'une masse de 1050 kg, a été réalisé sous la maîtrise d'œuvre du CNES. Mis en orbite le 1<sup>er</sup> décembre 1989 à bord du satellite russe *Granat*, Sigma comporte un masque à ouverture codée (voir ci-dessous) disposé à 2,5 m d'un plan détecteur dont le principe est inspiré de celui des caméras à scintigraphie. Cet arrangement, qui confère au télescope Sigma un pouvoir séparateur théorique de 13 minutes d'arc dans la gamme d'énergie de 35 keV à 1,3 MeV, permet de localiser les sources de photons  $\gamma$  avec une précision qui peut atteindre 30 secondes d'arc dans le cas des plus brillantes.

---

<sup>1</sup> Service d'Astrophysique du Commissariat à l'Énergie Atomique, Saclay, Centre d'Étude Spatiale des Rayonnements, Toulouse, France.



Principe d'imagerie à masque codée ; une source à l'infini selon une direction donnée produit sur le plan détecteur un motif spécifique, en correspondance bijective avec la direction de la source.

## ***Calcul de la matrice de réponse de Sigma***

J'ai donc créé une simulation Monte-Carlo complète du télescope spatial *Granat/Sigma*, afin de calculer sa matrice de réponse en énergie, selon la méthode décrite plus haut. J'ai pu mettre ainsi en évidence l'importance de la contribution de l'environnement lors des étalonnages ; une composante diffusée par l'environnement (la salle de mesure, le support de la source, ...), bien évidemment n'existant pas en vol, à soustraire absolument lors de la réalisation de la matrice de réponse. Les résultats de ces simulations ont été publiés dans la publication n°1.

## **L'observatoire Integral**

La finesse des images produites avec les données collectées par le télescope Sigma depuis 1990 à bord du satellite russe *Granat* démontre que les dispositifs à ouverture codée étaient alors les plus efficaces pour pratiquer des observations dans la bande des rayons  $\gamma$  de basse énergie. Il ne faut donc pas s'étonner que des appareils à ouverture codée, dont le principe s'inspire de celui de Sigma, soient à la base de la mission *Integral* (*International Gamma-Ray Astrophysics Laboratory*) de l'agence spatial européenne (ESA). L'innovation se situe plutôt au niveau des détecteurs sensibles à la position qui équipent les instruments. Cette nouvelle génération d'appareils généralise en effet l'usage des détecteurs semi-conducteurs, pour obtenir une meilleure résolution spectrale tout en conservant une bonne résolution angulaire.

La mission *Integral* a été sélectionnée en juin 1993 par le Comité des Programmes Scientifiques de l'ESA. Pour maintenir son coût dans les limites de celui d'une mission moyenne de la programmation à long terme de l'ESA (le programme Horizon 2000), *Integral* profita d'un véhicule spatial identique à celui de la mission *X.M.M.* (la mission d'astronomie X, une des quatre pierres angulaires du programme Horizon 2000), et d'un lancement par une fusée Proton fournie par la R.K.A. (l'Agence Spatiale Russe). La réalisation des équipements scientifiques et du centre des données scientifiques furent à la charge des états membres de l'ESA. Les instruments furent sélectionnés lors du premier semestre de 1995, en réponse à un appel d'offre émis en juillet 1994. Le satellite fut lancé en octobre 2002.

*Integral* a pour but principal l'exploration approfondie des sites célestes émissifs dans la bande spectrale de 15 keV à 10 MeV. La mission est basée sur la mise en œuvre simultanée du télescope Ibis (*Imager on Board the Integral Satellite*), apte à fournir des images à haute résolution angulaire et une information spectrale à moyenne résolution, et du spectromètre Spi (*Spectrometer for Integral*) chargé de la spectroscopie  $\gamma$  à très haute résolution. La mission *Integral* inclut également les deux instruments complémentaires Jem-X (*Joint European Monitor*) et l'O.M.C (*Optical Monitor Camera*), opérant respectivement dans la bande des rayons X au delà de 2-3 keV et dans le domaine visible, de 550 à 850 nm. La nature observatoire de la mission repose sur l'I.S.D.C. (*Integral Science Data Center*) dont la tâche principale sera de permettre aux non-spécialistes de mener des observations dans la bande spectrale d'*Integral*.



La mission Integral quelques semaines avant le lancement ; on reconnaît devant le spectromètre SPI, et à l'arrière l'imageur Ibis

*Le télescope Ibis.* L'objectif prioritaire d'Ibis, conçu par un consortium de laboratoires presque exclusivement européens<sup>2</sup>, est de fournir une localisation précise des sources dans la bande de 15 keV à 5 MeV, assortie d'une estimation de leur spectre et d'une mesure de leur variabilité. Combinant le meilleur de Sigma (l'ouverture codée pour produire des images fines du ciel), et le meilleur de l'expérience Comptel à bord de l'Observatoire à Rayons Gamma Compton (la signature Compton pour rejeter le bruit de fond), Ibis offre un excellent compromis masse/performance pour un télescope opérant dans la bande des rayons  $\gamma$  de basse énergie. Doté d'un pouvoir séparateur comparable à celui de Sigma, Ibis fait en effet montre d'une sensibilité accrue d'un ordre de grandeur et d'une couverture spectrale plus étendue.

<sup>2</sup> Istituto di Astrofisica Spaziale, Frascati, Istituto di Tecnologie e Studio sulle Radiazioni Extraterrestri, Bologne, Istituto di Fisica Cosmica ed Applicazioni Informatica, Palerme, Italie ; Service d'Astrophysique du Commissariat à l'Énergie Atomique, Saclay, France ; Université de Valence, Espagne ; Université de Tübingen, Allemagne ; Université de Bergen, Norvège ; Institut de Recherche Spatiale, Institut Copernicus, Varsovie, Pologne ; Nasa Marshall Space Flight Center, Huntsville, États-Unis.

Ibis comprend deux plans détecteurs de grande surface ( $3000 \text{ cm}^2$ ), montés à 10 cm l'un de l'autre. Le plan détecteur supérieur est une nappe de semi-conducteurs CdTe conférant à Ibis un seuil de détection vers 15 keV, un atout déterminant au vu des résultats de Sigma et de l'Observatoire à Rayons Gamma *Compton*. L'excellente résolution spatiale de cette couche détectrice – la taille des éléments CdTe est de 4 mm – est décisive pour localiser les sources avec précision. Compte tenu des qualités de spectrométrie  $\gamma$  du CdTe, Ibis montre une bonne sensibilité aux raies fines, en particulier dans la bande 15-100 keV où l'on s'attend à rencontrer certaines raies nucléaires clé, comme les raies à 68 et 78 keV que produit la désintégration du titane 44.

Le plan détecteur inférieur est formé d'une mosaïque de scintillateurs CsI couplés à des photodiodes. Un masque codé à base d'éléments de tungstène, monté à 3,1 m du plan de détection, procure à Ibis un pouvoir séparateur de 12 minutes d'arc et un champ de vue à mi-sensibilité de 350 degrés carrés. Un blindage passif, en forme de pyramide tronquée, joint les plans de détection et l'ouverture codée afin de réduire le bruit de fond induit par le rayonnement de basse énergie émis en dehors du champ de vue. Un blindage actif, constitué de panneaux de scintillateurs BGO (germanate de bismuth), couvre la base et les côtés de l'ensemble de détection pour atténuer le bruit à haute énergie. L'usage en coïncidence des deux plans détecteurs permet d'identifier la signature de l'interaction Compton, contribuant ainsi à accroître la sensibilité d'Ibis à haute énergie dans un mode d'observation particulier d'Ibis, le mode Compton, mode auquel j'ai beaucoup contribué avec mon étudiant Michaël Forot, et dont je reparlerai plus loin.

*Le spectromètre Spi.* Motivés par les résultats de l'Observatoire à Rayons Gamma *Compton* relatifs aux sources interstellaires de raies  $\gamma$ , les laboratoires européens et américains<sup>3</sup> impliqués dans la conception du spectromètre Spi ont adopté un champ de vue le plus vaste possible au détriment du pouvoir séparateur, l'effort portant avant tout sur la résolution en énergie dans la gamme 15 keV-10 MeV. Le plan détecteur de Spi est constitué d'un réseau hexagonal de 19 semi-conducteurs de germanium couvrant une surface utile de  $500 \text{ cm}^2$ . Les détecteurs germanium sont montés dans un cryostat qui les maintient à une température de 85 kelvins par une combinaison de dispositifs réfrigérants actifs et passifs. Les qualités de spectrométrie du germanium confèrent à Spi un pouvoir de résolution  $E/\Delta E \approx 650$  à 1,33 MeV, quinze fois meilleur que celui du spectromètre Osse à bord de l'Observatoire à Rayons Gamma *Compton*.

Le spectromètre Spi comporte lui aussi un masque codé à base d'éléments de tungstène monté à 1,7 m du plan de détection. Ce dispositif lui procure un pouvoir séparateur assez modeste ( $\sim 2$  degrés), bien meilleur toutefois que celui du spectromètre Osse, ainsi qu'un champ de vue

---

<sup>3</sup> Centre d'Étude Spatiale des Rayonnements, Toulouse, Service d'Astrophysique du Commissariat à l'Énergie Atomique, Saclay, France ; Max Planck Institut für Extraterrestrische Physik, Garching bei München, Allemagne ; Université de Valence, Espagne ; Istituto di Fisica Cosmica e Tecnologie Relative, Milan, Italie ; Université de Louvain-la-Neuve, Belgique ; Université de Birmingham, Royaume-Uni ; Université de Californie, San-Diego, Université de Berkeley, Nasa Goddard Space Flight Center, Greenbelt, États-Unis.

à mi-sensibilité de 490 degrés carrés. Un ensemble de scintillateurs BGO enveloppe presque complètement le dispositif de détection afin de réduire le bruit de fond de l'appareil. En se prolongeant loin au dessus du plan de détection, ce blindage actif contribue également à réduire la susceptibilité du spectromètre aux rayonnements émis en dehors du champ de vue de l'appareil.

## ***Simulations et étalonnages du télescope Integral/Ibis***

### **Simulations des configurations d'Ibis**

Grâce à l'expérience que j'avais obtenue sur Sigma, j'ai créé des modèles Monte-Carlo d'Ibis afin d'étudier et d'optimiser les différentes configurations envisagées au début du projet Integral en 1995 (deux plans détecteurs, trois plans détecteurs, positionnement de l'anticoïncidence, ...). Ces études ont permis d'aboutir petit à petit à la configuration d'Ibis tel qu'elle existe actuellement.

Elles ont aussi servi de base au simulateur qui a été ensuite développé, sous ma responsabilité, pendant 5 ans, regroupant la contribution de 6 pays européens. Ce simulateur détaille avec précision les différents détecteurs d'Ibis (ISGRI, PiCsIT, Veto) et prend en compte toutes les étapes du traitement électronique de l'information dans le télescope. Un site Web dédié a aussi été créé afin de faciliter l'interface utilisateur avec le simulateur. Ce simulateur est aussi maintenant régulièrement utilisé pour définir la réponse d'Ibis lors d'observations de sursaut  $\gamma$  en dehors du champ de vue du télescope (Marcinkowski et al., 2006). L'observation par Ibis de ces sursauts a d'ailleurs fait l'objet d'un communiqué de presse de l'ESA

### **Les étalonnages au sol**

J'ai participé à la définition du plan de calibration d'Ibis, afin de valider les résultats du simulateur en exposant, comme décrit précédemment, les différents sous-systèmes du télescope ainsi que le télescope complet, à plusieurs sources radioactives. Ce processus a ainsi permis de valider la simulation aux différentes phases de construction des sous-systèmes et du télescope entier.

J'ai assuré la coordination des étalonnages « end to end » du satellite *Integral* à l'ESA/ESTEC, au début 2002, au Pays-Bas, en binôme avec un ingénieur de l'ESA, en concevant le plan de calibration, en assurant la réalisation par le CEA du dispositif de calibration, contenant un porte source, un générateur de rayons X, et des cibles de fluorescence X composées de différents matériaux, et en supervisant les trois semaines d'étalonnage. Après avoir suivi une formation pour obtenir le CAMARI avec deux autres collègues du CEA, nous avons fait fonctionner le générateur de rayon X pendant la durée des étalonnages. Tous ces résultats nous ont permis d'obtenir une connaissance complète du satellite et de ces principaux télescopes à masque codée, Ibis, SPI et les deux Jem-X.

## **Les étalonnages en vol**

J'ai enfin participé à la définition et à la réalisation des étalonnages en vol, surtout durant la période de recette du satellite, en automne 2002. Depuis, *Integral* observe le Crabe deux fois par an afin, principalement, d'affiner notre connaissance de la réponse en énergie des télescopes et d'améliorer les matrices de réponses. Plus particulièrement orienté au départ vers l'étude de la réponse d'Ibis à basse énergie et/ou hors de l'axe du télescope, les mesures qui s'effectueront dans les prochaines années auront aussi pour objectifs de mieux connaître la réponse au MeV d'Ibis.

## ***Création des matrices de réponse Ibis***

Grâce au simulateur validé, comme on l'a vu, par les mesures d'étalonnage au sol et en vol, j'ai eu la responsabilité de créer les matrices de réponse des trois détecteurs d'Ibis: ISGRI, PiCsIT, et le mode Compton, que nous détaillerons plus loin. Ce travail se fait régulièrement, en conjonction avec le centre de données d'*Integral*, l'ISDC, tout au long de la mission, en parallèle avec les différentes versions du logiciel de traitement de données d'*Integral* (OSA). Les matrices sont de plus en plus perfectionnées, tentant de reproduire de plus en plus précisément le spectre observé, en prenant en compte notamment la perte de charge dans les cristaux de CdTe d'ISGRI, et les effets de l'électronique de traitement à bord. Ce processus est décrit dans la publication n°2.

## ***Développement de l'analyse de données du mode Compton d'Ibis***

Comme indiquée plus haut, le mode Compton d'Ibis utilise les événements qui produisent un signal dans les deux principaux détecteurs, ISGRI et PiCsIT. L'étude et l'analyse de ces événements permettent de produire des cartes du ciel avec la même finesse que celle d'ISGRI, mais en allant à plus haute énergie ; en effet, l'efficacité d'ISGRI chute après 150 keV alors que le mode Compton commence vers 200 keV et permet de monter jusqu'au MeV. L'avantage du mode Compton sur les autres moyens de mesure à haute énergie d'*Integral*, comme Ibis/PiCsIT et SPI, est son très faible niveau de bruit de fond. Les mesures au delà de 200 keV et jusqu'à plusieurs MeV des télescopes  $\gamma$  des années précédentes ont, en effet, toujours été rendues très difficiles de par un très important bruit de fond radioactif dans l'expérience, comparé à la faible luminosité des sources célestes observées.

Comme nous le verrons au chapitre 3 et 4, les signatures des systèmes doubles d'étoile à trou noir se trouvant aussi à haute énergie, je me suis beaucoup intéressé à ces données, et j'ai suivi la thèse de Michaël Forot afin de développer les algorithmes de traitement du mode Compton, décrit dans la publication n°3. Le principal inconvénient du mode Compton, qui nous a demandé un travail très précis, est le nombre relativement grand d'événement fortuit dans ce mode. Un événement fortuit est un événement ISGRI associé aléatoirement à un événement PiCsIT du fait qu'il se retrouve dans la même fenêtre de coïncidence temporelle,

et qui donc n'ont rien à voir avec l'effet Compton. Ces événements créent des fausses détections de sources dans les images et doivent être soustraits avec une très grande précision. Ce procédé est décrit dans la publication n°3.

Grace aux logiciels que nous avons développés avec Michaël, nous avons pu mettre en évidence la polarisation du Crabe entre 200 et 800 keV, polarisation qui n'avait jamais été mesurée auparavant. Cette grande première du satellite Integral, effectuée en parallèle avec des travaux analogues basés sur les données du spectromètre SPI, fait l'objet d'une publication soumise à l'*Astrophysical Journal Letters* en septembre 2008.

Ces logiciels nous ont aussi permis d'étudier un système de localisation en 3 dimensions d'une source radioactive, un système nouveau qui nous a conduit, mon collègue Olivier Limousin et moi-même, à déposer un brevet en 2006.

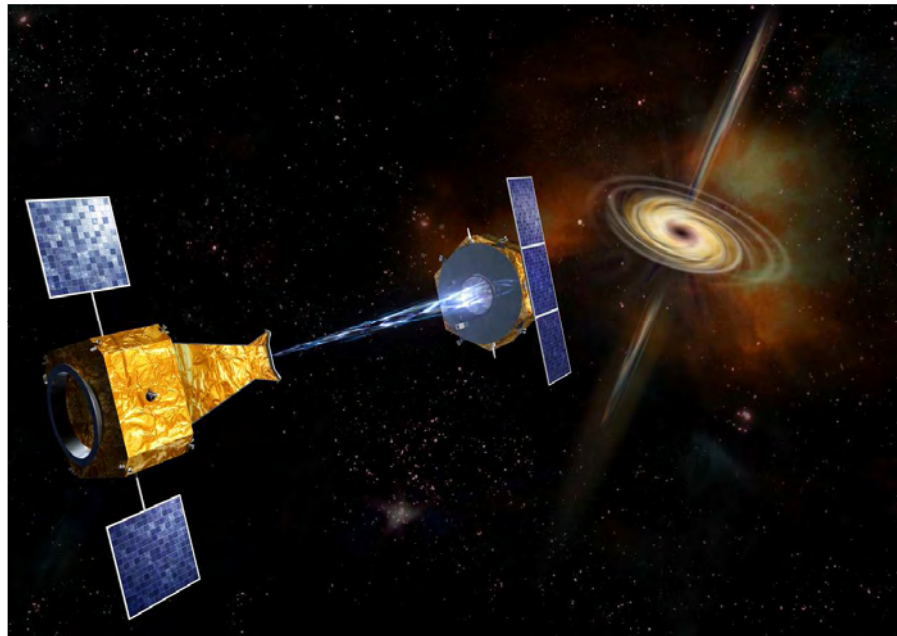
## ***Le projet Simbol-X***

Le projet Simbol-X est un télescope à haute énergie de nouvelle génération, financé par le CNES et l'Agence Spatiale Italienne (ASI). Il couvre la gamme s'étendant des rayons X « classiques » aux rayons X «durs», soit de 0.5 à 70 keV environ. En utilisant dans toute cette gamme un dispositif de focalisation réservé jusqu'alors aux rayons X de moins de 10 keV, via la construction d'un télescope de très longue focale s'appuyant sur deux satellites volant en formation, Simbol-X permet un gain d'environ deux ordres de grandeur en sensibilité et en résolution angulaire par rapport aux télescopes X-durs actuels. La sensibilité de Simbol-X est de moins de 1  $\mu$ Crab à 10 keV et de 5  $\mu$ Crab à 30 keV pour 100 ks d'observation (On peut observer en 100 000 s des sources aussi faibles qu'un millionième de la source la plus brillante du ciel, le pulsar du Crabe).

Le télescope Simbol-X est dans son principe similaire aux télescopes X classiques (tels XMM–Newton et Chandra). Il s'appuie ainsi sur une optique à base de miroirs attaqués en incidence rasante, dans la configuration optimale dite de Wolter I. L'obtention d'une optique focalisatrice pour des énergies de plusieurs dizaines de keV, avec une surface efficace importante, passe ainsi par des miroirs multicouches et une géométrie permettant de très faibles angles d'attaque pour des grands diamètres de miroir, c'est à dire de très grandes longueurs focales. Dans le cas de Simbol-X, une focale de 20 mètres a été jugée comme offrant le meilleur compromis. Une telle distance ne peut être raisonnablement atteinte qu'en s'appuyant sur deux satellites volant en formation.

Le concept du plan focal est un détecteur à deux plans imageurs superposés. Le tout sera muni d'une anticoïncidence active pour minimiser le bruit de fond, et d'un filtre optique pour supprimer la lumière optique et UV parasite. L'imageur basse énergie sera une matrice monolithique de détecteurs à dérive en silicium (« MPD »), de 450  $\mu$ m d'épaisseur. L'imageur haute énergie sera une mosaïque de détecteurs pixellisés à base de CdZnTe, de 2 mm d'épaisseur hybrides sur leur électronique de lecture.

L'orbite choisie pour Simbol-X est une orbite au delà des ceintures de radiation ( $> 70000$  km) ayant une période de 4 jours. En tenant compte des périodes de recette en vol, d'étalonnage, etc., une durée totale de mission de 5 ans est demandée (3 ans nominal plus 2 ans d'extension), et une date de lancement en 2014 est envisagée.



Vue d'artiste de la mission Simbol-X. Le satellite miroir, à l'arrière, focalise les rayons X en provenance d'une source céleste vers le satellite détecteur.

## ***Définition du projet Simbol-X et conception de l'anticoïncidence***

Dans le cadre du futur projet Simbol-X, j'ai pris depuis 2006 la responsabilité du groupe « Simulation » et du groupe « Bruit de fond », qui devront effectuer les mêmes travaux d'optimisation et d'estimation que ceux que j'ai effectués pour Ibis. Ces groupes devront en particulier étudier les différentes composantes du bruit de fond qu'enregistrera le satellite détecteur, et établir des stratégies à bord (coïncidence, anticoïncidence, ...), afin de les diminuer le plus possible. L'étude préliminaire de ce bruit de fond est décrite dans la publication n°4. À terme, le but du groupe « Simulation » sera aussi de produire un simulateur de Simbol-X aussi réaliste que possible, permettant, entre autre, de calculer les matrices de réponse de l'instrument.

Dans le même ordre d'esprit, j'ai pris la responsabilité scientifique à l'APC, depuis 2007, du système d'anticoïncidence actif et passif du détecteur de Simbol-X, ce qui m'amène, conjointement au chef de projet, à encadrer une équipe d'une dizaine de personnes regroupant mécaniciens, électroniciens, et instrumentalistes. L'année 2007 nous a amené à montrer la faisabilité de notre concept d'anticoïncidence à base de scintillateurs plastiques, de fibres, et

de PMs. Cela nous permis de clore de manière positive la phase A de la mission. Nous passons actuellement en phase B, où nous devrons concevoir les différents éléments de l'anticoïncidence et montrer que leurs performances correspondent bien à ce qu'on attend. Le suivi des performances, et la mise en œuvre des moyens pour ce faire, sera une de mes taches principales dans ce groupe.

## *Bibliographie*

Marcinkowski R. et al., 2006, A&A, 452, 113

## *Publications principales afférentes à ce chapitre*

**Calibration of detectors for soft gamma-ray astronomy: the Monte Carlo approach applied to the SIGMA telescope**

D. Barret, P. Laurent,

1991, *Nuclear Instruments and Methods in Physics Research, A* 307, 512

**Status of the Integral/Ibis telescope modeling and of the response matrices generation**

P. Laurent, O. Limousin, M. Cadolle-Bel, P. Goldoni, G. Malaguti, E. Caroli, G. De Cesare, M. Del Santo, A.J. Bird, J. Grygorczuk, J.M. Torrejon

2003, *Astronomy & Astrophysics*, 411, L185

**Compton Telescope with a Coded Aperture Mask: Imaging with the Integral/Ibis Compton Mode**

M. Forot, P. Laurent, F. Lebrun et O. Limousin

2007, *Astrophysical Journal*, 668, 1259

**Monte Carlo simulations of stacked X-ray detectors as designed for SIMBOL-X**

C. Tenzer, E. Kendziorra, A. Santangelo, M. Kuster, P. Ferrando, P. Laurent, A. Claret, R. Chipaux,

2006, *SPIE*, 6266, 78



# Calibration of detectors for soft gamma-ray astronomy: the Monte Carlo approach applied to the SIGMA telescope

D. Barret <sup>a</sup> and P. Laurent <sup>b</sup>

<sup>a</sup> Centre d'Etude Spatiale des Rayonnements, Toulouse, France

<sup>b</sup> Service d'Astrophysique, CEN Saclay, France

Received 8 February 1991

The general problem of calibrating soft gamma-ray (100 keV–1 MeV) detectors is illustrated in the case of the SIGMA experiment. Particularly, the advantage of coded mask experiments for spectroscopy and the related specific calibration difficulties are considered. It is shown that a Monte Carlo simulation can separate in the spectrum the components due to the experiment itself and those due to the scattering in the environment and permits to take into account experimental configuration modifications after the calibrations. A very detailed geometrical description of the SIGMA telescope is proposed and its in-flight energy response is estimated from Monte Carlo simulations.

## 1. Introduction

The soft gamma-ray domain (100 keV–1 MeV) is so dominated by the Compton scattering that calibration of a detector is really difficult because any measurement strongly depends on the detector environment. The calibrations should then be done in exactly the same environment as the observations. This is a major problem for space experiments for which the in-flight environment can be entirely different from the laboratory in which they are calibrated. In turn laboratory calibrations of the energy response of a detector have little to do with its in-flight performances.

One possible way to solve this problem is to estimate the energy response of the experiment from a Monte Carlo simulation. Such a way offers also the possibility to estimate the detector response in the energy ranges where no radioactive sources are available. This approach has been followed with some success in a few cases in the past [1–3]. In most cases, the difficulties were due to an insufficient knowledge of the detector housing [4], environment or to an oversimplified geometrical description of the experiment which was unavoidable because of the limited performances of yesterday's computers. Today a very accurate simulation is accessible without prohibitive computing time, however, it is not obvious to determine a priori which are the experimental components essential for an accurate simulation. This difficulty can be overcome by an iterative process in which the laboratory measurements are fitted with a Monte Carlo simulation of the experiment and its environment. Different components are

added in the simulation until the simulation reproduces the calibrations accurately. The in-flight energy response can then be obtained by adapting the simulated environment to the space conditions.

In this article the general problem of calibrating a soft gamma-ray experiment will be illustrated with a few measurements made in the laboratory in different conditions with the detector of the SIGMA experiment. The peculiarity of coded mask experiments for spectroscopy will be explained. A detailed geometrical model of the telescope and its laboratory environment, including all components contributing to the observed spectrum, will be proposed and it will be shown that it fits the calibrations. Finally, the in-flight energy response of the SIGMA experiment for celestial sources will be presented.

## 2. The SIGMA experiment

The SIGMA telescope, a French experiment onboard the soviet GRANAT satellite, has been launched on the first of December 1989 from the Baikonour space center and is successfully operating since then. SIGMA has been designed to provide high angular resolution (15') images of the sky in the domain 35 keV–1.3 MeV. It features basically a NaI(Tl) position sensitive detector based on the Anger camera principle [5] and a URA type coded mask [6] made of  $0.94 \times 0.94 \times 1.5$  cm tungsten elements. Noise in the detector comes from charged particles and off-axis gamma-rays. The lateral noise is reduced by the use of a thick CsI

anticoincidence well and the on-axis charged particle background is reduced by the use of a plastic anticoincidence disc mounted in front of the detector. A passive graded shield (Pb: 0.5 mm, Ta: 0.1 mm, Sn: 0.4 mm) is wrapped around the tube holding the mask in order to reduce the low energy background. Fig. 1 shows an exploded view of the telescope; for more details about the SIGMA experiment and mission, the reader is referred to ref. [7]. SIGMA can provide 95 consecutive energy bands in each of which an image of the sky is performed. The deconvolution of each image yields the position and flux of each detected source. It is then possible to obtain the spectrum of a source independently of the emission of its surrounding (others sources, diffuse emission). However a precise knowledge of the energy response function of the telescope is required to obtain the genuine source spectrum from the observed one.

### 3. Laboratory measurements

In this energy domain a number of radioactive elements decay in a reasonable time ( $> 1$  month) providing one or several lines which can be used to measure the energy response function of the experiment. The calibrations of the SIGMA experiment will be described in detail in ref. [8] but some relevant measure-

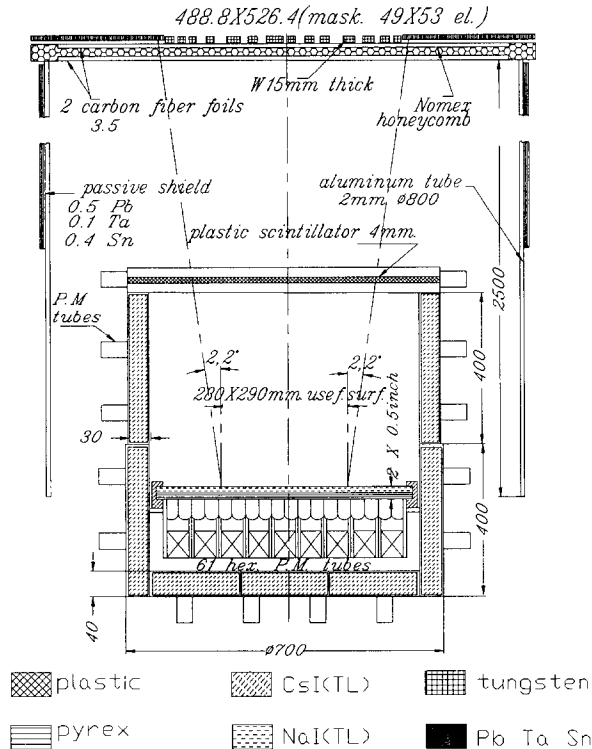


Fig. 1. Exploded view of the SIGMA telescope.

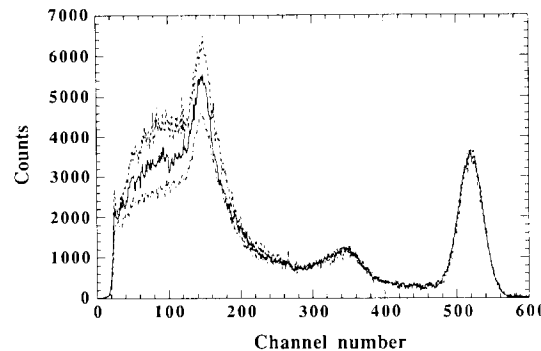


Fig. 2.  $^{137}\text{Cs}$  spectra obtained with various distances of the source from the ceiling of the laboratory: 0 m (dotted line), 1 m (continuous line), 2 m (interrupted line). Each channel is  $\sim 1.25$  keV wide.

ments will be quoted here when necessary. The energy response has been found to vary in different conditions and three examples will be given here.

Some measurements have been performed with the detector alone, mainly with the aim of measuring its spectral resolution. The detector of the SIGMA telescope is an Anger camera adapted to resist the launching vibrations. It consists of a NaI crystal 57 cm in diameter and 1.2 cm thick viewed by 61 hexagonal photomultiplier tubes through a 1.2 cm thick pyrex disc. The tubes are inserted in the cavities of a honeycomb carbon fiber glued to the pyrex disc. Each tube has been potted with silicon resin. The pyrex disc and mainly the tube potting induce a very strong backscattered component clearly visible in the spectra of fig. 6d.

#### 3.1. Room effect

The measurements have been made in a laboratory whose ceiling is 2.5 m from the ground, the upper side of the detector being 1.6 m below the ceiling. Fig. 2 illustrates the energy response of the detector for a  $^{137}\text{Cs}$  source placed at different heights above the detector. All spectra have been normalized on the photopeak. Clearly they differ strongly in the region of the backscattered peak. This illustrates the effect of the source distance from the ceiling, the backscattering being more and more important as the source is getting close to the ceiling.

Measurements have also been performed using a tungsten collimator. Here, even at 60 keV, the energy response and particularly the energy resolution depend on whether or not a collimator is used. This is illustrated in fig. 3 where two spectra of an americium source have been plotted. The wide peak obtained without the collimator is due to photons diffused in the environment (walls, ceiling, etc.) because, at this energy, losses by Compton scattering are small and the

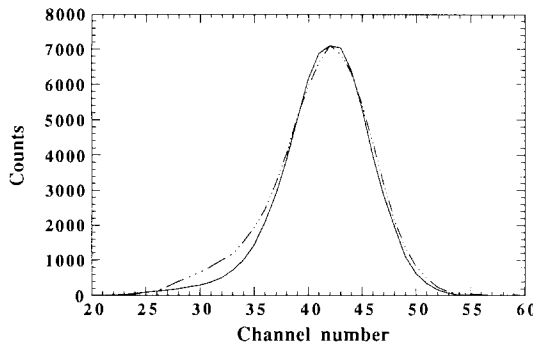


Fig. 3.  $^{241}\text{Am}$  spectra obtained with (continuous line) and without (interrupted line) a tungsten collimator. Each channel is  $\sim 1.25$  keV wide.

diffused photons have nearly the same energy as the photons coming directly from the source.

### 3.2. Source type effect

Standard radioactive sources can be provided mainly in two types, disc or pencil. In the disc type, the radioactive solution is deposited in the central part of a plastic support. In the pencil type, the radioactive element is contained in the nail of an aluminum pencil-shaped support. Fig. 4 shows the difference in the spectrum of a cesium source as a function of the type of source which has been used.

All these measurements illustrate the general problem of getting the intrinsic detector response and in particular, for space experiments, of getting the in-flight spectral response from laboratory measurements.

### 4. The case of coded mask experiments: the SIGMA telescope

In the case of the SIGMA telescope, and more generally for coded mask experiments, getting the in-

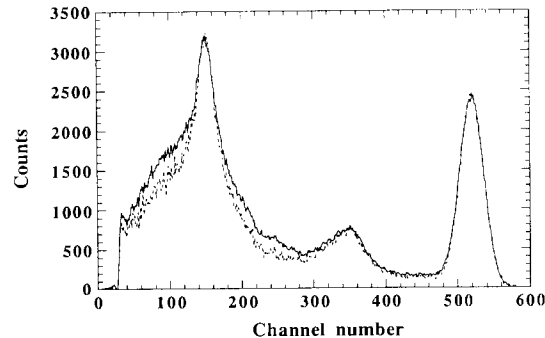


Fig. 4.  $^{137}\text{Cs}$  spectra obtained with a disc type (continuous line) and a pencil type source (interrupted line). Each channel is  $\sim 1.25$  keV wide.

flight spectral response is even more difficult because the image deconvolution process affects the energy response. One remarkable feature of the coded mask technique is that it not only provides a good angular resolution without loss of sensitivity (provided the spatial resolution of the detector is small compared to the mask-element size) but also improves the energy response of soft gamma-ray detectors. This is particularly true in the case of the SIGMA experiment, where, as noted earlier, the backscattered component is very important. The photons which interact primarily in the NaI give interaction locations distributed according to the mask pattern. The photons which experience a scattering prior to their detection in the NaI give almost uniformly distributed interaction locations. The effect of the spatial deconvolution on the spectrum shape is to suppress most of the photons scattered in other parts of the experiment before their interaction in the detector. This mainly reduces the backscattered peak and of course, the lower the backscattered peak, the better the spectral response.

The standard spatial deconvolution of an image obtained with a coded mask is the process of computing the correlation between the basic mask pattern and the image. The maximum correlation is obtained at the source position. At this position, the correlation can be expressed as the total number of counts in the image found in the transparent elements of the basic mask pattern (white cells) minus the total of those found in the opaque elements of the basic mask pattern (black cells). However, the shape of a source spectrum after spatial deconvolution is of course dependent on the size of the mask-element shadow which, of course, is smaller in flight where the celestial sources are at an infinite distance compared to a few meters for radioactive sources in the laboratory.

The only way to obtain the in-flight energy response for the deconvolved images is therefore to have a precise estimate of the spectral-shape dependence on the size of the mask-element shadow. Here again, a Monte Carlo simulation can provide this estimate. This point will be discussed later (see section 5.2).

### 5. Simulation of the SIGMA experiment

For the simulation of the SIGMA experiment, the Monte Carlo code EGS4, developed at Stanford University [9], has been used. Taking into account the EGS4 limitations and the nearly cylindrical shape of most components, the simulation features generally coaxial hollow or full cylinders with the only exception of the mask represented by a rectangular plane parallel layer.

Each component of the experiment in which source photons can interact has been taken into account. The

simulated telescope features the coded mask and its support (carbon fiber), the passive shield with three layers (Pb, Ta, Sn), the plastic anticoincidence and its support, the detector and its housing, the pyrex disc, the photomultipliers, the lower and lateral CsI anticoincidences with their housing (aluminum and silicon) and finally the platform. Fig. 5 gives a schematic view of the simulated telescope.

Complicated components, such as the ensemble of the photomultipliers and their electronic have been represented by a uniform layer with an average approximate composition, the density being adjusted to match the mass of the whole component. The cross sections

have been computed with the preprocessor PEGS4 which can impute cross sections for composite materials. Since the path length of a 1 MeV electron is of the order of 2.5 mm in the NaI, propagation of the electrons have been neglected. This considerably shortens the computing time. Fluorescent-photon escape has been taken into account at low energy ( $E < 200$  keV). For each interaction of a photon in the NaI, EGS4 gives the location of the interaction and the energy deposited. In order to match the calibrations, the spatial and energy resolution of the detector should then be taken into account. This is done using a Gaussian random generator with the dispersion measured during

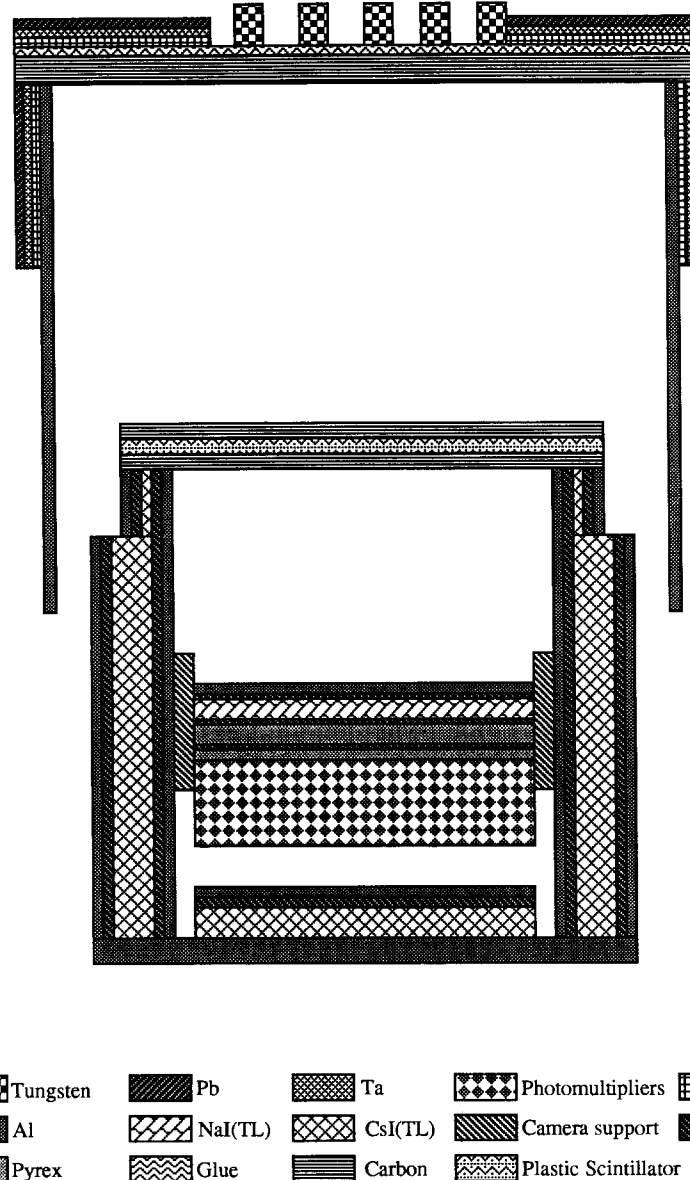


Fig. 5. Schematic of the SIGMA telescope geometrical description used for the simulations. For clarity, the dimensions of each component are not representative.

the calibrations. For multiple Compton interactions, the barycenter of the interactions should be taken with the sum of the deposited energies. However, since the effect of multiple scattering is already taken into account in the measures of the spatial resolution, the primary interaction location has been used instead of the barycenter. The simulation of the anticoincidence system takes into account the energy resolution and threshold of the CsI and the plastic scintillator for gamma-rays.

During the setup of the model, some of the critical effects, worth mentioning here, have been acknowledged. First, it has been noticed that the position of the Compton front and the height of the Compton continuum are strongly dependent on both the threshold and the energy resolution of the anticoincidence. Moreover, the efficiency at low energy ( $< 80$  keV) is strongly affected by the fluorescent-photon escape since the energy deposited in the detector by  $E > 35$  keV gamma-rays can be found under the lower detection threshold (i.e. 35 keV).

### 5.1. Total spectra

The spectra of all events detected on the detector regardless of their location is the total spectra. Disc-type sources have been found to be extended, some-

times by as much as 8 mm. For this reason only pencil type sources:  $^{241}\text{Am}$ ,  $^{109}\text{Cd}$ ,  $^{57}\text{Co}$ ,  $^{137}\text{Cs}$  and  $^{22}\text{Na}$  have been used for calibrations invoking spatial aspects. Due to the prohibitive computing time necessary to obtain the simulated spectra of the  $^{22}\text{Na}$  source, only the simulated spectra of the first four sources have been computed with sufficient accuracy.

The observed and simulated total spectra are displayed in figs. 6a–6d. A normalization has been applied to the simulated spectra by multiplying them by the total number of photons emitted by the calibration source during the measurement (corrected for dead time) and dividing them by the total number of photons generated in the simulation. In this way, not only the shape of the spectra can be compared but also the absolute efficiency.

The simulation described above could not exactly reproduce the total calibration spectra. In particular, in the case of the  $^{57}\text{Co}$ , the broad bump near 80 keV was too small by 20%. For the  $^{137}\text{Cs}$  spectrum, the backscattering peak was too small by about 10% and the small bump observed near 300 keV was not reproduced. The source used during the calibrations being of the pencil type, an aluminum cylinder of the proper dimensions has been added in the simulation just above the source. With this modification, the  $^{137}\text{Cs}$  backscattered peak was nicely reproduced. During the simula-

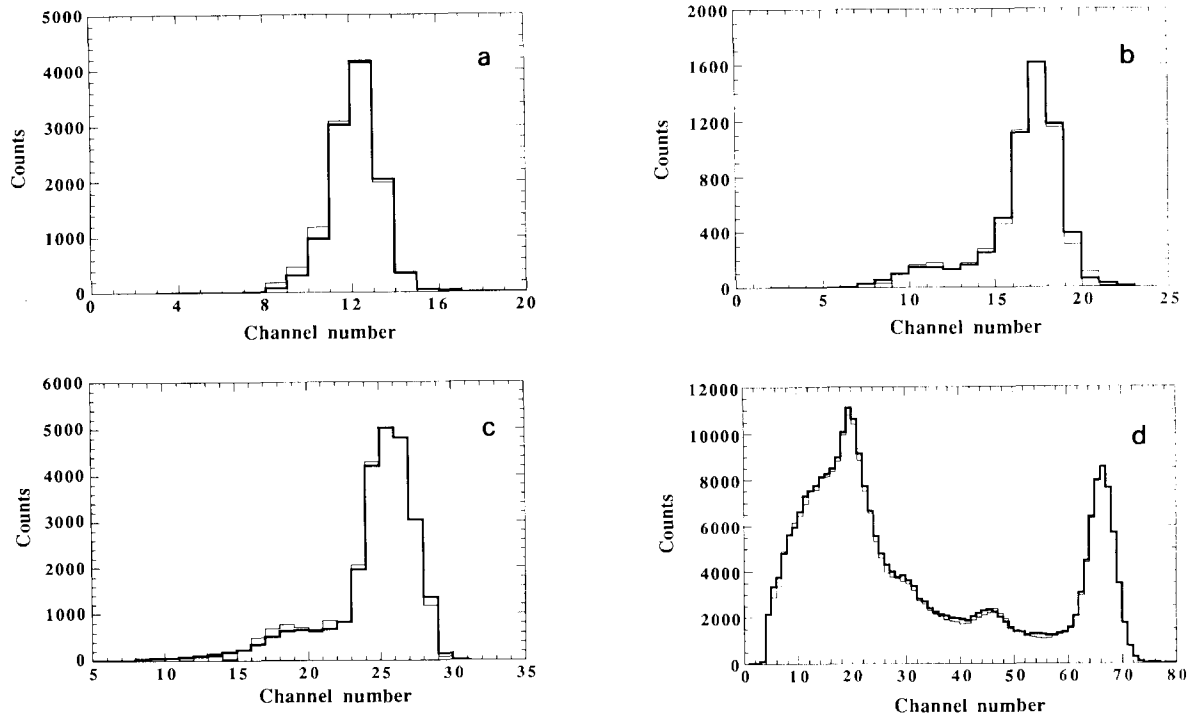


Fig. 6. Total spectra measured (thick line) and simulated (narrow line) for various radioactive elements (each channel is 5 keV wide, except for the  $^{137}\text{Cs}$  spectra for which the channel width is 10 keV).

tions, the source was held by a 5 mm thick plastic disc 15 cm in radius. Compton scattering of 662 keV photons in this disc gives  $\sim 300$  keV photons in the detector direction. Indeed, the inclusion of such a disc in the simulation adds a 300 keV bump of the proper shape and amplitude in the  $^{137}\text{Cs}$  spectrum and completes the 80 keV bump observed in the  $^{57}\text{Co}$  spectrum.

The left wing of the photopeak was higher in the calibration spectrum. It has been acknowledged that, since the source was not at infinity, the photon beam passing through the mask is not parallel and photons can scatter in the aluminum tube supporting the mask and the passive shield before being detected. Of course such a component will disappear from the spectrum in flight conditions.

### 5.2. Spectra after image deconvolution

The observed and simulated spectra after image deconvolution for the four sources considered earlier, are displayed in figs. 7a–7d. One can notice that the backscattered peak, although very much reduced, is still present. At low energy, it is mainly due to photons backscattered in the pencil source which come on the detector from a position very near the source and are therefore still spatially correlated with the source photons. At high energy it is mostly due to photons

backscattered near the detector (mainly in the pyrex disc).

For 662 keV photons, most events (75%), having their first interaction in the detector, will be found in white cells, the only loss (25% found in black cells) is due to the spatial resolution (which includes the effect of multiple scattering). Most of the backscattered photons are detected far from the position where they first crossed the detector; they yield therefore a more uniform coverage (60% in whites and 40% in blacks) and are thus mostly removed in the spatial deconvolution process. As a result, most of the backscattered component of the spectrum disappears during the spatial deconvolution. This is clearly visible in fig. 7d.

As noted earlier, the magnitude of this effect depends on the size of the mask-element shadow. To illustrate this dependence, the backscattered peak of the simulated spectra (before convolution with the energy resolution) found in white cells for a 513 keV source at 2.5 m and at infinity are displayed in fig. 8a. As expected, the backscattered peak for a nearby source (large cells) is higher than that for a remote source (small cells). The backscattered peak of the simulated spectra (before convolution with the energy resolution) found in black cells for both source distances is given in fig. 8b. Of course, the reverse situation is also observed i.e. the backscattered peak for a nearby source

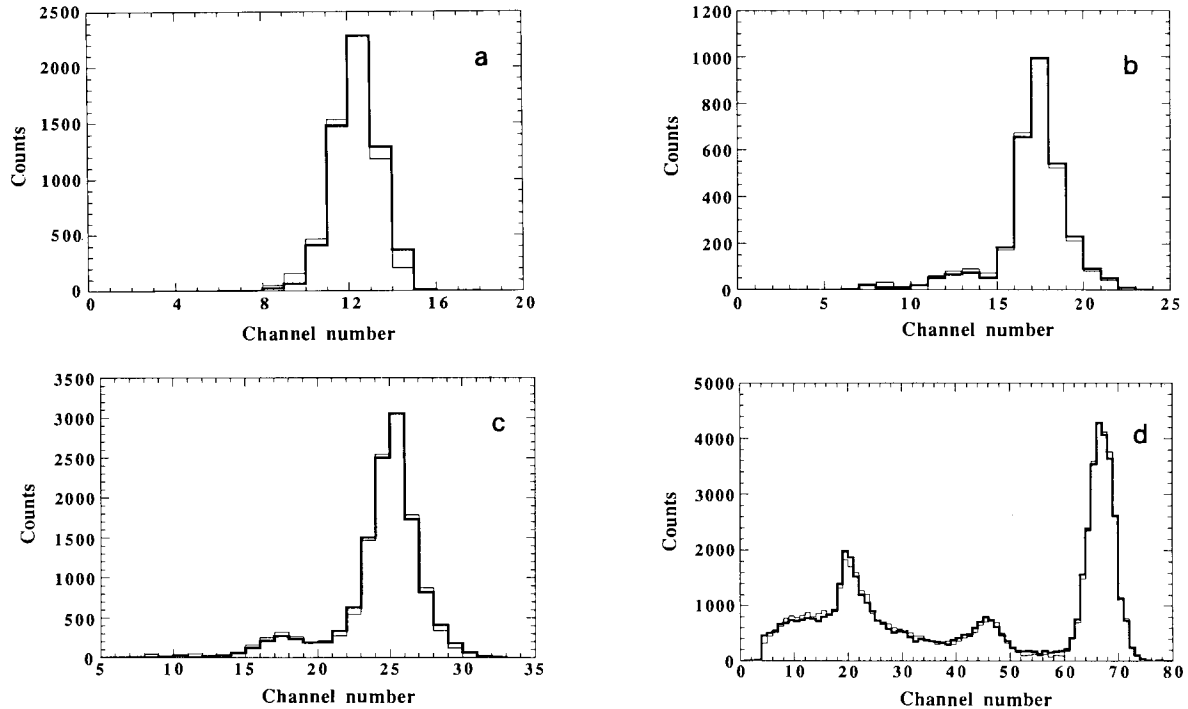


Fig. 7. Spectra measured (thick line) and simulated (narrow line) after image deconvolution (each channel is 5 keV wide, except for the  $^{137}\text{Cs}$  spectra for which the channel width is 10 keV).

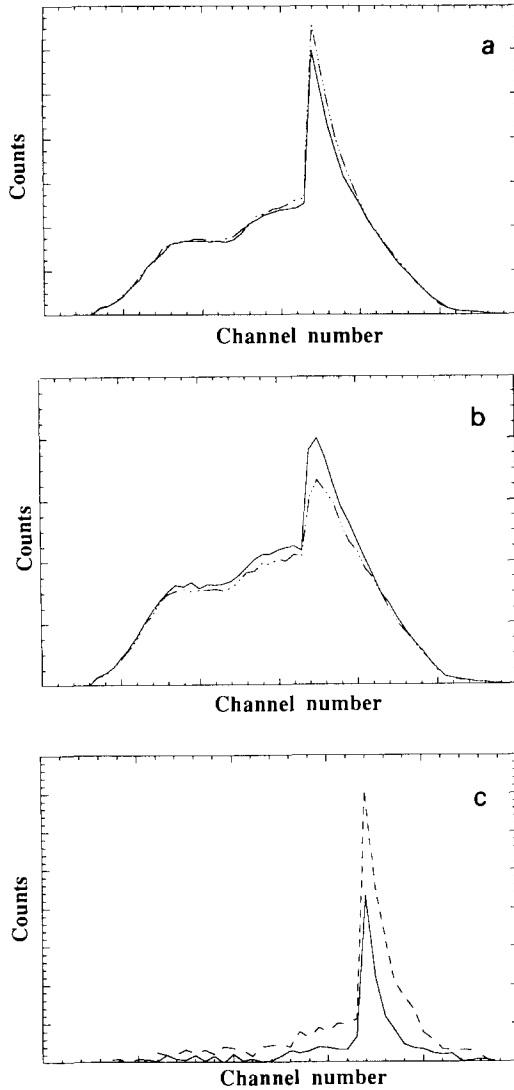


Fig. 8. (a) White cells backscattered peak of the simulated spectra (before convolution with the energy resolution) for a source at 2.5 m from the mask (interrupted line) and for a source at infinity (continuous line). (b) Black cells backscattered peak of the simulated spectra (before convolution with the energy resolution) for a source at 2.5 m from the mask (interrupted line) and for a source at infinity (continuous line). (c) backscattered peak of the simulated spectra (before convolution with the energy resolution) at the source position in the deconvolved images for a source at 2.5 m from the mask (interrupted line) and for a source at infinity (continuous line).

is lower than that obtained with the remote source. As a result, the deconvolved spectrum which is the difference "whites minus blacks" strongly depends on the source distance. Fig. 8c shows the backscattered peak

in the deconvolved spectrum for both source distances which shows that the in-flight spectra response is far better than the one measured in the laboratory.

## 6. The SIGMA energy-response matrix

The agreement between the calibration spectra and the simulation being satisfactory, it is now possible to adapt the simulation to the in-flight conditions. The main changes are: i) the photons come parallel to the telescope axis (source at infinity), ii) the aluminum cylinder of the calibration source is removed, iii) the plastic disc support of the sources is removed, iv) the spatial resolution is replaced by that measured in flight, and v) the lower threshold of the anticoincidence is set at its in-flight value.

Regarding point iv), it should be mentioned that a degradation of the spatial resolution at low energy has been noticed between the ground calibrations and the in-flight observations. The in-flight spatial resolution has been derived from the observations of strong sources as Cygnus-X1 and the Crab pulsar. This degradation is probably due to the noise induced in the detector by charged particles. Since the spatial resolution has a direct effect on the deconvolved spectra, mainly a reduction of the efficiency, the relevant value has to be used in the simulation. The lower anticoincidence threshold had to be raised because of the high background level inducing a too high dead time. With the ground threshold value, a number of photons interacting both in the detector and in the anticoincidence were removed. With the higher in-flight threshold value, far less photons are removed from the Compton continuum and the shape of the spectrum is thus modified.

It is worth noting that without the Monte Carlo approach it would not have been possible to take into account this evolution of the experiment characteristics.

With all these modifications, simulations all over the energy domain covered by SIGMA have been performed and have produced the in-flight energy response matrix of the experiment. This matrix has been successfully tested on the Crab nebula observations, yielding the canonical power law with an index of  $\sim -2$  [10], as observed by a number of experiments in this energy range [11,12].

## 7. Conclusion

Although the Monte Carlo approach is long and tedious, it offers a unique opportunity to take into account all differences between the in-flight and laboratory measurements and more generally to take into

account any evolution in the configuration or in the environment of an experiment. Namely, in the case of the SIGMA experiment, the following points could not have been tackled without a Monte Carlo simulation: i) dependence of the spectral shape on the size of the mask-element shadow, ii) the backscattering in the pencil type sources, iii) the scattering in the plastic disc support of the sources, iv) the evolution of the anticoincidence threshold, and v) the scattering in the aluminum tube during the laboratory measurements. In addition it allows a precise sampling of all the energy ranges covered by an experiment and more generally can provide information on the spectral response where no calibrations are available (off axis sources for example).

## References

- [1] E. Nardi, Nucl. Instr. and Meth. 83 (1970) 331.
- [2] M. Belluscio, R. De Leo, A. Pantaleo and A. Vox, Nucl. Instr. and Meth. 118 (1974) 553.
- [3] B. Grosswendt and E. Waibel, Nucl. Instr. and Meth. 133 (1976) 25.
- [4] K. Saito and S. Muriochi, Nucl. Instr. and Meth. 226 (1984) 449.
- [5] H.O. Anger, Brit. Astrophys. Trans. 5 (1966) 311.
- [6] E.E. Fenimore and T.M. Canon, Appl. Opt. 17 (1978) 337.
- [7] J.A. Paul et al., Adv. Space Res. (1991) in press.
- [8] P. Mandrou et al., (1991) paper in preparation.
- [9] W.R. Nelson, H. Hirayama and D.W.O. Rogers, EGS4 User Guide (1985).
- [10] L. Natalucci et al., Cospar, 1990, La Hague (1990).
- [11] W.A. Mahoney, J.C. Ling and A.S. Jacobson, Astrophys. J. 278 (1984) 784.
- [12] W.R. Cook et al., Adv. Space Res. (1991) in press.

## Status of the Integral/IBIS telescope modeling and of the response matrices generation

P. Laurent, O. Limousin, M. Cadolle-Bel, P. Goldoni, G. Malaguti, E. Caroli,  
G. De Cesare, M. Del Santo, A. J. Bird, J. Grygorczuk, and J. M. Torrejon

DSM/DAPNIA/SAp, CEA-Saclay, 91191 Gif-sur-Yvette Cedex, France

IASF/CNR, via Gobetti 101, 40129 Bologna, Italy

IAS, Area di Ricerca di Tor Vergata, via del Fosso del Cavaliere, 00133 Rome, Italy

University of Southampton, Highfield, SO17 1BJ, UK

CBK, Bartycka 18A, 00-716 Warsaw, Poland

Universidad de Alicante, Alicante, Spain

Received 25 September 2003 / Accepted 9 October 2003

**Abstract.** The main objective of the IBIS modeling activities is the generation of the IBIS spectral response matrices. This generation has been done step by step by firstly constructing a “calibrated model” of each IBIS sub-system. A “calibrated model” is defined as a GEANT Monte-Carlo model, further checked by intensive corresponding calibration. These calibrated models have been in a second step integrated in the whole IBIS Mass Model. This Mass Model has been checked then using the data obtained during the IBIS telescope calibration, the Payload Ground Calibration at ESA/ESTEC, and will be refined using In-flight calibration data acquired during the whole INTEGRAL mission. The different IBIS response matrices have been generated using the IBIS Mass Model. Here we will present a status of the Mass Model and of the response matrices generation, and show with the Crab pulsar calibration data that, with the new release of the spectral extraction software by ISDC, we will have a good IBIS/ISGRI response from 20 to 600 keV.

**Key words.** modeling – coded mask instruments – response matrices

### 1. Introduction

The IBIS instrument (Ubertini et al. 2003) launched on board the ESA INTEGRAL observatory on October 17 2002, is a coded aperture telescope. It consists of a dual detection layer operating in the energy range between  $\sim$ 15 keV and 10 MeV. The open end pixelized detector plane, ISGRI (Lebrun et al. 2003), is composed of 128 by 128 cadmium–telluride, CdTe, semiconductor detectors covering the energy range  $\sim$ 15 keV to 1 MeV. Beneath this plane, is situated a second detector, PiCsIT (Di Cocco et al. 2003), comprising 64 by 64 caesium–iodide, CsI, scintillation pixels functioning in the energy interval  $\sim$ 175 keV to 10 MeV. The detection unit is actively shielded by being encased on all but the sky side by bismuth germanate (BGO) scintillator elements, eight underneath and eight lateral modules. At energies below 100 keV, the BGO acts as a passive shield. Above this threshold, the BGO behaves as an active element eliminating coincident events with the detection layers. Thus polluting background events are vetoed using the BGO shield. 3.2 m above the mean detector plane, is placed the coded mask.

### 2. IBIS modeling

The generation of the IBIS response matrices have been done step by step by constructing a “calibrated model” of the IBIS telescope. A “calibrated model” is defined as a GEANT Monte-Carlo model, further checked by intensive corresponding calibration. We will detail below the status of this activity.

#### 2.1. IBIS QM modeling

In a first step, we have made a model of the IBIS Qualification Model (QM) by assembling the GEANT calibrated models of all the different IBIS sub-systems constituting the QM. This model has been used to plan the QM calibration, and check against the results of these calibration.

#### 2.2. IBIS detector assembly and flight model modeling

In a second step, every IBIS sub-system teams (ISGRI, PiCsIT, Veto, and detector frame) have created a calibrated model of its system in the in-flight configuration. These models have been then “integrated” to form the virtual Detector Assembly system, which has been checked against the calibration made in Fall 2001. Then, we have added to the Detector Assembly

model all the other IBIS sub-systems in order to create the model of the full IBIS Flight Model telescope (FM), and the results of the simulation have been compared to the IBIS FM calibration and Payload Calibration performed at ESA/ESTEC (December 2001 and January/February 2002).

### 3. Response matrices generation

#### 3.1. Response matrices generation planning

A simplified model of the response matrix was available for testing interfaces with the ISDC system in 2001. The first IBIS FM calibrated Mass Model has been available soon after the IBIS FM calibration, that is at mid 2002. This has enabled the generation of the first issue of the response matrix in Fall 2002, which has been checked with the Cygnus X-1 Performance Verification phase data (see below). A second issue of the matrices will be available at ISDC with the next version of the ISDC software to be delivered on July 2003, resulting from the comparison of IBIS extracted spectra with the results of the Crab pulsar observations performed on February–March 2003.

#### 3.2. Response matrices type and format

A response matrix has been generated for each IBIS main type of data: ISGRI, PiCsIT single, PiCsIT multiple, Compton single, and Compton multiple (see Ubertini et al. 2003 for a description of the IBIS modes). Three more matrices (not yet included into the ISDC system) can be constructed for the timing studies from ISGRI, Compton, and PiCsIT (Spectral Timing data). Up to now, these matrices have been constructed from the simulated IBIS response to an on-axis source.

The matrices format is adapted to have the maximal resolution for each detector in each peculiar mode. It is then up to the observer to decide which binning he/she wish for his/her scientific purpose. A standard binning is delivered by ISDC.

### 4. Tests of the response matrices

#### 4.1. Test of the IBIS spectral extraction software and response matrices compatibility

As seen in Fig. 1, the results of the IBIS modeling may be transformed in XSPEC compatible formats, and used within this package. In the figure, we have also taken into account the following estimates for the IBIS background values:

ISGRI mode: 1000 cts/s

PiCsIT mode (single + multiple): 5000 cts/s

Compton mode: 100 cts/s

in order to compute the error bars. We have then fit these spectra with XSPEC, giving the model spectrum shown in Fig. 1. This fitted spectrum is composed by a power law with photon index  $\alpha = -2.4$  and a line centered at an energy of 480 keV with a 22 keV width, parameters which are consistent within errors with the parameters we introduced as input in our Monte-Carlo simulations.

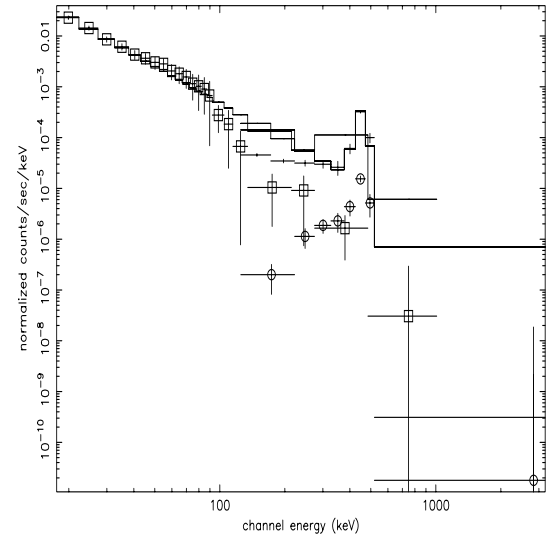


**Fig. 1.** Simulated IBIS raw spectra as introduced in XSPEC, shown with a powerlaw + 511 keV line fit. ISGRI points are indicated by squares, PiCsIT points by crosses and Compton points by ellipses. The fitted model spectrum composed by a power law with photon index  $-2.4$  and a line centered at an energy of 480 keV with a 22 keV width is also shown.

#### 4.2. Data reduction

The celestial source spectra that we will show now in this paper are all derived using the ISGRI component of the standard OSA (“Offline Scientific Analysis”) software, produced jointly by the Integral Science Data Center (ISDC), and the IBIS/ISGRI team at CEA/Saclay. This includes mainly software to build detector maps into different energy channels, and deconvolve them using standard techniques (Goldwurm et al. 2003; Gros et al. 2003). These software are the standard ones which are delivered to each INTEGRAL guest observers.

#### 4.3. Tests of the matrices during PV phase

At the end of 2002, we have tested the first issue of IBIS response matrices officially delivered to ISDC using the Cygnus X-1 data obtained during the PV phase. For one science window, that is around 30 min of observation, the 20–200 keV ISGRI spectrum was reasonably fitted with a Comptonised spectrum, with parameters in accordance to what was already observed from Cygnus X-1 (McConnell et al. 2002).

Also, the results are in accordance with what was obtained by SPI, and RXTE with simultaneous observations, which validates the ISGRI matrix in this energy range (Pottschmidt et al. 2003).

In order to test the response at higher energies, we have also computed ISGRI Cygnus X-1 mean spectra obtained by summing all the Cygnus X-1 on-axis observations during one given revolution. One of these spectra is shown in Fig. 2 for revolution 18, and indicates clearly a thermal comptonized shape. We thus fit these spectra up to 400 keV with a standard Sunyaev and Titarchuk thermal comptonization model (Sunyaev & Titarchuk 1980), obtaining a temperature of  $41.2 \pm 0.3$  keV, and an optical depth of  $3.09 \pm 0.02$ , which is

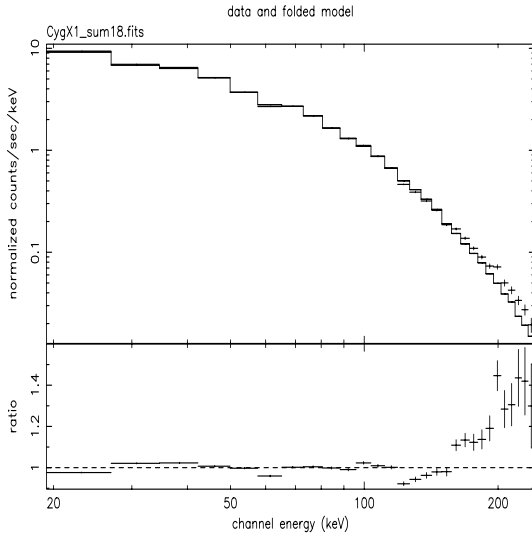


**Fig. 2.** ISGRI spectrum of Cygnus X-1 obtained summing all observations done during revolution 18. The line shows the ft with a Sunyaev-Titarchuk model (see text). The bottom figure give the ratio between the difference ft-data and the data.

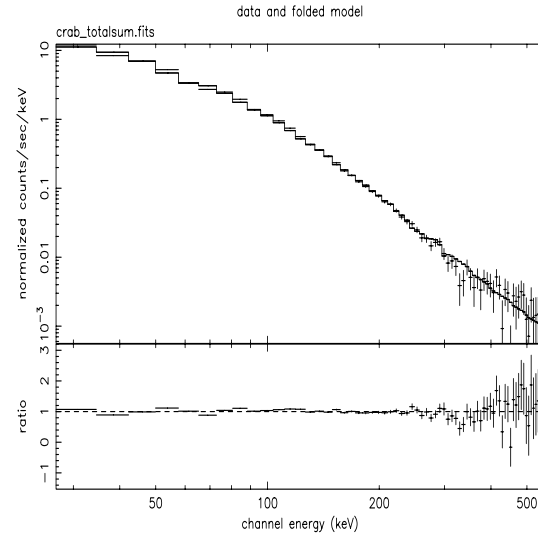


**Fig. 3.** ISGRI spectrum of the Crab obtained summing 90 ks of observations done during revolution 39. The line shows the ft with a power law model and the bottom figure give the ratio between the difference ft-data and the data (see text).

reminiscent of that already observed in the past from Cygnus X-1 (McConnell et al. 2002). The high reduced chi-square obtained (reduced chi-square = 18.7) could be partly due to a high energy excess above the model ft (see Fig. 2), similar to what reported by other instruments (McConnell et al. 2002). Besides the bad quality of the ft, which claims further verification of the origin of this excess, these results suggest that there are no strong deviations between the ISGRI results and previous spectral measurements of Cygnus X-1. This idea has then been further checked using the Crab observations.

#### 4.4. Tests of the matrices with the Crab in-flight calibration data

We have tested the matrix available at ISDC with the Crab data acquired in February/March 2003 during the Integral In-Flight Calibrations. The ft with a power law give an energy index of  $-1.93$  and a normalization at 1 keV of  $7.7 \text{ photons/cm}^2/\text{s/keV}$  between 20 and 500 keV. It is quite close to what is expected from the Crab nebula, but, at that time, some discrepancies were remaining. Indeed, large negative residuals below 20 keV were present, and a “snake” profile appeared for residuals below 150 keV. These features have been identified as due to three main factors:

- 1) the spectral extraction software had a bug at low energy which create this drop of counts around 20 keV;
- 2) the background correction of images was not perfect;
- 3) the sampling of the matrix at ISDC was not precise enough at low energy to correctly reproduce the variation of the ISGRI response. A new matrix with much more Monte Carlo points below 150 keV has been then computed and will be officially delivered with the new release of the ISDC software at the end of July 2003.

The example shown in Fig. 3 has been constructed using revolution 39, for a total acquisition time of 90 000 s, and using

the new software and matrix. The ft with a power law give now an energy index of  $-2.12 \pm 0.04$ , and a normalization at 1 keV of  $8.2 \pm 2 \text{ photons/cm}^2/\text{s/keV}$ , close to the canonical value.

## 5. Actual status of the ISGRI spectral extraction

A few months after the launch, the standard analysis actually available at ISDC is obviously still not perfect as a lot of work have been done to derive the instrument in-flight characteristics from the calibration obtained during the Crab 2003, February and March observations and this has not been yet included into the ISDC system. The ISGRI energy-channel relation, the background correction and the response matrices have been improved and tested using the Crab observations. Thus, a correct spectral analysis, taking into account all we learnt with the Crab observations, will be available soon at ISDC, and we will have valuable results with ISGRI between 20 and 600 keV for fully coded sources. A few problems still remain anyway that we will briefly summarize here.

### 5.1. Problems at very low energy

As we have seen, spectral extraction is correct above 20 keV, but we have still some problems below, between 13 keV (the ISGRI lower threshold) and 20 keV. These problems are not clearly identified yet, but we presume that there are related to a wrong estimate of the mask transparency in the open elements. This transparency is quite complex, as it is not uniform over the whole mask, as it is supposed in the Mass Model, and also depend on the source direction with respect to the telescope axis. A study taking into account measures made by the Spanish group, building the mask, and low energy measures done during the Payload Ground Calibration is on-going.

## 5.2. Problems with the partially coded sources

All the studies we have shown up to now concern the fully coded field of view. The spectral extraction and spectral fitting for partially coded sources is not perfect at present, as we could see from the off-axis measures made with the Crab. Whereas the projection of these sources through the mask is well defined and modeled, the modelization of the passive materials around the mask is not consistent between a non standard off-axis matrix, made at Saclay for tests purposes, and what is done in the deconvolution software. This is also under study at that moment.

## References

- Di Cocco G., Caroli E., Celesti E., et al. 2003, A&A, 411, L189  
Goldwurm A., David P., Foschini L., et al. 2003, A&A, 411, L223  
Gros A., Goldwurm A., Cadolle Bel M., et al. 2003, A&A, 411, L179  
Lebrun F., Leray J.P., Lavocat P., et al. 2003, A&A, 411, L141  
McConnell M. L., Zdziarski A.A., Bennett K., et al. 2002, ApJ, 572, 984  
Pottschmidt K., Wilms J., Chernyakova M., et al. 2003, A&A, 411, L383  
Sunyaev, R. A., & Titarchuk, L. G. 1980, A&A, 86, 121  
Ubertini P., Lebrun F., Di Cocco G., et al. 2003, A&A, 411, L131

## COMPTON TELESCOPE WITH A CODED APERTURE MASK: IMAGING WITH THE *INTEGRAL*/IBIS COMPTON MODE

M. FOROT, P. LAURENT, F. LEBRUN, AND O. LIMOUSIN

Service d'Astrophysique, CEA Saclay, F-91191 Gif-sur-Yvette, France; mforot@cea.fr

Received 2006 September 29; accepted 2007 June 24

### ABSTRACT

Compton telescopes provide good sensitivity over a wide field of view in the difficult energy range from a few hundred keV to several MeV. Their angular resolution is, however, poor and strongly energy dependent. We present a novel experimental design associating a coded mask and a Compton detection unit to overcome these pitfalls. It maintains the Compton performance while improving the angular resolution by at least an order of magnitude in the field of view subtended by the mask. This improvement is obtained at the expense only of efficiency, which is reduced by a factor of 2. In addition, the background correction benefits from the coded-mask technique, that is, simultaneous measurement of the source and background. This design is implemented and tested using the IBIS telescope on board the *INTEGRAL* satellite to construct images with 12' resolution over a 29° × 29° field of view in the energy range from 200 keV to a few MeV. The details of the analysis method and the resulting telescope performance, particularly in terms of sensitivity, are presented.

*Subject headings:* gamma rays: observations — telescopes

### 1. INTRODUCTION

The development of Compton telescopes began in the 1970s with balloon flights (Schönfelder & Lichti 1973; Herzo et al. 1975; Lockwood et al. 1979) and culminated with the flight of COMPTEL (Schönfelder et al. 1993) on board the *Compton Gamma Ray Observatory*. COMPTEL demonstrated for more than 9 years the capabilities of a Compton telescope to image the sky between 1 and 30 MeV thanks to the information provided by Compton kinematics (Boggs & Jean 2000). The study of astrophysical sites of nucleosynthesis, as illustrated by the first  $^{26}\text{Al}$  sky map (Diehl et al. 1995), greatly progressed with the COMPTEL data. On the other hand, COMPTEL barely achieved an angular resolution of 5° (FWHM) at 1 MeV. Future Compton telescopes could benefit from very significant detector progress, particularly in the semiconductor domain, to improve spectral resolution and, thus, angular resolution (Limousin 2003). The latter is however intrinsically limited by what is referred to as electron Doppler broadening, which results from the fact that an electron scattering in a detector is bound. This limits the angular resolution to about 5° at 511 keV in the best case (Zoglauer & Kanbach 2003).

One way to overcome this limitation is to adjoin a coded aperture (mask) to a Compton telescope. This design, which has never been used for gamma-ray space telescopes, maintains the advantages of a Compton telescope (high-energy response, low background, wide field of view) over most of the field of view, but it adds the coded mask's imaging properties (angular resolution, background subtraction) in the solid angle subtended by the mask. Indeed, in a coded-mask system, source and background are measured simultaneously, and the energy-independent angular resolution is more than an order of magnitude better than in classical Compton telescopes. With coded-aperture Compton telescopes (CACTs), one can obtain low-background images in the 200 keV–10 MeV energy range with an angular resolution better than a fraction of a degree (e.g., 10').

A CACT generally has lower efficiency than a classical coded-mask telescope, with, for instance, a thicker detector layer. However, the background in the energy range from 200 keV to a few MeV is dominated by the telescope's internal emission, which

increases with detector volume. A thicker detector will thus suffer a higher background. Therefore, the decision to use only one layer or to use two layers in coincidence for detecting the photons through the mask is a trade-off between detector background level and efficiency.

On the other hand, CACTs can be used to obtain full energy deposition from a high-energy photon, even if imaging is done only using the mask's projection on one layer. This will enable users to realize the improved energy response of a coded-mask telescope.

Lastly, CACTs are in general difficult to use at higher energies, near 10 MeV and above, as they would require a thick mask, even with tungsten, to stop photons, which will result in a large vignetting effect for off-axis sources. Also, at these energies, Compton scatterings and pair creation in the mask will affect the system's imaging properties and may degrade its angular resolution, which therefore becomes slightly energy dependent.

In this paper, we present the general principles of CACTs, their application to the *International Gamma-Ray Astrophysics Laboratory* (*INTEGRAL*) mission, the difficulties inherent to the use of CACTs, the analysis method for the Compton mode of the Imager on Board *INTEGRAL* (IBIS), and its resulting performance.

### 2. PRINCIPLES OF CODED-APERTURE COMPTON TELESCOPES

In a Compton telescope, consisting of two detector layers, gamma-ray photons are Compton scattered in one detector and absorbed in the second. The location of and energy deposit from each interaction are measured, as illustrated in Figure 1 for the IBIS detectors. The direction of the scattered photon,  $\mathbf{u}_{\text{sca}}$ , is determined from the interaction locations in the two detectors. The Compton scattering angle,  $\theta_{\text{Com}}$ , is measured from the energy deposits,  $E_1$  and  $E_2$ , recorded in the two detectors and is given by, for a forward scattering,

$$\cos \theta_{\text{Com}} = 1 - \frac{m_e c^2}{E_2} + \frac{m_e c^2}{E_1 + E_2}, \quad (1)$$

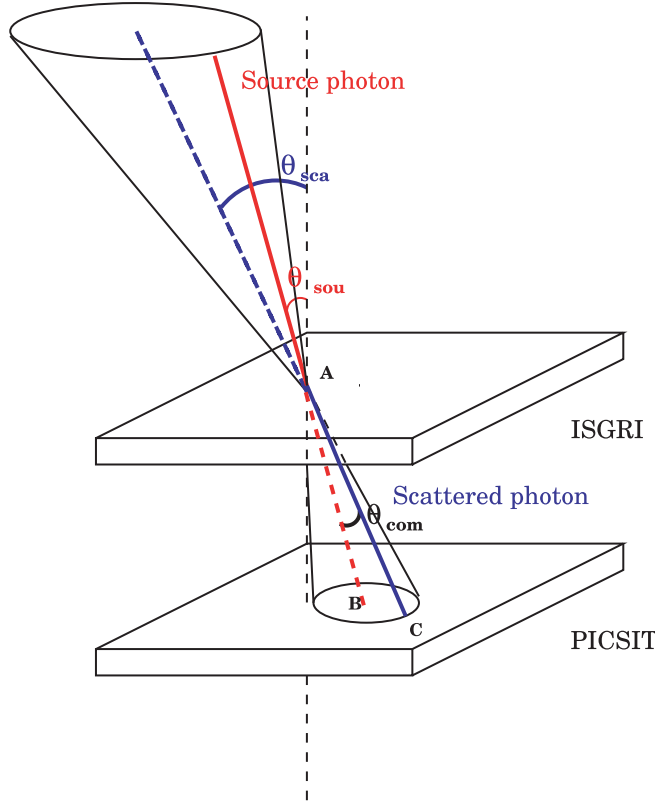


Fig. 1.—Forward scattering of a photon in the IBIS Compton mode. An incident photon (red) is scattered in ISGRI and absorbed in PICsIT (blue). Energy and position measurements at points A and C allow the derivation of the two angles  $\theta_{\text{Com}}$  and  $\theta_{\text{sca}}$ .

where  $m_e c^2$  is the electron rest-mass energy. The direction of the incoming gamma-ray photon lies on the edge of a cone, the Compton cone, with axis  $\mathbf{u}_{\text{sca}}$  and aperture  $\theta_{\text{Com}}$ . The density distribution of all the projected event circles, the intersection of the cones with the celestial sphere, allows one to reconstruct sky maps and to locate sources. Source polarization can also be measured, since the scattering azimuth is related to the polarization direction. The angular resolution of the telescope depends on the accuracy with which  $\theta_{\text{Com}}$  and  $\mathbf{u}_{\text{sca}}$  are determined and thus depends on the energy resolution and pixel size in each of the two detectors. Furthermore, background is hard to subtract, and as in optical cameras, several effects distort images. Use of a coded mask to reconstruct sky images can effectively address most of these difficulties.

In coded-aperture telescopes, the source radiation is spatially modulated by a mask of opaque and transparent elements. The projection of the mask shadow, recorded with a position-sensitive detector, produces a shadowgram. This allows simultaneous measurement of source plus background flux (shadowgram area corresponding to the mask holes) and background flux alone (area corresponding to the opaque elements) (Caroli et al. 1987). The background is removed by deconvolution of the shadowgram using the mask pattern. Mask patterns are designed to allow each source in the field of view to cast a unique shadow on the detector, in order to avoid ambiguities in the reconstruction of the sky image. The energy-independent angular resolution is given, in the thin-mask limit (see the discussion above for thicker masks), by  $d\alpha = \arctan(C/H)$ , where  $C$  is the size of a mask element and  $H$  is the distance between the coded mask and the detector. In such a telescope, the field of view is limited and depends on the mask

dimensions, the detector dimensions, and the mask-detector distance. The total field of view is divided into two parts:

1. FCFOV (fully coded field of view), for which the source radiation is completely modulated by the mask—this field exists only when the mask is larger than the detector; and
2. PCFOV (partially coded field of view), for which only a fraction of the source radiation is modulated by the mask.

The principle of a CACT takes advantage of both techniques. It is composed of a coded mask and two detector planes between which photons are Compton scattered. The flux on one detector is spatially modulated by the mask pattern. The sky image is obtained by a simple deconvolution of this shadowgram. Compton events that are incompatible with a given source direction can be discarded from the shadowgram, so a CACT can be regarded as a coded-mask telescope in which the Compton kinematics is used to reduce the background.

Then, two cases are possible: Either one wants to study a given source with a known position  $\mathbf{u}_{\text{sou}}$  on the celestial sphere, or one wishes to make an image of a given field of view. In the first case, we can select, using the Compton kinetics, events that fulfill the condition

$$\mathbf{u}_{\text{sou}} \cdot \mathbf{u}_{\text{sca}} = \cos \theta_{\text{Com}}, \quad (2)$$

within instrumental uncertainties, as by definition  $\theta_{\text{Com}}$  is the angle between the source and the scattered directions. In the case of an isotropic background, equation (2) typically enables one to remove more than 90% of the Compton forward background events while keeping 90% of the Compton forward source events, in the 200 keV–1 MeV energy range.

When one wants to study sources over a given field of view, the more conservative way of removing background events using the Compton kinetics is to remove all events whose Compton cones, within the uncertainties, do not intersect the field of view. This condition can be readily expressed in the plane containing the telescope axis and the source direction (for a forward scattering). Indeed, if we consider the case of a conical field of view of semiangle  $\theta_{\text{FOV}}$ , this selection condition means that the angle between the source direction and the telescope axis  $\mathbf{u}_{\text{tel}}$ , called  $\theta_{\text{sou}}$ , should be greater than the angle  $\theta_{\text{FOV}}$ . The angle  $\theta_{\text{sou}}$  can be easily computed from the Compton angle and the scattered-photon ones ( $\theta_{\text{sca}}$ , such that  $\cos \theta_{\text{sca}} = \mathbf{u}_{\text{sca}} \cdot \mathbf{u}_{\text{tel}}$ ). The background rejection condition then becomes

$$\theta_{\text{sou}} = \theta_{\text{sca}} - \theta_{\text{Com}} \geq \theta_{\text{FOV}}. \quad (3)$$

A similar formula can be obtained in the case of backward scattering.

### 3. THE INTEGRAL/IBIS COMPTON MODE

#### 3.1. The IBIS Telescope as a CACT

The IBIS instrument (Ubertini et al. 2003) is one of two major coded-aperture telescopes on board the ESA INTEGRAL gamma-ray observatory, launched on 2002 October 17. It consists of a dual detection layer designed and optimized to operate in the energy range between  $\sim 15$  keV and 10 MeV. The upper detector layer, ISGRI, covers the energy range from  $\sim 15$  keV to 1 MeV and is made of  $128 \times 128$  cadmium telluride (CdTe) semiconductor detectors (Lebrun et al. 2003). The lower detector layer, PICsIT, operates in the energy interval from  $\sim 190$  keV to 10 MeV and is made of  $64 \times 64$  cesium iodide (CsI) scintillation crystals (Labanti et al. 2003). Events from these two layers are timestamped, and an onboard hardware event processing unit (HEPI)

TABLE 1  
IN-FLIGHT IBIS COMPTON-MODE  
ENERGY RESOLUTION

Energy (keV)	Energy Resolution (% FWHM)
511.....	20
1274.....	15

can associate the ISGRI and PICsIT events if their arrival times coincide within a given time window (actually  $3.8 \mu\text{s}$ ). In the following, these are referred to as tagged Compton events. The detector spectral drifts (gain changes) can be monitored with a  $^{22}\text{Na}$  onboard calibration unit (OBCU). The detector layers are actively shielded, encased on all but the sky side by bismuth germanate (BGO) scintillator elements. The detector is also passively shielded from the low-energy celestial background with tungsten and lead foils. The coded mask is made of 16 mm thick tungsten elements that are 11.2 mm on a side. This thickness guarantees 50% modulation at 1 MeV. Placed 3.2 m above the CdTe detector plane, this mask ensures a  $12'$  angular resolution over a  $29^\circ \times 29^\circ$  PCFOV. Composed of two detector planes (ISGRI and PICsIT) able to work in coincidence and covered with a coded mask, IBIS is the first in-flight CACT.

### 3.1.1. Event Types

Tagged Compton events from the celestial source under study can be of two kinds:

1. True Compton events; and
2. Spurious events, where two independent ISGRI and PICsIT events, one of them coming from the source, fall by chance in the Compton coincidence time window and are recorded falsely as a true Compton event.

Below 500 keV, the vast majority of Compton scatters correspond to forward-scattering events (ISGRI  $\rightarrow$  PICsIT). With higher energy, photons can pass through ISGRI without any interaction, interact in PICsIT, and scatter back onto the ISGRI detection layer. In some cases, more than one scattering occurs. Multiple interactions in ISGRI are, however, discarded on board. In this paper we use only the events that underwent a forward scattering in ISGRI with a single energy deposit in PICsIT.

### 3.1.2. Spectral Resolution

In standard Compton telescopes, the spectral resolutions of each detector are key parameters, since they directly affect the angular resolution, which, in turn, governs the sensitivity. For a CACT, the angular resolution is driven by the mask's geometric properties ( $C$  and  $H$ ), but the sensitivity strongly depends on background rejection. The latter is based on measuring  $\mathbf{u}_{\text{sca}}$  and  $\theta_{\text{Com}}$ . The uncertainty on  $\theta_{\text{Com}}$ ,

$$\delta\theta_{\text{Com}} = \frac{m_ec^2}{E^2 \sin \theta} \sqrt{\delta E_1^2 + \left( \frac{E_1^2}{E_2^2} + 2 \frac{E_1}{E_2} \right)^2 \delta E_2^2}, \quad (4)$$

where  $\delta E_1$  and  $\delta E_2$  are the energy resolution of the first and second detector layers, respectively, is larger in IBIS than that on  $\mathbf{u}_{\text{sca}}$ , which relates to pixel size. We have used the Compton data tagged as calibration events by the OBCU to measure the onboard spectral resolution of the IBIS Compton mode. The FWHM of the two lines of the  $^{22}\text{Na}$  source (511 and 1274 keV) and the resulting energy resolution are presented in Table 1.

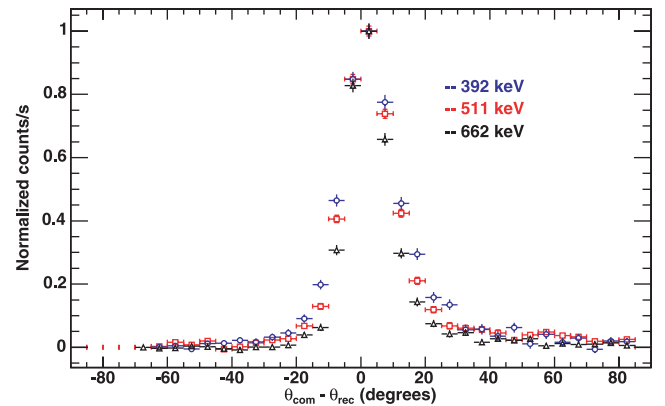


Fig. 2.—Distribution of Compton events with the angular shift  $\Delta\theta = \theta_{\text{Com}} - \theta_{\text{sca}}$ , after removal of spurious events, using ground calibration data from  $^{133}\text{Sn}$  (392 keV),  $^{22}\text{Na}$  (511 keV), and  $^{137}\text{Cs}$  (662 keV) sources ( $\theta_{\text{rec}}$  in this figure is equivalent to  $\theta_{\text{sca}}$  in the text).

## 4. IMAGING THE SKY WITH THE IBIS CODED-APERTURE COMPTON TELESCOPE

In this section, we focus on imaging analysis and the performance of the IBIS Compton mode.

### 4.1. IBIS Compton-Mode Imaging Analysis

#### 4.1.1. Event Selection

The first step in analyzing the IBIS Compton-mode data is to apply selections to the events: a selection in energy (generally between 200 keV and 1 MeV), and selection of ISGRI events with rise time between 0.6 and  $3.8 \mu\text{s}$  (see Lebrun et al. 2003 for a description of ISGRI data). Then we remove background events using the Compton kinetics, as described in § 2. As discussed there, depending on the purpose, there are two types of selection:

*Field-of-view selection.*—The IBIS field of view semiangle being  $\theta_{\text{FOV}} \simeq 15^\circ$ , only photons with  $\theta_{\text{sca}} - \theta_{\text{Com}} < 15^\circ$  are kept.

*Dedicated source selection.*—For a source with known direction  $\mathbf{u}_{\text{sou}}$ , a more restrictive selection given by equation (2) is applied. This condition can be rewritten as  $|\mathbf{u}_{\text{sou}} \cdot \mathbf{u}_{\text{sca}} - \cos \theta_{\text{Com}}| < \delta_{\text{lim}}$ , where  $\delta_{\text{lim}}$  is related to the instrumental error.

We compute values of  $\delta_{\text{lim}}$  in order to maximize the source signal-to-noise ratio, using ground calibration measures. We have used the Compton events obtained from three on-axis calibration sources, namely,  $^{133}\text{Sn}$  (392 keV),  $^{22}\text{Na}$  (511 keV), and  $^{137}\text{Cs}$  (662 keV). In fact, for an on-axis source, the telescope axis and source direction coincide, so

$$\mathbf{u}_{\text{sou}} = \mathbf{u}_{\text{tel}}. \quad (5)$$

Then, from equation (2), we have

$$\cos \theta_{\text{Com}} = \mathbf{u}_{\text{sou}} \cdot \mathbf{u}_{\text{sca}} = \mathbf{u}_{\text{tel}} \cdot \mathbf{u}_{\text{sca}} = \cos \theta_{\text{sca}} \quad (6)$$

from the definition of  $\theta_{\text{sca}}$ . Equation (2) then simplifies to

$$\Delta\theta = \theta_{\text{Com}} - \theta_{\text{sca}} = 0. \quad (7)$$

Figure 2 shows the angular shift ( $\Delta\theta$ ) diagrams. This distribution, centered on zero, is not a Dirac distribution because of instrumental uncertainties. Also, this distribution narrows with energy thanks to a better reconstruction of  $\theta_{\text{Com}}$ , which is linked

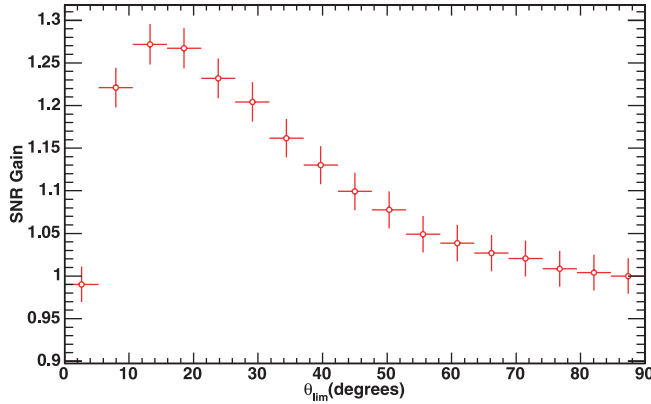


FIG. 3.—Evolution of the signal-to-noise ratio gain with  $\theta_{\text{lim}}$  for the  $^{133}\text{Sn}$  calibration source at 392 keV, on-axis.

to a better Compton-mode energy resolution at high energy. Yet, this variation with energy is small, and the optimal choice of  $\delta_{\text{lim}}$  (related to the width of the distribution shown in Fig. 2) has been checked not to change much with energy between 200 keV and 1 MeV.

Figure 3 illustrates how the signal-to-noise ratio varies with the allowed range of  $\Delta\theta \in [-\theta_{\text{lim}}, \theta_{\text{lim}}]$  for the  $^{133}\text{Sn}$  calibration source. The best value of  $\theta_{\text{lim}}$  at 392 keV is around  $10^\circ$ – $12^\circ$ .

#### 4.1.2. Subtraction of Spurious Events

Spurious events are generally neglected in standard Compton telescopes. Their uniform distribution does not induce false source detection. But the situation for a CACT is different.

Indeed, spurious events are caused by random events on the two layers. For a bright source, such as the Crab, the source's low-energy photons make an important contribution to the detectors' count rates. So, the probability that one of these random events is in fact a detected low-energy photon from the source is quite high. As such a photon has the mask signature induced by the source, it is not subtracted during the deconvolution process and would wrongly participate in the determination of source flux. We therefore have to take into account the contribution from spurious events with high accuracy in order to obtain a correct estimate of the source flux.

The dedicated source selection has the strong advantage of greatly reducing the number of spurious events, as most of them do not obey equation (2), but their residual contribution is not negligible. A statistical method must be applied to evaluate and subtract them.

To do so, we make use of ISGRI and PICsIT single events recorded in the same observation, that is, possibly having the source signature, and artificially associate them to create a sample of spurious events, called hereafter the “fake spurious events sample.” We apply to this sample the same selections in energy, rise time, and scattering angle as described above, in order to produce a fake shadowgram. The latter is scaled, by a scaling factor called the “spuriousness factor” or  $\alpha$ , to the number of spurious events recorded during the observation and then subtracted from the Compton data shadowgram.

The spurious count rate,  $N_{\text{sp}}$ , scales with the width of the time coincidence window ( $\sim 2\Delta T_e$ ), the total number of PICsIT events ( $N_{\text{PICsIT}} = N_p + N_{\text{OBCU}}$  from PICsIT simple and multiple detections, and from calibration events), and the total number of ISGRI events ( $N_{\text{ISGRI}} = N_I + N_{\text{sp}}$  from ISGRI single events and spurious events). The calibration events in ISGRI are tagged and discarded

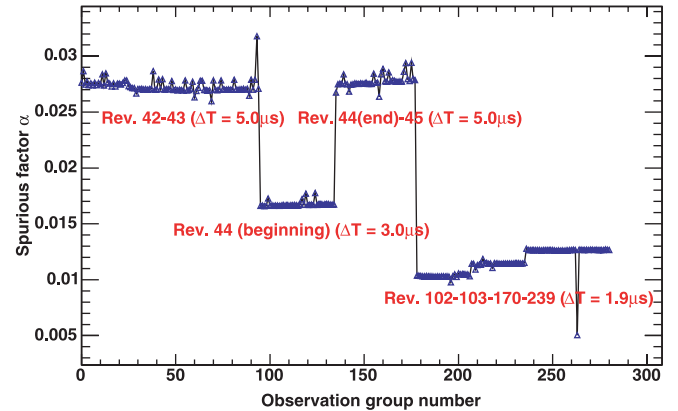


FIG. 4.—Evolution of the spuriousness factor for different values of the time coincidence window as derived from Crab pulsar observations.

on board. Using Poisson statistics in the coincidence window, one obtains the number of spurious events:

$$N_{\text{sp}} = (1 - e^{-(2\Delta T_e - \delta T)N_{\text{PICsIT}}})N_{\text{ISGRI}}, \quad (8)$$

where  $\delta T$  is the onboard time resolution, on the order of 250 ns. Yet, one measures only  $N_I$ , so the scaling factor is

$$N_{\text{sp}}/N_I = e^{(2\Delta T_e - \delta T)N_{\text{PICsIT}}} - 1. \quad (9)$$

One has to further correct this factor for the multiple PICsIT events in order to obtain the scaling factor for the single spurious events only. For a proportion of PICsIT single events of

$$\beta = \frac{N_p^{\text{simple}} + N_{\text{OBCU}}}{N_p^{\text{simple}} + N_p^{\text{multiple}} + N_{\text{OBCU}}} \quad (10)$$

( $\beta$  is of order 80% between 200 keV and 1 MeV for IBIS), one obtains the spuriousness factor,

$$\alpha = \beta(e^{(2\Delta T_e - \delta T)N_{\text{PICsIT}}} - 1). \quad (11)$$

Figure 4 shows the evolution of this factor for observations of the Crab over the mission's lifetime. It varies from 2.82% early on (revolution 39), when  $\Delta T_e$  was about 5.0  $\mu\text{s}$ , to around 1.1% after revolution 102, when  $\Delta T_e$  was decreased to 1.9  $\mu\text{s}$ . The value of  $\alpha$  is quite constant for a given coincidence window during short times, but it rises over longer periods (revolutions 102-103-170-239) because of the increase of the background flux, following the solar cycle.

The next step is to correct the resulting shadowgram (after subtraction of the spurious events) for nonuniformity and to deconvolve it.

#### 4.1.3. Uniformity Correction

Compton-mode shadowgrams are not spatially flat. The count rate falls near the edges because we lose the events that scatter at the edge of ISGRI and miss PICsIT. This nonuniformity is magnified by the decoding process, so if it is not corrected, strong systematic structures may result in the deconvolved images, with spatial frequencies similar to those originally present in the shadowgram. The shadowgram,  $\mathbf{D}$ , consists of a source component,

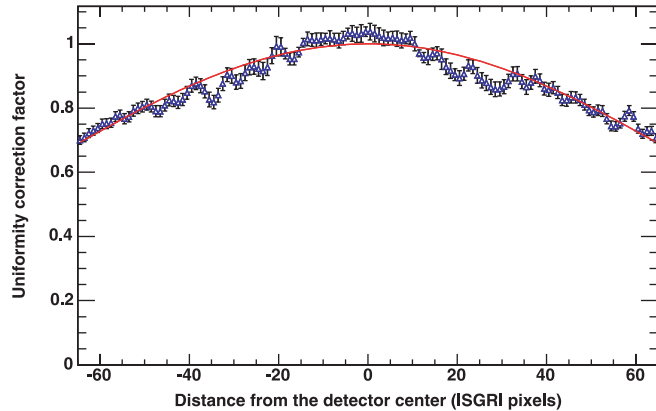


FIG. 5.—Distribution of background events with distance from the detector center, folded over the azimuthal direction. This distribution is well fitted by a two-dimensional Gaussian (red).

with count rate  $S$  and a spatial response map  $\mathbf{R}_S$ , and a background component, with count rate  $B$  and response map  $\mathbf{R}_B$ ; thus,

$$\mathbf{D} = S\mathbf{R}_S + B\mathbf{R}_B. \quad (12)$$

The modulation from the mask pattern is weak compared with the larger scale deformations we study here. To compare  $\mathbf{R}_S$  and  $\mathbf{R}_B$  under the same conditions, we need in-flight data from a strong enough source, as well as background. Whereas we have used the in-flight background distribution, no such source has been observed in-flight in Compton mode, so we used data from ground calibration to determine  $\mathbf{R}_S$ .

Both the background and source response maps are well fitted by a two-dimensional Gaussian function (see Fig. 5). The results are presented in Table 2 for the in-flight background measurements and the ground calibration source data for on-axis sources. The background and source response maps in several energy bands are found to be consistent. Off-axis sources have also been studied and display equivalent response maps. Residual background deformations on smaller scales, similar to what is observed in ISGRI images (Terrier et al. 2003), are still present; their correction is under study.

The final step is therefore to deconvolve the corrected shadowgram  $\mathbf{D}/R$ , renormalized to the total number of events, to reconstruct the source flux, using standard deconvolution techniques.

#### 4.1.4. Image Deconvolution

Representing the mask as an array  $\mathbf{M}$  with elements of 1 (transparent) and 0 (opaque) and the detector plane by an array  $\mathbf{D}$ , and denoting by  $\mathbf{G}^+$  and  $\mathbf{G}^-$  the decoding arrays related to the coded mask (see Goldwurm et al. 2003), the image deconvolution in the FCFOV can be extended to the total (both

TABLE 2  
RESPONSE MAP GAUSSIAN FITS

Source	Energy (keV)	$\sigma$ (pixels)
$^{113}\text{Sn}$ .....	392	$73 \pm 3$
$^{22}\text{Na}$ .....	511	$74 \pm 3$
$^{137}\text{Cs}$ .....	662	$71 \pm 4$
$^{54}\text{Mn}$ .....	835	$72 \pm 2$
$^{54}\text{Zn}$ .....	1120	$73 \pm 3$
Background.....	200–5000	$74 \pm 3$

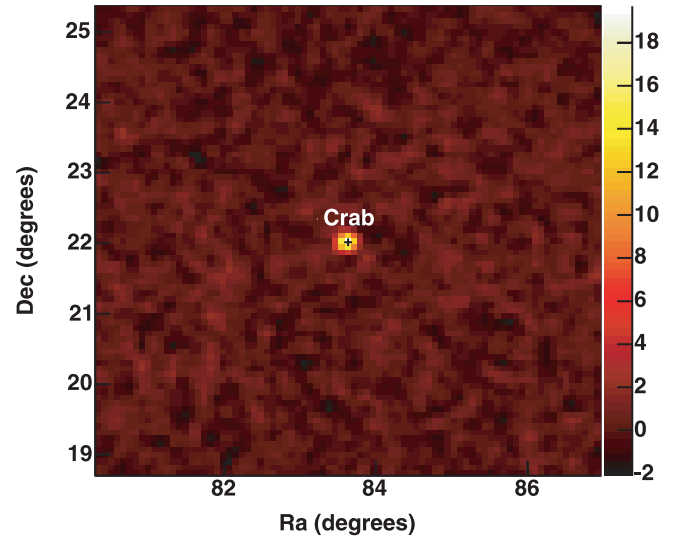


FIG. 6.—Deconvolved significance map for the Crab pulsar using the Compton mode between 200 and 500 keV for an exposure time of 300 ks.

fully and partially coded) field by correlation of  $\mathbf{D}$  in a noncyclic form with the  $\mathbf{G}$ -array extended and padded with 0-elements outside the mask (Gros et al. 2003). Since the number of correlated (transparent and opaque) elements in the PCFOV is not constant as in the FCFOV, the sum and subtractions for each sky position must be balanced and renormalized. The sky flux map is given by

$$\mathbf{F} = \left[ (\mathbf{W}\mathbf{D} * \mathbf{G}^+) - (\mathbf{W}\mathbf{D} * \mathbf{G}^-) \frac{\mathbf{W} * \mathbf{G}^+}{\mathbf{W} * \mathbf{G}^-} \right] / \left[ (\mathbf{W} * \mathbf{G}^+ \mathbf{M}) - (\mathbf{W} * \mathbf{G}^- \mathbf{M}) \frac{\mathbf{W} * \mathbf{G}^+}{\mathbf{W} * \mathbf{G}^-} \right] \quad (13)$$

and the variance map by

$$\mathbf{V} = \left[ (\mathbf{W}^2 \mathbf{D} * \mathbf{G}^{+2}) + (\mathbf{W}^2 \mathbf{D} * \mathbf{G}^{-2}) \left( \frac{\mathbf{W} * \mathbf{G}^+}{\mathbf{W} * \mathbf{G}^-} \right)^2 \right] / \left[ (\mathbf{W} * \mathbf{G}^+ \mathbf{M}) - (\mathbf{W} * \mathbf{G}^- \mathbf{M}) \frac{\mathbf{W} * \mathbf{G}^+}{\mathbf{W} * \mathbf{G}^-} \right]^2. \quad (14)$$

In these formulae, the  $\mathbf{W}$ -matrix removes dead or noisy pixels.

In the FCFOV, the variance is quite uniform and equals the total number of detector counts. The entire analysis procedure can be easily carried out by means of fast Fourier transforms. The result for a Crab pulsar observation is presented in Figure 6.

In Figure 7 (left), we show for comparison an ISGRI-only significance map, in the same energy range. As expected, because of its low thickness (2 mm), ISGRI is much less sensitive than the Compton mode between 200 and 500 keV, showing that the Compton mode is a real extension at high energy of ISGRI's capabilities. The right panel of Figure 7 shows the significance map made with the fake spurious events sample, using the same algorithms as used for Figure 6. It is clear there that this map is dominated by low-energy events coming from the Crab, as described in § 4.1.2.

#### 4.1.5. Angular Shift Diagrams as a Check on the Analysis Method

Angular shift diagrams illustrate the effectiveness of the spurious-event subtraction. One can use tagged Compton events from an on-axis calibration source and analyze them in regularly

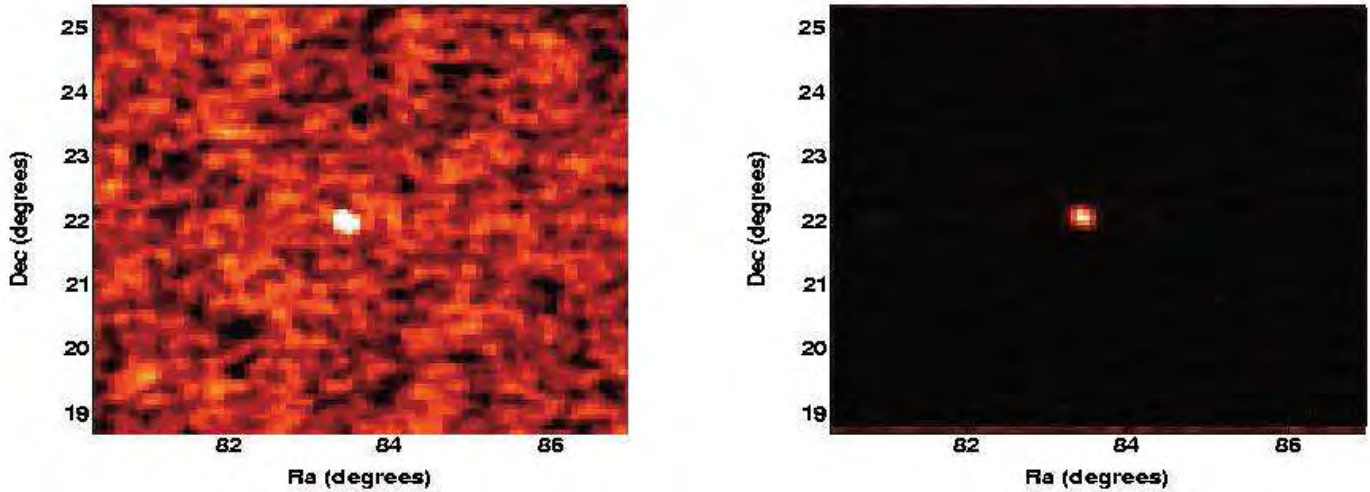


FIG. 7.—Left, ISGRI significance map for the Crab pulsar between 200 and 500 keV; right, significance map computed from the fake spurious events sample with the same algorithms as used for the map shown in Fig. 6.

spaced  $\Delta\theta$  bins. Then we select them based on energy and rise time as above. Their shadowgram is corrected for the spatial response and deconvolved to obtain the total source count rate, displayed in red in Figure 8. The corresponding constructed spurious events sample was analyzed in the very same way, and its count rate per  $\Delta\theta$  bin, scaled by the measured  $\alpha$ , is displayed in blue, showing that the spuriousness factor is adequate. The angular shift distribution of real Compton events (after subtraction of the spurious ones) is well centered around zero and falls to zero for  $|\Delta\theta| \geq 19^\circ$ , whereas the spurious distribution is clearly offset to negative values, as expected because most spurious events have a low energy deposition in ISGRI.

For celestial gamma-ray sources above 200 keV, the spurious rate dominates the source rate. Several Crab on-axis observations have been used to construct a  $\Delta\theta$  diagram, using the variance-weighted sum of the flux at the source position in each sky image. Thanks to the coded mask's background subtraction capabilities, only the true Compton and spurious contributions, as defined in § 3.1.1, are visible in Figure 9. The spurious component severely dominates, its negative offset being quite marked. True Compton events are around zero, as foreseen, and

the small flux excess of events for  $\Delta\theta \sim 20^\circ$ – $40^\circ$  is due to backward scattering.

#### 4.2. IBIS Compton-Mode Sensitivity

The analysis method described above has been applied to evaluate the signal-to-noise ratio of the Crab pulsar in different energy bands. The sensitivity of the IBIS Compton mode is presented in Figure 10. It is greater than that of PICsIT for a similar angular resolution. Yet, unlike PICsIT, the Compton mode has no major strong background problems, allowing one to study photons up to a few MeV in very small energy bands, in particular around spectral lines, with an angular resolution better than that of SPI (the Spectrometer on *INTEGRAL*). It also allows for polarization studies and imaging studies of compact objects with good timing resolution ( $\sim 100 \mu\text{s}$ ).

The next step we foresee in our analysis is to incorporate backward-scattering events and PICsIT multiple events and to compute background Compton correction maps (first-order background shadowgram from empty-field observations and second-order summed sky images after source subtraction) to reduce the residual structures in the response maps.

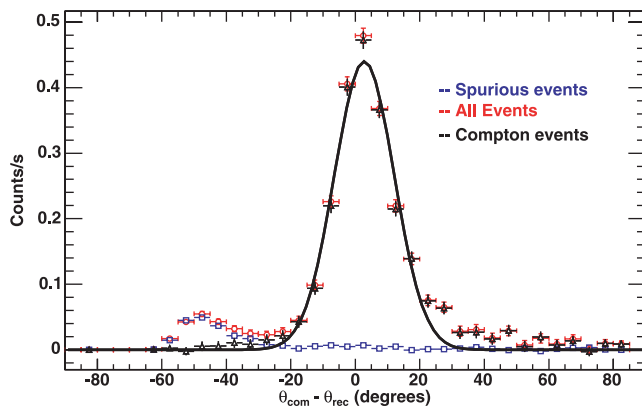


FIG. 8.—Angular shift distribution of events for a  $^{133}\text{Sn}$  source at 392 keV during ground calibration. Red data points represent all the Compton data (real Compton plus spurious data). Blue data points show the spurious contribution, which peaks at negative offset, and black data points are the derived Compton ones. The line is a Gaussian fit (FWHM  $\sim 19^\circ$ ) to these derived Compton data.

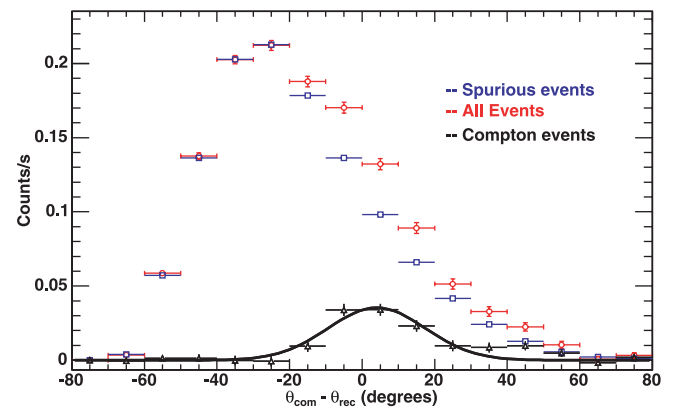


FIG. 9.—Crab count rate between 200 and 500 keV in different  $\Delta\theta$  bins. The total observation time is about 700 ks. Red data points represent all the Compton data (real Compton plus spurious data). Blue data points show the spurious contribution, and black data points are the derived Compton ones. The line is a Gaussian fit to the Compton data.

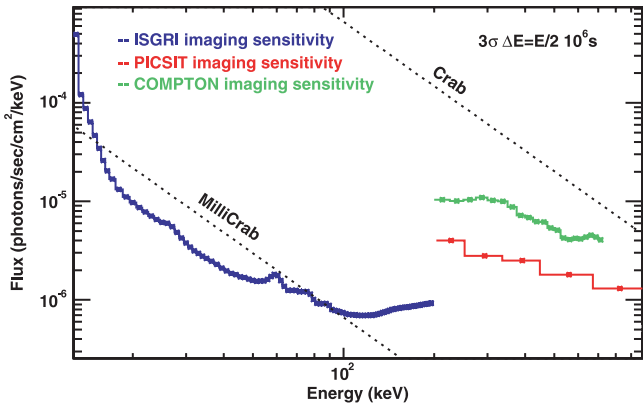


FIG. 10.—Sensitivity of the IBIS Compton mode compared with that of ISGRI and PICsIT.

An important goal of the IBIS Compton mode is also polarimetry. The interest of the astrophysics community in such detection is growing. It is in fact a powerful and direct tool to

constrain theoretical models of gamma-ray bursts, pulsars, solar flares, etc. The calibration and results of the IBIS Compton-mode polarimeter will be presented in a forthcoming paper.

## 5. CONCLUSIONS

The IBIS Compton mode is functional and provides an efficient new means to observe the sky at energies beyond  $\sim 190$  keV and up to a few MeV. With only forward-scattering events and thanks to the ISGRI shadowgram, we can reconstruct images with high spatial resolution by taking advantage of the coded aperture mask system. We have devised a scheme for subtracting the large contribution from spurious coincidences between the two detector planes. The resulting sensitivity, evaluated with in-flight data from the Crab pulsar, opens new perspectives for polarimetric and imaging studies in the 0.2–5 MeV energy band.

We thank the anonymous referee for interesting questions and helpful suggestions that significantly improved the whole paper.

## REFERENCES

- Boggs, S. E., & Jean, P. 2000, A&AS, 145, 311
- Caroli, E., Stephen, J. B., Di Cocco, G., Natalucci, L., & Spizzichino, A. 1987, Space Sci. Rev., 45, 349
- Diehl, R., et al. 1995, A&A, 298, 445
- Goldwurm, A., et al. 2003, A&A, 411, L223
- Gros, A., Goldwurm, A., Cadolle Bel, M., Goldoni, P., Rodriguez, J., Foschini, L., Del Santo, M., & Blay, P. 2003, A&A, 411, L179
- Herzo, D., Koga, R., Millard, W. A., Moon, S., Ryan, J., Wilson, R., Zych, A. D., & White, R. S. 1975, Nucl. Instrum. Methods, 123, 583
- Labanti, C., et al. 2003, A&A, 411, L149
- Lebrun, F., et al. 2003, A&A, 411, L141
- Limousin, O. 2003, Nucl. Instrum. Methods Phys. Res. A, 504, 24 (erratum 513, 651)
- Lockwood, J. A., Hsieh, L., Friling, L., Chen, C., & Swartz, D. 1979, J. Geophys. Res., 84, 1402
- Schönfelder, V., & Lichten, G. 1973, Proc. 13th Int. Cosmic-Ray Conf. (Denver), 2709
- Schönfelder, V., et al. 1993, ApJS, 86, 657
- Terrier, R., et al. 2003, A&A, 411, L167
- Ubertini, P., et al. 2003, A&A, 411, L131
- Zoglauer, A., & Kanbach, G. 2003, Proc. SPIE, 4851, 1302



# Monte Carlo simulations of stacked X-ray detectors as designed for SIMBOL-X

Christoph Tenzer<sup>a</sup>, Eckhard Kendziorra<sup>a</sup>, Andrea Santangelo<sup>a</sup>,  
Markus Kuster<sup>b</sup>, Philippe Ferrando<sup>c</sup>, Philippe Laurent<sup>c</sup>, Arnaud Claret<sup>d</sup> and Rémi Chipaux<sup>d</sup>

<sup>a</sup>Institut für Astronomie und Astrophysik, Universität Tübingen,  
Sand 1, 72076 Tübingen, Germany

<sup>b</sup>Institut für Kernphysik, TU Darmstadt, Schlossgartenstr. 9, 64289 Darmstadt, Germany

<sup>c</sup>UMR 7164 APC & DSM/DAPNIA/Service d’Astrophysique, CEA/Saclay, 91191  
Gif-sur-Yvette Cedex, France

<sup>d</sup>DSM/DAPNIA/Service d’Astrophysique, CEA/Saclay, 91191 Gif-sur-Yvette Cedex, France

## ABSTRACT

SIMBOL-X is a next generation X-ray telescope with spectro-imaging capabilities over the 0.5 to 80 keV energy range. The combination of a formation flying mirror and detector spacecraft allows to extend the focal length to several tens of meters (20 to 30 in the case of SIMBOL-X), resulting in a so far unrivaled angular resolution and sensitivity in the hard X-ray range. The focal plane detector system for SIMBOL-X is planned to consist of an array of so-called Macro Pixel Detectors (MPD) on top of a 2 mm thick CdZnTe pixellated detector array. Photons of energy less than about 17 keV will be primarily absorbed in the MPDs, whereas higher energy photons will be detected in the CdZnTe array below. A computer model of such stacked detectors and its interaction with the radiation environment encountered by the spacecraft in orbit is currently being developed by our group using the Monte Carlo toolkit GEANT4. We present results of the simulation and an outlook for possible optimizations of future detector geometry and shielding.

**Keywords:** SIMBOL-X, Geant4, stacked detectors, XMM-Newton, pn-CCD, EPIC, background

## 1. INTRODUCTION TO GEANT4

The GEANT4 toolkit provides a flexible and comprehensive software library package for Monte Carlo simulations that involve the interaction and tracking of particles through matter and electromagnetic fields. It efficiently handles complex particle tracks and geometries and allows their visualization through a variety of interfaces. The implemented physics processes cover electromagnetic interaction of charged hadrons, ions, leptons and photons from 250 eV up to several PeV, hadronic interactions from thermal energies to 1 PeV and also the production and propagation of optical photons. Today the toolkit is freely available at source-code level (object-oriented C++) over the Web<sup>1</sup> and developed and maintained by the GEANT4 Collaboration (see next section).<sup>2,3</sup>

### 1.1. Short History of Geant4

The first version of GEANT was written in the FORTRAN programming language in 1974 at CERN\* as a framework for tracking only few particles through simple detectors. Since then it has come a long way to the complexity and scale of the current version, the origin of which can be traced back to two independent studies at CERN and KEK<sup>†</sup> in 1993.<sup>2</sup> Merging these two activities resulted in a project named RD44, a worldwide collaboration involving about one hundred scientists and engineers from Europe, Russia, Japan, Canada and the United States. The first production release of GEANT4 was delivered in 1998 and the number and variety of its applications has been increasing steadily. The GEANT4 Collaboration today considers itself (in terms of size of the code and number of contributors) one of the largest object-oriented and geographically distributed software development projects.<sup>2</sup>

Further author information: send correspondence to Christoph Tenzer, email: tenzer@astro.uni-tuebingen.de

\*Centre Européen pour la Recherche Nucléaire, Geneva, Switzerland

<sup>†</sup>National Laboratory for High Energy Physics, Tsukuba, Japan

The results presented here have been obtained using the current version 4.8.0.p01 of GEANT, which has evolved from previous versions on the basis of the accumulated experience of many contributors to the field of Monte Carlo simulation of detectors and physics processes.

## 1.2. Design Overview

The key requirements for GEANT4 established by RD44 in the first year of the project were functionality, modularity, extensibility and openness.<sup>2</sup> This ultimately resulted in a modular and hierarchical structure of the code, which was decided to be developed in an object-oriented approach in the C++ language. It also led to the flexible concept of a 'toolkit', where the user may assemble the simulation from components taken from the toolkit and parts of his own code.

The GEANT4 toolkit today offers the user the possibility to create a geometric model (of a detector or experimental setup) with accurate representation of the physical properties of the involved materials. He may then define sensitive elements that record information needed to simulate a detector response. The user is provided with a whole set of physics processes (see below) - to which he can add his own or modify existing ones - for the behaviour of particles in matter and/or electromagnetic fields from which he can select those relevant for the simulation.

User interaction with the simulation is possible through various interfaces for in-/output parameters, application flow and visualization of the geometries and particle tracks. The simple creation of new interfaces to every aspect of the simulation is a key feature of GEANT4.

## 1.3. Physics Processes

In GEANT4 a particle is considered *transported* by the simulation rather than being *self moving*. The length of a transportation step (for a particle at rest, this is a time step) is proposed by the physics processes that are associated with the particle at that time. Depending on its nature, a physics process applies to a particle 1) *at rest*, 2) *along step* and/or 3) *post step*.

All physics processes are treated in this same manner from the tracking point of view. GEANT4 provides the user with the following major categories: *electromagnetic*, *hadronic*, *decay*, *photolepton-hadron* and *optical* processes. For the application described in this paper, i.e. simulating the background of an X-ray detector in a typical space radiation environment, the electromagnetic processes are the most significant of the above mentioned. Descending from the field of high energy physics, GEANT4 distinguishes the so called 'standard' electromagnetic processes from the 'low-energy' electromagnetic processes. The necessary low-energy code data files for photon and electron processes have been included into our simulations in order to increase the accuracy of the simulation down to energies of about 250 eV and to simulate such phenomena as X-ray production through fluorescence.

Long term radioactivity produced by nuclear interactions represents an important contribution to the background levels in space-borne X-ray instruments, as resulting events often occur outside the time-scales of any anticoincidence. To simulate this part of the background, a Radioactive Decay Module that is able to generate the  $\gamma$ - and X-rays associated with electron capture and  $\alpha$ -,  $\beta^\pm$ - and isomeric transition decays can be included into the simulations.

## 2. SIMULATION OF THE XMM-NEWTON PN-CAMERA INTERNAL BACKGROUND

The European Photon Imaging Camera (EPIC) on board of the XMM-Newton satellite consists of three X-ray CCD cameras. Two of them are metal oxide semiconductor (MOS) CCD arrays, while the third uses pn-CCDs and is referred to as the pn-camera.<sup>4</sup> We chose to simulate the internal background of the pn-camera as a first task to understand and verify the GEANT4 physics processes relevant for an in-orbit X-ray detector. The simulation results can be directly compared to measurements as the background of the pn-camera has been thoroughly investigated and published since the launch of XMM-Newton in December, 1999.<sup>5</sup>

The pn-camera covers an energy range from 0.15 keV to 15 keV with moderate spectral ( $E/\Delta E \approx 20-50$ ) and angular resolution (PSF: 6 arcsec FWHM). It has an imaging area of 6 cm x 6 cm divided into twelve 3 cm x 1

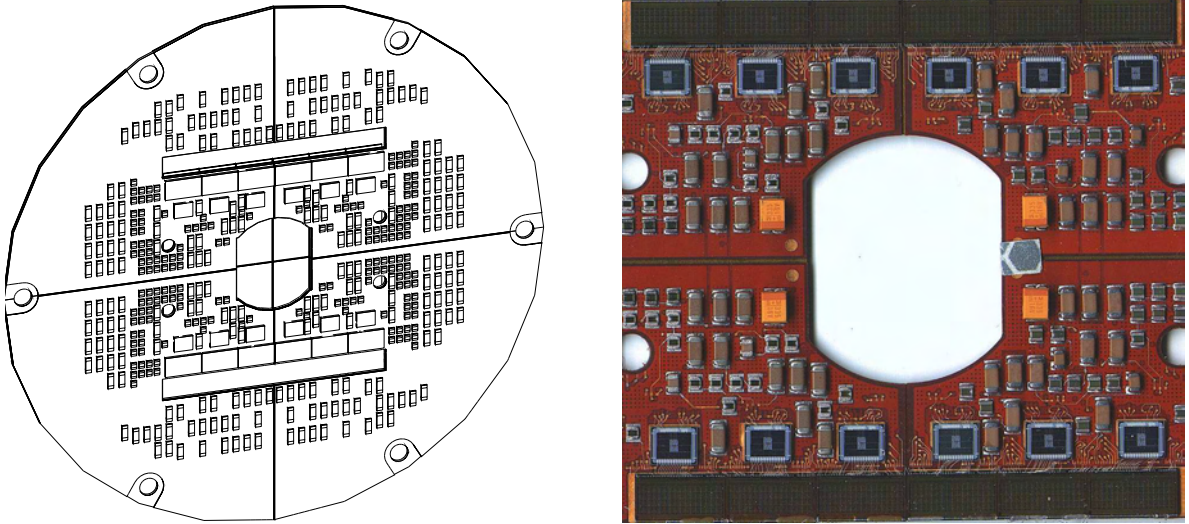


**Figure 1.** GEANT4 geometrical model (left) of the EPIC-pn focal plane printed circuit board (PCB) and a closeup photo of the area covered (on the backside) by the CCDs on a spare PCB (right). Among the components selected for the simulation are the CAMEX and TIMEX devices for each CCD as well as some smaller SMD components (resistors, capacitors).

cm pn-CCDs on a single wafer with  $200 \times 64$  pixels each. The pixel size is  $150 \times 150 \mu\text{m}^2$  and the covered field of view of the telescope is 30 arcmin.

The measured background can be roughly described as consisting of two parts: the Cosmic X-ray Background (CXB) and the instrumental background. The latter component may be further dissolved into detector noise (below 200–300 eV) and another component which is due to the interaction of high energy particles (above 100 MeV) with the structure surrounding the detector and the detector itself. This component produces a flat photon spectrum inside the detector box that is the dominant source of the background at energies above a few keV. Another contribution to the background that shows a strong and unpredictable variability are so-called *soft proton flares*, which are attributed to low energy protons with energies below  $\sim 300$  keV that are channeled onto the CCDs by the telescope mirrors.

## 2.1. Simulation

In our simulation we focussed on the X-ray fluorescence triggered by the interactions of the flat photon spectrum mentioned above with the materials inside the detector box close to the CCDs. This phenomenon has been very well measured and has been recently described by Freyberg et al.<sup>5</sup> For the simulation we created in GEANT4 a model of the CCDs and the focal plane printed circuit board (PCB) underneath the CCDs (see Fig. 1). The PCB consists of a molybdenum core with multiple copper layers on both sides that are divided into quadrants. Through the long rectangular holes, the CAMEX chips are connected via bond wires to the CCDs on the backside of the PCB. The photo on the right of Fig. 1 shows exactly the section that is covered by the CCDs on the other side. When modeling the components of the PCB, we tried to describe their material composition as accurately as possible to produce correct line amplitudes. The CCDs were defined as a sensitive detector for the simulations which measures energy and position of each interaction with particles or photons. The output of these events is then stored in FITS-format<sup>‡</sup> conforming to the XMM-Newton eventfile standards and can be further processed to images and spectra with the standard XMM-Newton science analysis software as if it were measured data.

---

<sup>‡</sup>Flexible Image Transportation System

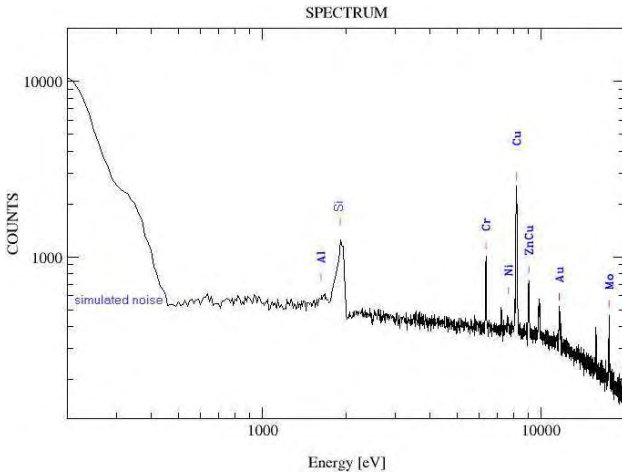


**Figure 2.** Spectrum generated from the photon events registered by the simulated CCDs showing X-ray fluorescence lines of the materials used for the PCB.

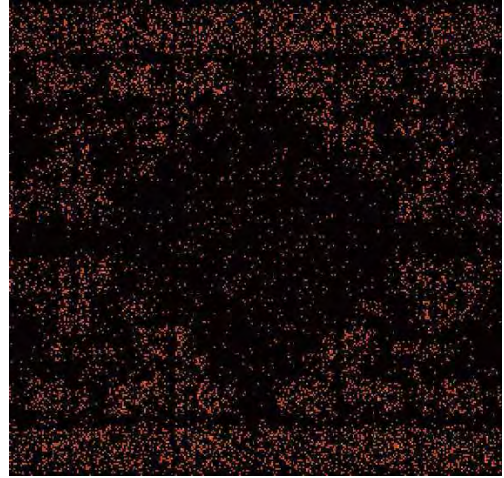


**Figure 3.** Sample energy slice image, generated of events with energy around the Ni-K $\alpha$  line (7300 - 7600 eV).

## 2.2. Results

A total of  $10^9$  isotropically emitted photons following a flat spectrum between 0.1 and 25 keV were created with the GEANT4 General Particle Source (GPS) inside the aluminum camera housing surrounding the PCB. Emphasis was laid on low energy physics processes including X-ray fluorescence emission by the irradiated materials. Time, position and deposited energy of each event inside the CCDs were recorded. The spacial dispersion of the charge cloud produced inside the CCDs by photon interactions was not simulated - thus no split events were produced. The resulting spectrum of this simulation (see Fig. 2) therefore has to be put up against a spectrum with recombined energies when comparing with measured data. Also not considered in this simulation are properties of the CCDs that relate to the readout process (CCE/CTE) or the readout electronics. Simulated Gaussian noise has been added to the spectrum afterwards to account for the electronic detector noise at lower energies. The shape of the fluorescence lines is simulated also with Gaussian distributions, their width corresponding to the respective energy resolution of the pn-camera.

When generating images around the various prominent lines of the spectrum (see Fig. 3), the PCB components where these X-ray fluorescence lines are produced can be identified as containing the respective materials.

## 2.3. Discussion

The slope of the continuum in Fig. 2 is matching the measured one and the images around the more prominent Cu, Ni and Mo K $\alpha$ -lines can be reproduced fairly well by the simulation. The relative amplitude of some of the lines however is not reproduced correctly. This is most probably due to the fact that not all parts of the camera interior contributing to the fluorescence background have yet been introduced in the geometric model. Soon we will further extend the simulation to include components like e.g. the aluminum shutter directly above the CCDs and the aluminum detector housing and its interaction with high energy particles. The detector housing is also mainly responsible for the strong Al line dominating the measured spectrum. Further simulations will show, how its contribution to the internal background could have been diminished by introducing a graded Z-shield inside the detector.

## 3. SIMULATIONS CONCERNING SYMBOL-X

SIMBOL-X is an X-ray mission that uses a  $\sim 20$  m focal length mirror to focus X-rays with energies between 0.5 and 80 keV. The focal length will be achieved by a formation flying configuration of a mirror spacecraft and a

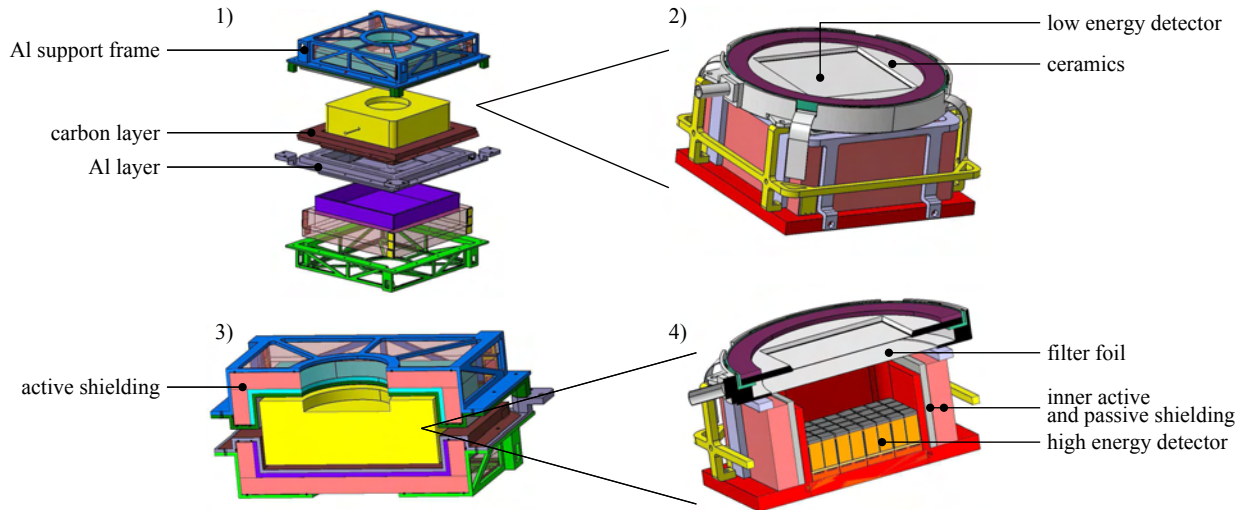


**Figure 4.** Baseline mechanical model of the SIMBOL-X focal plane. 1) Detector box - exploded view, 2) mechanical model of the inner detector assembly, 3) cut through the detector box, 4) cut through the inner detector assembly (B.P.F. Dirks et al.<sup>9</sup>).

detector spacecraft. After the end of a Phase 0 assessment study in autumn 2005, SIMBOL-X has been selected by CNES<sup>§</sup> for a one year Phase A study.

The SIMBOL-X telescope on the mirror spacecraft will be made of about one hundred Wolter Type-I nested shells, for the fabrication of which the industrial partners have already acquired a large experience through the building of the BeppoSAX, SWIFT and XMM-Newton mirrors. To ward off radiation from angles adjacent to the observing direction, the mirror spacecraft holds a 3 m diameter sky baffle.

The detector spacecraft is carrying the detector box with the high- and low-energy detectors and a collimator. The low-energy detector (LED) will be a MACRO PIXEL detector (developed by the Semiconductor Laboratory (HLL) of the Max-Planck-Institut für extraterrestrische Physik (MPE) and Werner-Heisenberg-Institut (WHI)), which is an array of depleted Field Effect Transistors (DEPFETs), each of them surrounded by a silicon drift chamber to increase the sensitive area. Prototypes of MACROPIXEL detectors have already been developed, built and tested by the HLL.<sup>6-8</sup> The LED consists of 128 x 128 pixels with a baseline size of 500 x 500  $\mu\text{m}^2$  with 450  $\mu\text{m}$  depletion depth and will be operated in a nominal energy range of 0.5 keV to 20 keV. The detector is logically and functionally divided into four quadrants of 64 x 64 pixels each that will be read out in parallel at a frame time of 256  $\mu\text{s}$ . This short integration time allows the operation of the detector even at room temperature. In order to reduce thermal noise and to achieve an energy resolution of <145 eV (FWHM) at 5.9 keV, the wafer must be cooled down to only -30°C.<sup>9</sup>

The high-energy detector (HED) of SIMBOL-X is a mosaic constructed of 8 x 8 Cd(Zn)Te crystals (10 x 10 x 2 mm<sup>3</sup>) covered with 256 pixels of about 500 x 500  $\mu\text{m}^2$ . Each crystal has its own readout electronics (developed by CEA/Saclay) located directly in a cube below. The HED will operate in the energy range of 5 to 100 keV, partially overlapping the LED's energy range. To fulfill the scientific objectives depicted below, a high energy resolution of about 1 keV at 60 keV is required. Prototypes of pixellated Cd<sub>0.9</sub>Zn<sub>0.1</sub>Te detectors are currently under study in Saclay.<sup>9</sup>

Taking the above described baseline parameters into account, the SIMBOL-X mission will provide unprecedented sensitivity and angular resolution with respect to non-focusing telescopes and will cover the sensitivity gap between XMM-Newton and the INTEGRAL observatory. To reach the intended sensitivity of below 1  $\mu\text{Crab}$ ,

---

<sup>§</sup>Centre National d'Études Spatiales, French space agency

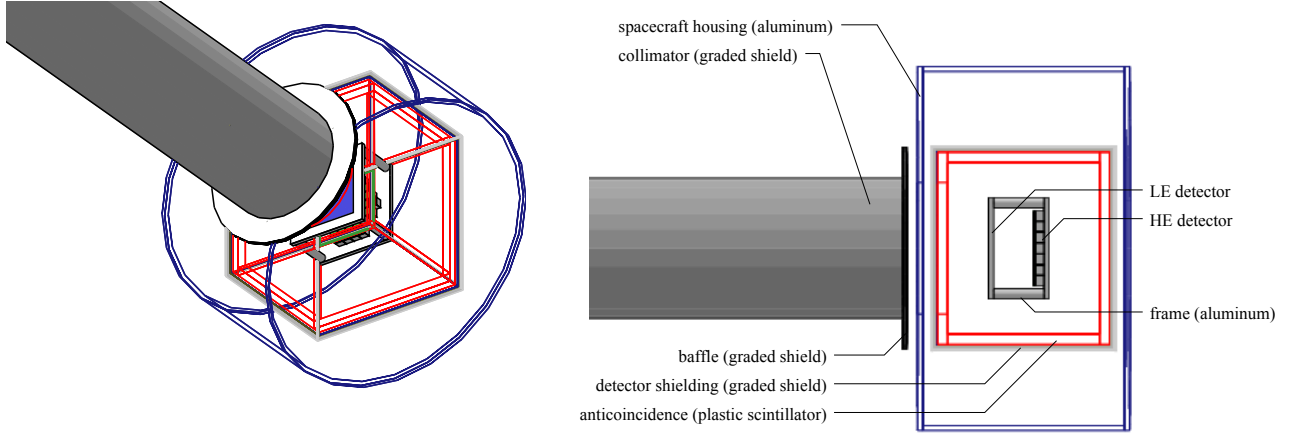


**Figure 5.** Preliminary geometric model used for the GEANT4 simulations of the SIMBOL-X detector. Wireframe 3D-view on the left and longitudinal section on the right.

the detectors need to show a very low residual background, the simulation of which is the present work of our group.

SIMBOL-X is now undergoing a phase A study, leading to a flight decision in the second quarter of 2007, with the launch scheduled 2013. The satellites will be placed in a highly excentric orbit of seven days (perigee: 44,000 km, apogee: 253,000 km) to minimize the radiation level, resulting in six days of scientific observation and one day for data downlink and formation correction. Scientific objectives include the dynamics of matter around compact objects, acceleration processes in supernova remnants, the controversial presence of a non-thermal X-ray component in clusters of galaxies and the Cosmic X-ray Background.<sup>10,11</sup>

### 3.1. Geometric Model of the Detector Spacecraft

A detailed mechanical model of the current baseline configuration of the detector housing and the detectors is shown in Fig. 4. The central elements of the geometric model are the two detectors that are interconnected through an aluminum frame. They are surrounded by an anti-coincidence shield (AC), which will most likely be consisting of plastic scintillator slabs that are connected to photo diodes. A graded shield is foreseen around or inside the AC to reduce the incoming photon flux. Its current baseline configuration is (from outside to inside) *tantalum* (1.3 mm), *tin* (2.2 mm), *copper* (0.48 mm), *aluminum* (0.27 mm) and *carbon* (0.1 mm) with a total thickness of 4.35 mm, leaving X-ray fluorescence below 0.3 keV and therefore below the detection limit of the LED. Different materials and geometric configurations for the active and passive shielding are under consideration at the moment. An aluminum structure encloses and stabilizes the active parts of the camera.

Above the aperture of the detector box, there is a 1.4 m long collimator to prevent photons coming from directions other than the FOV from hitting the detectors. It is also made of the materials that make up the graded shield. Its thickness, however, is decreasing with the distance from the detector to save weight and to maintain a constant effective thickness with respect to the incident angle of the incoming radiation. The model of the spacecraft used in our simulations is a simplified version of the mechanical model. A 3D-view and a longitudinal cut through the detector spacecraft are shown in Fig. 5.

### 3.2. Simulation of the Performance of the Collimator

Regarding the geometrical setup of the detector spacecraft, we first focussed on the performance of the collimator. Therefore  $10^8$  photons with an energy following the CXB spectrum (as compiled by D. E. Gruber et al.<sup>12</sup>) were fired at the detector spacecraft from the solid angle covered by the collimator. The countrates in both detectors were then recorded for different thickness settings of the collimator materials. Our aim was to show by simulation which thickness would suffice to reduce the background below the desired  $10^{-4}$  counts/s/cm<sup>2</sup>/keV.

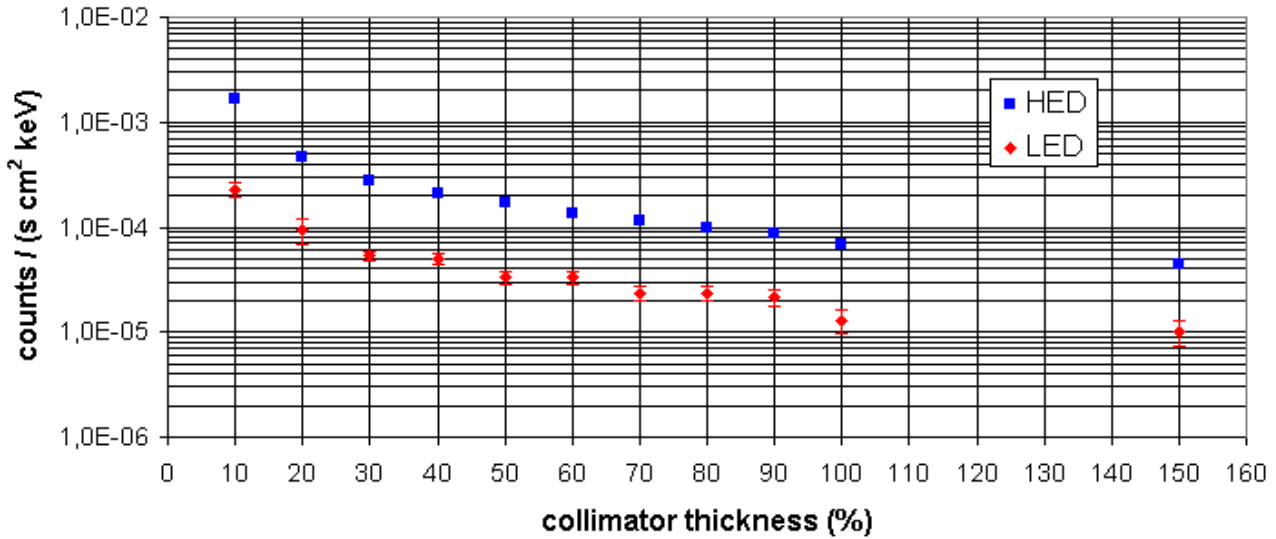


**Figure 6.** Simulated countrates in the high and low energy detector as a function of collimator thickness (100% corresponds to 4.35 mm of graded shield, see also Sect. 3.1; HED errors are smaller than plot symbols).

From the number of simulated photons and the input spectrum a virtual 'exposure time' can be calculated. In order to do this, the input spectrum has to be integrated over the energy range of the LED, the solid angle covered by the collimator and the active area of the LED. This value is then compared to the number of LED counts without collimator, taking into account the LED's quantum efficiency. Combining this exposure time with the number of hits on each detector, the detector area and the energy bandwidth, a background countrate for each detector as a function of the collimator thickness can be specified. The results of the simulations are shown in Fig. 6. An exponential decrease in the countrates with increasing thickness of the collimator is clearly observable and the thickness where the background drops below the above mentioned value is  $\sim 30\%$  for the LED and  $\sim 90\%$  of the standard settings for the graded shield for the HED.

When restricting the input spectrum (CXB) to energies below 100 keV (which is the value for up to which the collimator thickness was originally optimized by using a simple analytical model targeted at the center of the field of view), the LED detects no more photons at a collimator thickness  $> 25\%$  and at 100% no more photons are registered on both detectors. Regarding the parameters used in the simulations this can be expressed as countrates of less than  $7.1 \times 10^{-7}$  counts/s/cm<sup>2</sup>/keV for the LED and less than  $1.5 \times 10^{-7}$  counts/s/cm<sup>2</sup>/keV for the HED. The resulting background spectrum shows for 100% thickness no fluorescence lines from the collimator.

### 3.3. Simulation of the Proton-Induced Background

Another simulation study has been performed, with the purpose to estimate the level of prompt background induced by the cosmic proton flux and to quantify the efficiency of the anticoincidence shield for the rejection of this background. In that study, a slightly different geometry was used but with the same basic shielding components. Protons were shot isotropically at the whole spacecraft, in a range of energy between 10 MeV and 100 GeV. The simulations give directly the number of interactions in LED and HED and the deposited energy. Figure 7, for example, gives the number of interactions in the energy-range of interest (supposed to be 1 to 100 keV in HED and 0.5 to 15 keV in LED). Convolution with the cosmic proton flux calculated for a solar active year with the code CREME86<sup>13</sup> gives the counting rates reported in Table 1.

## 4. OUTLOOK

To test the properties of the AC and the effectiveness of the shielding for the detector box itself, a test bench has been developed where different materials for the AC (CsI, BGO, plastic) and various configurations for the

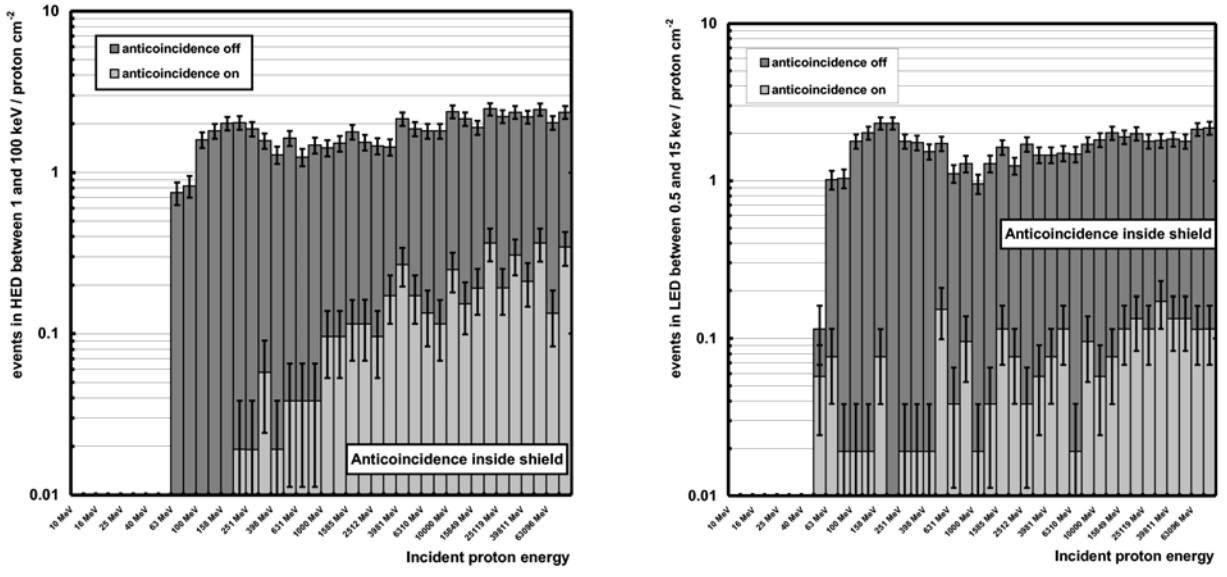


**Figure 7.** Mean number of interactions in the range of energy per proton · cm<sup>-2</sup> in HED (right) and LED (left). Anticoincidence is inside the passive graded shield.

**Table 1.** Calculated mean count rates in LED and HED due to cosmic protons, without (anticoincidence off) and after (anticoincidence on) veto. Rates in detectors are given for per cm<sup>2</sup> and per keV. Statistical errors on the last digits are indicated in parenthesis.

	Anticoincidence inside shield	Anticoincidence outside shield
Anticoincidence off		
Countrates in LED:		
Total ( $E_{LED} > 0$ )	$1.383(3)$ counts/s/cm <sup>2</sup> /keV	$1.377(4)$ counts/s/cm <sup>2</sup> /keV
In range ( $0.5 < E_{LED} < 5$ keV)	$8.39(22) \times 10^{-3}$ counts/s/cm <sup>2</sup> /keV	$6.27(27) \times 10^{-3}$ counts/s/cm <sup>2</sup> /keV
Over range ( $E_{LED} > 15$ keV)	$1.375(3)$ counts/s/cm <sup>2</sup> /keV	$1.370(4)$ counts/s/cm <sup>2</sup> /keV
Countrates in HED:		
Total ( $E_{HED} > 0$ )	$217.9(4) \times 10^{-3}$ counts/s/cm <sup>2</sup> /keV	$215.1(6) \times 10^{-3}$ counts/s/cm <sup>2</sup> /keV
In range ( $1 < E_{HED} < 100$ keV)	$1.03(3) \times 10^{-3}$ counts/s/cm <sup>2</sup> /keV	$0.69(3) \times 10^{-3}$ counts/s/cm <sup>2</sup> /keV
Over range ( $E_{HED} > 100$ keV)	$216.9(4) \times 10^{-3}$ counts/s/cm <sup>2</sup> /keV	$2.144(6) \times 10^{-3}$ counts/s/cm <sup>2</sup> /keV
Anticoincidence on		
Countrates in LED:		
Total ( $E_{LED} > 0$ )	$6.46(17) \times 10^{-3}$ counts/s/cm <sup>2</sup> /keV	$11.5(3) \times 10^{-3}$ counts/s/cm <sup>2</sup> /keV
In range ( $0.5 < E_{LED} < 5$ keV)	$0.37(5) \times 10^{-3}$ counts/s/cm <sup>2</sup> /keV	$0.20(4) \times 10^{-3}$ counts/s/cm <sup>2</sup> /keV
Over range ( $E_{LED} > 15$ keV)	$6.09(16) \times 10^{-3}$ counts/s/cm <sup>2</sup> /keV	$11.3(3) \times 10^{-3}$ counts/s/cm <sup>2</sup> /keV
Countrates in HED:		
Total ( $E_{HED} > 0$ )	$2.66(4) \times 10^{-3}$ counts/s/cm <sup>2</sup> /keV	$1.13(4) \times 10^{-3}$ counts/s/cm <sup>2</sup> /keV
In range ( $1 < E_{HED} < 100$ keV)	$0.07(1) \times 10^{-3}$ counts/s/cm <sup>2</sup> /keV	$0.02(1) \times 10^{-3}$ counts/s/cm <sup>2</sup> /keV
Over range ( $E_{HED} > 100$ keV)	$2.59(4) \times 10^{-3}$ counts/s/cm <sup>2</sup> /keV	$1.11(3) \times 10^{-3}$ counts/s/cm <sup>2</sup> /keV

graded shield can be simulated in a typical space radiation environment. The experience from this test bench will contribute to the decisions of whether to put the AC slabs inside or outside the shielding, whether a thin foil is required between the two detectors for additional shielding (and what material it should be made of) as well as to the overall geometric setup of the detector box. Adding an active shield to the base of the collimator is also an option that is considered and already queued for simulation. This could further reduce the background in the HED.

The part of the background that is due to delayed emission from material that became activated by protons will also be investigated by our group.

## ACKNOWLEDGMENTS

This work was partly supported by Bundesministerium für Wirtschaft und Technologie through Deutsches Zentrum für Luft- und Raumfahrt e.V. (DLR) grants FKZ 50QR0503 and FKZ 50OX002.

## REFERENCES

1. S. Giani et al., “An object-oriented toolkit for simulation in HEP,” <http://geant4.web.cern.ch>, *CERN/LHCC 98-44*, July 1998.
2. S. Agostinelli et al., “Geant4 - a simulation toolkit,” *Nuclear Instruments and Methods in Physics Research A* **506**, pp. 250–303, July 2003.
3. J. Allison et al., “Geant4 developments and applications,” *IEEE Transactions on Nuclear Science* **53**, pp. 270–278, 2006.
4. L. Strüder et al., “The European Photon Imaging Camera on XMM-Newton: The pn-CCD camera,” *A&A* **365**, pp. L18–L26, Jan. 2001.
5. M. J. Freyberg, U. G. Briel, K. Dennerl, F. Haberl, G. D. Hartner, E. Pfeffermann, E. Kendziorra, M. G. F. Kirsch, and D. H. Lumb, “EPIC pn-CCD detector aboard XMM-Newton: status of the background calibration,” in *X-Ray and Gamma-Ray Instrumentation for Astronomy XIII. Edited by Flanagan, Kathryn A.; Siegmund, Oswald H. W. Proceedings of the SPIE, Volume 5165*, pp. 112–122 (2004)., K. A. Flanagan and O. H. W. Siegmund, eds., pp. 112–122, Feb. 2004.
6. J. Treis et al., “Noise and spectroscopic performance of DEPMOSFET matrix devices of XEUS,” in *Proceedings of the SPIE*, **5898**, pp. 256–266, 2005.
7. J. Treis et al., “Advancements in DEPMOSFET device developments for XEUS,” in *Proceedings of the SPIE*, **6276-17**, 2006.
8. L. Strüder et al., “Active X-ray pixel sensors with scalable pixel sizes from  $1\mu m^2$  to  $10^8 \mu m^2$  in Heaven and on Earth,” in *Proceedings of the SPIE*, **6276-48**, 2006.
9. B.P.F. Dirks et al., “The focal plane of the SIMBOL-X space mission,” in *Proceedings of the SPIE*, **6276-45**, 2006.
10. P. Ferrando et al., “SIMBOL-X: a formation flying mission for hard-x-ray astrophysics,” in *Optics for EUV, X-Ray, and Gamma-Ray Astronomy II. Edited by Citterio, Oberto; O'Dell, Stephen L. Proceedings of the SPIE, Volume 5900*, pp. 195–204 (2005)., pp. 195–204, Aug. 2005.
11. P. Ferrando et al., “SIMBOL-X: mission overview,” in *Proceedings of the SPIE*, **6266-17**, 2006.
12. D. E. Gruber, J. L. Matteson, L. E. Peterson, and G. V. Jung, “The Spectrum of Diffuse Cosmic Hard X-Rays Measured with HEAO 1,” *The Astrophysical Journal* **520**, pp. 124–129, July 1999.
13. A. Claret, “Space environment of SIMBOL-X,” in *DAPNIA/SAp/CRS internal note*, Feb. 2006.



### 3. LES OBJETS : LES SYSTEMES BINAIRES X DANS LA GALAXIE

#### *Qu'est-ce qu'une binaire X ?*

Comme on l'a déjà évoqué, un système binaire X est un système double d'étoile composé d'une étoile de la séquence principale ou géante et d'un compagnon compact, trou noir ou étoile à neutrons. C'est en effet dans le domaine des rayons X que furent d'abord révélés les processus émissifs mis en œuvre par les astres compacts accrétaux, c'est à dire attirant gravitationnellement la matière de leur compagnon. Grâce aux missions spatiales d'astronomie X des quarante dernières années, nous détenons une masse impressionnante de données concernant ces systèmes binaires.

On admet en général que le compagnon cède une partie de sa masse à l'étoile effondrée, soit en débordant son lobe de Roche, soit par vent stellaire. Dans le cas d'un débordement du lobe de Roche, la matière ne tombe pas directement sur l'astre compact, mais forme en général un disque d'accrétion où le moment cinétique de la matière accrétae se dissipe par des processus de viscosité turbulente. Ainsi porté à très haute température, le disque d'accrétion suscite l'émission d'un intense rayonnement à haute énergie qu'un mécanisme régulateur limite dans le cas d'une émission stable<sup>4</sup>. La quantité d'énergie que dissipent les processus d'accrétion, autrement dit la luminosité d'accrétion  $L_{\text{acc}}$ , s'exprime par la relation suivante :

$$L_{\text{acc}} = \frac{GM\dot{M}}{R} = 1,3 \cdot 10^{33} \dot{M}_{16} M_1 R^{-4} \text{ erg s}^{-1}$$

où  $M_1$  est la masse de l'étoile effondrée en unité de masse solaire,  $R_4$  son rayon en unité de  $10^4$  km, et le taux d'accrétion en unité de  $10^{16} \text{ g s}^{-1}$  (ce qui équivaut à  $1,5 \cdot 10^{-10} M_\odot$  par an).

La Table 3.1, ci-dessous, fournit pour chacun des trois types d'astres effondrés une valeur approchée de la luminosité d'accrétion calculée au moyen de la relation précédente dans le cas où  $\dot{M} = 10^{16} \text{ g s}^{-1}$ . On constate qu'à taux d'accrétion identique, les naines blanches accrétales conduisent à des luminosités d'accrétion bien plus faibles que les deux autres types d'étoiles effondrées. Compte tenu du caractère généralement très mou – riche en photons de basse énergie – de leur émission dans le domaine X, les sources X binaires contenant une naine blanche ne sont pas souvent détectées par les télescopes actuels au delà de 15 keV.

---

<sup>4</sup> Si la luminosité induite par le processus d'accrétion s'avère supérieure à la luminosité d'Eddington (voir plus loin), le rayonnement ainsi produit repousse par pression de radiation la matière que l'astre compact tente d'accréter. L'accrétion s'arrête alors.

Type d'astre effondré	Masse (M <sub>⊕</sub> )	Rayon (km)	$L_{\text{acc}}$ (10 <sup>34</sup> erg s <sup>-1</sup> )
Naine blanche	1	10 000	0,1
Étoile à neutrons	1,4	10	200
Trou noir	5	15	400

Nous nous limitons donc dans les pages qui suivent aux systèmes binaires où l'accrétion est suscitée par une étoile à neutrons ou un trou noir d'origine stellaire. Les systèmes en question se divisent en deux familles, selon la nature du compagnon :

1. Les binaires X de petite masse, désignées par le sigle LMXB, de l'anglais *Low Mass X-ray Binary*. Le transfert de matière est produit par le débordement du lobe de Roche affectant un compagnon de petite masse.
2. Les binaires X massives, désignées par le sigle HMXB, de l'anglais *High Mass X-ray Binary*. Le transfert de matière résulte du vent stellaire engendré par un compagnon massif de type spectral O ou B.

Outre la masse du compagnon, les différences les plus significatives entre les deux familles de binaires X sont les suivantes :

1. Les HMXB sont des systèmes plus jeunes que les LMXB.
2. Le rayonnement dans le domaine visible provient principalement du disque d'accrétion dans le cas des LMXB et du compagnon dans le cas des HMXB.
3. La luminosité des LMXB dans le domaine des rayons X est très supérieure à leur luminosité dans le visible, contrairement au cas des HMXB.
4. L'intensité du champ magnétique suscité par l'astre compact, dans les systèmes renfermant une étoile à neutrons, est  $B \sim 10^{12}$  G dans le cas des HMXB et  $B \sim 10^8\text{-}10^9$  G dans le cas de la plupart des LMXB en raison de la différence d'âge entre les spécimens des deux familles de binaires X.

Avant de se préoccuper de leur émission dans le domaine des rayons X et  $\gamma$  de basse énergie, il me semble opportun de présenter les traits principaux des deux familles de binaires X identifiées ci-dessus.

## Les binaires de faible masse (LMXB)

On distingue trois types de LMXB. Les deux premiers concernent des systèmes renfermant une étoile à neutrons et se définissent selon la luminosité X du système, le troisième se rapporte à des systèmes abritant un trou noir.

1. Le premier type rassemble les LMXB les plus brillantes, localisées en général au sein du bulbe galactique. Dans le domaine X, leur luminosité  $L_X$  est proche de la luminosité d'Eddington ( $L_X \sim 10^{38}$  erg s<sup>-1</sup>, voir plus bas). Le débordement du lobe de Roche alimentant le processus d'accrétion pourrait être dû à l'évolution du compagnon (passage de la séquence principale au stade sous-géante). Les LMXB de ce type produisent peu d'émission dans le domaine des rayons X durs et  $\gamma$ .

2. Les LMXB du deuxième type sont beaucoup moins lumineuses dans le domaine X où leurs émissions présentent des variations brusques d'intensité accompagnées d'évolutions spectrales notoires. Le débordement du lobe de Roche serait dû à une perte de moment angulaire induite par émissions d'ondes gravitationnelles ou par freinage magnétique. Il en résulte un taux d'accrétion assez faible ( $\dot{M} \approx 10^{-10} - 10^{-9}$  M an<sup>-1</sup>) conduisant dans le domaine X à une luminosité qui s'avère bien inférieure à la luminosité d'Eddington. Les LMXB de ce type sont parfois à l'origine d'émissions  $\gamma$ ; elles se caractérisent également par des émissions X impulsives de nature répétitive.

3. Les LMXB abritant un trou noir constituent un type à part, caractérisé par une émission abondante dans la bande des rayons  $\gamma$  de basse énergie. La luminosité de certains de ces systèmes peut s'accroître en quelques jours de plusieurs ordres de grandeur, avant de décroître d'une manière plus ou moins régulière avec une constante de temps de l'ordre de quelques semaines.

On peut également classer les LMXB en fonction du stade d'évolution du compagnon (étoile sur la séquence principale, sous-géante ou naine blanche). Les systèmes dont les compagnons se trouvent dans chacun de ces trois stades présentent les schémas d'évolution suivants (d'après Rappaport *et al.*, 1982 ; Webbink *et al.*, 1983 ; Pylyser *et al.*, 1988) :

1. Les LMXB où le compagnon est une étoile sur la séquence principale présentent des périodes orbitales  $P$  telles que  $50$  mn  $\leq P \leq 9$  h. Comme évoqué plus haut, il s'agit de spécimens sous lumineux qui sont le siège d'émissions X impulsives de nature répétitive. Lorsque le moment angulaire orbital du système diminue, le lobe de Roche du compagnon se resserre et "épluche" l'étoile compagnon, la période orbitale du système décroît alors. Sa masse diminuant, l'étoile compagnon, qui n'est plus en mesure de maintenir en son centre des conditions suffisantes pour activer les réactions thermonucléaires, s'effondre en une naine blanche.

2. Les LMXB où le compagnon est une étoile sous-géante présentent des périodes orbitales  $P \sim 9$  h. Leur luminosité dans le domaine X étant proche de la limite d'Eddington, il est difficile de déterminer quelle proportion de l'enveloppe en expansion du compagnon est accrétée par

l'astre compact. En fin d'évolution, le compagnon devient également une naine blanche, évoluant alors dans un système à grande séparation orbitale.

3. Les LMXB où le compagnon est une naine blanche présentent des périodes orbitales  $P \sim 50$  mn. Contrairement aux compagnons dans les deux autres stades d'évolution, ceux dans le stade naine blanche voient leur rayon augmenter quand leur masse diminue, ce qui accroît la période orbitale du système. La période en question passe par un minimum (quelques dizaines de minutes) qui peut subsister assez longtemps, la masse  $M_1$  du compagnon étant alors très petite ( $M_1 < 0,1 M_\odot$ ). Le transfert de matière par débordement du lobe de Roche devient de moins en moins actif au fur et à mesure que diminuent les pertes de moment angulaire.

À noter que dans certaines conditions, l'évolution de LMXB abritant une étoile à neutrons peut conduire à la formation des pulsars en rotation ultra-rapide, dits pulsars "milliseconde". Si son champ magnétique est suffisamment faible, la rotation de l'étoile à neutrons peut en effet être accélérée par la matière qu'elle accrète. L'astre compact devient alors un pulsar de plus en plus rapide, émettant un rayonnement X et  $\gamma$  de plus en plus intense. Le pulsar tourne alors suffisamment vite pour que la pression de son rayonnement expulse le disque. Interceptant la partie du rayonnement  $\gamma$  émis dans le plan orbital du système, le compagnon s'évapore sous l'action des rayons  $\gamma$  qu'il reçoit. On expliquerait ainsi la présence de pulsars milliseconde isolés après avoir complètement volatilisé leur compagnon.

*Caractéristiques temporelles des LMXB.* Sous l'impulsion des observations menées dans le domaine X, les aspects temporels des LMXB ont été l'objet de nombreuses études. En balayant l'espace de Fourier, on peut ainsi passer en revue quelques uns des différents phénomènes propres aux LMXB. Les mouvements orbitaux peuvent être identifiés à des fréquences  $f < 1$  mHz. Comme détaillé ci-dessus, les périodes orbitales s'échelonnent de 10 minutes à 10 jours. De  $f \approx 1$  mHz à  $f \approx 1$  Hz, le spectre de puissance des LMXB s'ajuste à une loi de puissance d'indice compris entre 1,2 et 1,6. Ce spectre est caractéristique de phénomènes aléatoires auto-similaires se produisant dans des zones turbulentes qui pourraient se situer dans le disque d'accrétion et/ou au voisinage de l'astre compact.

On observe les oscillations quasi périodiques dans la bande 1-50 Hz (Lewin *et al.*, 1988). Ces manifestations ont été découvertes en 1985 à la suite des observations de GX\_5-1 (une LMXB brillante du bulbe galactique) menées dans le domaine des rayons X avec le satellite européen *Exosat*. Des phénomènes du même type ont ensuite été détectés dans des dizaines d'autres sources X. On suppose que ces oscillations sont créées au voisinage d'une étoile à neutrons faiblement magnétisée ( $B \sim 10^8 - 10^9$  G) accrétant à un taux proche de la limite d'Eddington. Considérées longtemps comme l'apanage des étoiles à neutrons, les oscillations quasi périodiques sont maintenant identifiées, mais à plus basse fréquence (entre 0,1 et 1 Hz), dans le rayonnement produit par des systèmes abritant un trou noir (Vikhlinin *et al.*, 1994, 1995). À noter que ces dernières manifestations furent le plus souvent détectées dans la bande des rayons  $\gamma$  de basse énergie. Récemment, des oscillations à hautes fréquences (plusieurs centaines de Hz) en provenance d'étoiles à neutrons ont été observées par le satellite d'astronomie X américain RXTE (une revue de ces observations est donnée dans Van der Klis, 2000).

## Les binaires massives (HMXB)

Il s'agit de systèmes où le compagnon est une étoile de type spectral O ou B, dont la masse est supérieure à 6-8 masses solaires, et dont le vent stellaire est à l'origine du transfert de matière entre les deux composantes du système. En raison du plus petit nombre de spécimens répertoriés, la modélisation détaillée de ce processus d'accrétion n'est pas encore achevée, d'autant plus que l'interaction d'une étoile à neutrons ou d'un trou noir avec un vent stellaire est un phénomène assez complexe. Il faut en effet prendre en compte les instabilités inhérentes aux vents eux-mêmes, ainsi que tous les effets induits par la gravité et par le rayonnement que suscite l'astre compact. Il s'agit par exemple des effets de marées qui déforment le compagnon, augmentant ainsi le transfert de matière. Mais il s'agit aussi de la photo-ionisation du matériau emporté par le vent stellaire qui empêche le rayonnement UV du compagnon de contribuer à l'accélération du vent. Des travaux théoriques ont pourtant été menés sur ce sujet, prenant en compte l'un ou l'autre de ces effets, mais aucune étude complète n'est encore disponible. Le transfert de matière est tel qu'un disque d'accrétion peut même apparaître de temps à autre.

Compte tenu de la nature du compagnon, les HMXB sont très lumineuses dans le visible où elles rayonnent jusqu'à 10 000 fois plus d'énergie que dans le domaine des rayons X. Et comme l'émission X suscitée par l'astre compact modifie peu les propriétés du compagnon, son étude spectroscopique dans le visible permet de déterminer la distance et les paramètres orbitaux des HMXB. Ces derniers sont d'autant plus facilement mesurables quand le plan orbital du système n'est pas trop incliné par rapport à l'axe de visée. Dans ce cas, en raison de sa taille, le compagnon occulte en effet périodiquement l'émission X suscitée par l'astre compact<sup>5</sup>.

L'étude de ces occultations permet de déterminer non seulement la période orbitale du système, mais également toute une série de paramètres concernant aussi bien le compagnon que l'étoile effondrée. Connaissant le type spectral du compagnon (ce qui permet d'en estimer la masse) et les paramètres orbitaux du système, il est alors possible de déterminer la masse de l'étoile effondrée grâce à la fonction de masse évoquée au chapitre 1. Dans le cas des étoiles à neutrons, on a pu ainsi montrer que leurs masses sont très proches de la valeur canonique de  $1,4 M_{\odot}$ . Toujours dans le cas de HMXB abritant une étoile à neutrons, l'émission à haute énergie présente le plus souvent un comportement de type pulsar, caractérisé par une variation périodique de l'émission, avec des périodes mesurées comprises entre quelques dizaines de millisecondes et plusieurs minutes.

Signalons enfin le cas des HMXB dont le compagnon massif est une étoile de type Be, un cas particulier d'étoile de type B possédant une enveloppe ténue de gaz éjectée probablement par un effet centrifuge lié à la rotation rapide de l'étoile. Les paramètres orbitaux (période et excentricité) des HMXB abritant une étoile de type Be sont en général tels que leur éclat dans

---

<sup>5</sup> La découverte des binaires X à éclipses, au tout début des années soixante-dix, confirma les prédictions de Shklovskii (1967) sur la nature binaire des sources X brillantes et sur le fait que des processus d'accrétion peuvent être à l'origine d'une abondante émission de rayonnement à haute énergie.

le domaine des rayons X est hautement variable, les phases de forte luminosité coïncidant avec le périastre. Dans le cas de la source 4U 0115+635, on note par exemple des variations d'éclat dont l'amplitude atteint un facteur de l'ordre de 10 000 dans la bande des rayons X “mous”. L'émission X des HMXB abritant une étoile de type Be est de nature quasi thermique, compatible avec celle d'un milieu porté à une température  $T$  telle que  $\approx 10$  keV.

## ***L'émission des binaires X***

### **La luminosité d'Eddington**

Dans la mesure où la matière accrétée est constituée d'atomes ionisés, ce qui est généralement le cas des sources accrétantes rayonnant dans les domaines des rayons X durs et des rayons  $\gamma$  de basse énergie, elle interagit principalement par diffusion Thomson avec le rayonnement éventuellement émis au voisinage de l'astre accrétant. La pression des photons s'exerce alors préférentiellement sur les électrons, beaucoup plus légers que les protons. Le rayonnement de luminosité  $L$  émis au voisinage de l'astre accrétant exerce alors à une distance  $r$  une force  $F_R$  répulsive sur les électrons accrétés qui s'exprime par l'équation suivante :

$$F_R = \frac{L\sigma_T}{4\pi r^2 c}$$

où  $\sigma_T$  est la section efficace de Thomson et  $c$  la célérité de la lumière. Cette force répulsive est communiquée aux ions par l'intermédiaire de l'attraction coulombienne entre ions et électrons. Elle s'oppose ainsi à la force gravitationnelle  $F_G$  qui elle s'exprime par la relation suivante :

$$F_G \approx \frac{GMm_p}{r^2}$$

où  $m_p$  est la masse du proton,  $G$  la constante de la gravitation et  $M$  la masse de l'astre accrétant. Ces deux forces s'exerçant toutes deux en raison de l'inverse du carré de la distance à l'astre accrétant, il existe une luminosité critique où elles s'équilibrent dans tout l'espace où l'accrétion se manifeste. Cette luminosité, dénommée luminosité d'Eddington, s'exprime par la relation suivante :

$$L_{Edd} = \frac{4\pi GMm_p c}{\sigma_T} = 1,310^{38} \frac{M}{M_s} erg s^{-1}$$

Dans le cas d'une étoile à neutrons de masse  $M = 1,4 M_s$ , la luminosité d'Eddington est égale à  $L_{Edd} \approx 1,8 \cdot 10^{38} \text{ ergs}^{-1}$ , comme noté précédemment. Si la luminosité induite par le processus d'accrétion est plus faible que la luminosité d'Eddington, l'accrétion n'est pas troublée par le rayonnement suscité par l'astre compact. Si par contre elle approche  $L_{Edd}$  (on dit alors que l'astre accrète à la limite d'Eddington), le rayonnement s'oppose à la matière accrétée au point de la repousser vers l'extérieur, pouvant ainsi annuler le processus d'accrétion.

## L'influence du champ magnétique induit par l'astre accrétant

Étudier l'interaction entre le gaz ionisé accrétré et le champ magnétique induit par l'astre accrétant est une entreprise particulièrement ardue en raison des très nombreuses instabilités magnétohydrodynamiques qui peuvent se développer dans le flot en accrétion. Nous nous contentons donc ici d'aborder le cas le plus simple, celui où un flot de matière de densité  $\rho$  s'écoulant à une vitesse  $u$  tombe d'une manière isotrope sur un astre magnétisé.

Lorsqu'un gaz ionisé est accrétré par un astre magnétisé, l'action du champ magnétique se fait sentir à une distance  $r_M$  où la valeur de la pression magnétique est *grossost modo* de l'ordre des termes prépondérants dans l'équation de Bernoulli qui décrit le flot de matière accrétee. Le flot étant largement supersonique au voisinage de l'astre accrétant, on peut négliger le terme de pression. On constate alors que si les autres termes de l'équation de Bernoulli relatifs respectivement à l'énergie cinétique globale des particules, à la force de gravité et au champ magnétique, sont tous trois du même ordre de grandeur, on obtient l'enchaînement de relations suivant :

$$\frac{\rho u^2}{2} \approx \frac{GM\rho}{r_M} \approx \frac{B^2}{8\pi} = \frac{\mu^2}{8\pi r_M^6}$$

où  $B$  est l'intensité du champ magnétique supposé dipolaire de moment  $\mu$ ,  $G$  la constante de la gravitation et  $M$  la masse de l'astre accrétant. De ce système de deux équations à trois inconnues  $u$ ,  $\rho$  et  $r_M$ , on tire les deux relations suivantes :

$$r_M = \frac{(8\pi GM\rho)^{\frac{1}{5}}}{\mu^{\frac{2}{5}}} \quad \text{et} \quad u \approx \sqrt{\frac{2GM}{r_M}}$$

Au moyen d'une troisième équation, relative à la loi de conservation de la masse :

$$\dot{M} = 4\pi r^2 \rho |u|$$

on obtient une estimation du rayon  $r_M$  par la relation suivante :

$$r_M \approx 2000 \dot{M}_{16}^{-\frac{2}{7}} M^{-\frac{1}{7}} \mu_{30}^{\frac{4}{7}} \text{ km}$$

où  $\dot{M}$  est le taux d'accrétion exprimé en unité de  $10^{16} \text{ g s}^{-1}$ ,  $M$  la masse de l'astre accrétant en masse solaire et  $\mu_{30}$  le moment magnétique en unité de  $10^{30} \text{ G cm}^{-3}$ . Le rayon  $r_M$ , dénommé rayon d'Alvén, correspond donc *grossost modo* au rayon de la magnétosphère de l'astre magnétisé comprimé par le flot accrétré. Au vu des équations précédentes, on constate que pour  $r < r_M$ , la pression magnétique augmente beaucoup plus rapidement que les autres termes de pression. Le flot de matière accrétee est donc largement dominé par le champ magnétique dès qu'il passe le rayon d'Alvén.

Dans le cas détaillé plus bas, où le processus d'accrétion s'effectue par l'intermédiaire d'un disque, on peut encore faire allusion à une surface d'Alvén. Comme dans le cas précédent, cette surface correspond *grosso modo* à la limite de la magnétosphère de l'astre magnétisé. Fortement comprimée par le disque, la surface d'Alvén, qui n'est donc plus vraiment sphérique, présente un rayon moyen qui correspond approximativement au rayon interne du disque d'accrétion ceinturant l'astre magnétisé. Pour une étoile à neutrons accrétant par le truchement d'un disque à un taux d'accrétion d'environ  $10^{16} \text{ g s}^{-1}$ , il apparaît que  $r_{\text{MD}} \approx 1000 \text{ km}$  pour  $B = 10^{12} \text{ G}$  et  $r_{\text{MD}} \approx 20 \text{ km}$  pour  $B = 10^9 \text{ G}$ .

On constate ainsi que la matière accrétee comprime très fortement la magnétosphère d'une étoile à neutrons faiblement magnétisée, c'est à dire telle que  $B \sim 10^9 \text{ G}$ . Pour un taux d'accrétion supérieur à  $10^{17} \text{ g s}^{-1}$ , la surface d'Alvén se confond avec celle de l'étoile et le champ magnétique n'a alors que peu d'influence sur l'accrétion. Le rayon interne du disque est dans ce cas très proche de la surface de l'étoile, ce qui entraîne la formation entre l'étoile et le disque d'une couche limite, *a priori* très turbulente et qui peut s'avérer émettrice de rayonnement  $\gamma$ . Au contraire, quand l'étoile à neutrons est fortement magnétisée, les lignes du champ magnétique canalisent le flot de matière accrétee en direction des pôles magnétiques de l'étoile. Il se forme alors une colonne de matière à la verticale des pôles, la "colonne d'accrétion", susceptible aussi de rayonner dans la bande des photons  $\gamma$  de basse énergie.

Toujours dans le cas où l'accrétion se fait par l'intermédiaire d'un disque, la matière aborde en spirale la magnétosphère de l'astre magnétisé. Si la matière accrétee tourne plus vite que la magnétosphère (cette dernière étant entraînée par la rotation de l'astre), elle s'emploie à accroître la vitesse angulaire de la magnétosphère et par conséquence celle de l'astre en question. À l'inverse, lorsque l'astre tourne plus vite que le disque d'accrétion, les phénomènes de friction qui apparaissent entre le disque et la magnétosphère ont tendance à diminuer la vitesse angulaire de l'astre (Ghosh et Lamb, 1979). Dans le cas extrême d'une étoile à neutrons tournant beaucoup plus vite que son disque d'accrétion, la force centrifuge qui en résulte est en mesure de repousser la matière accrétee, annulant ainsi par effet d'hélice le processus d'accrétion (Illarionov et Sunyaev, 1975).

## Le modèle standard des disques d'accrétion

En raison du moment cinétique non nul emporté par la matière soutirée à l'étoile compagnon, l'accrétion dans un système binaire n'est généralement pas sphérique, mais passe par l'intermédiaire d'un disque d'accrétion. Ces structures, étudiées au début des années soixante-dix par de nombreux auteurs, sont décrites par le modèle de Shakura et Sunyaev (1973), connu également sous le nom de modèle standard. La difficulté principale liée à la construction d'un tel modèle provient de notre méconnaissance de la manière dont la viscosité s'exerce au sein des disques d'accrétion. Le mérite du modèle standard de Shakura et Sunyaev est d'avoir résumé notre ignorance à un seul facteur, le paramètre  $\alpha$ .

Dans ce cadre, un disque d'accrétion s'organise en général en trois zones :

La zone 1 correspond aux régions internes du disque ( $r < r_1$ ) où la pression de radiation  $P_R$  est supérieure à la pression  $P_G$  du gaz. La température est telle que dans ce milieu où les atomes

sont totalement ionisés, les électrons du plasma perdent principalement leur énergie par diffusion Thomson – voire par diffusion Compton si la température du milieu dépasse  $10^8$  K.

La zone 2 correspond aux régions intermédiaires du disque ( $r_1 < r < r_2$ ), où la pression du gaz prend le dessus sur la pression de radiation. La diffusion Thomson reste le processus de refroidissement des électrons jusqu'à la limite de la zone 2 au delà de laquelle les processus Bremsstrahlung deviennent prépondérants.

La zone 3 correspond aux régions externes du disque ( $r > r_2$ ), où la pression du gaz domine totalement la pression de radiation. Les électrons y perdent leur énergie par Bremsstrahlung. Dans les régions les plus externes du disque d'accrétion, la température peut descendre au dessous de 10 000 K, entraînant la recombinaison de l'hydrogène. Il convient alors d'entreprendre un calcul de transfert de rayonnement suffisamment précis pour déterminer le spectre d'émission de ces régions.

### **Emettre des rayons X durs/ $\gamma$ ?**

Il ne suffit pas qu'une étoile effondrée suscite un processus d'accrétion pour émettre dans le domaine des rayons  $\gamma$ . En effet, quand le disque d'accrétion produit un rayonnement de nature thermique, comme c'est le cas général pour des milieux émissifs optiquement épais, l'énergie moyenne des photons émis est de l'ordre du kiloélectronvolt, en plein dans le domaine des rayons X. En témoigne la très longue liste des sources X, dont beaucoup sont associées à des astres compacts accrétants. Or peu d'entre elles se retrouvent dans la plus courte liste des sources détectées dans la bande des rayons  $\gamma$  de basse énergie. Quelles caractéristiques doit donc présenter une étoile effondrée accrétante pour susciter un puissant rayonnement  $\gamma$  ? Pour y parvenir, l'astre accrétant doit présenter l'une des particularités suivantes :

1. L'astre accrétant est une étoile à neutrons faiblement magnétisée : l'émission  $\gamma$  est sans doute produite par la couche limite entre la surface de l'astre compact et le disque d'accrétion. Il s'agit de ces LMXB sous lumineuses à sursauts d'émission X répertoriées sous le nom de « burster » X de type I.
2. L'astre accrétant est une étoile à neutrons fortement magnétisée : La matière qui se précipite à la surface de l'étoile est canalisée par le champ magnétique ; elle forme alors une colonne d'accrétion, dont la base, la zone la plus dense et la plus chaude, confine le milieu émissif à haute énergie. Sous l'effet des chocs à l'œuvre dans cette colonne, la température du milieu y atteint des valeurs de l'ordre de 500 millions de degrés, ce qui rend le milieu en question apte à rayonner dans la bande des rayons  $\gamma$  de basse énergie. Ce site émissif se situe au-dessus des pôles magnétiques de l'astre compact ; pour peu que l'axe des pôles magnétiques ne coïncide pas avec l'axe de rotation (comme c'est par exemple le cas de la Terre), le télescope  $\gamma$  “voit” la zone émissive sous un aspect qui varie en phase avec la rotation de l'étoile. L'émission  $\gamma$  observée présente alors un comportement périodique manifeste.
3. L'astre accrétant est un trou noir : l'émission  $\gamma$ , qui peut s'étendre largement au delà de 100 keV, est produite par des processus de comptonisation à l'œuvre dans les régions centrales du disque, comme nous le verrons plus loin.

## **Evolution récentes des modèles de disque**

Dans les années 90, des travaux de magnétohydrodynamique menés par le professeur Chakrabarti du Bose National Institute à Calcutta en Inde, ont donné une vision un peu différente des disques d'accrétion (Chakrabarti et Titarchuk, 1995). En particulier, ils ont montré l'importance d'une nouvelle composante dans le flot accrétré, en supplément du disque, due aux particules s'échappant du compagnon avec un faible moment cinétique. Ces particules en effet tomberaient directement sur l'objet compact produisant une sorte de vent autour du disque. Il a montré aussi que pour un système abritant un trou noir, une zone de choc devrait se créer à environ 10-20 rayons de Schwarzschild, le flot alors supersonique devenant subsonique. Ce choc, créant une élévation de température du plasma accrétré, devrait produire une zone d'émission de rayons X durs et  $\gamma$ . J'ai commencé une collaboration avec le professeur Chakrabarti afin de modéliser le transfert du rayonnement dans cette zone, en utilisant le programme qui sera décrit au chapitre 4.

## ***Observations Sigma des binaires X***

### **Les binaires X observées par Sigma**

Sigma a observé de nombreuses binaires X, appartenant aux différents types décrits précédemment et détaillées ci-dessous :

Nom usuel	Nature de l'astre effondré	Type de LMXB
GRS 1716-249	Trou noir	Trou noir accrétant
1E 1740.7-2942	Trou noir	Trou noir accrétant
GRS 1758-258	Trou noir	Trou noir accrétant
GX 1+4	Étoile à neutrons	Pulsar accrétant
GX 354-0	Étoile à neutrons	Sursauteur X
Terzan 2	Étoile à neutrons	Sursauteur X
A 1742-294	Étoile à neutrons	Sursauteur X
Terzan 1	Étoile à neutrons	Sursauteur X
SLX 1735-269	Étoile à neutrons	Non identifié
GRS 1743-290	Étoile à neutrons	Non identifié

### **Observations Sigma des trous noirs accrétaux**

Comme il sera détaillé au prochain chapitre, si l'équilibre thermique d'une zone proche de l'objet compact est gouverné par la diffusion Compton des photons sur un gaz d'électrons chauds, cette zone est susceptible d'émettre par effet Compton inverse un abondant rayonnement  $\gamma$  à basse énergie. Cependant, dans le cas où l'astre accrétaux est une étoile à neutrons, sa surface, chauffée par le rayonnement, émet vers cette dernière un flux notable de

photons X de basse énergie, dont la diffusion Compton contribue à refroidir la température du gaz d'électrons. L'émission de la zone proche n'est pas alors significative dans le domaine  $\gamma$ .

Par contre, dans le cas où l'astre compact est un trou noir, il n'émet aucun rayonnement. Pour refroidir la zone proche, il ne faut plus compter que sur les photons émis à la périphérie du disque. Le spectre de l'émission peut alors s'étendre loin dans la bande des photons  $\gamma$  de basse énergie, ce qui confère aux sources de ce type observées par Sigma une grande luminosité absolue au delà de 100 keV. C'est sur la foi de ce critère spectroscopique, développé dans ma thèse, que nous avons présumé que certaines des sources repérées à la suite des observations menées par Sigma dans la direction des régions centrales de la Galaxie, abritent d'authentiques trous noirs. L'observation Sigma de ces sources fait l'objet des publications 1 et 2.

## ***Observations Integral des binaires X à trou noir***

Suite aux observations Sigma, mon projet de recherche a donc été de d'observer les binaires X à trou noirs avec Integral dans sa bande haute énergie, au delà de 150 keV. Comme décrit précédemment, c'est dans cette perspective que je me suis intéressé aux données Compton, à très bas bruit de fond. Malheureusement, contrairement aux observations X, les observations de sources à quelques centaines de keV sont très longues et difficiles à traiter, et les résultats ne sortent que depuis 2006, soit quatre ans après le lancement. Néanmoins, on peut s'attendre à ce que les observations haute énergie apportent maintenant les principaux résultats d'Integral.

Dans le cadre du temps garanti Integral, j'ai eu l'opportunité de participer, avec Marion Cadolle-Bel, à l'observation à plusieurs reprises du candidat trou noir Cygnus X-1, observé dans un état à forte émission au delà de 100 keV, ce qui nous a permis de confirmer notre critère spectroscopique. Cela a fait l'objet de la publication n°3. Je participe actuellement, avec Julien Malzac dont j'ai fait partie du jury de thèse, à un autre article accepté par l'Astrophysical Journal qui décrit une éruption de Cygnus X-1, en septembre 2006. Le flux de Cygnus X-1 était à ce moment là presque deux fois plus intense que celui du Crabe, habituellement la source la plus brillante du ciel. Un point important de ces observations est qu'une émission au TeV en provenance de ce système a été détectée au même moment par l'expérience au sol Magic. Même si cette émission au TeV demande encore confirmation, c'est la première fois qu'un système binaire à trou noir a été observé à ces énergies. Aucun modèle théorique n'est encore en mesure d'expliquer cette observation.

## ***Bibliographie***

- Chakrabarti S. et Titarchuk L., 1995, ApJ, 455, 623  
Chakrabarti S. et Mandi S., 2006, ApJ, 642, L49  
Ghosh P. et Lamb F.K., 1979, ApJ, 234, 296  
Illiaronov A. et Sunyaev R., 1975,A&A, 39, 185  
Lewin W., Van Paradijs J. et Van der Klis M., 1988, Space Science Review, 46, 273  
Malzac, 2008, accepted for publication in ApJ  
Pylyser E., et Savonije G., 1988, A&A, 208, 52  
Rappaport S., Joss P.C., et Webbink R.F., 1982, ApJ, 254, 616  
Shakura N. et Sunyaev R., 1973, A&A, 24, 337  
Shklovskii I., 1967, ApJ, 148, L1  
van der Klis, M., 2000, Annual Review of Astronomy and Astrophysics. 38, 717-760  
Vikhlinin A. et al., 1994, ApJ, 424, 395  
Vikhlinin A. et al., 1995,ApJ, 441, 779  
Webbink R.F. et al., 1983, ApJ, 270, 678

## *Publications principales afférentes à ce chapitre*

### **SIGMA observations of the soft gamma-ray source GRS 1758-258**

P. Laurent, B. Cordier, A. Goldwurm, J. Paul, J.-P. Roques, L. Bouchet, M. Denis, P. Mandrou, R. Sunyaev, E. Churazov, 1993, *Advances in Space Research*, 13, (12)751

### **Spectral distinction between black holes and neutron stars: the contribution of the SIGMA telescope**

P. Laurent, P David  
1997, *Advances in Space Research*, Volume 19, Issue 1, 45

### **The broad-band spectrum of Cygnus X-1 measured by Integral**

M. Cadolle Bel, P. Sizun, A. Goldwurm, J. Rodriguez, P. Laurent, A. Zdziarski, L. Foschini, P. Goldoni, C. Gouiffès, J. Malzac, E. Jourdain & J.-P. Roques, 2006, *Astronomy & Astrophysics*, 446, 591



## SIGMA OBSERVATIONS OF THE SOFT GAMMA-RAY SOURCE GRS 1758-258

P. Laurent,\* B. Cordier,\* A. Goldwurm,\* J. Paul,\*  
J. P. Roques,\*\* L. Bouchet,\*\* M. Denis,\*\* P. Mandrou,\*\*  
R. Sunyaev,\*\*\* E. Churazov,\*\*\* M. Gilfanov,\*\*\*  
N. Khavenson,\*\*\* B. Novikov,\*\*\* A. Dyachkov,\*\*\*  
R. Kremnev† and K. Sukhanov†

\* Service d'Astrophysique, CEN Saclay, 91191 Gif-sur-Yvette Cedex, France

\*\* Centre d'Etude Spatiale des Rayonnements, 9 Avenue du Colonel Roche,  
BP 4346, 31029 Toulouse Cedex, France

\*\*\* Space Research Institute, Profsoyuznaya, 84/32, Moscow 117296,  
Russia

† Lavochkin Association, Khimki, Moscow District, Russia

### ABSTRACT

The field containing the newly discovered soft  $\gamma$ -ray source GRS 1758-258, located 40 arcmin. away from GX 5-1, was observed by the SIGMA telescope on board the soviet spacecraft GRANAT in the course of the five extensive galactic-center surveys performed in 1990, 1991 and 1992. In both 1990 surveys, as well as in the February-April 1991 survey, the source exhibits a Cygnus X-1 like spectrum with nearly constant flux, while in the most recent measurements on September-October 1991 and spring 1992, a long term low-state has been discovered with an upper limit on the source flux five time lower than the average flux measured by SIGMA during all the observations from March 1990 until April 1991.

### SOURCE IMAGING

Discovered on Spring 1990 during the first survey of the galactic center /1/ of the SIGMA telescope /2,3,4/, GRS 1758-258 is located only nearly 40 arcmin. away from the well-known X-ray source GX 5-1. Due to this proximity, hard X-rays emitted from this region have been tentatively attributed in the past to GX 5-1, while we know now that GRS 1758-258 dominates that region above 30 keV /5/. It is worth noting that a reanalysis of the 3-30 keV data collected in July and in August 1985 by the Spacelab 2 coded mask telescope revealed a significant excess clearly to be identified with GRS 1758-258 /6/. Moreover, HEAO-1 A4 has observed a soft  $\gamma$ -ray emission from this region in 1978 which is probably due to this new source /7/. Finally, GRS 1758-258 has also been seen by the POKER experiment in 1989 /8/. All this show that this source was bright in the eighties.

The last published GRANAT/ART-P position of the source /5/ was  $\alpha_{1990} = 269.529^\circ$ ,  $\delta_{1990} = -25.74^\circ$  with an error box of 1 arcmin. Based upon this position, analysis of EXOSAT data and then of ROSAT data have improved the error box to give a final source position of  $\alpha_{1990} = 269.530^\circ$ ,  $\delta_{1990} = -25.741^\circ$  with an error radius of 10 arcsec very close to the ART-P position. Searches to find an optical or radio counterpart of GRS 1758-258 in this sky region have yet not been successful /9,10/.

Now that we have nearly 300 hours of observations from GRS 1758-258, accumulated between March 1990 and March 1991, we can improve the SIGMA error box by fitting the image obtained by summing all positive observations of the source (see Figure 1) with the instrument

point spread function. The error is now mainly dominated by the attitude reconstruction uncertainty whose value is nearly  $0.01^\circ$ . The new SIGMA position we have obtained is  $\alpha_{1990} = 269.536^\circ$ ,  $\delta_{1990} = -25.745^\circ$  (90 % error circle radius : 0.82 arcmin.) fully compatible with previous measurement.

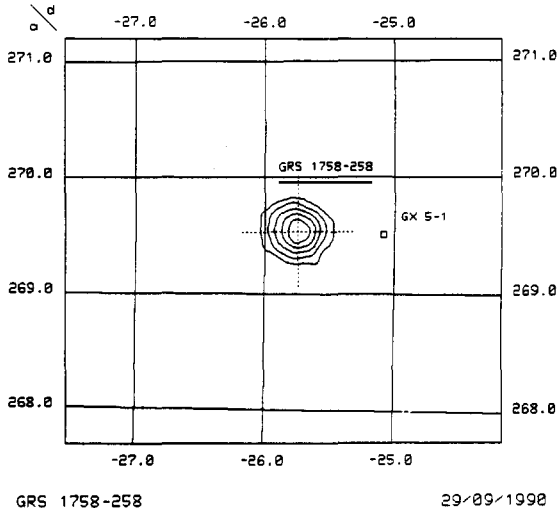


**Fig. 1.** SIGMA image of the GRS 1758-258 region in the 40-150 keV energy band. Contour levels begin at  $3\sigma$  and are spaced every  $2\sigma$ . The position of GX 5-1 and the ROSAT position of GRS 1758-258 are also shown.

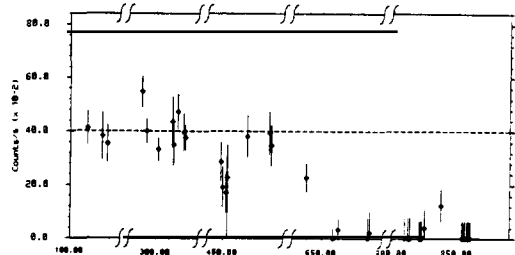


**Fig. 2.** Light curve of GRS 1758-258 in the 40-150 keV energy band during 1990-1992. The straight line shows the 1990 mean level ("standard state").  $2\sigma$  upper limits are shown when the source has not been detected.

## TIME VARIABILITIES

The source light curve from March 1990 to March 1992 is shown on Figure 2. The source was on a bright state until spring 1991. In fact, GRS 1758-258 and 1E1740.7-2942 have dominated the galactic center region during all year 1990. Day to day variations during this period show that the source size must be less than  $10^{16}$  cm. On February 1991, the source flux has declined by a factor  $\approx 2$  from the 1990 "standard state". And, on fall 1991, the source intensity also decreased, passing below the SIGMA detection limit /11/.

No periodicities between 8 to 30000 s was found from GRS 1758-258 analyzing the all set of observations when the source was on. Two observations performed with a better time resolution (1 ms), has also revealed no periodic signal from the source between 2 and 5000 s.

## SPECTRA

A spectrum has been obtained for each observation on its bright state. As no statistically evident differences has been observed between all session during which the source was in its "standard state" (that is in 1990, and at the beginning of 1991), we have summed all of them to improve the signal to noise ratio. The result has then been fitted with different model spectra convoluted by the SIGMA energy response matrix /12/. Although the statistics allow us to fit every single spectrum only by a power law model, the mean spectrum of 1990 is best fitted by models with

a break after 150 keV. Models of comptonization /13/ works well as it could be seen in Table 1, giving an electron temperature of 35 keV, and a Thomson optical depth of 1.7. If we consider that observations of February 1991 can be modeled with the same comptonization model as the mean spectrum, we find that the flux has dropped during this period down to  $0.27 \cdot 10^4$  ph/s/cm<sup>2</sup>/keV at 100 keV, that is 1.7 time lower than the mean level /14/.

TABLE 1 Spectral Analysis of GRS 1758-258

Spectral Model		Best fit results
<u>Comptonized disk</u>	$F_{100}^*$	$0.47 \pm 0.02$
	$kT_e$ (keV)	$34.6 \pm 4.9$
	$\tau$	$1.7 [1.0 - 2.8]$
	$\chi^2$ , ( 16 d.o.f.)	0.84

\*  $F_{100}$  : Flux in  $10^4$  ph/cm<sup>2</sup>/s/keV.

Assuming a distance of 8.5 kpc, the source luminosity in the "standard state" is  $1.1 \cdot 10^{37}$  erg/s between 40 and 200 keV. An upper limit on the fall 1991 luminosity is  $1.5 \cdot 10^{36}$  erg/s.

### GRS 1758-258: A BLACK HOLE CANDIDATE ?

Although not as well-known as the 1E1740.7-2942 source, GRS 1758-258 has some similar characteristics which could enable it to ask its admission in the black hole candidates club: Its variability and the spectral break after 150 keV in the mean spectrum compared to a power law model lead to think that this source is not a isolated pulsar. This is corroborated by the absence of pulsation found until now.

So, the emission of soft  $\gamma$ -rays should be due rather by an accretion process. As we don't know any optical counterpart of the source, we can't tell much about its binary nature.

Anyway, we can notice that among all the accreting systems observed by SIGMA, a high luminosity above 150 keV (that is higher than  $10^{36}$  erg/s), was observed only from the black holes candidates Cygnus X-1, GX 339-4, 1E 1740.7-2942 and Nova Musca /15/. By comparison, the upper limit on the luminosity above 150 keV of neutron star accreting system derived from SIGMA observations is  $2 \cdot 10^{35}$  erg/s /16/. The fact that only a accreting black hole can have a strong luminosity above 150 keV could be due to the absence of cooling soft X photons arising normally from a neutron star surface /5/. With a luminosity above 150 keV of  $2 \cdot 10^{36}$  erg/s, GRS 1758-258 should be then on the list of black hole candidates.

### REFERENCES

1. Mandrou P., IAU Circ. n°5032.
2. Paul J., Mandrou P., Ballet J., Cantin M., Chabaud J.P., Cordier B., Ehanno M., Goldwurm A., Lambert A., Landé J., Laurent P., Lebrun F., Leray J.P., Ména B., Niel M., Roques J.P., Rouaix G., Salotti L., Souleille P., and Vedrenne G., Adv. Space Res. 11, #8, 289, 1991.

3. Mandrou P., Chabaud J.P., Ehanno M., Landé J., Niel M., Roques J.P., Rouaix G., Souleille P., Paul J., Ballet J., Cantin M., Cordier B., Goldwurm A., Laurent P., Lebrun F., and Leray J.P., in *Gamma Ray Line Astrophysics*, ed. P. Durouchoux and N. Prantzos, Saclay, (NY:AIP), p 492, 1991.
4. Leray J.P., Ballet J., Goldwurm A., Lebrun F., Paul J., Lei F., Mandrou P., Bouchet L., Roques J.P., and Niel M., 22<sup>nd</sup> ICRC (Dublin) 2, 495 (OG 10.1.11), 1991.
5. Sunyaev R., Churazov E., Gilfanov M., Pavlinsky M., Grebenev S., Babalyan G., Dekhanov I., Yamburenko N., Bouchet L., Niel M., Roques J.P., Mandrou P., Goldwurm A., Cordier B., Laurent P., and Paul J., *A&A* 247, L29, 1991.
6. Skinner G.K., in *Gamma Ray Line Astrophysics*, ed. P. Durouchoux and N. Prantzos, Saclay, (NY:AIP), p 358, 1991.
7. Levine A.M., Lang F.L., Lewin W.G.H., Primini F.A., Dobson C.A., Doty J.P., Hoffman J.A., Howe S.K., Scheepmaker A., Wheaton W.A., Matteson J.L., Baity W.A., Gruber D.E., Knight F.K., Nolan P.L., Pelling R.M., Rothschild R.E., and Peterson L.E., *ApJ Supp. Series* 54, 581, 1984.
8. Bazzano A., Cocchi M., La Padula C., Sood R., and Ubertini P., *A&A Suppl. Series*, in press, 1992.
9. Bignami G.F., Caraveo P.A., Mereguetti S., Paul J., Cordier B., Goldwurm A., Mandrou P., Roques J.P., and Vedrenne G., *The Messenger* 66, 10, 1991.
10. Mirabel I.F., Rodriguez L.F., Cordier B., Paul J., and Lebrun F., *A&A Suppl. Series*, in press, 1992.
11. Cordier B., IAU Circ. n° 5377.
12. Barret D., and Laurent P., *Nucl. Inst. and Methods* A307, 512, 1991.
13. Sunyaev R.A., and Titarchuk L., *A&A* 86, 121, 1980.
14. Cordier B., PHD Thesis, Paris VII University, 1992.
15. Laurent P., Claret A., Cordier B., Lebrun F., Denis M., Bouchet L., Lei F., Barret D., Churazov E., Gilfanov M., Sunyaev R.A., Diachkov A., Khavenson N., Kremnev R., Sukhanov K., and Kuleshova N., *A&A Supp. Series*, in press, 1992.
16. Laurent P., PHD Thesis, Paris VII University, 1992.



# SPECTRAL DISTINCTION BETWEEN BLACK HOLES AND NEUTRON STARS: THE CONTRIBUTION OF THE SIGMA TELESCOPE

P. Laurent and M. Denis

*Service d'Astrophysique, C.E.N. Saclay, 91191 Gif-sur-Yvette Cedex, France*

## ABSTRACT

After more than four years of operation, the imaging  $\gamma$ -ray telescope SIGMA has accumulated several days of observation toward black holes and neutron stars. So far, more than twenty five of them have been detected with SIGMA. Although all these sources have spectra dominated by comptonisation, it is remarkable that suspected black hole systems are particularly numerous among the most luminous sources above 150 keV. Also, two black hole candidates have shown a strong transient emission around 511 keV, which has been interpreted as electron-positron annihilation features. We will discuss in this paper the reliability of these two phenomena, a strong luminosity above 150 keV and the emission of an annihilation line, as potential black hole criteria.

©1997 COSPAR. All rights reserved

## BLACK HOLE CRITERIA

As they have quite similar mass and compactness, a black hole and a non-magnetized neutron star in a binary system produce nearly the same effects to their environment. They are then very difficult to distinguish observationally, and the only sure criterion we have to discern between them is their mass. So, as a neutron star mass theoretically cannot exceeds  $\sim 3 M_{\odot}$ , any object which have a greater measured mass is declared a "black hole candidate".

With a most probable mass of  $7 M_{\odot}$  /1/, Cygnus X-1 was the first genuine black hole candidate. Accordingly, all its properties have been investigated as possible black hole criteria (see Tanaka /2/ for a review). The best X-ray spectral criterion seems now to be the observation of a single power law down to keV energies when the overall X-ray luminosity is stronger than  $10^{37}$  erg/s. A neutron star indeed might show a black body component with  $kT \approx 2$  keV due to its heating by the accreted material /2/.

In the same way, as the SIGMA energy range (30 keV - 1 MeV) is devoted mostly to the observation of black holes and neutron stars (see Table 1), we have tried to define other criteria using SIGMA data. The study of the spectra of these sources has revealed us two phenomena which could be regarded as signatures of black holes: firstly, all the most luminous SIGMA sources above 150 keV are black hole candidates, and then observed transient emission of annihilation lines come from two sources which are also two good black hole candidates. In this paper, we will explore in more details this two possible criteria and see how far they are reliable.

**TABLE 1** SIGMA catalog (6 January 1994).

SIGMA NAME	OTHER NAMES	BEHAVIOR	NATURE
SIG 0418+327	Nova Persei	Exponential Decay	Stellar Black Hole ?
SIG 0531+219	M1/PSR 0531+21	Stable, periodic	Nebula/ radio pulsar
SIG 0834-429	GS 0834-429	Transient	Neutron Star
SIG 1124-683	Nova Muscae	Exponential Decay	Stellar Black Hole
SIG 1208+396	NGC 4151	Slightly variable	Seyfert 1
SIG 1223+129	NGC 4388	Slightly variable	Seyfert 2
SIG 1226+023	3C 273	Slightly variable	Quasar
SIG 1227+025	GRS 1227+025	Transient	Quasar z=0.57 ?
SIG 1322-428	Centaurus A	Variable	AGN
SIG 1510-590	PSR 1509-58	Stable	Nebula?/radio pulsar
SIG 1524-616	TrA X-1	Transient	Stellar Black Hole ?
SIG 1656-415	OAO 1657-415	Transient, periodic	Neutron Star
SIG 1659-487	GX 339-4	Very variable	Stellar Black Hole ?
SIG 1700-377	4U 1700-37	Very variable, eruptive	Neutron Star ?
SIG 1716-249		Transient	Stellar Black Hole ?
SIG 1724-307	Terzan 2	Persistent	Neutron Star ?
SIG 1728-338	4U/MXB 1728-34	Very variable, eruptive	Neutron Star
SIG 1729-247	GX 1+4	Very variable, periodic	Neutron Star
SIG 1731-260	KS 1731-260	Transient	Neutron Star ?
SIG 1732-304	Terzan 1	Transient	Neutron Star ?
SIG 1734-292	GRS 1734-292	Transient	Neutron Star ?
SIG 1734-269	SLX 1735-269	Persistent	
SIG 1740-297	1E 1740.7-2942	Very variable	Stellar Black Hole ?
SIG 1742-288	GRS 1741.9-2853		
SIG 1742-294	A 1742-294	Transient	Neutron Star
SIG 1743-290		Variable	
SIG 1747-341		Persistent	
SIG 1758-257	GRS 1758-258	Very variable	Stellar Black Hole ?
SIG 1912+108	GRS 1915+105	Transient	
SIG 1956+350	Cygnus X-1	Variable	Stellar Black Hole

## HIGH LUMINOSITY ABOVE 150 keV ?

Table 2 shows that indeed black hole candidates are intrinsically more luminous sources than neutron stars above 150 keV. The luminosity of black holes above 150 keV deduced from the SIGMA observations is greater than  $10^{36}$  erg s $^{-1}$ , to be compared to less than  $2 \cdot 10^{35}$  erg s $^{-1}$  for neutron stars. So, the  $L_{>150}$  criterion seems reliable. We can notice then that this criterion does not depend on the strength of the neutron star magnetic field, as pulsars as well as bursters are present in Table 2.

**TABLE 2** Black holes vs neutron stars comparison (May 1993). Question marks means that the source distance is poorly known

	Sources	$L_{150-500}$ ( $10^{35}$ erg/s)
Black Hole Candidates	Cygnus X-1	$\approx 20$
	GX 339-4	$\approx 30$
	Nova Muscae	$\approx 50$
	Nova Persei	$\approx 115$ ?
	GRS 1758-258	$\approx 20$
Neutron Star	1E 1740.7-2942	$\approx 40$
	4U 1700-377	$\approx 5$
	OAO 1657-415	$\leq 1$
	A 1742-294	$\leq 5$
	GX 1+4	$\leq 2$
	KS 1731-260	$\leq 2$ ?
	GX 354-0	$\leq 3$
Crab		$\approx 40$

In fact, this criterion does not depend also on the underlying emission process, which could be thermal or non-thermal. However, the more commonly accepted explanation, i.e. the "Compton cooling", for this phenomena is a thermal one /3/. It suppose that the hard X-ray emitting plasma around neutron stars or black holes is cooled by soft photons (Compton scattering) and warmed by the accreted protons (Coulombian collisions). The disk and an eventual corona are natural sources of cooling soft photons for the two types of object. But a neutron star solid surface acts as an additional source of cooling photons, in such a way that the temperature of the medium close to the compact object has to be lower in neutron star systems. It is this difference that we will try to precise below, deriving a "mean" electron temperature for the hard X-ray emitting medium in the two type of sources.

### Compton Cooling In Black Hole Candidates

As shown in Figure 1, black hole candidates spectra are generally well-fitted with a comptonized Sunyaev-Titarchuk model (hereafter ST model /4/). Table 3 gives the result of this fitting for all the candidates we have detected with SIGMA. We see in this table that the electron temperature of these black hole candidates is always higher than 30 keV.

It can be seen from Table 3 that, for an unknown reason, novae have generally a higher temperature than persistent sources. We can note also that among these persistent sources, the three which are supposed to be in low mass systems (GX 339–4, 1E 1740.7 – 2942, and GRS 1758 – 258) have a significantly lower temperature than the high mass system Cygnus X–1. This may be an indication of a possible correlation between the electron temperature and the companion type.

**TABLE 3** Spectral fits of black hole candidates with a Sunyaev-Titarchuk model

SOURCE NAMES	$F_{\text{iso}}$ ( $10^4 \text{ ph/cm}^2/\text{s/keV}$ )	$kT_e$ (keV)	$\tau_{\text{Disk}}$
Nova Muscae	$4.4 \pm 0.1$	$74 \pm 30^*$	$0.4 \pm 0.2$
Nova Persei	$11 \pm 0.3$	$58 \pm 1$	$2.0 \pm 0.05$
Nova Ophiuchi	$6 \pm 0.1$	$45 \pm 2$	$0.75 \pm 0.03$
GX 339–4	$1.8 \pm 0.1^{**}$	$34 \pm 6$	$1.3 \pm 0.4$
1E 1740.7 – 2942	$0.7 \pm .06^{**}$	$38 \pm 12$	$1.5 \pm 0.5$
GRS 1758 – 258	$0.5 \pm 0.02$	$35 \pm 5$	$1.7 \pm 0.8$
Cygnus X–1	$6.4 \pm 0.1$	$63 \pm 6$	$2.1 \pm 0.2$

\* Best fitted by a power law of index  $\approx -2.3$

\*\* "High state"

\*\*\* "Standard state".

Moreover, if we look closely to the spectrum of Nova Persei shown in Figure 1.b, we see that the points deviate significantly from the fit above 300 keV. This behavior has also been observed by OSSE for Cygnus X–1 and GX 339–4 /5/. Three different non-exclusive explanations of this phenomenon have been given up to now:

- 1) Above some tenth of a keV, electrons are relativistic, and the ST model based upon the non-relativistic Thomson cross section is no longer valid. A relativistic treatment using the Klein-Nishina cross section can account for the high energy observed excess /6/.
- 2) It is also quite certain that it exists in the inner part of the disk several regions with different temperatures. So, a multi-temperatures model is somewhat more suitable /7/. For instance, The Cygnus X–1 spectrum can be well fitted by the superposition of two ST models /5/.
- 3) If the temperature in the inner region is high, pions production can occur, and the electromagnetic cascade resulting from the annihilation of these pions can give birth to an additional component similar to the observed excess /8/.

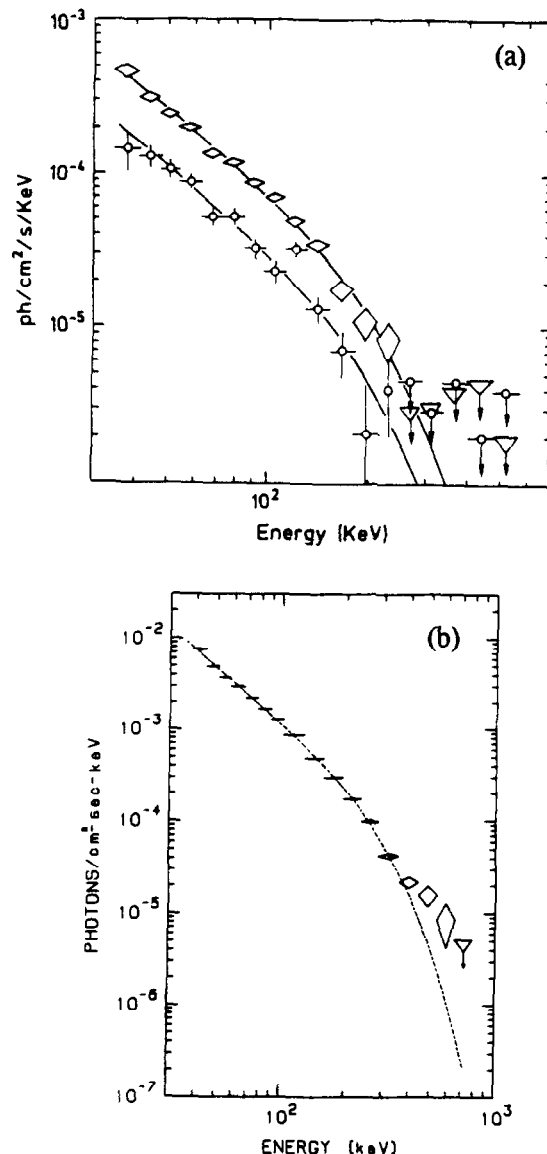


Fig.1 (a) Spectrum of 1E 1740.7-2942 in the "standard" and "sub luminous" states /9/; (b) Spectrum of Nova Persei /10/. The best fit with a ST model is also shown

All these models require a very high electron temperature ( $\approx 100$  keV) close to the black hole. So, the "mean" temperature we search can be of the order of one hundred keV. This is furthermore corroborated by the observation of annihilation lines in two black hole candidates. Let us see now what could be the value of this "mean" temperature in the vicinity of neutron stars.

### Compton Cooling In Neutron Stars

During the years 1990–1994, SIGMA had detected many neutron stars, mostly in binary systems (see Table 1). Among these binaries, only two of them were bright enough to allow detailed spectral fits: GX 1+4 and 4U 1700–377. GX 1+4 is a 2 minutes period binary X–ray pulsar close to the galactic center /11/, and 4U 1700-377 is a 3.4 day eclipsing massive system /12/. The 4U 1700–377 X-ray spectrum and the optical mass function show that the X-ray source should be a pulsar, although no X-ray pulsations have been observed so far /13/.

The observation-to-observation spectra of these sources are generally well fitted by a thermal bremsstrahlung model with a temperature of about 40 keV, which is comparable to the lower temperature obtained from black holes. We may think then that the cooling due to the soft photons produced at the surface of the heated neutron star is not so efficient. But, as this thermal bremsstrahlung fit gives us also the emission measure of the source, we can verify the implicit assumption of an optically thin emitting medium. Given a typical radius of the emitting region ( $10^8$  cm, for the magnetosphere for instance), and the source distances we find that the Thomson optical depth of this medium is larger than 1. So, the hypothesis of a optically thin medium currently used in the past is not justified, or only for an emitting region of radius greater than  $10^{10}$  cm. We have then to use comptonized models to describe the spectra. Using a ST model, we find the parameters given in Table 4 for the two sources under consideration.

**TABLE 4** Spectral fits of GX 1+4 and 4U 1700–377 with a ST model

Fit parameters	GX 1+4 (1991)	4U 1700–377 (Normal state)	4u 1700–377 (Flare state)
$F_{100}^*$	$1.5 \pm 0.3$	$0.35 \pm 0.13$	$1.33 \pm 0.34$
$kT_e$	$17 \pm 7$	$14.3 [12,22]$	$15.3 [12,20]$
$\tau^-$	$5 \pm 3$	$12.0 [3.5, +\infty[$	$6.9 [3.9, +\infty[$

\* Flux at 100 keV in  $10^4$  photon/cm<sup>2</sup>/s/keV

– Thomson optical depth (spherical cloud)

The temperatures we get by taking into account comptonisation processes are surprisingly stable, around 15 keV, while the flux can vary by a factor four. This temperature is now much lower than the one derived for the black holes candidates ( $\approx 50$  keV and probably around 100 keV in some systems), showing that the plasma surrounding neutron stars is significantly cooler.

### THE PRESENCE OF AN ANNIHILATION LINE ?

Another possible black hole criterion which can be derive from the SIGMA observations is the presence of an annihilation line. But, whereas it is true that the lines we observed was emitted from black hole candidates, there is no reason *a priori* to suppose that this emission cannot occur also in neutron star binaries. Indeed, non thermal processes around a neutron star in a low mass

system can theoretically produce pairs, and then give rise to a 511 keV line /14/. So, the observation of an annihilation line does not seem to be, for the moment, a good black hole criterion *per se*. Nevertheless, such an observation can give precise information on the geometry and the physics of the system in consideration, which can help for the determination of the nature of the compact object, as we will see below.

### The Annihilation Line in 1E 1740.7–2942

1E 1740.7–2942 is one of the two hard X-ray sources seen above 150 keV in the galactic bulge. This source has been continuously monitored by SIGMA since 1990, showing strong intensity variations on month time scales /15/. Due to the similarity of its 35–300 keV spectrum with the Cygnus X–1 one, 1E 1740.7–2942 may be thought as a black hole candidate. On October 13–14, 1990, the source underwent a strong high energy outburst above 200 keV, whose shape suggests positron annihilation radiation /16,17/. The observation of this event has triggered a multi-wavelength campaign of observations of this source, which has revealed in the radio domain a double-sided jet and a central core which was attributed to the compact object /18/.

The annihilation line seen in 1E 1740.7–2942 has been modelled by Maciolek-Niedzwiecki & Zdziarski /19/. They have shown that the line must have been produced in a medium with a temperature of nearly 40 keV consistent with the temperature derived from the underlying continuum, and very close to the compact object ( $\sim 3 R_s$ , where  $R_s$  is the Schwarzschild radius). This rules out the candidature of a less than  $1.5 M_\odot$  neutron star as the compact object, as this means that the line would be produced below its surface.

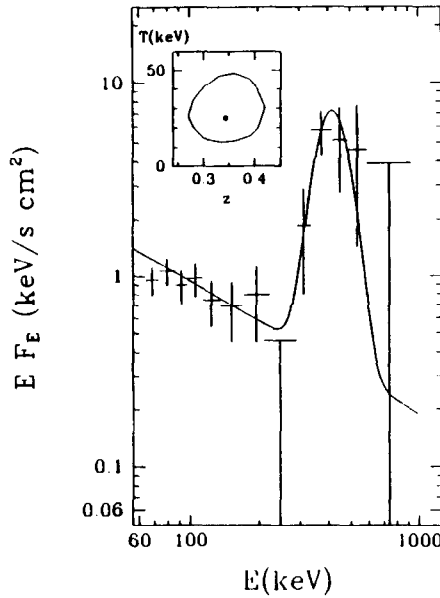


Fig. 2. Spectrum of 1740.7-2942 during the September 1990 event. The best fit with the Maciolek-Niedzwiecki & Zdziarski model is also shown /19/.

Also, as the line is not broadened by Compton scattering, the optical thinness of the medium enable the authors to derive some constraints on the geometry of the emitting region. After having ruled out spherical geometries, they show that the most likely emitting medium for the

511 keV photons is the jet, seen edge on. As we said above, this illustrates that the observation of an annihilation line can lead to get severe constraints on the geometry of the system. We will see now that this is even more true in the case of Nova Muscae.

### The Nova Musca Case.

SIGMA was conveniently on hand when a nova appeared in January 1991. The GRANAT observatory has then monitored the source from the beginning of the flare /20,21/. The light curve in the SIGMA domain is very different from the one obtained at X-ray energies, showing a very sharp increase a few days before the soft X-ray peak, which then decayed very fast. Afterwards, the light curve shows a long period of slow decrease (1 month), with a drop at hard X-ray energy at the same time as an enhancement of the soft X-ray flux. Then, after 6 months of absence, the source was again detected by SIGMA. Measurements of the mass function of the Nova Musca binary system give a lower limit for the compact object mass of  $3.1 \pm 0.5 M_{\odot}$  /22/, which put definitively this nova on the list of black hole candidates.

The source spectral shape observed has not varied much during the flare, and is well modelled by a power law of index  $\approx -2.4$ . On January 20–21, 1991, a high energy feature appeared during nearly 10 hours in the spectrum (see Figure 3). It was centered at 480 keV with a line width (FWHM) lesser than 100 keV, and was accompanied by another feature at lower energy ( $\approx 200$  keV). If the 480 keV line is due to an  $e^+ e^-$  annihilation process, its width indicates an emitting region temperature lower than 10<sup>8</sup> K. The presence of another feature at lower energies, if due to the Compton backscattering, also induces, beside a high Thomson optical depth, a low temperature (< 10 keV). Moreover, as it is clearly seen from Figure 3, the underlying spectrum keeps the same spectral shape from 10 to 400 keV, with no evidence of a low energy excess (around 100 keV) due to multiple Compton scattering. This rules out most spherical and disk geometry for the scattering medium /23,24/.

In fact, we have shown /24/ that the only way to take into account all these constraints is to consider that there is a jet in Nova Muscae. This seems quite reasonable as, up to now, three jets have been detected from black hole candidates (1E 1740.7–2942, GRS 1758–258, and Nova Ophiuchi). If, furthermore, we make the reasonable assumption that the end of the jet far from the compact object is relatively cool (< 10 keV), a relatively narrow Doppler redshifted annihilation line, and a blueshifted backscattering line can be efficiently produced and detected if we look at a relativistic jet face on /24/. On the other hand, the backscattering line would be strongly broadened at higher inclinations due to multiple scatterings.

The narrowness of the observed backscattered line implies then that if there was effectively a jet in Nova Muscae, we have looked at it face on. So, as this implies that the inclination of the system is around 10° or lower, we can deduce from the mass function /22/ that the mass of the compact object is greater than  $30 M_{\odot}$ . This rather high mass may be an argument against our jet model. If so, we don't know any other geometry which can account for the phenomenon observed in Nova Muscae /24/. So, we may have to reject one of the following hypothesis:

- . The 480 keV line is due to electron-positron annihilation and/or
- . the 200 keV line results from the backscattering of the 480 keV line.

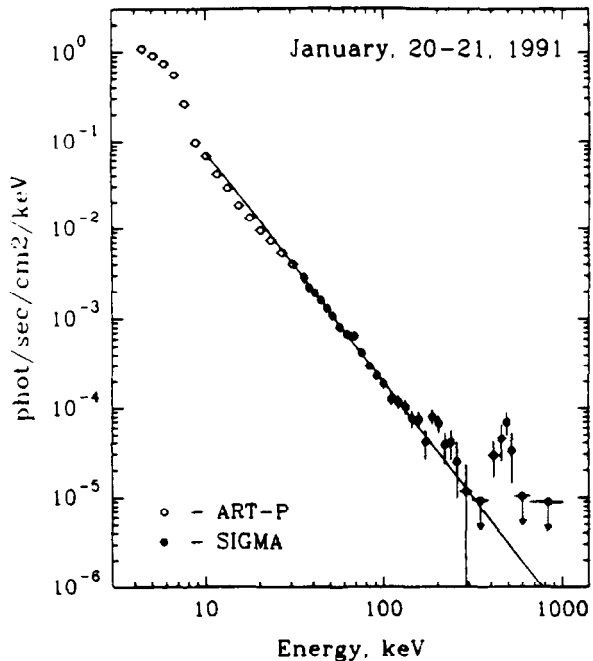


Fig. 3. Spectrum of Nova Muscae (January 1991) /21/.

## CONCLUSION

We have seen that the  $L_{>150}$  criterion seems reliable for the identification of black holes. If we suppose that this criterion results from the "Compton cooling" effect, SIGMA observations have shown that the "mean" temperature of the hard X-ray emitting plasma is indeed lower for neutron stars ( $\approx 15$  keV), than the one of black holes ( $> 50$  keV). In another way, the emission of annihilation lines can theoretically occurred in neutron star and black hole systems. Nevertheless, we have shown that the observation of lines from compact objects, even if it is not a black hole criterion *per se*, gives strong indications on the nature of the central compact object.

## REFERENCES

1. Gies D.R., Bolton C.T., 1986, ApJ, 304, 371.
2. Tanaka Y., 1989, Proc. 23rd ESLAB Symp., Italy, ESA SP-296, 1
3. Sunyaev R., Churazov E., Gilfanov M., et al., 1991, A&A 247, L29
4. Sunyaev R.A., Titarchuk L.G., 1980, A&A, 86, 121.
5. Johnson W.N., Kurfess S.D., Purcell W.R., et al., 1993, A&AS, 97, 21
6. Grebenev S., Sunyaev R., Pavlinski M., et al., 1993, A&AS, 97, 281

7. Liang E., 1991, Proc. Compton Observatory Science Workshop, Annapolis, NASA, 3137, 173
8. Jourdain E., Roques J.P., 1994, ApJ, 426, L11
9. Cordier B., Paul J., Goldwurm A., et al. 1993, A&A, 272, 277
10. Roques J.P., Bouchet L., Jourdain E., et al., 1994, ApJS, 92, 451
11. Laurent P., Salotti L., Paul J., et al., 1993, A&A, 278, 444
12. Laurent P., Goldwurm A., Lebrun F., et al., 1992, A&A 260, 237
13. Gottwald M., White N.E., and Stella L., 1986, MNRAS, 222, 21P
14. Kluzniak W., Ruderman M., Shaham J., and Tavani M., 1988, Nature, 336, 558
15. Cordier B., Paul J., Goldwurm A., et al., 1993, A&A, 272, 277
16. Bouchet L., Mandrou P., Roques J.P., et al., 1991, ApJ, 383, L45
17. Sunyaev R., Churazov E., Gilfanov M., et al., 1991, ApJ, 383, L49
18. Mirabel I.F., Rodriguez L.F., Cordier B., et al., 1992, Nature, 358, 215
19. Maciolek-Niedzwiecki A., Zdziarski A.A., 1994, to appear in ApJ
20. Goldwurm A., Ballet J., Cordier B., et al., 1992, ApJ, 389, L79
21. Sunyaev R. A., Churazov E., Gilfanov M., et al., 1992, ApJ, 389, L75
22. Remillard R.A., Mc Clintock J.E., Bailyn C.D., 1992, ApJ, 399, L145
23. Hua X-M, Lingenfelter R.E., 1993, ApJ, 416, L17
24. Laurent P., 1994, in preparation

# The broad-band spectrum of Cygnus X-1 measured by INTEGRAL

M. Cadolle Bel<sup>1,2</sup>, P. Sizun<sup>1</sup>, A. Goldwurm<sup>1,2</sup>, J. Rodriguez<sup>1,3,4</sup>, P. Laurent<sup>1,2</sup>, A. A. Zdziarski<sup>5</sup>, L. Foschini<sup>6</sup>, P. Goldoni<sup>1,2</sup>, C. Gouiffès<sup>1</sup>, J. Malzac<sup>7</sup>, E. Jourdain<sup>7</sup>, and J.-P. Roques<sup>7</sup>

<sup>1</sup> Service d'Astrophysique, CEA-Saclay, 91191 Gif-Sur-Yvette, France  
e-mail: mcadolle@cea.fr

<sup>2</sup> APC-UMR 7164, 11 place M. Berthelot, 75231 Paris, France

<sup>3</sup> AIM-UMR 7158, France

<sup>4</sup> ISDC, 16 Chemin d'Ecogia, 1290 Versoix, Switzerland

<sup>5</sup> N. Copernicus Astronomical Center, 00-716 Warsaw, Poland

<sup>6</sup> INAF/IASF, Sezione di Bologna, Via Gobetti 101, 40129 Bologna, Italy

<sup>7</sup> Centre d'Etude Spatiale des Rayonnements, 31028 Toulouse, France

Received 15 March 2005 / Accepted 31 August 2005

## ABSTRACT

The *INTEGRAL* satellite extensively observed the black hole binary Cygnus X-1 from 2002 November to 2004 November during calibration, open time and core program (Galactic Plane Scan) observations. These data provide evidence for significant spectral variations over the period. In the framework of the accreting black hole phenomenology, the source was most of the time in the Hard State and occasionally switched to the so-called “Intermediate State”. Using the results of the analysis performed on these data, we present and compare the spectral properties of the source over the whole energy range (5 keV–1 MeV) covered by the high-energy instruments on board *INTEGRAL*, in both observed spectral states. Fe line and reflection component evolution occurs with spectral changes in the hard and soft components. The observed behaviour of Cygnus X-1 is consistent with the general picture of galactic black holes. Our results give clues to the physical changes that took place in the system (disc and corona) at almost constant luminosity during the spectral transitions and provide new measures of the spectral model parameters. In particular, during the Intermediate State of 2003 June, we observe in the Cygnus X-1 data a high-energy tail at several hundred keV in excess of the thermal Comptonization model which suggests the presence of an additional non-thermal component.

**Key words.** black hole physics – stars: individual: Cygnus X-1 – gamma rays: observations – X-rays: binaries – X-rays: general

## 1. Introduction

Galactic Black Holes (BH) X-ray binary systems display high-energy emission characterized by spectral and flux variabilities on time scales ranging from milliseconds to months. These systems are generally found in two major states mainly defined by the relative variable contributions of soft and hard X-ray components, radio spectral properties and timing behaviour (McClintock & Remillard 2003; Nowak 2002). In the Hard State (HS), the X-ray and  $\gamma$ -ray spectrum is generally described by a power law model with an exponential cutoff at a few hundred keV, accompanied by relevant radio emission; it can be modeled by thermal Comptonization of cool seed photons in a hot electron plasma (Gierliński et al. 1997; Dove et al. 1998). The soft ( $\sim$ 0.1–2 keV) black body component is very weak or too soft to contribute significantly. The Thermal Dominant State (TDS) instead shows a strong thermal component with a characteristic temperature of at most a few keV that dominates the X-ray spectrum. No, or very weak and spectrally steep, hard X-ray emission is observed; the radio emission is quenched or very faint. This spectrum is generally

associated with a geometrically thin and optically thick accretion disc (Shakura & Sunyaev 1973). In addition to these two canonical states, other states have been identified, characterized either by an even greater luminosity than in the TDS (the “Steep Power law State”) or by variability and X-ray spectral properties mostly intermediate between the HS and the TDS (Belloni et al. 1996): the “Intermediate State” (IS).

Cygnus X-1/HDE 226868 is one of the first X-ray binaries detected; it belongs to the BH binary category. Among the brightest X-ray sources of the sky, it is also very variable on different time scales. The assumption that Cygnus X-1 ranks among the microquasars has been confirmed by the detection of a relativistic jet (Stirling et al. 2001). Since its discovery in 1964 (Bowyer et al. 1965), it has been extensively observed as the prototype of BH candidates in radio/optical wavelengths and with all high-energy instruments, from soft X-rays to  $\gamma$ -rays, e.g., with *ASCA* (Gierliński et al. 1999), *SIGMA* (Salotti et al. 1992), *RXTE* (Dove et al. 1998; Pottschmidt et al. 2003a), *BeppoSAX* (Frontera et al. 2001; Di Salvo 2001) and *CGRO* (McConnell et al. 2000, 2002). This persistent source, located at  $\sim$ 2.4  $\pm$  0.5 kpc

(McClintock & Remillard 2003, Table 4.1), accretes via a strong stellar wind coming from its companion, a O9.7I star of  $20 M_{\odot}$  (Ziółkowski 2005) with an orbital period of 5.6 days. The mass function constrains the inclination angle of the system between  $25^{\circ}$  and  $67^{\circ}$  (Gierliński et al. 1999) and we adopted the value of  $45^{\circ}$ .

Cygnus X-1 spends most of its time (90% until 1998 see, e.g., Gierliński et al. 1999) in the HS, with a relatively low flux in soft X-rays ( $\sim 1$  keV) and a high flux in hard X-rays ( $\sim 100$  keV). Its spectrum is roughly described by a power law with a photon index  $\Gamma$  between 1.4–2.1; a break at energies higher than  $\sim 50$  keV is present. This state is also characterized by a large timing variability. Occasionally, the source switches to the TDS with  $\Gamma > 2.3$ . During 1996 June, in addition to the dominant black body component and the hard component, a high-energy tail extending up to 10 MeV was discovered (McConnell et al. 2002). In this state little variability is observed. The IS, in which the source exhibits a relatively soft hard X-ray spectrum ( $\Gamma \sim 2.1$ – $2.3$ ) and a moderately strong soft thermal component (Méndez & van der Klis 1997), often appears when the source is about to switch from one main state to another. When not associated with a clear spectral transition, this state is called a “Failed State Transition” (FST). In the IS, the source displays a complicated pattern of timing properties. In the past few years, the source has been deeply observed in the IS and in the TDS (Zdziarski et al. 2002; Pottschmidt et al. 2003a; Gleissner et al. 2004a; Zdziarski & Gierliński 2004). In addition to the thermal and power law components, other spectral features can be present in the spectrum: a reflection component peaking around 30 keV and, most noticeably, a Fe K $\alpha$  line and Fe edge between 6 and 7 keV. These features can be visible in both spectral states.

The *INTERNATIONAL Gamma-Ray Astrophysics Laboratory (INTEGRAL)* mission (Winkler et al. 2003) is an European Space Agency satellite launched on 2002 October 17, carrying two main  $\gamma$ -ray instruments, IBIS (Ubertini et al. 2003) and SPI (Vedrenne et al. 2003), and two X-ray monitors JEM-X (Lund et al. 2003). Composed of two detectors, ISGRI (Lebrun et al. 2003) and PICsIT (Di Cocco et al. 2003), the IBIS coded mask instrument covers the energy range between 15 keV and 10 MeV. The SPI telescope works in the 20 keV–8 MeV range and the JEM-X monitors provide spectra and images in the nominal 3–35 keV band. As a bright hard X-ray source, Cygnus X-1 is a prime target for *INTEGRAL* and has been extensively observed during the Performance Verification (PV) Phase of the mission, when the source was in the HS (Bazzano et al. 2003; Bouchet et al. 2003; Cadolle Bel et al. 2004; Pottschmidt et al. 2003b). Pottschmidt et al. (2005) also reported on preliminary analysis of the high time-resolution Galactic Plane Scan (GPS) observations of Cygnus X-1 (up to 2004 April) in the 15–70 keV range. In the present work, we report the results over a wide energy band (from 5 keV up to 1 MeV) of several sets of observations of Cygnus X-1, including part of the PV-Phase observations not yet exploited, the first observations of Cygnus X-1 in the Open Time program, a larger amount of GPS data than previously

analyzed and the data from the 2004 November calibration period. For the first time, up to 1.5 Ms of *INTEGRAL* data of Cygnus X-1, collected over two years from 2002 November to 2004 November, are presented, fully exploiting the broad-band capability of all high-energy instruments of the mission.

## 2. Observations and data reduction

Table 1 reports the general periods (epochs) of the observations used, giving for each of them the instrument data available, date range, exposure (per instrument) and observing modes. Epoch 1 includes part of the PV-Phase observations of Cygnus X-1. To discuss the time evolution of the source, we report here the IBIS/ISGRI light curves and hardness ratios obtained during most of the PV-Phase observations of Cygnus X-1 (first line of Table 1), but since spectral results were presented in previous works, we studied more specifically the broad-band spectrum (using JEM-X, IBIS and SPI data) only for those PV-Phase observations not yet fully exploited, i.e., those performed between 2002 December 9–11 (epoch 1). The Open Time observation was performed on 2003 June 7–11 (epoch 2) with a  $5 \times 5$  dither pattern (Jensen et al. 2003). The effective exposure time was 275 ks for JEM-X2, 292 ks for IBIS and 296 ks for SPI. For this latter period, preliminary results can be found in Malzac et al. (2004) and Cadolle Bel et al. (2004) but we report here the complete study of the average spectrum while, in a future work, Malzac et al. (2005, submitted) will present the variability properties of the source. Epoch 3 and epoch 4 refer respectively to the set of Cygnus X-1 observations during the core program GPS and the 2004 November calibrations. Unfortunately, for the short interrupted GPS exposures, the SPI data are unusable because a sensitive evaluation of the background is not possible: only JEM-X and IBIS/ISGRI data are used. The periods of our different *INTEGRAL* observations, presented in Table 1, are also indicated in Fig. 1 (epochs from numbers 1 to 4).

We reduced the IBIS and JEM-X data with the standard analysis procedures of the Off-Line Scientific Analysis OSA 4.2 released by the ISDC, whose algorithms are described in Goldwurm et al. (2003) and Westergaard et al. (2003) for IBIS and JEM-X respectively. A basic selection was performed to exclude those pointings too close to radiation belt entry or exit, or spoilt by too much noise. To avoid uncertainties in the response files for high off-axis angles, we also selected the IBIS data of the observations for which the source was in the fully coded field of view, i.e., with an offset from the telescope axis no larger than  $4.5^{\circ}$ , and JEM-X data for maximum offset angles of  $3^{\circ}$ . Following recommendations of the OSA 4.2 release, IBIS/ISGRI events were selected to have corrected energies  $> 20$  keV and rise time channels between 7 and 80. For the background correction, we used a set of IBIS/ISGRI maps derived in 256 energy channels from empty field observations (these maps will be the default IBIS/ISGRI correction maps for the OSA 5.0 release) combined with our chosen energy bins while, for the off-axis correction maps and the response matrices, we used those of the official OSA 4.2 release. In the analysis, we considered the presence of the two other sources of the region, Cygnus X-3 and EXOSAT 2030+375, when they

**Table 1.** Log of the Cygnus X-1 observations analyzed in this paper.

Epoch	Instrument	Observation Period (date yy/mm/dd)	Exposure (ks)	Observation Type
	IBIS	02/11/25–02/12/15	810	staring, $5 \times 5^a$ , hex <sup>b</sup>
1	IBIS/SPI/JEM-X	02/12/09–02/12/11	365/365/31	$5 \times 5$
2	IBIS/SPI/JEM-X	03/06/07–03/06/11	292/296/275	$5 \times 5$
3	IBIS/JEM-X	03/03/24–04/09/10	269/35	GPS <sup>c</sup>
4	IBIS/SPI/JEM-X	04/11/22	8/8/6	calibration

Notes:

<sup>a</sup>  $5 \times 5$  dither pattern around the nominal target location.

<sup>b</sup> Hexagonal pattern around the nominal target location.

<sup>c</sup> Individual exposures separated by  $6^\circ$  along the scan path, shifted by  $27.5^\circ$  in galactic longitude.

(Observations indicated on the first line also used, together with epochs 1–4, for Figs. 2 and 3.)

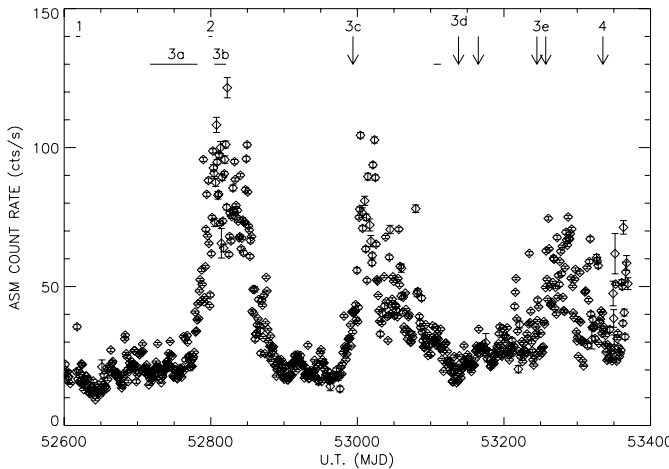


**Fig. 1.** RXTE/ASM daily average (1.5–12 keV) light curve of Cygnus X-1 from 2002 November to 2004 November (MJD = JD – 2 400 000.5) with the periods of our *INTEGRAL* observations (see text and Tables 1 and 2 for epoch definitions).

were active. For the IBIS/ISGRI spectral extraction however, we implemented the most recent module (prepared for the OSA 5.0 delivery) which is based on the least squares fit done on background and efficiency corrected data, using coded source zones only. This option minimizes spurious features in the extracted spectra, which appear in particular when the sources are weak, partially coded and the background poorly corrected (A. Gros, private communication). For the PICsIT spectral extraction, we took the flux and error values in the mosaic image at the best-fit position found for the source. We used the response matrices officially released with OSA 4.2, rebinned to the 8 energy channels of the imaging output.

The SPI data were preprocessed with OSA 4.2 using the standard energy calibration gain coefficients per orbit and excluding bad quality pointings which have anomalous exposure and dead time values (or with a high final  $\chi^2$  during imaging). The spiros 9.2 release (Skinner & Connell 2003) was used to extract the spectra of Cygnus X-1, Cygnus X-3 and EXO 2030+375, with a background model proportional to the saturating event count rates in the Ge detectors. Concerning the instrumental response, version 15 of the IRF (Image Response Files) and version 2 of the RMF (Redistribution Matrix Files) were used for epoch 1 and 2, e.g., prior to detector losses, while

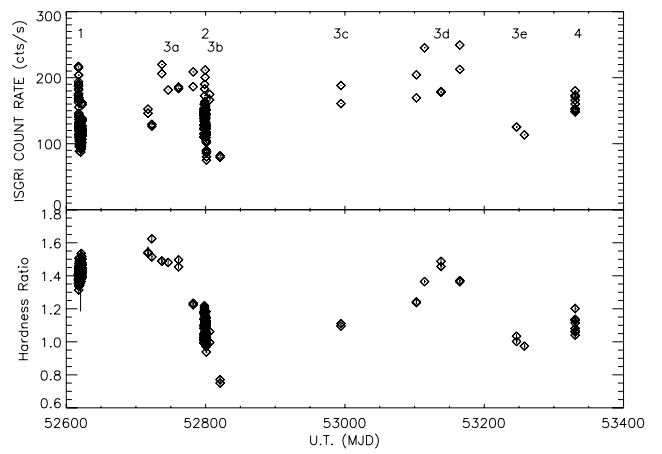


**Fig. 2.** The 20–200 keV IBIS/ISGRI light curve of Cygnus X-1 from 2002 November 25 until 2004 November 22 and corresponding HR between the 40–100 and the 20–30 keV energy bands (see text and Tables 1 and 2 for epoch definitions).

versions 17 and 4 respectively were taken for epoch 4, e.g., after the failure of two detectors.

### 3. Results of the analysis

As shown in Fig. 1, during the epoch 2 *INTEGRAL* observations, the 1.5–12 keV ASM average count rate of Cygnus X-1 ( $\sim 1.3$  Crab) was larger than during epoch 1 ( $\sim 290$  mCrab) by a factor of 4.5. The derived IBIS/ISGRI 20–200 keV light curves and Hardness Ratio (HR) of Cygnus X-1 are shown respectively in Fig. 2 (general overview of part of PV-Phase and epochs 1 to 4) and Fig. 3 (specific zooms on part of PV-Phase, epochs 1 and 2). From epoch 1 to epoch 2, while the ASM average count rate increased, the 20–200 keV IBIS/ISGRI one decreased from  $\sim 910$  to  $\sim 670$  mCrab as shown in Fig. 3 (where, in the 20–200 keV range, 1 Crab =  $205\text{ cts s}^{-1}$ ). This probably indicates a state transition between epochs 1 and 2, as also suggested by the decrease in the IBIS HR (Fig. 3). Similar transition, with a change in the ASM light curves and an evolving IBIS HR, occurred again during GPS data (epoch 3). Figure 2 (bottom) shows the IBIS HR behaviour over the whole 2002–2004 period indicated in Table 1.

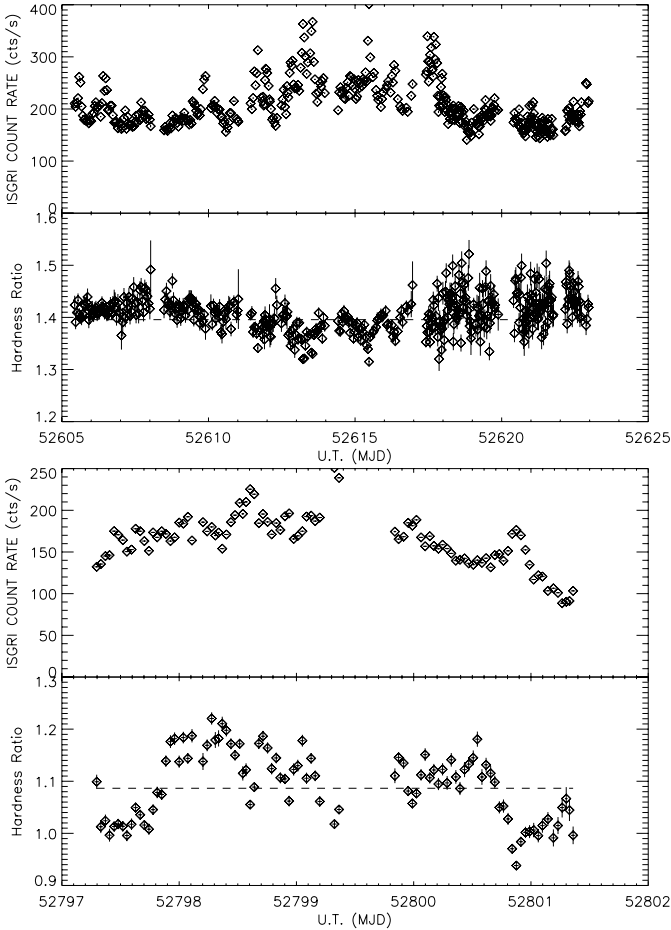


**Fig. 3.** *Top:* zoom on the 20–200 keV IBIS/ISGRI light curve of Cygnus X-1 from 2002 November 25 until December 15 and corresponding HR between the 40–100 and the 20–30 keV energy bands (average level denoted by dashed line). *Bottom:* same as above for epoch 2.

We sampled epoch 3 in five distinct sub-groups (noted *a* to *e*) of close pointings which appear to occur, according to Figs. 1 and 2, in different regimes of ASM count rate and of average IBIS HR. The data of each epoch (and sub-group) were summed to obtain an average spectrum studied separately. We added 3% systematic errors for JEM-X (5–30 keV range), IBIS (20 keV–1 MeV range) and SPI (22 keV–1 MeV range) and fitted the resultant spectra simultaneously using XSPEC v11.3.0 (Arnaud et al. 1996). In order to account for uncertainties in the cross-calibration of each instrument, a multiplicative constant was added in the spectral fits to each instrument data set: it was set free for IBIS and SPI and frozen to 1 for JEM-X.

Several models were used in the course of the spectral analysis. In XSPEC notation, we used a multicolour disc black body DISKBB (Mitsuda et al. 1984) plus a Comptonization model COMPTT (Titarchuk 1994) and, when necessary, we added a Gaussian for the Fe line with the GAUSSIAN model and the reflection component REFLECT (Magdziarz & Zdziarski 1995). This latter component models the X-ray reflection of the comptonized radiation from neutral or partially ionized matter, presumably the optically thick accretion disc (Done et al. 1992;

Gierliński et al. 1997, 1999; Magdziarz & Zdziarski 1995). For this source, we always used a fixed absorption column density  $N_{\text{H}}$  of  $6 \times 10^{21} \text{ cm}^{-2}$  (Balucińska-Church et al. 1995). We also tied the input soft photon temperature  $kT_0$  of the COMPTT model to the inner disc temperature  $kT_{\text{in}}$  value found by the DISKBB model. In order to compare all our data (from epochs 1 to 4) with the same model, we show the parameters obtained from the current fitted model described above (multicolour disc black body plus Comptonization convolved by reflection and Gaussian when necessary). We also tried more complex models such as COMPPS and EQPAIR, developed respectively by Poutanen & Svensson (1996) and Coppi (1999), coupled to the GAUSSIAN and the DISKBB (or DISKPN for EQPAIR only, see Sect. 3.2) models: we present such results only for epoch 2, when the statistics were significantly better, the instrument configurations stable and during which the presence of a non-thermal component appeared more pronounced.

### 3.1. The hard state spectrum

Figure 4 shows the resultant count spectrum obtained in epoch 1 (2002 December 9–11) from 5 keV up to 1 MeV with the JEM-X, SPI, IBIS/ISGRI and PICsIT data. A simple power law model does not fit the spectra well (photon index  $\Gamma$  of  $1.9 \pm 0.1$  and reduced chi-square  $\chi^2_{\text{red}} = 12.90$  with 213 degrees of freedom, hereafter d.o.f.). A cutoff in the model, with a typical folding energy of approximately 150 keV, clearly improves the fit ( $\chi^2_{\text{red}} = 2.12$  with 212 d.o.f.) and better describes the available data. Since a cutoff power law is usually attributed to thermal Comptonization, we replaced this phenomenological model by a more physical model of Comptonization (COMPTT, Titarchuk 1994). Some residuals were still visible around 10 keV so we added a model of reflection (with an inclination angle equal to  $45^\circ$ ) to account for this excess. The final tested model therefore includes thermal Comptonization convolved by reflection (REFLECT), with solar abundances for Fe and He (Anders & Grevesse 1989). We obtain a plasma temperature  $kT_e$  of 67 keV with an optical depth  $\tau$  of 1.98 and  $\Omega/2\pi = 0.25$ , with  $\chi^2_{\text{red}} = 1.45$  (230 d.o.f.). The disc black body is very weak or below the energy range of JEM-X: this component was not used in our fits. As it gives no contribution, we froze the  $kT_0$  temperature of COMPTT at 0.20 keV. Normalization constants between instruments (JEM-X, IBIS/ISGRI, SPI, IBIS/PICsIT) are respectively equal to 1, 1.2, 1.3 and 0.9.

Note that some residual points are visible in this plot, in particular for the SPI data at low energies (and for the IBIS data around 200 keV). This is mostly related to the non perfect cross-calibration between the INTEGRAL instruments. Indeed, by fitting separately the different instrument data, the residuals are reduced, with little change in the spectral parameters. Future improvement in the cross-calibration of INTEGRAL telescopes will allow a better determination in the relative flux normalizations and also a better agreement of the derived spectral shapes. The IBIS configuration was not stable in the first phases of the mission: in particular, the PV-Phase spectra may suffer from the fact that the IBIS responses were built from the

**Table 2.** Best-fit parameters of Cygnus X-1 for the current thermal model in the different observation epochs.

Epoch	Dates (MJD)	Disc Norm. <sup>a</sup>	$kT_{\text{in}}$ or $kT_0$ (keV)	$kT_e$ (keV)	$\tau$	$E_{\text{Fe}}$ line (keV)	$\Omega/2\pi^b$	$\chi^2_{\text{red}}$ (d.o.f.)
1	52617–52620	-	0.20 (frozen)	$67^{+8}_{-6}$	$1.98^{+0.21}_{-0.23}$	-	$0.25^{+0.03}_{-0.04}$	1.45 (230)
2	52797–52801	$250^{+89}_{-59}$	$1.16 \pm 0.07$	$100^{+29}_{-17}$	$0.98^{+0.25}_{-0.28}$	$7.07^{+0.12}_{-0.11}$	$0.57^{+0.09}_{-0.06}$	1.69 (236)
3a	52710–52780	-	0.20 (frozen)	$68^{+22}_{-12}$	$2.08^{+0.51}_{-0.84}$	$6.48 \pm 0.13$	$0.32^{+0.05}_{-0.07}$	1.07 (190)
3b	52801–52825	$312^{+25}_{-24}$	$1.15 \pm 0.03$	$93 \pm 42$	$0.80^{+0.86}_{-0.40}$	$6.40 \pm 0.73$	$0.58^{+0.20}_{-0.18}$	0.93 (190)
3c	52990	$361^{+61}_{-67}$	$0.99 \pm 0.08$	$58^{+54}_{-15}$	$1.60^{+0.64}_{-0.80}$	$6.96 \pm 0.19$	$0.23^{+0.17}_{-0.09}$	0.99 (190)
3d	53101–53165	-	0.20 (frozen)	$56^{+12}_{-7}$	$2.28^{+0.40}_{-0.41}$	$6.11 \pm 0.26$	$0.27 \pm 0.06$	0.81 (190)
3e	53240–53260	$132 \pm 10$	$1.39 \pm 0.77$	$48^{+20}_{-6}$	$1.85^{+0.40}_{-0.07}$	$6.49 \pm 0.38$	$0.49^{+0.37}_{-0.32}$	1.56 (190)
4	53335	$232^{+21}_{-32}$	1.16 (frozen)	$128^{+84}_{-63}$	$0.74^{+0.88}_{-0.38}$	$7.78^{+0.44}_{-0.42}$	$0.47^{+0.18}_{-0.14}$	0.97 (221)

Notes:

<sup>a</sup> Disc normalization K is given by  $K = (R/D)^2 \cos \theta$  where R is the inner disc radius in units of km, D is the distance to the source in units of 10 kpc and  $\theta$  the inclination angle of the disc.

<sup>b</sup> Solid angle of the reflection component.

Model applied in XSPEC notations: CONSTANT\*WABS\*(DISKBB+GAUSSIAN+REFLECT\*COMPTT) with  $N_{\text{H}}$  fixed to  $6 \times 10^{21} \text{ cm}^{-2}$  and  $kT_0$  value tied to disc  $kT_{\text{in}}$ . Errors are at 90% confidence level ( $\Delta\chi^2 = 2.7$ ).

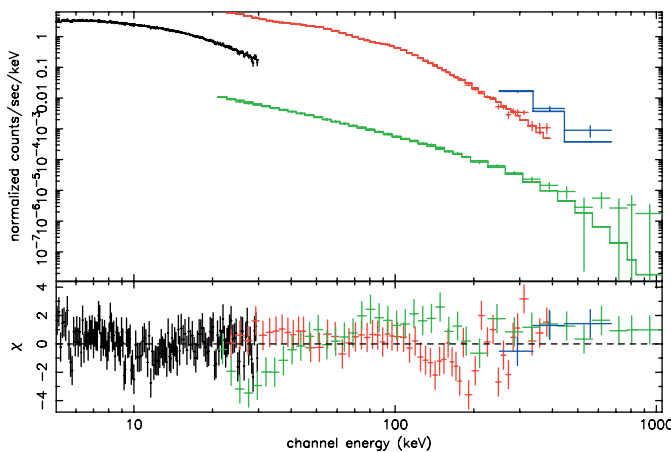


**Fig. 4.** Spectra of Cygnus X-1 in 2002 December 9–11 (epoch 1) with the JEM-X (black), SPI (green) and IBIS (ISGRI: red; PICsIT: blue) data. The best-fit model is a Comptonization model with reflection (see Table 2). Residuals in  $\sigma$  units are also shown.

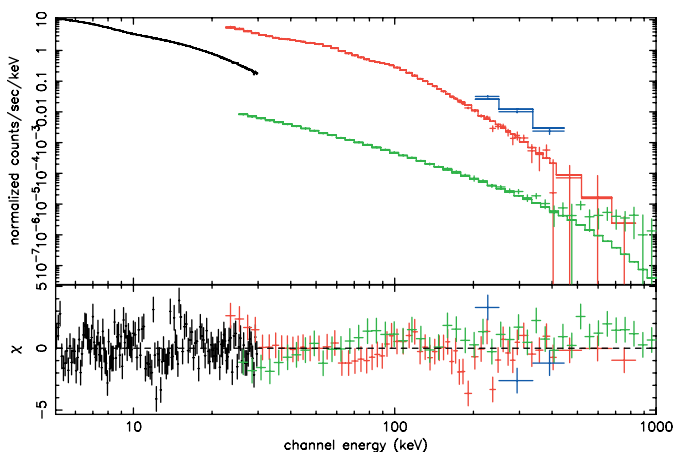


**Fig. 6.** Spectra of Cygnus X-1 in 2003 June 7–11 (epoch 2) with the JEM-X (black), SPI (green) and IBIS (ISGRI: red; PICsIT: blue) data. The best-fit model is a multicolour disc black body and a Comptonization model with Gaussian and reflection components (see Table 2). Residuals in  $\sigma$  units are also shown.

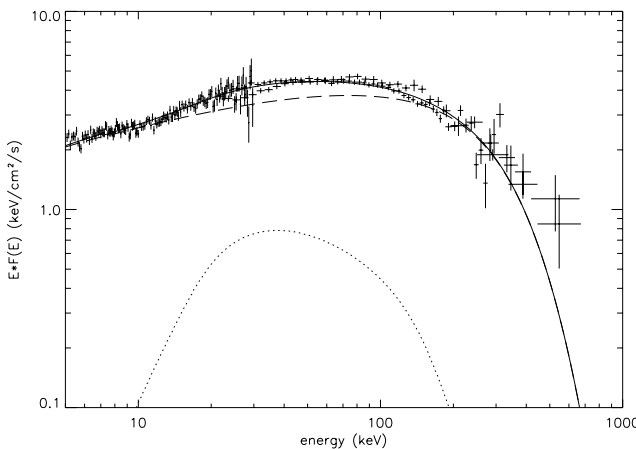


**Fig. 5.** Epoch 1 unabsorbed  $EF(E)$  spectrum of Cygnus X-1 along with the best-fit model described in Table 2 with the JEM-X, SPI and IBIS (ISGRI and PICsIT) data. Dotted: reflection. Long dashes: comptonization. Thick: total model.

Crab nebula observations performed in later periods, with a defined and stable configuration.

In spite of these caveats, all spectra overlap relatively well and do define the same set of spectral parameters. Figure 5 shows the resultant  $EF(E)$  spectrum and its best-fit with the JEM-X, IBIS and SPI data. Table 2 summarizes all fit results. While the 20–100 keV luminosity is  $6.5 \times 10^{36} \text{ erg s}^{-1}$  (with a distance to the source fixed at 2.4 kpc), the bolometric luminosity (extrapolated from 0.01 keV to 10 MeV) has the value of  $2.2 \times 10^{37} \text{ erg s}^{-1}$ . The best-fit parameters we obtain are consistent with those found in BH binaries in the HS (McClintock & Remillard 2003) and with previous results reported on Cygnus X-1 in the HS, in particular from the INTEGRAL data (Bazzano et al. 2003; Bouchet et al. 2003; Pottschmidt et al. 2003b). These authors generally give plasma temperatures between 50–100 keV and optical depths in the 1.0–2 range. In particular, our SPI spectrum is fully compatible with the one reported by Bouchet et al. (2003). These authors observed that the derived spectrum had an excess component

with respect to a Sunyaev & Titarchuk (S-T) Comptonization model (1980) and that it was better described by a cutoff power law with  $\Gamma = 1.5$  and a cutoff energy of 155 keV. We find exactly the same results for our SPI spectrum alone if we fit it with an S-T model or a cutoff power law. This excess emission, with respect to the simple S-T model, was already observed in a number of cases for the HS spectra of BH systems, e.g., Jourdain & Roques (1994). However, with the Titarchuk (1994) model (which better describes the Comptonization for high plasma temperatures), no significant excess is observed in epoch 1 spectra of Cygnus X-1.

### 3.2. The transition to a softer state in 2003 June

As visible in the change of the ASM light curve of Cygnus X-1 (see Fig. 1) and its corresponding high-energy HR shown in Fig. 3 (average value of 1.1 for epoch 2 compared to more than 1.4 for epoch 1), the source softens during epoch 2. Although a single power law does not fit the data properly ( $\chi^2_{\text{red}} = 23.51$  with 245 d.o.f.), the derived slope is softer ( $\Gamma = 2.2 \pm 0.1$ ). As for the HS spectrum analysis, an inspection of the residuals reveals what kind of component can be added to build a proper model. The need for each new component is then checked with the results of the fits and the final model is further verified by repeating the procedure with components added in a different order.

First, we included a cutoff in the power law and we improved the  $\chi^2$  by  $\Delta\chi^2 = 7.8$ : this indicates that the new component is significant at more than the 95% confidence level. A cutoff in the power law model, with a typical folding energy of approximately 200 keV, better describes the available data, so we tried the physical Comptonization model (COMPTT) as we did for epoch 1. Moreover, since very large residuals are visible in the soft X-rays and since we suspect a transition to the IS, we added a multicolour disc black body (DISKBB), which is in fact required by the data ( $\chi^2_{\text{red}} = 14.87$  and 239 d.o.f. without this component). Some residuals around 10 keV indicate the need for a reflection component. Therefore, the best model for the continuum consists of a multicolour disc black body (DISKBB) and thermal Comptonization (COMPTT) convolved by reflection (REFLECT, with parameters as above). The Comptonization temperature  $kT_0$  was fixed to the  $kT_{\text{in}}$  value returned by the DISKBB. Finally, we added a Gaussian to account for the residuals in the JEM-X data around 6–7 keV ( $\chi^2_{\text{red}} = 2.42$  and 237 d.o.f. without this component).

Table 2 summarizes the best-fit parameters and the  $\chi^2_{\text{red}}$  obtained from 5 keV up to 1 MeV. We obtained a plasma temperature  $kT_e$  of  $100^{+29}_{-17}$  keV and an optical depth  $\tau$  of  $0.98^{+0.25}_{-0.28}$ , respectively higher and lower than in epoch 1 ( $kT_e = 67^{+8}_{-6}$  keV,  $\tau = 1.98^{+0.21}_{-0.23}$ ). The inner disc temperature reached 1.16 keV and a significant line is detected at a centroid energy of 7.07 keV, with an Equivalent Width (EW) of 1.4 keV. With the same assumed distance, the luminosity is  $6.5 \times 10^{36}$  erg s $^{-1}$  in the 0.5–10 keV range and  $5.2 \times 10^{36}$  erg s $^{-1}$  in the 20–100 keV band. The bolometric luminosity, extrapolated from 0.01 keV up to 10 MeV, has the value of  $2.0 \times 10^{37}$  erg s $^{-1}$ ; the disc accounts for 26 % of the total luminosity.

The derived disc normalization is possibly underestimated and not well constrained by the JEM-X data (which start at 5 keV). The multicolour disc black body is only an approximation of the soft component: the direct derivation of physical parameters of the disc from the best-fit values may suffer from some important effects (Merloni et al. 2000). According to these authors, the dominant effect seems to be that, in the inner part of the disc, the opacity is dominated by electron scattering rather than free-free absorption. The net result is that the derived temperature given by the  $kT_{\text{in}}$  parameter overestimates the effective inner temperature by a factor of 1.7 or more (Shimura & Takahara 1995). This has an effect on the estimation of the inner disc radius as well. Assuming an inclination angle of 45°, the derived internal radius from the best-fit disc normalization has the unphysical value of  $4.50^{+0.74}_{-0.56}$  km. For a  $10 M_\odot$  BH, this value corresponds to  $0.15 R_s$  (where  $R_s$  is the Schwarzschild radius), i.e., smaller than the last stable orbit even around a maximally spinning Kerr BH.

A comparatively strong reflection component ( $\Omega/2\pi = 0.57^{+0.09}_{-0.06}$  while it was  $0.25^{+0.03}_{-0.04}$  for epoch 1) is also necessary to fit the data ( $\chi^2_{\text{red}} = 4.57$  and 237 d.o.f. without this component). Our  $\Omega/2\pi$  value is consistent with ASCA, RXTE (Gierliński et al. 1996, 1999) and BeppoSAX observations (Frontera et al. 2001). The best-fit model, over-plotted on data from JEM-X, SPI, IBIS/ISGRI and PICsIT, is reported in count units in Fig. 6. Figure 7 shows the resultant  $EF(E)$  spectrum with its best-fit. Note that we have rebinned, for illustrative purposes, the SPI high-energy points above 750 keV to reach the level of  $3\sigma$ , but the fit was performed on the original energy channels of the spectrum (50 bins over the 22 keV–1 MeV band). Normalization constants are respectively equal to 1, 1, 1.2 and 1. Residuals again show that improvements in the instrument cross-calibration and responses are still needed to obtain a fully satisfactory fit of the INTEGRAL combined data, but we believe that the general spectral model and parameters are well determined.

Considering the behaviour of the ASM light curve (Fig. 1), the evolution of the high-energy IBIS HR (Fig. 3, lower panel), the relative softness of the spectrum and the presence of a relatively strong hard energy emission, it appears that during the 2003 June observations Cygnus X-1 was in the IS (or in the FST). This is also confirmed by radio observations of Malzac et al. (2004) who suggested that the fluctuations of the radio luminosity were associated with a pivoting of the high-energy spectrum. The derived thermal Comptonization parameters are consistent with those found in BH binaries in soft states (McClintock & Remillard 2003).

As it can be seen in Fig. 7, an excess with respect to the Comptonized spectrum above 400 keV is observed in the SPI data that is not present in epoch 1. We tried different models of the background, we used different selections of pointings with two data processings (the standard pipeline and the specific softwares developed by the SPI instrument team); however, this feature is always present. To evaluate the possible presence of an instrumental feature, we re-analyzed the Crab observation performed with SPI on 2003 February 22–24, with the same configuration and dither pattern as those of our Cygnus X-1 observations. We obtained a spectrum consistent with the one

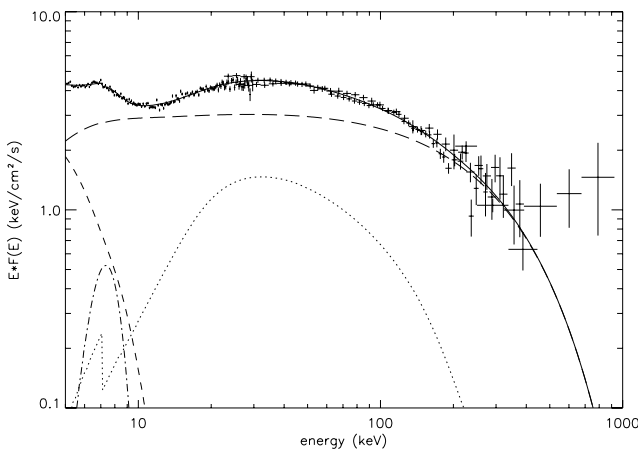


**Fig. 7.** Epoch 2 unabsorbed  $E\cdot F(E)$  spectrum of Cygnus X-1 along with the best-fit model described in Table 2 with the JEM-X, SPI and IBIS (ISGRI and PICsIT) data. *Dashed*: Disc. *Dotted-dashed*: Gaussian line. *Dotted*: Reflection. *Long dashes*: Comptonization. *Thick*: Total model.

reported by Roques et al. (2003). With 3% systematics added to the 200 ks SPI data, the Crab spectrum is well described by a power law with  $\Gamma = 2.1$  over the 22–1000 keV energy range and no high-energy excess above 400 keV is observed. This test shows that it is unlikely that the observed high-energy tail in the Cygnus X-1 IS spectrum is due to a systematic effect.

We fitted this excess with an extra component, in addition to our current Comptonization model. Using a power law for all the data (except JEM-X), we obtain a best-fit photon index  $\Gamma$  of  $2.12^{+0.31}_{-0.16}$ . The improvement in the  $\chi^2_{\text{red}}$  is relatively important (1.65 with an absolute chi-square reduced by 10 for 2 additional free parameters), making this component significant. An F-test (Bevington & Robinson 1992) provides a chance probability that this improvement is due to fluctuations of about  $10^{-2}$  (but see Protassov et al. 2002 about the limitations of the F-test). At the same time, the parameters obtained for the current model are different to those obtained without the power law. We obtained a plasma temperature of 50 keV, an optical depth of 2.1 and  $\Omega/2\pi$  is around 0.49. While the IBIS high-energy data do not require this additional component, IBIS points are also consistent, due to the large error bars, with this additional power law model. A better  $\chi^2_{\text{red}}$  (equal to 1.55, with an absolute chi-square reduced by 35, giving now a chance probability of  $10^{-5}$  for the additional power law that the improvement is due to fluctuations) is obtained when PICsIT data are neglected. Since the SPI telescope is certainly the best calibrated *INTEGRAL* instrument at energies higher than 400–500 keV, we consider this feature to be significant.

Consequently, in order to account for this high-energy emission with more physical models, we fitted the data with the hybrid models COMPPS and EQPAIR (coupled to the usual disc and Gaussian line components). They combine both thermal and non-thermal particle distributions in the calculation of the emergent spectrum, as fully described by Poutanen & Svensson (1996) and Coppi (1999). Those models use a hot

plasma cloud, mainly modeled as a spherical corona around the compact object (configuration taken in our fits) or as the well-known “slab” geometry, illuminated by soft thermal photons coming from an accretion disc. These photons are Compton scattered by both thermal (Maxwellian) and non-thermal (power law) electrons that lose energy by Compton, Coulomb and bremsstrahlung interactions. The number of electrons is determined by  $\tau$ , the corresponding (total) vertical Thomson optical depth of the corona.

Both EQPAIR and COMPPS models allow one to inject a non-thermal electron distribution with Lorentz factors between  $\gamma_{\min}$  and  $\gamma_{\max}$  and a power law spectral index  $\Gamma_p$ . In the EQPAIR model, the system is characterized by the power  $L_i$  supplied to its different components, expressed as the dimensionless compactnesses  $l_i = (L_i \sigma_T) / (R m_e c^3)$  (where  $R$  is the corona size). This model has two advantages with respect to the COMPPS: first, it is valid both for high  $kT_e$  and low  $\tau$  and vice-versa (while COMPPS should be used for  $\tau < 3$  only). Secondly, the EQPAIR model also takes into account the electron-positron annihilation process. We used the DISKPN and DIKSBB routines in the XSPEC package to describe the soft emission from the accretion disc in the two hybrid models (EQPAIR and then COMPPS). With the DISKPN, the main characteristic is that the disc spectrum incident on the plasma is computed assuming a pseudo-Newtonian potential for the accretion disc, extending from 3 (the minimum stable orbit) to  $500 R_s$ .

Both the purely thermal and the thermal/non-thermal best-fit parameters of these hybrid models for the Cygnus X-1 spectrum of 2003 June are reported in Table 3. The pure thermal models obviously do not improve the fit with respect to the thermal Comptonization model, but when the effect of a non-thermal electron distribution is included, the  $\chi^2$  are reduced by a significant amount and the high-energy component appears well fitted by these models, in particular by the non-thermal EQPAIR.

First, for EQPAIR, with frozen values of  $\gamma_{\min}$  and  $\gamma_{\max}$  at respectively 1.5 and 1000 and with the same value for  $N_H$  and abundances as before, we obtain the dimensionless parameters  $l_h/l_s = 4.57^{+0.04}_{-0.87}$  and  $l_{\text{nth}}/l_h = 0.16^{+0.11}_{-0.08}$  (where  $l_s$ ,  $l_{\text{th}}$ ,  $l_{\text{nth}}$  and  $l_h = l_{\text{th}} + l_{\text{nth}}$  correspond to the compactness in soft disc photons irradiating the plasma, in direct thermal electron heating, in electron acceleration and in total power supplied to electrons in the plasma respectively). These parameters indicate that the power in the non-thermal component is  $\sim 16\%$  of the total power supplied to the electrons in the corona. With a  $\chi^2_{\text{red}} = 1.55$  (232 d.o.f.), clearly better than the current epoch 2 model and the pure thermal version of the EQPAIR model (values also reported in Table 3), the derived thermal values of  $\tau$ ,  $\Omega/2\pi$ ,  $E_{\text{Fe}}$  centroid and EW match, within the uncertainties, the parameters obtained in Table 2. The value of  $kT_e$  decreases from the pure thermal model as expected and it is similar to the value we get when adding a power law to our current model. While fitting a soft state spectra from 0.5–200 keV with the same hybrid model, Frontera et al. (2001) found  $\Gamma_p$  equal to  $2.5 \pm 0.1$ , an  $EW \sim 300$  eV and  $\Omega/2\pi$  around 0.63. These values match well with our non-thermal results. However, they obtained a lower  $l_h/l_s \sim 0.36$  and a higher  $l_{\text{nth}}/l_h \sim 0.77$ . For what they called a typical soft state, McConnell et al. (2002) found a  $\Gamma_p$

**Table 3.** Best-fit parameters of Cygnus X-1 for thermal/non-thermal hybrid models in the epoch 2 observations.

Model	eqpair (thermal)	eqpair (non-thermal)	compps (thermal)	compps (non-thermal)
$l_h/l_s$	$5.3^{+0.8}_{-0.4}$	$4.57^{+0.04}_{-0.87}$	—	—
$l_{\text{nth}}/l_h$	—	$0.16^{+0.11}_{-0.08}$	—	—
$\tau$	$0.66^{+0.02}_{-0.09}$	$0.49^{+0.24}_{-0.02}$	$0.57^{+0.03}_{-0.01}$	$1.43 \pm 0.10$
$\Gamma_p$	—	$2.4^{+0.5}_{-1.0}$	—	$3.72^{+0.17}_{-0.22}$
$\gamma_{\min}, \gamma_{\max}$	—	1.5, 1000 (frozen)	—	1.34, 1000 (frozen)
$\Omega/2\pi$	$0.73^{+0.07}_{-0.03}$	$0.63 \pm 0.08$	$0.60 \pm 0.05$	$0.87^{+0.12}_{-0.28}$
$E_{\text{Fe}}$ (keV)	$7.18^{+0.16}_{-0.14}$	$7.06 \pm 0.06$	$7.20^{+0.10}_{-0.22}$	$7.14 \pm 0.09$
$EW$ (eV)	287	379	238	412
$kT_0$ (keV)	$1.44^{+0.07}_{-0.03}$	$1.39^{+0.27}_{-0.01}$	1.20 (frozen)	1.20 (frozen)
$kT_e$ (keV)	$103^a$	$42^a$	$111^{+3}_{-6}$	$39^{+33}_{-2}$
$\chi^2_{\text{red}}$ (d.o.f.)	1.68 (234)	1.55 (232)	1.72 (233)	1.69 (230)

Notes:

<sup>a</sup> The electron temperature is calculated for the best-fit model (i.e., not free parameters).

Model applied in XSPEC notations: CONSTANT\*WABS\*(DISKPN+GAUSSIAN+EQPAIR) or CONSTANT\*WABS\*(DISKBB+GAUSSIAN+COMPPS) with  $N_{\text{H}}$  fixed to  $6 \times 10^{21} \text{ cm}^{-2}$  and  $kT_0$  value tied to disc  $kT_{\text{in}}$ . Errors are at 90% confidence level ( $\Delta\chi^2 = 2.7$ ).

compatible with ours (around 2.6) but, again,  $l_h/l_s \sim 0.17$  and  $l_{\text{nth}}/l_h \sim 0.68$  different from our values. For another soft state, Gierliński et al. (1999) found even higher values for these latter three parameters, in the range 2.6–3.4, 0.25–1.6 and 0.77–1. All these comparisons suggest that, in epoch 2, Cygnus X-1 was not in the typical soft state, but was rather in the IS.

Second, the thermal part of the hybrid model COMPPS fits the data for a  $\chi^2_{\text{red}} = 1.72$  (233 d.o.f.). Most of the crucial parameters like  $kT_e$ , the optical depth,  $\Omega/2\pi$  and the  $E_{\text{Fe}}$  centroid are compatible with those obtained with our current model (reported in Table 2) with a comparable  $\chi^2_{\text{red}}$ . Trying to improve our fits, we then used the non-thermal part of the COMPPS model with an electron distribution of index  $3.72^{+0.17}_{-0.22}$  and we report all the derived parameters in Table 3. Comparing the different  $\chi^2_{\text{red}}$  (now equal to 1.69 for 230 d.o.f.), the improvement is significant but not as strong as the EQPAIR non-thermal model. Again,  $kT_e$  decreases from the value obtained with a pure thermal model, which is compatible with McConnell et al. (2002). Using the non-thermal part of the COMPPS model to fit a soft state, these authors found temperatures ( $\sim 60$  keV), reflection factors and energy index  $\Gamma_p$  ( $\sim 3.5$ ) again compatible with ours.

Some authors, e.g., Belloni et al. (1996) and Ibragimov et al. (2005, submitted) claim that the soft states observed in 1996, 1998 and 1999 were in fact IS. Modeling the spectra with EQPAIR and a non-thermal high-energy component, Ibragimov et al. showed spectral results consistent with the non-thermal values we report here, including a high  $l_h/l_s$  value. According to the different soft states of Cygnus X-1 analyzed, they obtained for this parameter values between 4.2 and 12 and for  $\tau$ , values in the range 0.9–1.6. These results are consistent with ours.

We find that the non-thermal hybrid EQPAIR model the best able to fit our epoch 2 data: this model clearly accounts for the high-energy tail observed. The non-thermal component represents 16% of the total power supplied to the electrons in the

corona and the inferred luminosity in the 20–100 keV range is  $6 \times 10^{36} \text{ erg s}^{-1}$  while the bolometric one is  $3.3 \times 10^{37} \text{ erg s}^{-1}$ .

### 3.3. Evolutions occurring during epochs 3 and 4 (2003–2004)

We separated epoch 3 in five sub-groups as follows: *a*) before epoch 2 (MJD  $\sim 52710$ –52780); *b*) just after epoch 2 (MJD  $\sim 52801$ –52825); *c*) at MJD = 52990 when the source switches again to a softer state; *d*) when a harder state is then observed (MJD  $\sim 53101$ –53165); *e*) observations when the ASM count rate slightly increases while the IBIS HR decreases (MJD  $\sim 53240$ –53260). The IBIS HR shown in Fig. 2 indicates spectral evolution with time: from groups *a* to *e*, the mean HR value is 1.55, 0.8, 1.1, 1.4 and 1.05. Accordingly, a simple power law model fits the data with different indexes:  $\Gamma = 1.9$ , 2.3, 2.2, 1.9 and  $2.3 \pm 0.1$  for groups *a* to *e*.

We fitted from 5 keV to 400 keV the JEM-X and IBIS/ISGRI spectra of the data collected during these sub-groups, using our current Comptonization (COMPTT) model for the HS and the IS defined above. We fixed the seed photon temperature  $kT_0$  to the  $kT_{\text{in}}$  value given by the DISKBB (or frozen to 0.20 keV when the disc emission is not detected). The best-fit parameters are listed in Table 2. Normalization constants between the two instruments are very close to each other ( $\sim 1$ –1.2 for IBIS/ISGRI when JEM-X constant is frozen to 1). Variations in amplitude and overall spectral shape are observed between the epoch 3 sub-groups. While no disc emission is detected for groups *a* and *d*, a disc component is required for groups *b*, *c* and *e*. The  $EW$ s are also changing: the softer the source, the larger the  $EW$  ( $\sim 110$  eV for group *a* compared to  $\sim 780$  eV for group *e*). These results and the IBIS HR (Fig. 2) indicate that, during sub-groups 3 *a* and *d*, Cygnus X-1 was in a HS (as in epoch 1) while, in sub-groups 3 *b*, *c* and *e*, the source was in a softer state.

During epoch 4, the simple power law slope is  $\Gamma = 2.2 \pm 0.1$  and the mean IBIS HR value is 1.1. This indicates that the

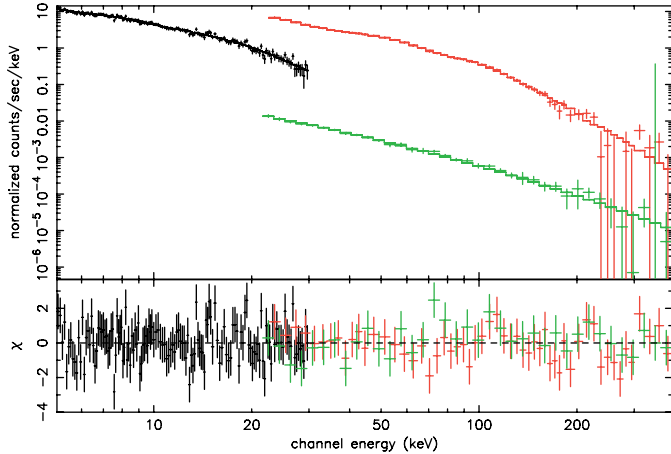


**Fig. 8.** Epoch 4 spectra of Cygnus X-1 with the JEM-X (black), SPI (green) and IBIS/ISGRI (red) data along with the best-fit current model (see Table 2). Residuals in  $\sigma$  units are also shown.

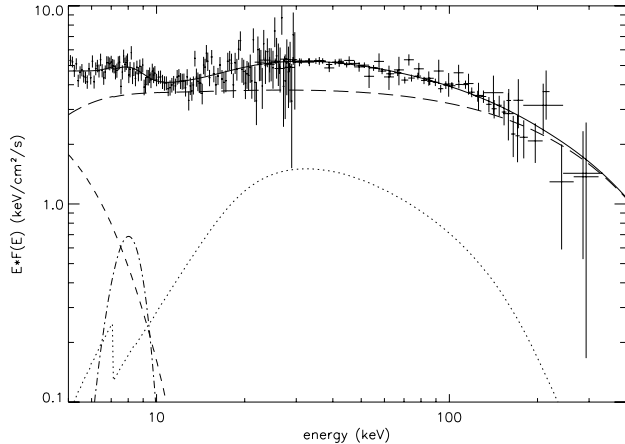


**Fig. 9.** Epoch 4 unabsorbed  $EF(E)$  spectrum of Cygnus X-1 along with the best-fit model described in Table 2 with the JEM-X, IBIS/ISGRI and SPI data. Dashed: Disc. Dotted-dashed: Gaussian line. Dotted: Reflection. Long dashes: Comptonization. Thick: Total model.

source was again in a softer state than the HS. The count spectrum is presented in Fig. 8. Figure 9 shows the resultant  $EF(E)$  spectrum and its best-fit model overplotted on the data obtained from JEM-X, IBIS/ISGRI and SPI (high-energy IBIS points are rebinned at the  $3\sigma$  level above 200 keV for illustrative purposes). Cross-calibration constants are respectively 1, 1 and 1.3. Using the current Comptonization (COMPTT) model defined above for epoch 2, we present in Table 2 the best-fit parameters obtained. Since we obtained a best-fit solution similar to the one of epoch 2, we fixed, to define the errors for the other parameters, the  $kT_{in}$  to the epoch 2 value of 1.16 keV and we obtained  $kT_e = 128$  keV,  $\tau = 0.74$ ,  $\Omega/2\pi = 0.47^{+0.18}_{-0.14}$  (close to the epoch 2 value of  $0.57^{+0.09}_{-0.06}$ ) and  $E_{Fe} = 7.78$  keV. Although the temperature is little constrained and errors are large, these values indicate that the source was again in a rather soft state.

#### 4. Discussion

During the broad-band (5 keV–1 MeV) *INTEGRAL* observations of Cygnus X-1 presented in this paper, the source was detected in at least two different spectral states. For epoch 1 (part of PV-Phase) and during some of the GPS observations (epoch 3, sub-groups *a* and *d*), the source was in the typical HS with a high-energy spectrum extending up to 800 keV, well characterized by a thermal Comptonization model. Parameters are typical of BH binaries and consistent with previous observations of Cygnus X-1 in the HS. We find that the Comptonization component must be modified by reflection. The subtended angle we derived is also compatible with values previously found for this source in the HS, either from *Ginga* and *CGRO/OSSE* ( $kT_e \sim 100$  keV,  $\tau \sim 1$ –2, and  $\Omega/2\pi \sim 0.19$ –0.34, Gierliński et al. 1997), or from *BeppoSAX* ( $kT_e \sim 60$  keV,  $\tau \sim 1$ –2 and  $\Omega/2\pi = 0.25$ , Frontera et al. 2001). Di Salvo et al. (2001) observed even higher temperatures for the HS, from 111 to 140 keV, and  $\Omega/2\pi \sim 0.1$ –0.3, within our error bars. Also, our results are compatible with those reported by Bazzano et al. (2003), Bouchet et al. (2003) and Pottschmidt et al. (2003b) who used *INTEGRAL* data from other PV-Phase observations, when Cygnus X-1 was also in the HS. We did not detect any Fe line nor disc emission during this period. Indeed, we could determine a 90% confidence level upper limit of 94 eV EW for a narrow line ( $\sigma = 0.1$  keV) at 6.7 keV and of 172 eV EW for a broad one ( $\sigma = 1$  keV). These limits are compatible with the typical EWs ( $\sim 150$  eV) of broad lines observed in HS from this BH system (Frontera et al. 2001). The lack of strong Fe line and disc emission is not surprising since, in the HS, the disc does not extend close to the BH, its inner disc temperature is low and contribution at  $>5$  keV is negligible.

Cygnus X-1 underwent a clear evolution to a softer state from epoch 1 to epoch 2. We indeed observed in 2003 June *INTEGRAL* data hardness variations (Figs. 2 and 3) and photon index changes, along with the appearance of a significant soft component well fitted by a disc black body model. The changes in the high-energy component are obvious from the best-fit parameters of the current model reported in Table 2. The Comptonization parameter  $y$  is characterized by both values  $(kT_e, \tau)$  where  $y = (kT_e/m_ec^2) \max(\tau, \tau^2)$ . While  $y \sim 0.51^{+0.10}_{-0.09}$  for epoch 1, its value drops to  $0.19^{+0.07}_{-0.06}$  for epoch 2.

As shown previously, these changes were correlated with evolutions of the *RXTE/ASM* light curve (Fig. 1) which indicate the rise of the soft disc emission. The increase in disc emission (up to about 26% of the bolometric luminosity) combined with an increase of the inner disc temperature to about 1.16 keV suggest that the accretion disc has extended down very close to the BH horizon. However, the inferred inner radius (4.5 km) is not compatible with the size of the innermost stable circular orbit, even for a maximally spinning Kerr BH. Besides uncertainties on the inclination angle and on the disc normalization, a number of effects can lead to such unphysical estimations. As mentioned in Sect. 3.2, electron scatterings can produce a diluted black body (Shimura & Takahara 1995) and cause the observed temperature  $kT_{in}$  to be higher and the disc normalization lower. Consequently, the inner disc radii could be underestimated by a factor of 5 or more (Merloni et al. 2000). Another

possible explanation for such a high temperature could be that the disc emission is Comptonized by a different warm corona at a temperature of a few keV, as sometimes suggested (Frontera et al. 2001; Malzac et al. 2005).

The softening of the hard component and the appearance of the disc emission were accompanied by significant increase in reflection and changes in Fe line emission. During epoch 2 data, the Fe line is needed in the spectra (while not for epoch 1) and  $\Omega/2\pi$  increases (it is more than twice the value found for epoch 1): this again indicates that a larger disc, closer to the BH, reflects more radiation coming from the hot plasma. Figures 5 and 7 show the resultant unabsorbed  $EF(E)$  spectra for both epochs 1 and 2: we clearly see differences in amplitudes and in the relative contributions of the various components, from soft to hard X-rays/ $\gamma$ -rays. Similar spectral transitions are observed during epochs 3 and 4:  $y = 0.57^{+0.27}_{-0.34}$  for epoch 3 sub-group *a* (while it drops to  $0.14^{+0.16}_{-0.09}$  for group *b*), and  $y = 0.18^{+0.24}_{-0.13}$  for epoch 4. The  $y$  evolution, combined with the changes in the IBIS HR and in the ASM light curve, indeed shows transitions from the HS (epoch 1, epochs 3 *a* and *d*) to softer states (epochs 2, 3 *b*, *c*, *e* and 4).

The transition to a soft state is generally attributed to an increase in the accretion rate. In this case, the total luminosity should increase significantly. For example, the total luminosity measured by Frontera et al. (2001) in the TDS of Cygnus X-1 was about a factor of 3 higher than in the HS, with a contribution of the disc emission higher than 50% of the total luminosity. From our analysis, the spectral transition seems to occur with only a slight change in the bolometric luminosity, mainly due to the appearance of a high-energy tail which represents less than 2% of the Eddington luminosity ( $\sim 1.5 \times 10^{39}$  erg s $^{-1}$  for a  $10 M_\odot$  BH). Therefore, we can interpret the component evolution as a spectral pivoting between soft and hard X-rays at almost constant luminosity. This has already been reported for other BH such as for the microquasar XTE J1550-564 (Rodriguez et al. 2003). When the total luminosity does not change much, the spectral evolution cannot be explained simply by a large variation in the accretion rate. An additional physical parameter (for example linked to the temperature and geometry of the Comptonizing cloud or to the magnetic field) must probably vary in the system to trigger the spectral changes from the HS to a softer state at almost constant luminosity.

While our data start at 5 keV, leading to a possible underestimation of the bolometric luminosity (which in a real soft state is dominated by the soft component), the near constancy of the luminosity between epochs 1 and 2 and other facts show that the soft state we observed in this latter period is not the typical TDS observed in Cygnus X-1. Our spectral analysis and the comparisons with previous results obtained on Cygnus X-1 (see Sect. 3.2) led us to conclude that, during epoch 2, the source was rather in the IS. The need for a cutoff in the high-energy spectrum of epoch 2 shows that the thermal Comptonization is still a dominant process for the high-energy component. The hybrid thermal/non-thermal models lead to a significant improvement in the fit of our data, compared to the thermal Comptonization models, like COMPTT, or the pure thermal versions of EQPAIR and COMPPS. However, our best-fit non-thermal parameters are sometimes intermediate between

hard and soft state values (like  $l_h/l_s$ ,  $l_{nth}/l_h$  or  $\Gamma_p$ ): this again shows that Cygnus X-1 was in the IS (or in the FST). Such a conclusion was also reached by Malzac et al. (2004) on the basis of the observed correlation of the spectral hardness with the radio flux during this period.

In recent years, it has become apparent that in the HS, the BH binaries become bright in radio and display clear correlations between the X-ray and radio luminosities (Corbel et al. 2003; Gallo et al. 2003) as often observed for Cygnus X-1 (Brocksopp et al. 1999; Gleissner et al. 2004b; Nowak 2005). Models where the base of a compact jet plays a major role in the physical processes of such BH systems have been proposed (Markoff et al. 2001). In such scenarios, the high-energy emission seen during the HS is interpreted as synchrotron emission from the jet that extends from radio to hard X-rays, naturally explaining the correlations observed during the HS. Those models explain the observed (or inferred) outflows: the radio emission is proportional to the jet power which in turn is correlated with the accretion rate and with the X-ray emission (Heinz & Sunyaev 2003; Merloni et al. 2003) as discussed for GX 339-4 (Zdziarski et al. 2004). However, detection of radio emission was reported during the TDS, for example in the BH XTE J1650-500 (Corbel et al. 2004) and the scenario increases in complexity (see Fender et al. 2005 for a complete review). More recently, Markoff et al. (2004) have proposed jet models where the synchro-self Compton or the external Comptonization radiation are the dominant processes generating X-ray spectra in BH binaries. These models seem to fit the experimental data as well as the thermal Comptonization models do.

While we did not observe any significant high-energy tail during the PV-Phase observations, it appears that, in the SPI spectra of 2003 June, when the source was in the IS, some data points above 400 keV are not well described by the thermal Comptonization models (see Figs. 6 and 7). All the tests we have performed using different SPI background models and the Crab nebula spectrum indicate that this feature comes from the source. Similar excess over a Comptonization law has been previously observed, in particular with CGRO/OSSE (2002) which detected a power law like component extending beyond 1 MeV during a (so classified) TDS of Cygnus X-1. In our case, the SPI data of the observed IS spectrum of Cygnus X-1 imply a rather bright high-energy tail. The bolometric luminosity of the source, including this new component, is 1.65 times higher than the one obtained with the best-fit thermal current model.

This kind of steep power law, without a high-energy break (at least up to 1 MeV) was modeled in the past including a non-thermal component in the accretion flow, with the so-called hybrid thermal/non-thermal models from Poutanen & Svensson (1996) and Coppi (1999). Using these same models, we obtain a better fit of our data, which indicate the necessity to include a non-thermal distribution of electrons, with a power law energy index between 2.4–3.7, depending on the model used.  $\Gamma_p$  between 2 and 3 are expected from shock acceleration models. We find that most of the crucial parameters such as  $\tau$ ,  $\Omega/2\pi$ ,  $E_{Fe}$  centroid,  $EW$  or  $kT_e$  are compatible with previous results reported by McConnell et al. (2002), Frontera et al. (2001) and Gierliński et al. (1999). With the non-thermal

EQPAIR model, we found an unabsorbed bolometric luminosity of  $3.3 \times 10^{37}$  erg s $^{-1}$  (higher than the one obtained with the current thermal model). This value is  $\sim 1.9$  times lower than the one observed by McConnell et al. (2002) in the (so classified) TDS: this, along with the differences seen in the  $l_h/l_s$ ,  $l_{\text{nth}}/l_h$  and  $\Gamma_p$  values (see Sect. 3.2), definitely shows that our epoch 2 observations did not happen during a TDS but rather in the IS, with an intermediate luminosity.

Alternatively, Comptonization on a population of (thermalized) electrons with bulk motion, e.g., Titarchuk et al. (1997), Laurent & Titarchuk (1999), is sometimes invoked to explain the power law high-energy component. This could describe the observed high-energy emission seen in epoch 2, as it predicts  $\Gamma > 2$  or even softer, even if the lower energy cutoff should be around 100 keV. In addition to hybrid thermal/non-thermal models presented above, a stratified Comptonization region, providing a larger range of both electron temperatures and optical depths, could model the spectrum. Ling et al. (1997) reached the same conclusions based on Monte Carlo modeling of *CGRO*/BATSE spectra combined with (non contemporaneous) *CGRO*/COMPTEL data (McConnell et al. 1994). Thermal gradients are incorporated into several other models, which then lead to the generation of a high-energy tail, e.g., Skibo & Dermer (1995), Chakrabarti & Titarchuk (1995) and Misra & Melia (1996).

## 5. Summary and conclusions

Using the broad-band capability of *INTEGRAL*, it has been possible to accumulate a large amount of simultaneous data on Cygnus X-1 between 5 keV–1 MeV and to follow its spectral evolution from 2002 November to 2004 November. These data were helpful to characterize the evolution of the Comptonization parameters of the source correlated to the presence of a variable disc emission, indicating transitions between the HS and a softer (Intermediate) state. We also observed the presence in the SPI data of a high-energy tail during the IS (or the FST), emerging from the Comptonization component between 400 keV–1 MeV and probably associated with a non-thermal component. The extent to which the spectrum hardens at energies approaching 1 MeV has now become an important issue for theoretical modeling of the accretion processes and radiation mechanisms in BH binaries. Data from both IBIS and SPI instruments offer the best opportunity to define more precisely the high-energy X-ray binary spectra. We hope to further investigate this using *INTEGRAL* data from this source and other bright BH X-ray binaries.

**Acknowledgements.** We thank the anonymous referee for his/her helpful comments and suggestions. MCB thanks J. Paul for a careful reading and comments on the manuscript. AAZ has been supported by KBN grants PBZ-KBN-054/P03/2001, 1P03D01827 and 4T12E04727. We thank the ESA ISOC and MOC teams for they support in scheduling and operating observations of Cygnus X-1. The present work is based on observations with *INTEGRAL*, an ESA project with instruments and science data center funded by ESA member states (especially the PI countries: Denmark, France, Germany, Italy, Switzerland, Spain, Czech Republic and Poland, and with the participation of Russia and the USA).

## References

- Anders, E., & Grevesse, N. 1989, Geochim. Cosmochim. Acta, 53, 197
- Arnaud, K. A. 1996, ASP Conf., 101, 17
- Bazzano, A., Bird, A. J., Capitanio, F., et al. 2003, A&A, 411, L389
- Balucińska-Church, M., Belloni, T., Church, M. J., et al. 1995, A&A, 302, L5
- Belloni, T., Méndez, M., van der Klis, M., et al. 1996, ApJ, 472, L107
- Bevington, P. R., & Robinson, K. D. 1992, Data Reduction and Error Analysis for the Physical Sciences, 2nd Ed., (New York: McGraw-Hill)
- Bouchet, L., Jourdain, E., Roques J.-P., et al. 2003, A&A, 411, L377
- Bowyer, S., Byram, E. T., Chubb, T. A., & Friedman, H. 1965, Science, 147, 394
- Brockopp, C., Fender, R. P., Larionov, V., et al. 1999, MNRAS, 309, 1063
- Cadolle Bel, M., Sizun, P., Rodriguez, J., et al. 2004, accepted for publication in the Proceedings of the 35th COSPAR Scientific Assembly (ASR Publication)
- Chakrabarti, S. K., & Titarchuk, L. G. 1995, ApJ, 455, 623
- Coppi, P. S. 1999, 161, 375, ASP Conf. Ser., 161, 375
- Corbel, S., Nowak, M. A., Fender, R. P., et al. 2003, A&A, 400, 1007
- Corbel, S., Fender, R. P., Tomsick, A. K., et al. 2004, ApJ, 617, 1272
- Di Cocco, G., Caroli, E., Celesti, E., et al. 2003, A&A, 411, L189
- Di Salvo, T., Done, C., Zycki, P. T., Burderi, L., & Robba, N. R. 2001, ApJ, 547, 1024
- Done, C., Mulchaey, J. S., Mushotzky, R. F., & Arnaud, K. A. 1992, ApJ, 395, 275
- Dove, J. B., Wilms, J., Nowak, M. A., Vaughan, B. A., & Begelman, M. C. 1998, MNRAS, 289, 729
- Esin, A. A., Narayan, R., Cui, W., et al. 1998, ApJ, 505, 854
- Fender, R. P., Belloni, T., & Gallo, E. 2005, to appear in From X-ray Binaries to Quasars: Black Hole Accretion on All Mass Scales, ed. T. J. Maccarone, R. P. Fender, and L. C. Ho (Dordrecht: Kluwer), [arXiv:astro-ph/0506469]
- Frontera, F., Palazzi, E., Zdziarski, A. A., et al. 2001, ApJ, 546, 1027
- Gallo, E., Fender, R. P., & Pooley, G. G., 2003, MNRAS, 334, 60
- Gierliński, M., Zdziarski, A. A., Johnson, W. N., et al. 1996, Proc. Röntgenstrahlung from the Universe, ed. H. U. Zimmermann, J. Trümper, & H. Yorke; MPE Report 263, 139
- Gierliński, M., Zdziarski, A. A., Done, C., et al. 1997, MNRAS, 288, 958
- Gierliński, M., Zdziarski, A. A., Poutanen, J., et al. 1999, MNRAS, 309, 496
- Gleissner, T., Wilms, J., Pottschmidt, K., et al. 2004a, A&A, 414, 1091
- Gleissner, T., Wilms, J., Pooley, G. G., et al. 2004b, A&A, 425, 1061
- Goldwurm, A., David, P., Foschini, L., et al. 2003, A&A, 411, L223
- Heinz, S., & Sunyaev, R. A. 2003, MNRAS, 343, 59
- Ibragimov, A., Poutanen, J., Gilfanov, M., et al. 2005, MNRAS, submitted [arXiv:astro-ph/0502423]
- Jensen, P.-L., Clausen, K., Cassi, C., et al. 2003, A&A, L7
- Jourdain, E., & Roques, J.-P. 1994, ApJ, 426, L11
- Laurent, P., & Titarchuk, L. G. 1999, ApJ, 511, 289
- Lebrun, F., Leray, J. P., Lavocat, P., et al. 2003, A&A, 411, L141
- Ling, J. C., Wheaton, W. A., Wallyn, P., et al. 1997, ApJ, 484, 375
- Lund, N., Buttdz-Jorgensen, C., Westergaard, N. L., et al. 2003, A&A, 411, L231
- Magdziarz, P., & Zdziarski, A. A. 1995, MNRAS, 273, 837
- Malzac, J., Petrucci, P. O., Jourdain, E., et al. 2004, Proceedings of the 5th *INTEGRAL* Workshop The *INTEGRAL* Universe, (Munich, February 2004), ESA Special Publication SP-552, [arXiv:astro-ph/0411069]
- Malzac, J., Petrucci, P. O., Jourdain, E., et al. 2005, A&A, submitted

- Markoff, S., Falcke, H., & Fender, R. 2001, A&A, 372, L25
- Markoff, S., & Nowak, M. A. 2004, ApJ, 609, 972
- McClintock, J. E., & Remillard, R. A. 2003, to appear in Compact Stellar X-ray Sources, ed. W. H. G. Lewin & M. van der Klis [arXiv:astro-ph/0306213]
- McConnell, M. L., Forrest, D., Ryan, J., et al. 1994, ApJ, 424, 933
- McConnell, M. L., Ryan, J. M., Collmar, W., et al. 2000, ApJ, 543, 928
- McConnell, M. L., Zdziarski, A. A., Bennett, K., et al. 2002, ApJ, 572, 984
- Méndez, M., & van der Klis, M., 1997, ApJ, 479, 926
- Merloni, A., Fabian, A. C., & Ross, R. R. 2000, MNRAS, 313, 193
- Merloni, A., Heinz, S., & di Matteo, T. 2003, MNRAS, 345, 1057
- Misra, R., & Melia, F. 1996, ApJ, 467, 405
- Mitsuda, K., Inoue, H., Koyama, K., et al. 1984, PASJ, 36, 741
- Nowak, M. A., 2002, in New Views on Microquasars, ed. P. Durouchoux, Y. Fuchs, & J. Rodriguez (Kolbata: Centre for space Physics), 11
- Nowak, M. A., Wilms, J., Heinz, S., et al. 2005, ApJ, 626, 1006
- Pottschmidt, K., Wilms, J., Nowak, M. A., et al. 2003a, A&A, 407, 1039
- Pottschmidt, K., Wilms, J., Chernyakova, M., et al. 2003b, A&A, 411, L383
- Pottschmidt, K., Wilms, J., Nowak, M. A., et al. 2005, accepted for publication in the Proceedings of the 35th COSPAR Scientific Assembly, ASR publication [arXiv:astro-ph/0504403]
- Poutanen, J., & Svensson, R. 1996, ApJ, 470, 249
- Poutanen, J. 1998, in Theory of Black Hole Accretion Discs, ed. M. A. Abramowicz, G. Bjornsson, & J. E. Pringle (Cambridge: Cambridge Univ. Press), 100
- Poutanen, J., & Coppi, P. 1998, Phys. Scr., 77, 57 [arXiv:astro-ph/9711316]
- Protassov, R., van Dyk, D., Connors, A., et al. 2002, ApJ, 571, 545
- Rodriguez, J., Corbel, S., & Tomsick, J. A. 2003, ApJ, 595, 1032
- Roques, J.-P., Schanne, S., von Kienlin, A., et al. 2003, A&A, 411, L91
- Salotti, L., Ballet, J., Cordier, B., et al. 1992 A&A, 253, 145
- Shakura, N. I., & Sunyaev, R. A. 1973, A&A, 24, 337
- Shimura, T., & Takahara, F. 1995, ApJ, 445, 780
- Skibo, J. G., & Dermer, C. D., 1995, ApJ, 455, L25
- Skinner, G., & Connell, P. 2003, A&A, 411, L123-126
- Stirling, A., Spencer, R. E., de la Force, C. J., et al. 2001, MNRAS, 327, 1273
- Sunyaev, R. A., & Titarchuk, L. 1980, A&A, 86, 21
- Titarchuk, L. G. 1994, ApJ, 434, 570
- Titarchuk, L. G., Mastichiadis, A., & Kylafis, N. D. 1997, ApJ, 487, 834
- Ubertini, P., Lebrun, F., Di Cocco, G., et al. 2003, A&A, 411, L131
- Vedrenne, G., Roques, J.-P., Schönfelder, V., et al. 2003, A&A, 411, L63
- Westergaard, N. J., Kretschmar, P., Oxborrow, C. A., et al. 2003, A&A, 411, L257
- Winkler, C., Courvoisier, T. J.-L., Di Cocco, G., et al. 2003, A&A, 411, L1
- Zdziarski, A. A., Grove, J. E., Poutanen, J., Rao, A. R., & Vadawale, S. V. 2001, ApJ, 554, L45
- Zdziarski, A. A., Poutanen, J., Paciesas, W. S., & Wen, L. 2002, ApJ, 578, 357
- Zdziarski, A. A., & Gierliński, M. 2004a, Progr. Theor. Phys. Suppl., 155, 99
- Zdziarski, A. A., Gierliński, M., Mikolajewska, J., et al. 2004b, MNRAS, 351, 791
- Ziółkowski, J., 2005, MNRAS, 358, 851

## 4. VERS UNE SIGNATURE DES SYSTÈMES A TROU NOIR ...

### *Les différents états spectraux des systèmes binaires comportant un trou noir*

Un système binaire comportant un trou noir s'observe dans principalement deux états spectraux différents, appelés l'état dur et l'état mou, que nous allons décrire ci-dessous. Comme les différents systèmes observés semblent osciller au fil des jours et des mois entre ces deux états, des états intermédiaires ont été aussi souvent observés par Integral, par exemple en provenance de Cygnus X-1. Un état très mou (« ultrasoft » en anglais) peut être aussi observé, dans lequel les sources ne produisent pas de photons au delà de quelques dizaines de keV. L'étude théorique de cet état, non réellement expliqué jusqu'à maintenant, sera un de mes thèmes de recherche futurs.

#### **L'état dur**

Dans l'état dur, la source montre un spectre dur au delà de 20 keV, pouvant se modéliser par une loi de puissance d'index -1.5 environ, et présentant une cassure spectrale vers 100-200 keV. En dessous de 20 keV, une composante faible correspondant à un spectre de corps noir à quelques keV de température peut aussi être détectée.

#### **L'état mou**

Dans l'état mou, la composante de corps noir décrite précédemment devient prépondérante. Le spectre au delà de 50 keV devient mou, pouvant se modéliser par une loi de puissance d'index -2.8. Il semblerait qu'il n'y pas de cassure spectrale à cette loi de puissance et qu'elle puisse s'observer à haute énergie. La détermination de cette cassure est un des objectifs majeurs des futures observations au delà de 200 keV d'Integral.

Ce sont ces deux états que j'ai essayé de modéliser grâce à une simulation Monte-Carlo, dont je donne le principe plus loin. Ce programme n'a pas, à ma connaissance, d'équivalent dans le petit monde des astronomes X et  $\gamma$ .

### *Le modèle générique de l'émission X des binaires à trous noirs*

Lorsqu'une particule de masse  $m$  tombe sur un corps céleste, elle acquiert de l'énergie cinétique en puisant dans le réservoir d'énergie potentielle de nature gravitationnelle de l'astre

en question. Le rendement  $\eta$  de ce processus – le rapport entre le gain d'énergie ainsi obtenu et l'énergie de masse de la particule – s'exprime de la manière suivante :

$$\eta = \frac{\delta E}{mc^2} = \frac{GM}{Rc^2} = \frac{R_s}{2R}$$

où  $M$  et  $R$  sont respectivement la masse et le rayon de l'astre,  $R_s$  son rayon de Schwarzschild,  $G$  la constante de la gravitation et  $c$  la célérité de la lumière. Ce rendement est très faible ( $\eta \approx 10^{-5}$ ) pour une étoile de type solaire. Il est par contre d'environ 10 % dans le cas d'une étoile à neutrons, d'environ 1,4 fois la masse du soleil pour un rayon de 10 km. Une particule tombant dans le champ gravitationnel d'un astre effondré (une étoile à neutrons ou mieux, un trou noir) peut donc gagner un surcroît d'énergie égal (voire supérieur) à 10% de son énergie de masse.

En ne relâchant qu'environ 0,7 % de l'énergie de masse des particules qu'elles font fusionner, les réactions de fusion thermonucléaire affichent un rendement bien moindre que l'accrétion quand elle précipite ces mêmes particules sur un astre compact. L'accrétion de matière par un astre effondré se présente donc *a priori* comme un processus très efficace pour convertir la matière en énergie. Reste à expliquer comment un tel corps céleste parvient à tirer parti de ce mécanisme pour susciter les abondants débits d'énergie que l'on observe dans les domaines des rayonnements X et  $\gamma$ .

## **Rayonnement émis par un disque d'accrétion**

Nous avons vu précédemment qu'un disque d'accrétion peut se diviser en trois zones. Nous allons survoler le rayonnement attendu en provenance de ces zones.

La zone 3, la plus externe, est la plus ample du disque. Le rayonnement émis atteint un maximum pour des photons d'énergie telle que  $T \sim 10^5\text{-}10^6$  K, et est donc observable surtout dans les domaines UV et X. Il en résulte que l'éventuel rayonnement  $\gamma$  de basse énergie qu'un disque d'accrétion est susceptible d'émettre ne peut pas provenir de la région externe.

Dans la zone 2, la température du disque, optiquement épais, est de l'ordre de  $10^6$  à  $10^7$  kelvins. Ils sont donc conduits à émettre des rayonnements riches en photons dont les énergies tombent dans la gamme de 0,1 à 1 keV, c'est à dire dans la bande des rayons X mou. La seule région d'un disque d'accrétion ceinturant un trou noir ou une étoile à neutrons faiblement magnétisée *a priori* favorable à l'émission de photons X durs ou  $\gamma$  ne peut donc être que la zone 1, la plus interne comprise entre la zone interne du disque et le trou noir.

## **Rayonnement émis par la région interne : la comptonisation**

Il s'agit du mécanisme à l'œuvre dans un milieu fortement diffusif faisant écran à la propagation des photons X et  $\gamma$ . Le spectre des photons est alors plus ou moins profondément altéré par les diffusions multiples qu'ils subissent dans le milieu en question au point que le spectre émergeant s'avère parfois très différent du spectre source. Ce phénomène, dit de "comptonisation", a été modélisé analytiquement dans la bande des rayons X durs et des rayons  $\gamma$  de très basse énergie par Sunyaev et Titarchuk (1980). Le modèle de Sunyaev et Titarchuk (dénommé ci-après modèle ST) s'applique au cas de milieux écran à géométrie simple, comme une sphère ou un disque, et dont la température électronique  $T_e$  est telle que  $T_e \approx 10^8$  K.

Puisqu'il s'agit d'un milieu que l'on peut qualifier de froid, la section efficace Compton est alors constante et égale à la section efficace de Thomson  $\sigma_T$ . Utilisé en un premier temps pour interpréter les observations menées dans le domaine des rayons X, le modèle ST est aujourd'hui d'usage courant pour décrire les spectres de nombreuses sources de photons  $\gamma$  de basse énergie. Le modèle ST doit cependant être utilisé avec précaution, car bien des hypothèses qu'il admet sont parfois contestables, surtout dans le domaine X durs et  $\gamma$  :

1. En toute généralité, la vitesse des électrons ne peut pas être tenue pour négligeable ; on ne peut donc pas supposer *a priori* que les électrons du milieu diffusant soient au repos.
2. Dans le domaine  $\gamma$ , la section efficace Compton ne peut plus être considérée comme égale à la section efficace de Thomson car cette dernière s'avère alors dépendante des énergies des photons et des électrons mis en jeu dans le processus interactif (section efficace de Klein-Nishina).
3. Toujours dans le domaine  $\gamma$ , la variation relative d'énergie des photons  $\Delta E/E$  ne peut plus être considérée comme largement inférieure à l'unité.

Les effets 2 et 3 ont été pris en compte dans le nouveau modèle de comptonisation calculé par Lev Titarchuk en 1994.

## ***Modèle simple de l'émission X dur et $\gamma$ de l'environnement immédiat du trou noir***

Nous allons maintenant décrire un modèle simple de l'émission X dur de l'environnement d'un trou noir, modèle que j'ai développé à partir du raisonnement proposé par Zeldovich et Shakura (1969) dès la fin des années soixante, et que j'ai présenté dans le cadre d'un cours pour l'«International Relativistic Astrophysics Ph.D.», dans le cadre de l'I.C.R.A., à Nice Sophia Antipolis, en 2006.

Ne seront abordés dans la suite que les seuls systèmes accrétants dont la luminosité est inférieure ou égale à la luminosité d'Eddington. Les régimes où l'accrétion dépasse la limite

d'Eddington, que l'on dénomme “super eddingtoniens”, sont beaucoup trop complexes pour être détaillés ici. Ils se traduisent par de fortes éjections de matière qui peuvent se manifester selon les caractéristiques du système soit par un vent générant un halo de matière autour de l'astre accrétant, soit sous la forme de jets de matière plus ou moins collimatés.

L'accrétion reste bien sûr la source principale d'énergie en transformant l'énergie gravitationnelle de l'astre accrévant en énergie cinétique des particules accrétées. Les particules communiquent alors par diffusion coulombienne tout ou partie de cette énergie au plasma confiné à proximité de l'astre accrévant. Les processus émissifs contribuent alors à refroidir ce plasma.

Le Bremsstrahlung et l'effet Compton inverse sont les principaux mécanismes de perte d'énergie à l'œuvre au sein des plasmas susceptibles de rayonner dans le domaine X dur ou  $\gamma$ . Il convient maintenant de déterminer les conditions physiques (telles que température, densité de matière et densité de rayonnement) qui font que l'un ou l'autre de ces deux mécanismes s'impose au sein du plasma émissif, ce qui permet ensuite d'esquisser les processus qui prévalent à proximité d'un astre accrévant.

## **L'énergie disponible dans la région proche du trou noir**

L'énergie des protons accrétés initialement au repos à l'infini, et en chute libre jusqu'aux alentours du trou noir, est donnée par l'équation suivante :

$$E_p = \frac{m_p c^2}{\sqrt{1 - \frac{r_s}{r}}} \approx 210 \text{ MeV} @ r = 3r_s$$

où  $m_p$  est la masse du proton. On se rend ainsi bien compte que l'interface entre le flot accrété et la surface d'une étoile à neutrons pourrait être émetteur de rayons  $\gamma$ .

## **Un mécanisme de chauffage**

L'énergie fournie par la matière accrétée est convoyée principalement par les protons et les ions, beaucoup plus lourds que les électrons. Les protons et les ions communiquent leur énergie aux électrons du plasma lors de diffusions coulombiennes multiples qui contribuent à freiner les particules accrétées. Avant de s'arrêter, un proton parcourt ainsi une longueur caractéristique  $l_M$  qui, en fonction de son énergie  $E_p$  et de la quantité de matière traversée, s'exprime par la relation suivante :

$$l_{\text{proton}} \approx 200 \frac{E_p^2}{\rho} \text{ kilometers}$$

où  $E_p$  est exprimée en unité de 200 MeV et  $\rho$  en unité de  $10^{-6} \text{ g cm}^{-3}$ . Ces valeurs numériques sont représentatives du voisinage du trou noir où les protons accrétés se présentent avec une énergie cinétique de l'ordre de 210 MeV, comme nous l'avons vu précédemment.

Si on suppose que les particules ont toutes la même énergie cinétique incidente  $E_C$ , elles s'arrêtent alors à la même profondeur  $l_0$  dans le plasma. Si on postule de plus que la perte d'énergie par unité de temps et de masse est uniforme jusqu'à la profondeur  $l_0$ , le terme de chauffage Q est alors défini par la relation suivante :

$$Q \approx \frac{L_{\text{acc}}}{A\rho_{\text{proton}}} \text{ erg/s/g}$$

où  $A$  est la surface de la région interne, et  $L_{\text{acc}}$  est l'énergie fournie par le processus d'accrétion dans les régions internes du disque :

$$L_{\text{acc}} = \dot{M} c^2 \quad \text{où } \dot{M} \text{ est le taux d'accrétion}$$

## Deux mécanismes de refroidissement

*Refroidissement par Bremsstrahlung.* Dans des plasmas du type de ceux évoqués ci-dessus, les électrons adoptent très rapidement une distribution en énergie de type Maxwell-Boltzmann, et ce quelle que soit leur distribution initiale. On est donc le plus souvent en présence d'un milieu dont les caractéristiques sont celles d'un plasma d'électrons de masse volumique  $\rho$  en équilibre thermique à la température électronique  $T_e$ . L'émissivité Bremsstrahlung  $J_B$  d'un tel plasma par unité de temps et de masse s'exprime alors par la relation suivante :

$$J_B \approx 7.2 \cdot 10^{20} \rho \sqrt{T_e} \text{ erg s}^{-1} \text{ g}^{-1}$$

*Refroidissement par comptonisation.* Dans un champ de rayonnement de densité d'énergie  $U$ , un électron non relativiste d'énergie  $E$  subit par effet Compton une perte d'énergie par unité de temps qui s'exprime par la relation suivante :

$$-\dot{E} \approx \frac{8}{3} \sigma_T U \frac{E}{m_e c}$$

où  $\sigma_T$  est la section efficace de Thomson,  $m_e$  la masse de l'électron et  $c$  la célérité de la lumière. Dans la mesure où  $E \approx \frac{3}{2} kT_e$  (où  $k$  est la constante de Boltzmann), l'émissivité Compton  $J_C$  par unité de temps et de masse s'exprime alors par la relation suivante (où  $m_p$  est la masse du proton) :

$$J_C = 4 \frac{\sigma_T U}{m_p} \frac{kT_e}{m_e c} \approx 8 U T_e \text{ erg s}^{-1} \text{ g}^{-1}$$

*Comparaison des deux mécanismes de refroidissement.* La comptonisation est le mécanisme de refroidissement prépondérant si  $J_C > J_B$ , donc si l'inégalité suivante est vérifiée :

$$1.110^{20} \frac{U\sqrt{T_e}}{\rho} > 1$$

## Bilan énergétique

La comptonisation s'avère donc le mécanisme dominant dans le cas de plasmas très chauds ( $T_e$  grand), peu denses ( $\rho$  petit) et baignés par un champ de radiation  $U$  particulièrement intense, conditions qui prévalent au voisinage d'un trou noir. Comme noté précédemment, le taux de refroidissement par Comptonisation est donné par l'équation suivante :

$$Q \approx \frac{4 \sigma_T U k T_e}{m_p m_e c} \approx 8 U T_e \text{ erg s}^{-1} \text{ g}^{-1}$$

Quant à la densité d'énergie  $U$  de photons X froids, elle s'exprime par la relation suivante :

$$U \approx \frac{f U_X}{A c} \approx \frac{f f_X L_{acc}}{A c} \text{ erg cm}^{-3}$$

où  $L_{acc}$  est l'énergie fournie par le processus d'accrétion,  $f_X$  est la fraction de l'énergie fournie par l'accrétion rayonnée dans la bande des photons X froids,  $A$  est la surface de la région interne, et  $f$  la fraction de cette surface susceptible illuminée.  $f$  dépend donc de la géométrie de l'illumination de la zone interne.

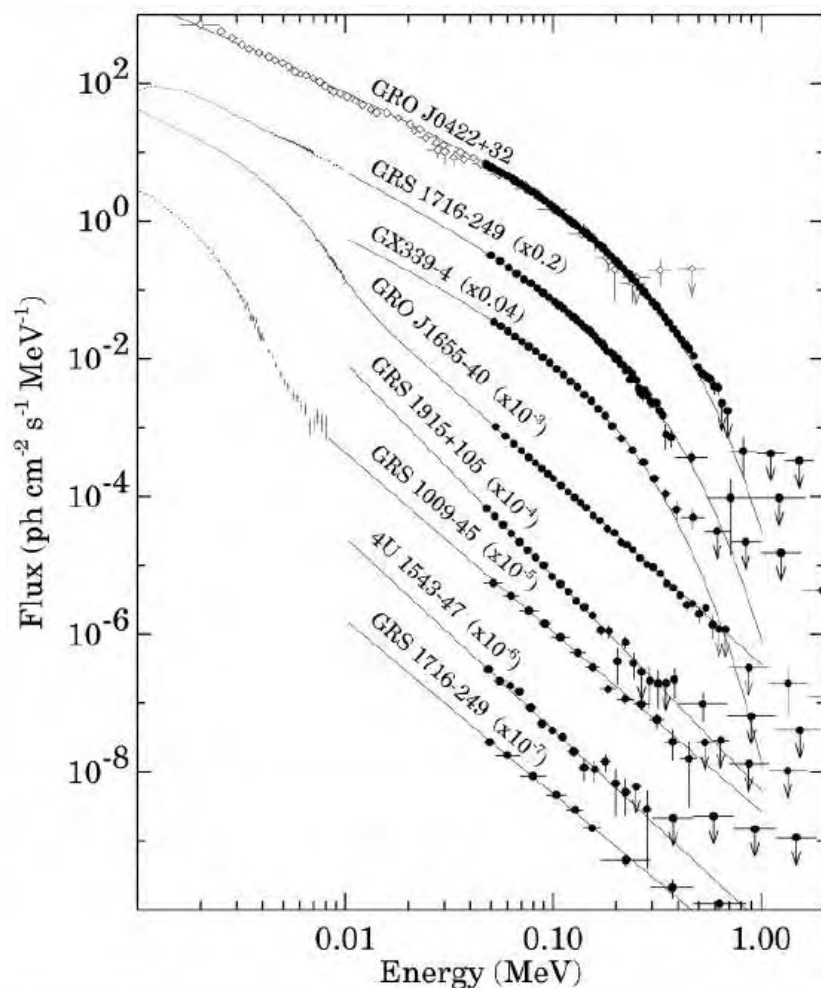
En égalisant le terme de chauffage et le terme de refroidissement, on obtient la température du plasma :

$$T_e \approx \frac{310^9}{f \rho l_{proton}} \approx 10^8 - 10^9 \text{ K}$$

Cette température, de l'ordre de 10-100 keV, est donc suffisante pour que ces milieux rayonnent en abondance dans le domaine X durs et gamma de basse énergie. Ce modèle simple débouche aussi sur deux conclusions importantes :

1. La zone proche du trou noir se refroidit préférentiellement par comptonisation, même dans le cas où les valeurs qui décrivent les conditions physiques de cette zone s'écartent notablement de celles adoptées ci-dessus.
2. Il est également remarquable que la température du plasma à proximité immédiate d'un trou noir ne dépende pas directement du taux d'accrétion. La température du plasma à

proximité immédiate de l'astre accréterant ne change pas si le taux d'accrétion diminue (donc si la luminosité du disque diminue dans la bande X), du moins tant que la structure du bourrelet interne du disque reste plus ou moins la même. L'allure du spectre du rayonnement  $\gamma$  émis par un disque d'accrétion ceinturant un trou noir n'est donc, en général, pas susceptible d'évoluer en fonction de la luminosité X du système. Cette dernière propriété a été confirmée par de nombreuses observations comme on peut le voir sur la figure ci-dessous. Cette propriété n'est toutefois pas valide si la région interne est refroidie par une autre émission de photons que celle du disque.



Spectres observés par GRO/OSSE de différents systèmes abritant un trou noir (Grove et al. 1998). La partie à haute énergie diffère peu alors que la luminosité du système augmente de plusieurs ordres de magnitude.

## **Binaires X à trous noirs dans l'état mou**

Dans l'état mou, on suppose que le disque s'étend jusqu'à la dernière orbite stable, soit  $3 r_S$  pour un trou noir de Schwarzschild. Comme montré précédemment, on observe aussi un spectre thermique proéminent, correspondant à une température de quelques keV, et provenant probablement du bord interne du disque. La région interne est donc baignée d'un intense flux de photons X, ce qui implique un fort refroidissement de ce plasma. La température de ce plasma est donc  $\approx 10^8$  K, et on ne doit donc pas observer de composante de comptonisation thermique, telle que décrit par le modèle ST, ce qui est le cas. Il reste que l'origine de la loi de puissance observée à haute énergie dans cet état est un sujet de débat, auquel j'ai contribué, et qui sera décrit en détail plus loin.

## **Binaires X à trous noirs dans l'état dur**

Dans l'état dur, le disque recule jusqu'à  $10 r_S$  environ, ce qui expliquerait la chute de la composante de basse énergie. En effet, le modèle standard du disque d'accrétion prévoit que la température du disque devient d'autant plus élevée que le rayon interne est petit. Si le rayon interne du disque augmente, la température maximale du disque diminue et il est alors plus visible au dessus de un keV, comme on l'observe dans l'état dur. De plus, si le disque s'éloigne du trou noir, l'illumination des régions proches du trou noir par celui-ci devient plus faible et la température du plasma dans les régions internes devient plus élevée ( $\approx 10^9$  K), comme on l'a vu précédemment. On observe alors un spectre thermique comptonisé comme décrit dans le modèle ST, et observé par les télescopes X durs et  $\gamma$ .

## ***Simulation Monte-Carlo de la « bulk motion Comptonization (BMC) »***

Pour comprendre la présence de la loi de puissance observée dans l'état mou, j'ai donc développé, avec l'aide de Lev Titarchuk, une simulation Monte-Carlo du transfert de rayonnement dans le voisinage d'un trou noir, simulant principalement la comptonisation. L'idée était qu'il fallait prendre en compte aussi, dans la comptonisation, le mouvement de chute libre de la matière dans le trou noir, mouvement qui domine tout autre mouvement, thermique ou non, dès qu'on s'approche suffisamment de l'horizon. J'ai donc effectué une simulation pour vérifier si ce mouvement de chute libre des électrons pouvait induire, par effet Compton inverse, la loi de puissance observée. Les premiers résultats montrèrent effectivement une loi de puissance, mais d'un index plus faible que celui observé, donc un spectre plus dur. J'ai alors modifié la simulation pour prendre en compte les effets de Relativité Générale, c'est-à-dire la courbure de la trajectoire des photons, et le rougissement gravitationnel ; ces modifications ont donné des résultats satisfaisants, comme nous le verrons ci-dessous.

## La simulation Monte-Carlo en relativité générale

Comme décrit au chapitre 2, tout au long de notre simulation numérique de type “Monte-Carlo”, on suit pas à pas le parcours d'un photon se propageant dans le milieu considéré jusqu'à son « absorption » par le trou noir, ou son échappement du système considéré. Ce parcours prend en compte la métrique de Schwarzschild, les photons ayant une trajectoire courbe au voisinage du trou noir. Le modèle géométrique est composé d'une sphère représentative de la zone proche du trou noir, et d'un disque représentant le disque d'accrétion. En modulant le rayon interne du disque, on peut reproduire les effets dus à l'illumination, observés dans les états mous et durs. Les photons sont initiés à partir du bord du disque, avec une distribution en énergie simulant une distribution thermique.

A chaque pas  $i$ , on calcule la profondeur optique parcourue  $\tau_i$ , en fonction de la densité électronique  $\rho$  et de la section efficace  $\sigma$  au point donné :

$$\tau_i = \tau_{i-1} + d\tau \quad \text{avec} \quad d\tau = \rho\sigma dl$$

$\rho$  et  $\sigma$  dépendent a priori du point où on calcule cette profondeur optique,  $\sigma$  dépendant, par exemple, de la température et de la vitesse d'ensemble (« bulk motion ») au point donné. En effet, en chaque point du système, on considère que le mouvement des électrons est composé d'un mouvement brownien thermique de moyenne nul, auquel est ajouté un mouvement d'ensemble. Dans le cas que nous considérerons pour la simulation de l'état mou, ce mouvement d'ensemble est la chute libre des électrons.

On détermine aussi la profondeur optique  $\tau_l$  que le photon parcourt effectivement avant de subir une interaction. Pour estimer  $\tau_l$ , on pratique un tirage aléatoire selon la loi de probabilité exprimée par l'équation suivante :

$$P(\tau_l) = e^{-\tau_l}$$

Si  $\tau$  devient supérieure à  $\tau_l$  sans que le photon s'échappe, il y a une interaction Compton. Cette interaction est simulée en suivant les prescriptions données dans l'article de Pozniakov, Sobol et Sunyaev (1974). À partir des caractéristiques de l'interaction, on détermine alors l'énergie et la direction du photon issu de l'interaction, photon que l'on suit ensuite jusqu'à son absorption ou son échappement. Les photons qui s'échappent sont sauvegardés afin d'établir le spectre de la source observée à l'infini.

## Etude de l'émission X dur des systèmes à trou noir dans l'état dur

Si on suppose dans la simulation que la température du plasma dans la zone proche du trou noir est de l'ordre de 50 keV, on retrouve un spectre observé de comptonisation thermique semblable au modèle ST. De plus, les photons issus du disque qui ne sont pas « comptonisés » dans la sphère permettent de reproduire la partie de basse énergie observée dans l'état dur.

## **Etude de l'émission X dur des systèmes à trou noir dans l'état mou**

Si la température du plasma dans la zone proche décroît, l'effet de la vitesse d'ensemble commence à dominer sur l'effet du mouvement thermique dans la comptonisation. On a pu déterminer grâce aux simulations que l'effet de la chute libre domine lorsque la température devient plus faible que 10 keV. Le spectre simulé présente une loi de puissance d'index -2.8 environ, similaire à ce qui est observé dans l'état mou. Le changement d'état dans les systèmes à trou noir semble donc être dû aux changements de température du plasma entourant le trou noir. Comme nous l'avons vu précédemment, ces changements de température peuvent être dû à des variations du flux de rayons X baignant le plasma, variations qui pourraient, quant à elles, être reliées à des changements du rayon interne du disque. La situation peut donc se résumer dans le tableau suivant :

	Rayon interne	illumination	température	Type de Comptonisation
Etat mou	$\sim 3 r_S$	forte	Faible ( $\sim 5$ keV)	Chute libre
Etat dur	$\sim 10 r_S$	faible	Elevée ( $\sim 50$ keV)	thermique

Tous ces résultats sont présentés dans la publication n°1.

## **Etude des variations temporelles des systèmes à trou noir.**

Les photons ayant subis des interactions dans le plasma entourant le trou noir ont un plus long parcours que ceux qui s'échappent directement. Ceux-ci doivent donc arriver à l'observateur légèrement avant les photons « comptonisés ». Ce décalage temporel dépendant des interactions subies par les photons doit donc être dépendant de leur énergie. Dans la publication n°2, nous avons vérifié que ce phénomène est effectivement observé dans les systèmes à trou noir, validant notre hypothèse que les composantes à haute énergie observées sont effectivement dues à l'effet Compton.

## ***Une signature controversée : l'élargissement de la raie du Fer***

Avec Lev Titarchuk et son étudiant Nikolaï Shaposhnikov, nous avons aussi étudié l'élargissement de la raie du fer, une autre signature très connue des trous noirs dans le domaine des X mous, et proposée par l'astronome Andy Fabian (Fabian et al., 1989). L'idée vient du fait qu'une lumière émise par un objet qui se rapproche d'un trou noir est vue de plus en plus décalée vers le rouge par un observateur à l'infini. La raie de fluorescence du Fer, à 6.4 ou 7.1 keV par exemple (les valeurs précises dépendant de l'état d'ionisation de l'atome de Fer dans le milieu considéré), est observée dans la plupart des plasmas astrophysiques. Donc, si on observe un plasma émetteur situé en différents points plus ou moins proches du trou noir, la raie du fer émise sera plus ou moins rougie. Le spectre résultant présentera alors un élargissement vers le rouge, dont la forme donne une indication sur la métrique aux alentours du trou noir, et donc sur ses propriétés (en particulier, sa vitesse de rotation). Ce

modèle du rougissement de la raie du fer a un grand succès et a été utilisé pour mesurer la vitesse de rotation de nombreux trous noirs, en particulier pour les galaxies extérieures (Miller, 2007).

L'observation récente de raies du fer « rougies » dans des systèmes contenant certainement des étoiles à neutrons nous a fait penser que ce phénomène n'est peut-être pas la signature d'un trou noir, et qu'il peut ne pas être relié à l'objet compact central. L'étude du BMC nous avait montré que la comptonisation sur un faisceau d'électrons convergeant (tel qu'il se présente lorsque ces électrons tombent en chute libre dans un trou noir) permet d'augmenter l'énergie des photons, créant la loi de puissance observée dans l'état mou. Nous avons donc postulé qu'un faisceau divergent (comme par exemple un vent sphérique s'échappant du système), devait diminuer l'énergie des photons incidents. C'est ce que j'ai simulé, considérant un plasma au centre de mon système émettant une raie monochromatique. Cette raie passe ensuite dans un milieu où la vitesse d'ensemble est radiale, vers l'extérieur du système, simulant ainsi un vent. La comptonisation dans ce vent produit, comme on l'avait prévu, un rougissement de la raie, similaire à ce qui est observé.

Nous avons donc postulé que le rougissement de la raie du fer observé était donc plutôt dû à la comptonisation dans un vent entourant le système et s'échappant de celui-ci. Les observations que nous avons ajustées avec notre modèle nous ont permis d'obtenir des paramètres de ce vent ( $T \approx 0.1$  keV,  $v_w \approx 3000$  km s $^{-1}$ ), raisonnable pour ce genre de système, et en accord, pour les galaxies extérieures, avec les valeurs mesurées en optique. Tous ces résultats sont présentés dans la publication n°3.

## ***Bibliographie***

- Fabian A. et al., 1989, MNRAS, 238, 729  
Grove J.E. et al., 1998, ApJ, 500, 899  
Miller J., 2007, Annual Review of Astronomy and Astrophysics, 45, 441  
Pozniakov L., Sobol I. et Sunyaev R., 1983, Astrophysics and Space Science Review, 2, 189  
Sunyaev R. et Titarchuk L., 1980, A&A, 86, 121  
Titarchuk L., 1994, ApJ, 434, 570  
Zeldovich Y.B. et Shakura N.I., 1969, Soviet Astronomy, 13, 175

## *Publications principales afférentes à ce chapitre*

**The Converging Inflow Spectrum Is an Intrinsic Signature for a Black Hole: Monte Carlo Simulations of Comptonization on Free-falling Electrons**

P. Laurent, L. Titarchuk.

1999, *ApJ*, 511, 289

**Timing and Spectral Properties of X-Ray Emission from the Converging Flows onto a Black Hole: Monte Carlo Simulations**

P. Laurent, L. Titarchuk.

2001, *ApJ*, 562, 67

**Effects of Downscattering on the Continuum and Line Spectra in Powerful Wind Environment. II Monte Carlo Simulations, Analytical Results and Data Analysis**

P. Laurent, L. Titarchuk.

2007, *ApJ*, 656, 1056



## THE CONVERGING INFLOW SPECTRUM IS AN INTRINSIC SIGNATURE FOR A BLACK HOLE: MONTE CARLO SIMULATIONS OF COMPTONIZATION ON FREE-FALLING ELECTRONS

PHILIPPE LAURENT<sup>1</sup> AND LEV TITARCHUK<sup>2,3</sup>

Received 1998 March 23; accepted 1998 August 25

### ABSTRACT

An accreting black hole is, by definition, characterized by the drain. Namely, matter falls into a black hole much the same way as water disappears down a drain: matter goes in and nothing comes out. As this can only happen in a black hole, it provides a way to see “a black hole,” a unique observational signature of black holes. The accretion proceeds almost in a free-fall manner close to the black hole horizon, where the strong gravitational field dominates the pressure forces. In this paper we calculate (by using Monte Carlo simulations) the specific features of X-ray spectra formed as a result of upscattering of the soft (disk) photons in the converging inflow (CI) within about 3 Schwarzschild radii of the black hole. The full relativistic treatment has been implemented to reproduce these spectra. We show that spectra in the soft state of black hole systems (BHS) can be described as the sum of a thermal (disk) component and the convolution of some fraction of this component with the CI upscattering spread (Green’s) function. The latter boosted photon component is seen as an extended power law at energies much higher than the characteristic energy of the soft photons. We demonstrate the stability of the power spectral index ( $\alpha = 1.8 \pm 0.1$ ) over a wide range of the plasma temperature, 0–10 keV, and mass accretion rates (higher than 2 in Eddington units). We also demonstrate that the sharp high-energy cutoff occurs at energies of 200–400 keV, which are related to the average energy of electrons  $m_e c^2$  impinging on the event horizon. The spectrum is practically identical to the standard thermal Comptonization spectrum (Hua & Titarchuk) when the CI plasma temperature is getting of order of 50 keV (the typical ones for the hard state of BHS). In this case one can see the effect of the bulk motion only at high energies, where there is an excess in the CI spectrum with respect to the pure thermal one. Furthermore, we demonstrate that the change of spectral shapes from the soft X-ray state to the hard X-ray state is clearly to be related to the temperature of the bulk flow. We derive a generic formula for the temperature of the emitting region (CI) that depends on the ratio of the energy release in this very region and in the disk. Using this formula, we demonstrate that the temperature of the emission region in the hard state of the BHS is approximately 2 times higher than the ones of neutron star systems (NSS) in the hard state, which is confirmed by recent *RXTE* and *Beppo-SAX* observations of the hard state of NSS. The effect of the bulk Comptonization compared with the thermal one is getting stronger when the plasma temperature drops below 10 keV. These Monte Carlo simulated CI spectra are an inevitable stamp of the BHS where the strong gravitational field dominates the pressure forces.

*Subject headings:* black hole physics — radiation mechanisms: nonthermal — X-rays: general

### 1. INTRODUCTION

A lot of theories and models have been suggested to explain the observational situations of black hole systems (BHS); for recent reviews of the astrophysics of black holes see, e.g., Liang & Narayan (1997), Zhang et al. (1997), and Titarchuk (1996, 1997).

The BHS are generally observed in two spectral states: one with a high-luminosity soft thermal bump and a low-luminosity power law extending to several hundred keV (hereafter called the soft state) and the other at high luminosity in high energies (greater than 10 keV) showing a typical thermal Comptonization component (hereafter called the hard state).

It is now clear that the observed X-ray spectra resulting from the accretion of matter onto the central object are divided according to the connection between the two

effects: (1) the gravitational energy of matter is released in the disk because of the viscous dissipation between the adjacent layers (Shakura & Sunyaev 1973, hereafter SS73). The energy release occurs in the optically thick medium, and thus the disk emits a soft blackbody-like radiation (related to the effective disk area; SS73) of a fraction of keV and tens of eV for Galactic and extragalactic sources, respectively. (2) Another mechanism is related to the geometric compression of the matter accreting in advection-dominated manner, where the radial velocity is some fraction of the free-fall velocity, but the viscous heating can be essential in the flow too (e.g., Chakrabarti & Titarchuk 1995, hereafter CT95; Narayan & Yi 1994). Energy is mostly transferred by the protons because of their much higher mass. These protons afterward transfer their energy to the ambient electrons through Coulomb collisions in a relatively dense cloud (called the Compton cloud) close to the black hole. This cloud can be a result of the propagation (accretion) of the sub-Keplerian component toward the black hole. In such a type of accretion, shocks or centrifugal barrier regions can be formed (CT95).

Since the cross sections for radiative processes are inversely proportional to the mass of the emitter, it is the

<sup>1</sup> CEA/DSM/DAPNIA/SAp, CEA Saclay, 91191 Gif sur Yvette, France; fil@mir.saclay.cea.fr

<sup>2</sup> Laboratory for High Energy Astrophysics, NASA Goddard Space Flight Center, Greenbelt, MD 20771; titarchuk@heavx.gsfc.nasa.gov.

<sup>3</sup> George Mason University/Institute for Computational Sciences and Informatics, Fairfax, VA.

electrons that then radiatively cool the plasma. In such a high-temperature plasma, the main electron-cooling process is the Comptonization of the ambient soft photons. The plasma temperature of the zone emitting the hard radiation is regulated by the supply of soft photons from the disk.

It was demonstrated in CT95 that the hard-to-soft state transition in BHS is regulated by the redistribution of mass accretion rates between the quasi-spherical (sub-Keplerian) and Keplerian disk components. It was also shown there for the first time that the converging inflow spectral feature (as an intrinsic signature of a black hole) can be seen in the soft state. Namely, near the horizon the strong gravitational field is expected to dominate the pressure forces and thus to drive the accreting material in almost a free fall, i.e., a converging inflow (Titarchuk & Zannias 1998, hereafter TZ98). Unlike for other compact objects, the pressure forces are becoming dominant as their surface is approached, and thus such a free-falling state is absent. In contrast, CT95 emphasized that in the soft state the optically thick Compton cloud surrounding a black hole is cooled down by the disk soft photons, and the extended power law will be observed.

The fact of the presence of the geometrically thin disk in BHS leads to a very important statement regarding the dominance of gravitational forces over radiative forces: *because the gravitational force in the disk is a small H/R fraction of the gravitational force acting in the radial direction (where H and R are the disk height and radius, respectively), the local luminosity in the disk cannot be higher than H/R times the Eddington limit.* At some certain point the disk is disrupted or terminated, for example because of general relativistic effects: the stable orbits do not exist below 3 Schwarzschild radii. Then the matter is forced to proceed toward the black hole in almost free-fall manner, the radiative forces being negligible with respect to the gravitational forces. The next question then is to know how the soft disk photons illuminating the bulk inflow can be up-Comptonized to energies of the order of  $m_e c^2$ .

TZ98 show that the production of hard photons as a function of the radius from the black hole peaks at around 2 Schwarzschild radii ( $2r_s$ ), and most of the hard continuum photons observed are produced within  $3r_s$  from the black hole. Shrader & Titarchuk (1998, hereafter ShT98) demonstrate that the emergent spectra of the converging inflow atmosphere successfully explain the continuum X-ray spectra of BHS in their soft state.

To check these statements and predictions, we have simulated the emergent energy spectrum, treating as precisely as possible the Comptonization process. To do this, we need to know first the movement of the high-energy electrons: it is in fact a composition of the free-fall motion onto the black hole and of the Brownian (thermal) motion, which can be characterized by a temperature. Whereas the thermal Comptonization has been already explored in several ways (e.g., Sunyaev & Titarchuk 1980; Pozdnyakov, Sobol', & Sunyaev 1983, hereafter PSS; Nagirner & Poutanen 1994; Titarchuk 1994, hereafter T94; Titarchuk & Lyubarskij 1995; Hua & Titarchuk 1995; Giesler & Kirk 1997), the effects of the free-fall motion of the electrons on the resulting spectrum is not yet clearly understood. Also, the general relativistic effects close to the black hole were not yet plainly taken into account. In a series of papers, Titarchuk, Mastichiadis, & Kylafis (1996, 1997, hereafter TMK96 and TMK97, respectively) present the exact

numerical and approximate analytical solutions of the problem of spectral formation in a converging inflow, taking into account the inner boundary condition, dynamical effects of the free fall, and thermal motion of the electrons. The inner boundary has been taken at a *finite* radius, with the spherical surface being considered as a fully absorptive.

TMK have used a variant of the Fokker-Plank formalism, where the inner boundary mimics a black hole horizon; no relativistic effects (special or general) have been taken into account. Thus their results are instructively useful, but they are not directly comparable with the observations. *However, using these numerical and analytical techniques, they demonstrated that the extended power laws are present in the resulting spectra in addition to the blackbody-like emission at lower energies.*

Our approach is to determine a realistic emergent Comptonization spectrum using two different approaches: one, purely analytical, is described in detail in TZ98, and the other, numerical, is presented below. TZ98 analyzed the exact general relativistic integrodifferential equation of radiative transfer, describing the interaction of low-energy photons with a Maxwellian distribution of the relativistic electrons in the gravitational field of a Schwarzschild black hole. They proved that because of Comptonization, an initial arbitrary spectrum of low-energy photons unavoidably results in spectra characterized by an extended power-law feature. They examined the spectral index  $\alpha$  by using both analytical and numerical methods in the lower temperature limit ( $\Theta = kT_e/m_e c^2 \ll 1$ ), where  $T_e$  is the electron temperature and  $m_e c^2$  the electron rest mass energy, with a varying mass accretion rate. They demonstrated the stability of the ( $\alpha \sim 1.8$ ) power law, which is mainly due to the asymptotic independence of the spectral index on the mass accretion rate and its weak dependence on plasma temperatures in the lower temperature limit. In fact, all corrections to the index due the temperature effects are related to the corrections of the kernel of the relativistic kinetic equation (TZ98), which are of the order of the dimensionless temperature  $\Theta$ .

In this paper, we will describe the numerical approach, briefly outlining the main features of the Monte Carlo simulation code in § 2. We will present the results in the “flat” case in § 3, for which we assume the propagation of the photons in straight lines. We will show what we have obtained in the most realistic general relativistic case in § 4. In §§ 3 and 4, we will compare these results with the ones obtained by different (analytical and numerical) methods in the same physical framework (TMK97; TZ98). We will show that the observed spectral transitions in BHS is clearly to be related to the bulk flow temperature in § 5. We will demonstrate the relevance of the converging inflow model to the recent high-energy observations in § 6. Finally, we will summarize our work and draw conclusions in § 7.

## 2. THE MONTE CARLO SIMULATION

As was explained above, this signature originates from upscattering of low-energy photons by fast-moving electrons with velocities,  $v$ , approaching the speed of light,  $c$ . A soft photon of energy  $E$ , in the process of multiple scattering off the electrons, gets substantially blueshifted. For a single scattering, the photon scattered off an electron moving with velocity  $v$  changes its energy due to the Doppler effect as

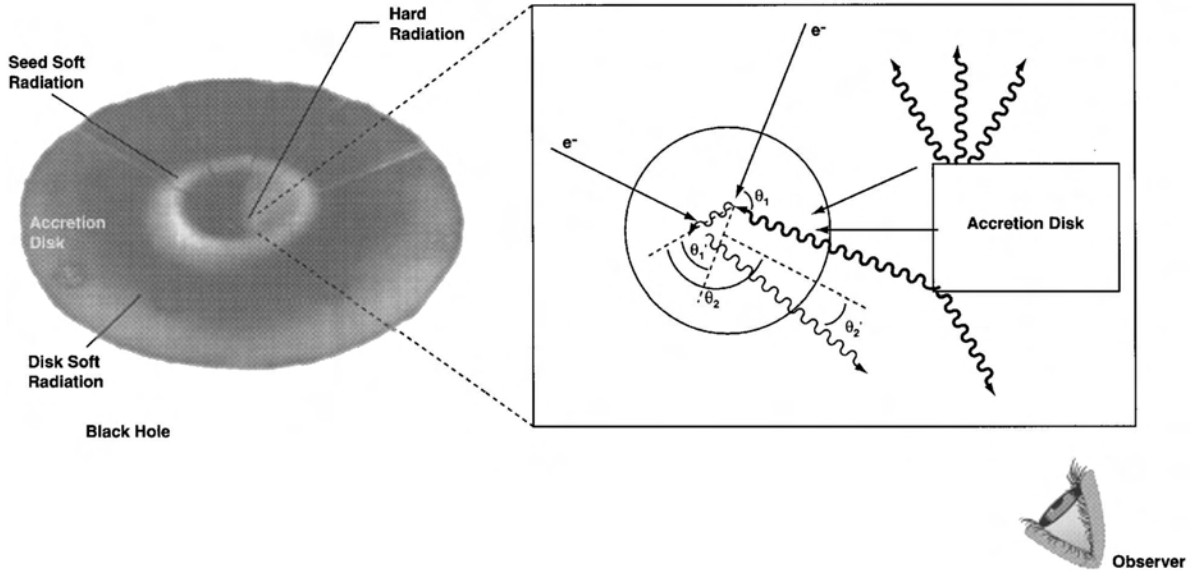


FIG. 1.—Left-hand panel is an artist's conception of an accretion disk surrounding a black hole. The approximate sites from which the soft-seed radiation is produced, the more general soft radiation that is directly viewed by the observer (thick solid line), and the hard-radiation emission (thin solid line) are indicated. Also, the dotted lines indicate the scale and location of the bulk-motion scattering site. The schematic diagram in right-hand panel depicts a typical sequence of scatterings within the bulk-motion inflow region. Some details are given in the text.

follows:

$$E' = E \frac{1 - (v/c) \cos \theta}{1 - (v/c) \cos \theta'}. \quad (1)$$

The photon is then significantly blueshifted if, at least, it gets scattered once in the direction of the electron motion (i.e., when  $\cos \theta' \approx 1$ ). This is schematically illustrated in Figure 1 for two scattering events. In the first event the soft photon is effectively up-Comptonized, and in the second one the photon is scattered in such a direction that it can be detected by an observer.

In the first scattering event, we assume the direction of incident photon,  $\theta_1$ , to be nearly normal to the electron velocity and the direction of the scattered photon to be nearly aligned with the electron velocity. During its outward propagation through the converging-inflow medium, the angle between the photon and electron velocity increases. Thus, in the second event the cosine angle,  $\cos \theta_2$ , tends to approach zero. The angle of the outgoing photon,  $\theta'_2$ , has to be large enough for the Doppler-boosted photon to reach an observer.

The geometry mostly used in these simulations is shown in Figure 2: it consists of a thin disk surrounding a spherical cloud harboring a black hole in its center. The disk is always supposed to be optically thick, whereas we are assuming a free fall for the background flow, where the bulk velocity of the infalling plasma is given by  $v(r) = c(r_s/r)^{1/2}$ .

In our simulations (see also the kinetic formalism in TZ98) we use the number density  $n$  measured in the local rest frame of the flow that is  $n = \dot{m}(r_s/r)^{1/2}/(2r\sigma_T)$ . Here  $\dot{m} = \dot{M}/\dot{M}_E$ ,  $\dot{M}$  is the mass accretion rate,  $\sigma_T$  is the Thomson cross section,  $\dot{M}_E \equiv L_E/c^2 = 4\pi GMm_p/\sigma_T c$  is the Eddington accretion rate, and  $M$  is the black hole mass. Then the optical thickness of the cloud is computed through the mass accretion rate  $\dot{m}$  according to the following formula:

$$\tau = \dot{m} \left( 1 - \sqrt{\frac{r_s}{r_{out}}} \right), \quad (2)$$

where  $r_{out}$  and  $r_s$  are the outer boundary and the Schwarzschild radii, respectively. In most of all results given below, except otherwise presented in § 4, the cloud radius  $r_{out}$  has been taken to be  $3r_s$ . The different values of  $\dot{m}$  that have been used in those simulations are  $\dot{m} = 0.5, 1, 1.5, 2, 4, 7$ .

We have varied the cloud electron temperature from 0 to 50 keV. In addition to the thermal motion of the electrons in the cloud, we have also taken into account their free fall onto the central black hole. The seed X-ray photons were generated uniformly and isotropically at the surface of the inner edge of the accretion border of the disk. For our simulations we use as an example the disk thermal spectrum with a temperature of 0.5 keV.

In the simulations we have followed the trajectory of each photon in the following way: first, we have made a random generation according to an exponential law,  $P(\tau) = e^{-\tau}$ , to get the value of the optical thickness  $T$  that a photon will travel before interacting. Second, we have integrated the optical thickness  $\tau = \rho\sigma l$  along the photon path up to  $T$ , taking into account the variation of the cloud density  $\rho$  and of the cross section  $\sigma$  with the radius. The gravitational shift endured by the photon was also computed at each step of this integration.

The photon paths are straight lines in what we called the "flat" case or curves in terms of the Schwarzschild geometry in the general relativistic case. In fact, the variation of the photon energy and of the photon position (with respect to the local normal) along the photon trajectory can be extracted from the full kinetic equation presented in TZ98 (eq. [12]). The characteristics of the differential part of the equation provides these dependencies.

If at the end of the integration, the photon has not left the cloud, we simulate a Compton scattering with an electron according to the method described in PSS, taking into account the exact motion of the electron, which is a composition of its free-fall motion onto the black hole with its Brownian thermal motion. To do this, we first compute the scattering-electron momentum and derive the scattered photon and electron characteristics from the Compton-

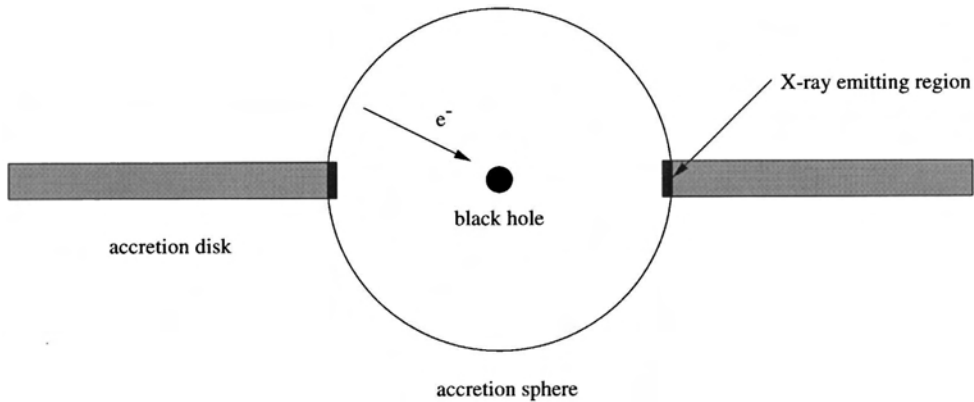


FIG. 2.—Scheme of the geometrical setup used in the Monte Carlo simulations. We vary the accretion sphere radius  $r_{\text{out}}$  from  $3r_s$  to  $20r_s$  in our simulations (see text).

scattering kinetics. We then check whether this event is consistent with the Compton scattering probabilities: if so, the event is kept; if not, another scattering electron is generated, and the process goes on until the event is accepted. This process has been successfully checked by comparing its results with the analytical ones of Hua & Titarchuk (1995) in the case of relativistic thermal electrons.

Once the new energy and direction of the photon have been determined by the Compton kinematics, we track it in the same way as above until it makes another scattering, escapes from the cloud, or until it is “absorbed” by the black hole at its horizon.

The parameters of the simulations are the Compton cloud electron temperature,  $T_e$ , the cloud outer radius,  $r_{\text{out}}$ , and the mass accretion rate,  $\dot{m}$ .

### 3. “FLAT” CASE

We have first investigated what could be the emergent spectrum in the “flat” case, which supposes that photons go in straight lines. But the relativistic effects such as gravitational redshift, dependence of the Klein-Nishina cross section on energy, or “absorption” of photons at the black hole horizon were correctly taken into account in these computations. Even if this case is not physically consistent, as we cannot separate in theory the gravitational redshift effects from the light bending, it is instructive, as it will enable us to derive the consequences of space curvature around the black hole on the emerging spectrum by comparing this case with the general relativistic one described below.

We have calculated the spectrum emerging from a plasma cloud of temperature 5 keV for  $\dot{m}$  equal to 2 with an outer radius  $r_{\text{out}} = 3r_s$ . They are typically the physical conditions of the soft state. As was foreseen theoretically (TMK96, TMK97), the spectrum observed at infinity consists of a soft component (blackbody-like) coming from input photons that escaped after a few scattering without any significant energy change and the high-energy part (a power law) extending to high energies of order 300 keV. The shape of spectrum is reminiscent of what is observed from BHS in their soft state (ShT98), and it is almost identical to the spectrum presented in TMK97 (Fig. 1).

We have then fitted the Monte Carlo spectra (see Fig. 5 below) with a test spectrum composed of two components: a Planckian spectrum with a fixed temperature of the soft

photons and convolution of some fraction of this component with the converging inflow upscattering Green’s function. The fit parameters were then the color temperature of the soft component, the normalization of the upscattering component relative to the soft one, and the spectral index of the power law. An example of this fit to the spectrum shown in Figure 5 below (which is a spectrum obtained in the general relativistic case, with  $kT_e = 20$  keV and  $\dot{m} = 4$ ) is given in Figure 3.

The fitting parameters are  $kT_c = 0.4$  keV, the fraction of the illumination of the bulk inflow atmosphere by the disk photons is  $f = 0.48$ , and the spectral index is  $\alpha = 1.5$ . It is worth noting that the fitting temperature  $kT_c = 0.4$  keV measured by an observer is less than the input temperature of the soft photons by 0.5 keV because of the gravitational redshift.

*However, it is clear that even in the low-temperature case the spectrum we obtained is too hard to account for what is observed from soft state BHS. Indeed, as it could be seen in*

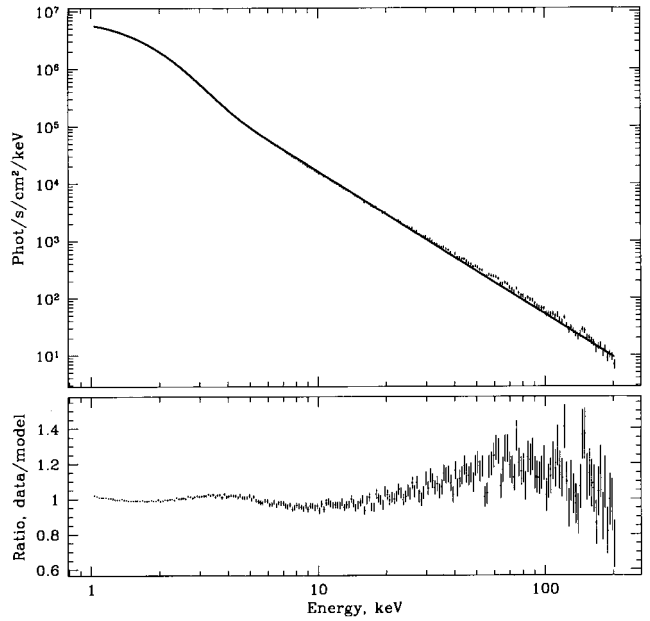


FIG. 3.—Monte Carlo photon spectrum (see below, Fig. 5) is fitted to the test (analytical) spectrum composed of two components, a Planckian spectrum with a fixed temperature of the soft photons and convolution of some fraction of this component with the CI upscattering Green’s function.

TABLE 1

SPECTRAL INDEX OF THE POWER-LAW TAIL, OBTAINED IN THE  
“FLAT” CASE

$kT_e$ (keV)	$\dot{m} = 0.5$	$\dot{m} = 1$	$\dot{m} = 1.5$	$\dot{m} = 2$	$\dot{m} = 4$	$\dot{m} = 7$
0 .....	2.4 <sup>a</sup>	1.6 <sup>a</sup>	0.9	0.8	0.9	1.2
5 .....	2.1 <sup>a</sup>	1.1	0.8	0.8	0.9	1.0
10.....	2.0 <sup>a</sup>	1.1	0.8	0.8	0.9	1.0
50.....	1.6	1.1	0.8	0.9	0.7	0.5

<sup>a</sup> The spectral index determination is less accurate for these values of parameters because the hard component of the spectrum is less pronounced in the fit region (10–50 keV).

*Table 1, the spectral index we found by fitting the computed spectrum in the “flat” case is around or harder than 1, which is harder than it has been observed in the soft state (around 1.5; see, e.g., Ebisawa, Titarchuk, & Chakrabarti 1996, hereafter ETC). It is worth noting that the spectral indices presented in Table 1 are very close to TMK97 results (see their Fig. 6) made with an assumption of a purely Newtonian geometry.*

So, as expected, the modeling we made in the “flat” case is not realistic. It has been shown, moreover, that it is possible to soften the emergent spectrum by taking into account general relativistic curvature effects (TZ98). We have verified this result by computing the Comptonized spectrum in a fully general relativistic case, taking into account the space curvature around the black hole horizon.

#### 4. THE GENERAL RELATIVISTIC CASE

For this case we have modified our simulation code to take into account the space curvature around the black hole horizon: instead of following the photon path along a straight line, we have computed at each step the exact curved trajectory of the photon. The other physical effects (Compton diffusion, redshift, electrons’ thermal and free-fall motion, etc.) have been computed in the same way as was described previously. This description is then now fully consistent with the general relativity theory. We can see in Figure 4 an example of the resulting emerging spectrum for  $kT_e = 5$  keV and  $\dot{m} = 2$ : as expected, this spectrum is softer than the one we obtained in the “flat” case (compare Tables 1 and 2; also see TMK97).

A summary of the results we calculated for different physical conditions is given in Table 2, where we have put the spectral index of the power law, while we fit our spectrum with a two-component test spectrum as described above. The relative error on the quoted value of the spectral index in Table 2 is always around  $\pm 5\%$ . We can notice from this table that, as was discussed in TZ98, the spectral index we found in the low  $kT_e$  regime is only slightly depen-

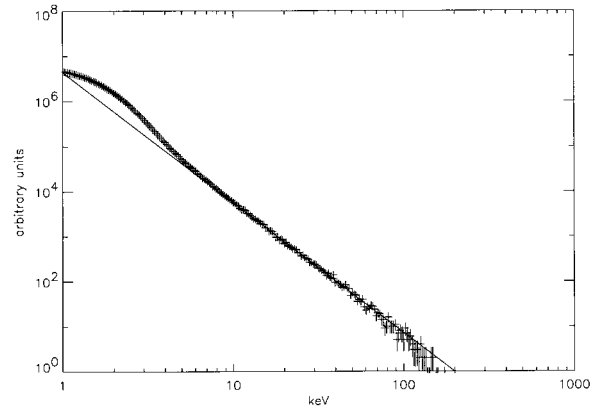


FIG. 4.—Emergent Comptonized photon spectrum in the general relativistic case: in this simulation, the cloud has a temperature of 5 keV and  $\dot{m}$  is equal to 2. The best power-law fit also shown has a photon number index of 2.9 (or the spectral index  $\alpha = 1.9$ ).

dent of the mass accretion rate  $\dot{m}$  provided that  $\dot{m}$  is larger than 1.

Finally, we can see in Table 2 that the index of the computed spectra in the soft state are now between 1.5 and 2.0, which is closest to the observations.

It is worth noting here that the observed power-law index of the narrow-line Seyfert 1 galaxy population, which may represent the extragalactic analog of the BHS in the high-soft state, is around 1.8. This is close to what we have obtained in the low  $kT_e$  regime, as it is expected from Comptonization on electrons whose motion is dominated by the bulk free fall.

As is seen from Figures 4 and 5, the power-law part of the spectrum occurs at energies  $E$ , lower than that of the exponential cutoff,  $E_e$  (where  $E_e$  is the average electron energy).

TZ98 have exactly solved the radiative transfer equations in the Doppler regime (when the photon energy is less than the energy of the electrons) in the same fully relativistic framework than the one we present here. Namely, they demonstrated that the Green’s function is a broken power law, and they calculated exactly the high-energy power index in the low-temperature limit, for  $\Theta \ll 1$ .

We have compared our results with the results of TZ98 obtained for the low-temperature limit for three different geometries of the Monte Carlo simulation. The geometries used are the following: (1) a  $3r_s$  sphere with a monochromatic soft X-ray source ( $E_p = 0.5$  keV) placed at the edge of the accretion disk, as shown in Figure 2; (2) the same as above but with a sphere radius of  $20r_s$ ; (3) a  $20r_s$  Comptonization cloud, with the source of 0.5 keV X-ray photons placed inside in a ring at  $5r_s$ .

First, we found only small differences in the spectral indices for all three cases, i.e., differences that are all within the error range of the spectral index determination, around 0.1 for  $\dot{m}$  greater than 2–3. Second, we found the mean spectral-index value is exactly 1.8, in agreement with TZ98. We also note from this comparison that, as it is theoretically expected, the power-law part of the spectra is almost independent of the soft photon distribution. In other words, it is independent of the illumination of the bulk-motion site by the accretion disk flow.

In Figure 5 we give the result of our computations for  $kT_e = 20$  keV and  $\dot{m} = 4$ , which reproduces the main features of the spectra observed in the high state of BHS: a

TABLE 2

SPECTRAL INDEX OF THE POWER-LAW TAIL, OBTAINED IN THE  
GENERAL RELATIVISTIC CASE

$kT_e$ (keV)	$\dot{m} = 0.5$	$\dot{m} = 1$	$\dot{m} = 1.5$	$\dot{m} = 2$	$\dot{m} = 4$	$\dot{m} = 7$
0 .....	2.8	2.3	2.1	2.05	2.0	1.9
5 .....	2.8	2.2	2.0	1.9	1.8	1.8
10.....	2.8	2.1	1.9	1.9	1.7	1.7
50.....	1.8	1.4	1.2	1.0	0.9	0.7

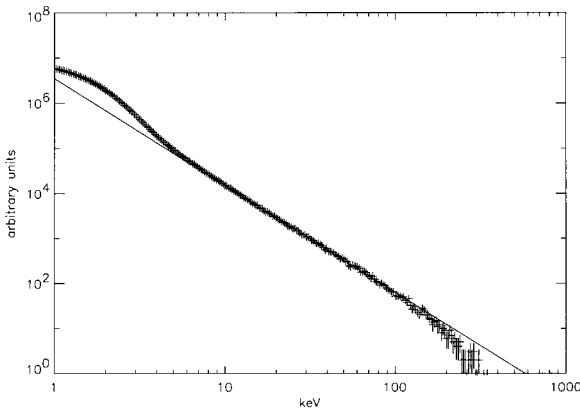


FIG. 5.—Emergent Comptonized photon spectrum in the general relativistic case: the physical conditions of the cloud are now  $kT_e = 20$  keV and  $\dot{m} = 4$ . The best power-law fit also shown has a photon number index of 2.5 (or a spectral index  $\alpha = 1.5$ ).

spectral index of 1.5 and an high-energy cutoff around 500 keV. The effect of the thermal motion for temperatures higher than 10 keV is clearly seen. The spectrum is getting harder, i.e., the index decreases, and the high-energy cutoff increases.

Furthermore, the spectra obtained at high  $kT_e$  and  $\dot{m}$  greater than 2 have a spectral index around 0.8, which is what is observed from BHS in the hard state, where the thermal Comptonization is thought to dominate (ETC).

This is also shown in Figure 6, where we present the results of the computation for  $kT_e = 50$  keV and  $\dot{m} = 4$  compared with the analytical solution of Hua & Titarchuk (1995; eq. [6]) derived for the pure thermal Comptonization case. The spectrum is practically identical to the standard thermal Comptonization spectrum. In this case, the effect of the bulk motion can be seen only at high energies, where there is an excess in the converging inflow spectrum due to coupling of the thermal and bulk-motion velocities. It is worth noting here that this excess is really detected in the observation of the hard state of the Cygnus X-1 source (e.g., Ling et al. 1997; see also for details the model of Skibo & Dermer 1995).

So the change of spectral shapes from the soft X-ray state to the hard X-ray state is clearly to be related to the temperature of the bulk flow. In other words, the effect of the

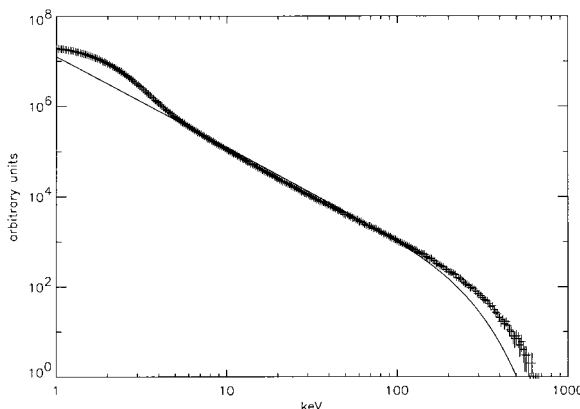


FIG. 6.—Emergent Comptonized photon spectrum in the general relativistic case with  $kT_e = 50$  keV and  $\dot{m} = 2$ . The high-energy part of the spectrum is compared with the thermal Comptonization spectrum (Hua & Titarchuk 1995, eq. [6]).

bulk Comptonization, compared with the thermal effect, is getting stronger when the plasma temperature drops below 10 keV. Also, as it could be seen by comparing the results in the “flat” and general relativistic cases, the spectral index of the Comptonized spectrum is very dependent of space curvature effects, so its observation should be a very powerful tool to determine the nature of the central object.

##### 5. SPECTRAL STATE TRANSITION AND TEMPERATURE OF THE CONVERGING INFLOW ATMOSPHERE

To complete the discussion of the Monte Carlo simulations and their application to the observed spectra of BHC systems, we present some details of the thermal balance treatment of the bulk-motion atmosphere (see CT95; Titarchuk, Lapidus, & Muslimov 1998).

The total count rate from the source increases with an increasing accretion rate. The X-ray spectrum becomes softer because of the increase of the supply of soft photons from the disk illuminating the advection-dominated region (shocks, centrifugal barrier), where the energy release is due to geometrical compression of the non-Keplerian accreting matter. This region, the so-called Compton cloud, is the source of hard X-ray radiations that are produced as a result of the upscattering of the soft photons emitted from the disk. In the final stage of the accretion (this is within a few Schwarzschild radii), the matter goes toward the black hole almost free falling, as the radiation pressure cannot stop matter falling in.

The Compton cloud (CC) region can be treated as a potential wall at which the accreting matter releases its gravitational energy. *This occurs in an optically thin region where the column density is of order of a few grams or where the Thomson optical thickness  $\tau_0 \sim$  a few.* The amount of energy released per second is a fraction of the Eddington luminosity, since the CC region is located in the very vicinity of a central object [ $\sim (3-6)r_s$ ]. The heating of a gas due to the gravitational energy release should be balanced by the photon emission. For high gas temperatures, Comptonization is the main cooling channel, and the heating of electrons is due to their Coulomb collisions with protons. Under such physical conditions the energy balance can be written as (see e.g., Zeldovich & Shakura 1969, hereafter ZS69, eq. [1.3])

$$F/\tau_0 = C_0 \times \varphi(\alpha)\epsilon(\tau)T_e/f(T_e). \quad (3)$$

Here  $\tau$  is the current Thomson optical depth in the emission region (e.g., in a slab),  $\alpha$  is the energy spectral index for a power-law component of the Comptonization spectrum,  $\epsilon(\tau)$  is a distribution function for the radiative energy density,  $f(T_e) = 1 + 2.5(kT_e/m_e c^2)$ ,  $T_e$  is the plasma temperature in K,  $C_0 = 20.2 \text{ cm s}^{-1} \text{ K}^{-1}$  is a dimensional constant, and, finally,  $\varphi(\alpha) = 0.75\alpha(1 + \alpha/3)$  if  $\varphi(\alpha) \leq 1$ , otherwise  $\varphi(\alpha) = 1$ . The latter formula is obtained by using the relationship between the zero- and first-order moments (with respect to energy) of the Comptonized radiation field (Sunyaev & Titarchuk 1985, § 7.3, eq. [30]). The distribution of the radiative energy density in the emission region  $\epsilon(\tau)$  can be obtained from the solution of the diffusion equation (see ZS69, eq. [1.4]),

$$\frac{1}{3} \frac{d^2\epsilon}{d\tau^2} = - \frac{(F/c)}{\tau_0}, \quad (4)$$

subject to the two appropriate boundary conditions.

The first boundary condition must imply that there is no scattered radiation from the outer side of the emission region, i.e.,

$$\frac{d\epsilon}{d\tau} - \frac{3}{2}\epsilon = 0, \quad \text{for } \tau = 0. \quad (5)$$

In our case, this condition holds at the inner surface of a slab facing a central object (black hole).

The second boundary condition requires that at the outer surface of a slab the incoming flux should be equal to the net flux  $F_{\text{net}}$ ,

$$\frac{1}{3} \frac{d\epsilon}{d\tau} = \frac{F_{\text{net}}}{c}, \quad \text{at } \tau = \tau_0. \quad (6)$$

The solution of equations (4)–(6) provides us with the distribution function for the energy density,

$$\epsilon(\tau) = \frac{F + F_{\text{net}}}{c} \left\{ 2 + 3\tau_0 [\tau/\tau_0 - 0.5(\tau/\tau_0)^2 F/(F + F_{\text{net}})] \right\}. \quad (7)$$

Thus, from equations (3) and (7) we get

$$\frac{\varphi(\alpha) T_e \tau_0}{f(T_e)} \lesssim 0.75 \left( 10^9 \frac{F}{F + F_{\text{net}}} \right) \text{ K}. \quad (8)$$

In the hard state, the net flux from the outer boundary is negative. The flux from the disk is negligible with respect to  $F$  and the photons only escape through the outer boundary, so  $F_{\text{net}} = -F/2$ . But in the hard state of NSS, this outgoing flux ( $-F/2$ ) is balanced by the soft photon flux coming from the neutron star surface to the slab, so  $F_{\text{net}} = 0$ . Now it is evident from equation (8) that for the same free path of energy release  $\tau_0$ , the temperature of the emission region for the hard state of BHS is 2 times higher than that of NSS. Recent RXTE observations of the hard state of NSS in the Terzan 2 globular cluster support Barret et al. 1999; Guainazzi et al. 1999 this estimate.

It is also worth noting that the product  $T_e \tau_0 / f(T_e)$  (and hence  $\alpha$  as function of this product) is insensitive to the total luminosity of the emission region  $F$  (Roques et al. 1994). The observed value of spectral index  $\alpha \lesssim 1$  (which is characteristic of the hard state of BHS and NSS) is consistent with equation (8).

When the net flux  $F_{\text{net}}$  becomes positive and comparable with the internal energy release,  $F$ , the cooling becomes more efficient not only due to Comptonization but also to free-free cooling, and therefore the electron temperature unavoidably decreases,  $T_e \ll 10^9 \times F/(F + F_{\text{net}})$  K (see CT95 for the numerical calculations of spectral indices and temperature).

This illumination effect can explain the hard-soft transition when the temperature of the Compton cloud drops substantially with the increase of the soft photon flux from the disk. As it is seen above (eq. [8]), the temperature drops from 50–60 keV in the hard state (i.e., when  $F_{\text{net}} \ll F$ ) to 5–10 keV in soft state (when  $F_{\text{net}}$  and  $F$  are comparable). For this particular range of temperatures the Monte Carlo simulations have been done in this paper.

## 6. THE RELEVANCE OF BULK-MOTION COMPTONIZATION MODEL TO THE RECENT HIGH-ENERGY OBSERVATIONS

ShT98 have already shown that the spectral shape of Compton scattered photons in converging flow is very close

to the observed spectra. However, it is still necessary to show how many photons *escape* from the central region when a given number of photons are injected in the Monte Carlo simulations. For example, in the case of  $kT_e = 20$  keV and  $\dot{m} = 4$  (see Fig. 5), among  $10^5$  generated photons there are 15,372 photons, or 15.4%, escaping without interacting, 45,557 photons, or 45.6%, going through the black hole horizon, 13,393 photons, or 13.4%, scattered in the accretion disk (but not in the converging Compton cloud), the inner radius temperature of which equals 0.5 keV, and 25,678 photons, or 25.7%, scattered in the Compton cloud (some of these photons being also scattered in the disk). Thus almost the same photon flux (for our particular geometry see Fig. 2), 28.8% (15.4% + 13.4%), goes directly to observer, and 25.6% after scattering in the converging Compton cloud. But a smaller flux of the detected photons emerges after multiple scattering, and they form the hard tail of the resulting spectrum (Fig. 5). We remind the reader (for details see Sunyaev & Titarchuk 1980; T94; TMK97) that the photons undergoing multiple scatterings produce the specific space distribution (in accordance to the first space eigenfunction, see TZ98, Fig. 3), and that fraction of photons undergoing multiple scattering in the plasma cloud,  $f_{\text{ms}}$ , is related to the expansion coefficient of the space source distribution over the first space eigenfunction. In the simplest case, the uniform source distribution  $f_{\text{ms}}$  is approximately 0.8. But in our case, when the source photon distribution is produced by an external illumination of the converging inflow (CI) region by the soft disk photons, and the optical depth of the converging region is of order of 1 ( $\tau \sim \dot{m}[1.5^{-1/2} - 3^{-1/2}] \approx 1$ ), this fraction is slightly less. Here for the optical depth estimate we use formula (2) with an assumption that  $r_{\text{out}} = 3r_s$  and  $r_{\text{in}} = 1.5r_s$  are of a photon-bending radius (TZ98).

Thus the fraction of photons undergoing multiple scattering and detected by the observer, with respect those photons undergoing a few scattering and detected or coming directly to the observer from the disk, is estimated as

$$f \lesssim \frac{0.26 \times 0.8}{0.26 \times 0.2 + 0.29} = 0.6. \quad (9)$$

The exact number of these photons can be determined through the fitting of the simulated resulting spectrum to the test spectrum composed of two components, a Planckian spectrum with a fixed temperature of the soft photons and convolution of some fraction  $f$  of this component with the CI-upscattering Green's function. It is easy to prove (using the property of the Green's function to conserve the number of the scattering photons) that  $f$  is exactly the fraction of photons (with respect to the thermal component) multiply scattered in the converging inflow. As was shown in § 3,  $f = 0.48$  (for our case), and the flux of the escaping hard photons is large enough to explain the observations. We remind the reader that the empirically determined fractions are 0.32 and 0.72 for GRO J1655–40 and GRS 1915+105, respectively (ShT98), and *thus Comptonization by the converging inflow is consistent with the observations*.

It is worth noting that the number of the photons forming the very hard tail (for energies  $E \gg kT_c$ ),

$$N_{\text{hard}}(E) = \int_E^\infty I(E_0) \frac{dE_0}{E_0}, \quad (10)$$

is much less than the number of photons in the thermal component  $N_{\text{th}}$ , i.e.,

$$\frac{N_{\text{hard}}(E)}{N_{\text{th}}} < f(E/2kT_c)^{-\alpha} \ll 1. \quad (11)$$

For example, this ratio is about  $8 \times 10^{-2}$  for  $E = 10$  keV in the cases of GRO J1655–40 and GRS 1915+105. In other words, only 8% of the photons seen as coming from the disk are effectively scattered off electrons within a few Schwarzschild radii  $[(2-3)r_s]$  and form the extended power law tail of the spectrum. Inequality (11) can be readily proved using a formula for the hard-tail energy flux  $I(E)$  (eq. [10]) presented in the convolution form (see ShT98, eq. [2]).

In the end of this section we discuss a issue related with the illumination of the CI atmosphere by the disk photons. First, we assume that the disk emitting isotropically is extended from the inner radius  $r_{\text{in}}$  to the outer radius  $r_{\text{out}}$ , and the outer radius of the CI atmosphere is  $r_{\text{sp}}$ . Second, we assume that  $r_{\text{sp}} \leq r_{\text{in}}$ .

In fact, the disk flux intercepted by the CI atmosphere with radius  $r_{\text{sp}}$  (see Fig. 2) is calculated through the integral

$$F_{\text{int}} = \pi \int_{r_{\text{in}}}^{r_{\text{out}}} r dr \int_{-\pi/2}^{\pi/2} \cos \varphi d\varphi \int_{\mu_*}^1 (1 - \mu^2)^{1/2} d\mu, \quad (12)$$

where  $\mu_* = \sqrt{1 - (r_{\text{sp}}/r)^2}$ . In the case when the disk illuminates the slab (with half-width  $\Delta r = r_{\text{in}} = 3r_s$  and half-height  $H$ ) situated in the center,  $\mu_* = (r - r_{\text{in}})/\sqrt{(r - r_{\text{in}})^2 + H^2}$ .

The two internal integrals of equation (12) are calculated analytically. The first is equal to 2, and the second is  $\theta_* - 0.5 \sin 2\theta_*$ , where  $\theta_* = \arccos \mu_*$ . Even the triple integral of equation (12) can be estimated analytically with an accuracy of better than 10% for the spherical case with the aforementioned assumption that  $r_{\text{sp}} \leq r_{\text{in}}$ :

$$F_{\text{int}} = \frac{2\pi}{3} r_{\text{sp}}^3 (r_{\text{in}}^{-1} - r_{\text{out}}^{-1}). \quad (13)$$

In the case where the part of the disk is covered by the CI atmosphere the flux,  $F_{\text{int}}$  is calculated by integration from  $r_{\text{sp}}$  to  $r_{\text{out}}$ , followed by adding  $\pi^2(r_{\text{sp}}^2 - r_{\text{in}}^2)$ , the disk flux emitted inside the atmosphere.

The fraction of the disk photons illuminating the CI atmosphere is

$$f_{\text{ill}} = \frac{F_{\text{int}} p_{\text{sc}}}{\pi^2(r_{\text{out}}^2 - r_{\text{in}}^2)}, \quad (14)$$

where  $p_{\text{sc}}$  is a probability of scattering of the disk photons in the CI atmosphere, which is of order  $1 - e^{-\tau}$ .

The factor  $f$ , used in the spectral fitting, can be estimated from here:

$$f \sim \frac{f_{\text{ill}} f_{\text{ms}} A}{(1 - f_{\text{ms}}) f_{\text{ill}} A + \mu(1 - f_{\text{ill}})}, \quad (15)$$

where  $\mu$  is the cosine of inclination angle of the disk and  $A$  is a spherical albedo of the CI atmosphere.

The quantity  $A$  can be estimated as follows (e.g., Sobolev 1975):

$$A = 1 - \frac{1}{3\tau/4 + 1}. \quad (16)$$

This formula is obtained in the Eddington approximation with an assumption of isotropic scattering at any event and the pure absorptive inner boundary. Despite the Eddington approximation the albedo, formula (16) provides an accuracy of order 10% for any optical depth. For optical depth 1,  $A = 0.42$ , which is slightly higher than the value obtained in our Monte Carlo simulations,  $A_{\text{MC}} = 25.7/(25.7 + 45.6) = 0.36$  (see above), because of the photon bending.

Now we present the numerical estimates of the factor  $f$  for two different cases. The first one related with our Monte Carlo simulations when  $p_{\text{sc}} \sim 1 - e^{-1} = 0.63$ ,  $f_{\text{ms}} = 0.8$ ,  $A = 0.42$ , and we assume that  $\mu \sim 1$ . Then we get  $f \sim 0.5$ , which is very close to what we get from the spectral fitting of the Monte Carlo simulated spectrum. It is worth noting here that in the limit of the high optical depth (or mass accretion rate),  $f \sim f_{\text{ms}}/(1 - f_{\text{ms}})$  because  $p_{\text{sc}}, f_{\text{ill}}$ , and  $A$  converge to one. Thus, in this particular case, the factor  $f$  can be of order of one or more.

For another case we assume that the soft radiation comes from the extended disk with the inner radius  $r_{\text{in}} = 3r_s$  and  $r_{\text{out}} = 11r_s$ , which is the size of the disk emission region related to the color temperature of 0.85 keV (for details of this model, see Borozdin et al. 1998) and the inclination direction cosine  $\mu = 0.5$ . Also, we use the above values of  $p_{\text{sc}} \sim 0.63$ ,  $f_{\text{ms}} \sim 0.8$ , and  $A \sim 0.42$ . Using equations (12) and (14)–(15), we obtain  $f = 0.68 \times 10^{-2}$  if we consider that the illumination of the sphere is situated in the center with  $r_{\text{sp}} = 3r_s$ . The factor  $f$  is  $1.7 \times 10^{-2}$  in the case of the illumination of the slab with the half-height,  $H = 3r_s$ .

To conclude this section, we emphasize once again that the Comptonizing region must overlap with the inner region of the disk in order to get the high fraction of the seed photons from the disk (see ShT98). But on the other hand, the high fraction,  $f$  (of order 10% and higher), can be also obtained if the innermost region of the disk is puffed up to heights of order of  $3r_s$  and the disk is almost seen at edge-on. More details of this discussion and comparison with the RXTE observations would be presented in our upcoming paper (Borozdin et al. 1998).

## 7. CONCLUSIONS

We show that spectra in the soft and hard states are formed by upscattering of the disk soft photons by the matter (electrons) moving in the strong gravitational field.

The presence of the event horizon, as well as the behavior of the null geodesics in its vicinity, largely determine the dependence of the spectral index on the flow parameters. The efficiency of gravitational-to-radiative energy conversion is of order 5% or less in the disk around black hole (e.g., SS73; Narayan, Barret, & McClintock 1997). Thus it is natural to expect that radiation pressure cannot hold back the matter that is almost in free fall. But the shape of the spectrum (the spectral index and the position of the high-energy cutoff) depends on the temperature of the bulk-motion atmosphere, which is determined by the efficiency of the cooling of the atmosphere by the flux coming from the disk (see § 5; CT95; Titarchuk et al. 1998). In the hard state most gravitational energy is released out of the disk (see possible scenarios in CT95), and the bulk-motion zone is getting very hot (because there are not enough cooling agents [soft disk photons] to cool down the environment). The plasma temperature is of the order of 50 keV.

In this case, the contribution of the outer part of the bulk-motion atmosphere in the resulting spectrum is signifi-

cant because of the large volume of this region and the high thermal velocities. In fact, the hard photons are produced mainly by effective scatterings of the disk soft photons on electrons at angles near  $\pi$  (Hua & Titarchuk 1995, Fig. 2). But in the outer layer the gravitational bending and redshift are less pronounced, and thus the effect of general relativity on the spectral index is smaller for larger values of electron temperature, as is shown in Table 2. Indeed, the spectrum is practically identical to the standard thermal Comptonization spectrum (see Fig. 6).

When the mass accretion rate in the disk increases, the plasma temperature goes down to such a level (of order 10 keV or less) that only the free-falling electrons transfer their momentum to the soft photons, producing the power-law component extending to energies comparable with the kinetic energy of electrons in the converging inflow, i.e., of order  $m_e c^2$ . In this case, the spectrum observed at infinity consists of a soft component produced by those input photons that escape after a few scattering without any significant energy change and a hard component (described by a power law at the energies much higher than the characteristic energy of the disk soft photons) produced by the photons that undergo significant upscattering.

The luminosity of the power-law component is relatively small compared with that of the soft component. The power law is quite steep because of the strong photon bending and the gravitational redshift near the black hole (within 1.5–2 Schwarzschild radii). We demonstrate through our Monte Carlo simulations how many photons escape from the central region when a given number of photons are injected in the Monte Carlo simulations, and that fraction is perfectly consistent with the recent high-energy observations (ShT98).

We also show that our Monte Carlo spectra are fitted quite well by the analytical bulk-motion Comptonization model (BMC), which allows one to use this model for the fitting of the real observational data. The analytical model BMC contains only three parameters. Two of them are the color temperature of the seed photons  $T_c$  and the relative weight of the soft component in the entire spectrum,  $1/1 + f$ , which are the main characteristics of the soft component. Thus it is getting possible to determine the color-temperature dependence on the energy flux in the soft-

energy band. The disk origin of the soft seed photons can be confirmed or refuted by this dependence (see details in Borozdin et al. 1998).

We demonstrate using our Monte Carlo simulation that the main features of the simulated spectra (a spectral index of 1.5 and a high-energy cutoff around 500 keV) are consistent with the observed X-ray spectra in the high state of BHS (e.g., Grove et al. 1998). The predicted high-energy cutoff (assuming a relativistic Maxwellian electron distribution) is in the energy range between 200 and 400 keV (see Figs. 4–5). It is slightly less than that observed in the superluminal source GRO J1655 by OSSE (Grove et al. 1998, Table 2 and Fig. 2). It is worth noting that the break energy is quite sensitive to the electron distribution. In future work, we will show that the observed spectrum (including the position of the high-energy break) can indeed be accounted for by the converging model's quantitatively using other electron distributions. In fact, we plan to investigate the possibility of nonthermal tails to the electron distribution in accreting systems and the expected radiation signatures in the hard X-ray band.

*Thus our results of the Monte Carlo simulations strongly support the idea that the bulk-motion Comptonization might be responsible for the extended power-law spectra seen in the black hole X-ray sources in their soft state. The hard-soft states transition is regulated by the plasma temperature of the converging inflow into a black hole.*

*On the other hand, during the soft states of neutron star systems, when the mass accretion rate is close to the Eddington limit, the bulk-motion infall is not present. Indeed, the radiation pressure caused by such a mass accretion rate prevents the flow from free-falling toward the neutron star surface.*

L. T. would like to acknowledge support from NASA grant NAG 5-4965, C. Shrader, W. Cui, and J. Swank for encouragement and discussion, and M. Revnivtsev and K. Borozdin for help to fit the Monte Carlo spectra to XSPEC analytical models. P. L. and L. T. would also like to acknowledge P. Goldoni for discussion and J. Paul for support of this work. Particularly, we thank the anonymous referee for interesting questions and helpful suggestions that significantly improved the paper's presentation.

#### REFERENCES

- Barret, D., Grindlay, J. M., Harrus, I. M., & Olive, J. F. 1999, A&A, in press
- Borozdin, K. I., et al. 1998, in preparation
- Chakrabarti, S. K., & Titarchuk, L. G. 1995, ApJ, 455, 623 (CT95)
- Ebisawa, K., Titarchuk, L., & Chakrabarti, S. K. 1996, PASJ, 48, 59 (ETC)
- Giesler, U., & Kirk, J. 1997, A&A, 323, 259
- Grove, J. E., Johnson, W. N., Kroeger, R. A., McNaron-Brown, K., & Skibo, J. G. 1998, ApJ, 500, 899
- Guainazzi, M., Parmar, A. N., Segreto, A., Stella, L., Dal Fiume, D., & Oosterbroek, T. 1999, A&A, in press
- Hua, X. M., & Titarchuk, L. 1995, ApJ, 449, 188
- Liang, E., & Narayan, R. 1997, in AIP Conf. Proc. 410, Proc. Fourth Compton Symp., ed. C. D. Dermer, M. S. Strickman, & J. D. Kurfess (New York: AIP), 461
- Ling, J. C., et al. 1997, ApJ, 484, 375
- Nagirner, D. I., & Poutanen, Yu. J. 1994, Astrophys. Space Phys. Rev., 9, 1
- Narayan, R., Barret, D., & McClintock, J. E. 1997, ApJ, 478, 448
- Narayan, R., & Yi, I. 1994, ApJ, 428, L13
- Podnyakov, L. A., Sobol', I. M., & Sunyaev, R. A. 1983, Space Sci. Rev., 2, 189 (PSS)
- Roques, J. P., et al. 1994, ApJS, 92, 491
- Shakura, N. I., & Sunyaev, R. A. 1973, A&A, 24, 337 (SS73)
- Shrader, C., & Titarchuk, L. G. 1998, ApJ, 499, L31 (ShT98)
- Skibo, J. G., & Dermer, C. D. 1995, ApJ, 455, L25
- Sobolev, V. V. 1975, Light Scattering in Atmospheres (Oxford: Pergamon)
- Sunyaev, R. A., & Titarchuk, L. G. 1980, A&A, 86, 121
- \_\_\_\_\_. 1985, A&A, 143, 374
- Titarchuk, L. G. 1994, ApJ, 434, 570
- \_\_\_\_\_. 1996, in Proc. Second Integral Symp., ed. C. Winkler, T. J.-L. Courvoisier, & Ph. Durouchoux (ESA-SP 382) (Paris: ESA), 163
- \_\_\_\_\_. 1997, in AIP Conf. Proc. 410, Proc. Fourth Compton Symp., ed. C. D. Dermer, M. S. Strickman, & J. D. Kurfess (New York: AIP), 477
- Titarchuk, L. G., Lapidus, I. I., & Muslimov, A. 1998, ApJ, 499, 315
- Titarchuk, L. G., & Lyubarskij, Yu. E. 1995, ApJ, 450, 876
- Titarchuk, L. G., Mastichiadis, A., & Kylafis, N. D. 1996, A&AS, 120, C171 (TMK96)
- \_\_\_\_\_. 1997, ApJ, 487, 834 (TMK97)
- Titarchuk, L. G., & Zannias, T. 1998, ApJ, 493, 863 (TZ98)
- Zeldovich, Ya. B., & Shakura, N. I. 1969, AZh, 46, 225 (English transl. in Soviet Astron. 13, 175) (ZS69)
- Zhang, S. N., Mirabel, I. F., Harmon, B. A., Kroeger, R. A., Rodriguez, L. F., Hjellming, R. M., & Rupen, M. P. 1997, in AIP Conf. Proc. 410, Proc. Fourth Compton Symp., ed. C. D. Dermer, M. S. Strickman, & J. D. Kurfess (New York: AIP), 141



## TIMING AND SPECTRAL PROPERTIES OF X-RAY EMISSION FROM THE CONVERGING FLOWS ONTO A BLACK HOLE: MONTE CARLO SIMULATIONS

PHILIPPE LAURENT<sup>1</sup> AND LEV TITARCHUK<sup>1,2,3</sup>

Received 2001 August 27; accepted 2001 October 11; published 2001 October 26

### ABSTRACT

We demonstrate that an X-ray spectrum of a converging inflow (CI) onto a black hole is the sum of a thermal (disk) component and the convolution of some fraction of this component with the Comptonization spread (Green's) function. The latter component is seen as an extended power law at energies much higher than the characteristic energy of the soft photons. We show that the high-energy photon production (source function) in the CI atmosphere is distributed with the characteristic maximum at about the photon bending radius,  $1.5r_s$ , independently of the seed (soft) photon distribution. We show that high-frequency oscillations of the soft photon source in this region leads to the oscillations of the high-energy part of the spectrum but not of the thermal component. The high-frequency oscillations of the inner region are not significant in the thermal component of the spectrum. We further demonstrate that Doppler and recoil effects (which are responsible for the formation of the CI spectrum) are related to the hard (positive) and soft (negative) time lags between the soft and hard photon energy channels, respectively.

*Subject headings:* accretion, accretion disks — black hole physics — radiation mechanisms: nonthermal — X-rays: general

### 1. INTRODUCTION

Accreting stellar mass black holes (BHs) in Galactic binaries exhibit so-called high-soft and low-hard spectral states (e.g., Borozdin et al. 1999, hereafter BOR99). An increase in the soft blackbody luminosity component leads to the appearance of an extended power law. An important observational fact is that this effect is seen as a persistent phenomenon only in BH candidates, and thus it is apparently a *unique* BH signature. Although in neutron star systems similar power-law components are detected in the intermediate stages (Strickman & Barret 1999; Iaria et al. 2001; Di Salvo et al. 2000), they are of a transient nature, disappearing with increasing luminosity (Di Salvo et al. 2000).

It thus seems a reasonable assumption that the unique spectral signature of the soft state of BH binaries is directly tied to the BH event horizon. This is the primary motivation for the bulk motion Comptonization model introduced in several previous papers and recently applied with striking success to a substantial body of observational data (Shrader & Titarchuk 1998; BOR99; Titarchuk & Shrader 2001, hereafter TS01). A complete theory of BH accretion must, however, be also able to accommodate in a natural manner a growing number of observational traits exhibited in the temporal domain. For example, it is now well established that BH X-ray binaries exhibit quasi-periodic oscillation (QPO) phenomena in three frequency domains:  $\sim 0.1$ ,  $\sim 1\text{--}10$ , and  $\sim 10^2$  Hz. The  $\sim 10^2$  Hz QPOs seem to occur during periods of flaring and when the spectra (although in the high-soft state) tend to be relatively hard, i.e., the relative importance of the power-law component with respect to the thermal. Furthermore, the QPO amplitudes increase with energy; that is, there is a higher degree of modulation of the signal in the hard power law than in the thermal excess

component. In addition to the QPO phenomena, it has been noted by Nowak et al. (2001; also see Cui, Zhang, & Chen 2000) that measures of the coherence between the intensity variations in the hard power law and thermal components is negligible.

We argue that the BH X-ray spectrum in the high-soft state is formed in the relatively cold accretion flow with a sub-relativistic bulk velocity  $v_{\text{bulk}} \leq c$  and with a temperature of a few keV and less ( $v_{\text{th}} \ll c$ ). In such a flow, the effect of the bulk Comptonization is much stronger than the effect of the thermal Comptonization, which is a second order with respect to  $v_{\text{th}}/c$ . In this Letter, we present results of Monte Carlo simulations probing the spatial, spectral timing and time lag properties of X-radiation in a converging inflow (CI) atmosphere in §§ 2–4. Comparisons are drawn to the recent X-ray observations of BH sources. Our summary and conclusions follow in § 5.

### 2. EMERGENT SPECTRUM AND HARD PHOTON SPATIAL DISTRIBUTION

The geometry used in these simulations is similar to the one used in Laurent & Titarchuk (1999, hereafter LT99), consisting of a thin disk with an inner radius of  $3r_s$  merged with a spherical CI cloud harboring a BH in its center, where  $r_s = 2GM/c^2$  is the Schwarzschild radius and  $M$  is a BH mass. The cloud outer radius is  $r_{\text{out}}$ . The disk is assumed always to be optically thick.

In addition to free fall into the central BH, we have also taken into account the thermal motion of the CI electrons, simulated at an electron temperature of 5 keV. This is likely to be a typical temperature of the CI in the high-soft state of Galactic BHs (see Chakrabarti & Titarchuk 1995 and BOR99 for details). The seed X-ray photons were generated uniformly and isotropically at the surface of the border of the accretion disk, from  $r_{d,\text{in}} = 3r_s$  to  $r_{d,\text{out}} = 10r_s$ . These photons were generated according to a thermal spectrum with a single temperature of 0.9 keV, similar to the ones measured in BH binary systems (see, for example, BOR99). In fact, BOR99 also demonstrate that the multicolor disk spectrum can be fitted by the

<sup>1</sup> Centre d'Etudes de Saclay, CEA, DSM/DAPNIA/SAp, 91191 Gif-sur-Yvette Cedex, France; plaur@cea.fr

<sup>2</sup> George Mason University/Center for Earth Observing and Space Research, Fairfax, VA 22030-4444.

<sup>3</sup> US Naval Research Laboratory, Space Science Division, 4555 Overlook Avenue, SW, Washington, DC 20375-5352; lev@xip.nrl.navy.mil.

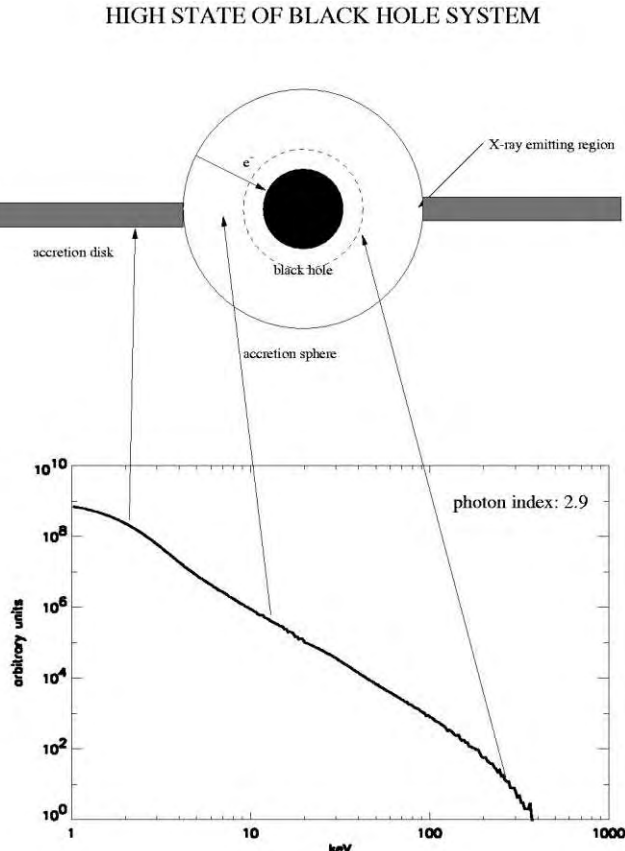


FIG. 1.—Monte Carlo-simulated emergent spectrum of CI. Mass accretion rate is in Eddington units,  $\dot{m} = 4$ ; the electron temperature of the flow  $kT_e = 5$  keV.

effective single-temperature blackbody spectrum in the energy range of interest (for photon energies higher than 2 keV). The parameters of our simulations are the BH mass  $m$  in solar units; the CI electron temperature,  $T_e = 5$  keV; the mass accretion rate,  $\dot{m} = 4$ , in Eddington units (see LT99); and the cloud outer radius,  $r_{\text{out}} = 10r_s$ . It is worth noting that, for these parameters, the bulk motion effects are not significant at  $r > 10r_s$ .<sup>4</sup>

In Figure 1, we present the simulated spectrum of the X-ray emission emerging from the CI atmosphere. The spectrum exhibits three features: a soft X-ray bump, an extended power law, and a sharp exponential turnover near 300 keV. As demonstrated previously (Titarchuk & Zannias 1998, hereafter TZ98; LT99), the extended power law is a result of soft photon upscattering off CI electrons. The qualitative explanation of this phenomena was given by Ebisawa, Titarchuk, & Chakrabarti (1996, hereafter ETC) and later by Papathanassiou & Psaltis (2001). The exponential turnover is formed by a small fraction of those photons that undergo scatterings near the horizon where the strong curvature of the photon trajectories prevent us from detecting most of them. In Figure 1, we indicate with arrows the places in the CI atmosphere where photons of a particular energy mainly come from.<sup>5</sup>

A precise analysis of the X-ray photon distribution in the

<sup>4</sup> In general, the bulk motion Comptonization is effective when  $\tau v_{\text{bulk}}/c = m r_s/r$  is not smaller than unity (e.g., Rees 1978; Titarchuk, Mastichiadis, & Kylafis 1997).

<sup>5</sup> Recently, Reig, Kyrlafis, & Spruit (2001) show that the extended power law can be also formed as a result of the bulk motion Comptonization when the rotational component is dominant in the flow. The photons gain energy from the rotational motion of the electrons.

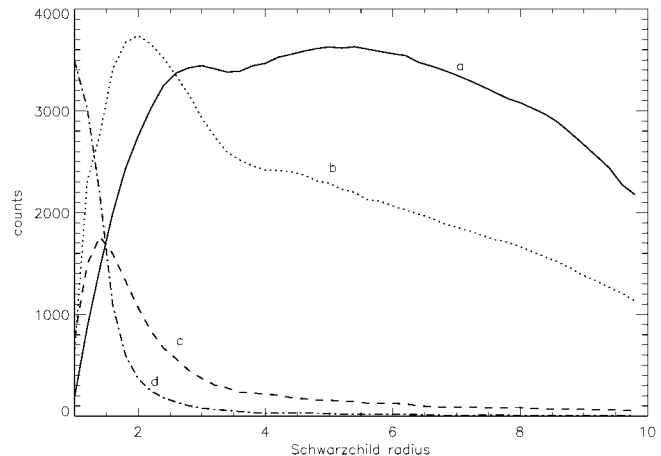


FIG. 2.—Source photon spatial distribution in the CI atmosphere for different energy bands. Curve a: 2–5 keV; curve b: 5–13 keV; curve c: 19–29 keV; curve d: 60–150 keV.

CI atmosphere can be made through calculation of the source function, either by semianalytical methods solving the relativistic kinetic equation (RKE; TZ98) or by Monte Carlo simulations (LT99). TZ98 calculate the photon kinetics in the lab frame, demonstrating that the source function has a strong peak near the photon bending radius,  $1.5r_s$  (their Fig. 3). In Figure 2, we show the Monte Carlo simulated source functions for four energy bands: 2–5 keV (curve a), 5–13 keV (curve b), 19–29 keV (curve c), and 60–150 keV (curve d). The peak at around  $(1.5-2)r_s$  is clearly seen for curves b and c, which is in good agreement with TZ98's source function.<sup>6</sup>

TZ98 calculated the upscattering part of spectrum neglecting the recoil effect. Our Monte Carlo simulations, not limited by TZ98's approximation, reproduce the source function spatial distribution for high-energy bands (Fig. 2, curve d). We confirm that the density of the highest energy X-ray photons is concentrated near the BH horizon. Comparison of TZ98's semi-analytical calculations and our Monte Carlo simulations leads us to conclude that the source function really follows the RKE first eigenfunction distribution until very high energies. At that point, the upscattering photon spatial distribution also becomes a function of energy. As seen from Figure 2, the source function in the soft energy band (curve a) has two maxima: one is at  $2.2r_s$ , related to the photon bending radius, and another (wide one) is at  $5r_s$ , affected by the disk emission area.

### 3. AN ILLUMINATION EFFECT OF CI ATMOSPHERE AND HIGH-FREQUENCY QPO PHENOMENA

We remind the reader that the emergent spectrum is a result of integration of the product of the photon escape probability and the source function distribution along a line of sight (e.g., Chandrasekhar 1960). The normalization of the upscattering spectrum is determined by the fraction of the soft (disk) photons that illuminate the inner region of the CI atmosphere below  $3r_s$ , i.e., around the maximum of the upscattered photon source function. From the Monte Carlo simulations, we extract the fraction of the soft photons emitted at some particular disk radius  $r$  that form the high-energy part of spectrum (for  $E >$

<sup>6</sup> TZ98 implemented the method of separation of variables to solve the RKE Green function. They then showed that the source function of the upscattered photons is distributed according to the first eigenfunction of the RKE space operator defined by eqs. (21)–(24) in TZ98.

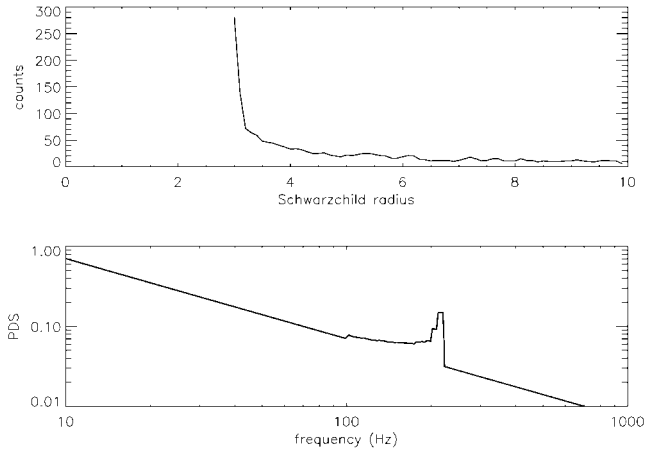


FIG. 3.—Upper panel: Distribution of soft photons over disk radius, which upscatters to energies 10 keV and higher in the CI atmosphere. Lower panel: PDS for photon energies higher than 10 keV. It is assumed that any disk annulus oscillates with Keplerian frequency. The continuum is a red noise.

10 keV). This distribution is presented in the upper panel of Figure 3. As seen from this plot, the strength of the high-energy tail is mostly determined by the photons emitted at the inner edge of the disk. Thus, any perturbation in the disk should be immediately translated to the oscillation of the hard tail with a frequency related to the inner disk edge. The CI atmosphere manifests the high-frequency QPO of the innermost part of the disk. In the lower panel of Figure 3, we present the power density spectrum (PDS) for the simulated X-ray emission coming from the CI atmosphere in the energies higher than 10 keV. We assume that the PDS is a sum of the red noise component (where the power-law index equals 1) and QPO power proportional to the illumination factor for a given disk radius,  $r$  (see the upper panel). We also assume that the perturbation frequency at  $r$  is related to the Keplerian frequency  $\nu_K = 2.2(3r_s/r)^{1.5}/m$  kHz.

There is a striking similarity between the high-frequency QPO and spectral energy distribution of the Monte Carlo results and real observations of BH candidates in their soft-high state. For example, in XTE J1550–564 the ~200 Hz QPO phenomenon tends to be detected in the high state at times when the bolometric luminosity surges and the hard power law spectral component is prominent (TS01). The noted lack of coherence between intensity variations of the high-soft state low-energy bands is also in good agreement with our simulations where the high-energy tail intensity *correlates* with the supply of the soft photons from the inner disk edge but *it does not correlate* with the production of the disk photons at large.

#### 4. POSITIVE AND NEGATIVE TIME LAGS

Additional important information related to the X-ray spectral energy distribution can be extracted from the time lags between different energy bands. The hard and soft lags have been observed for several sources (e.g., Reig et al. 2000, hereafter R00, and Tomsick & Kaaret 2001 for GRS 1915+105; Wijnands, Homan, & van der Klis 1999 and Remillard et al. 2001 for XTE J1550–564).

It is natural to expect the positive time lags in the case of the unsaturated thermal Comptonization. The primary soft photons gain energy in the process of scattering off hot electrons; thus, the hard photons spend more time in the cloud than the soft ones. Nobili et al. (2000) first suggested that in a corona

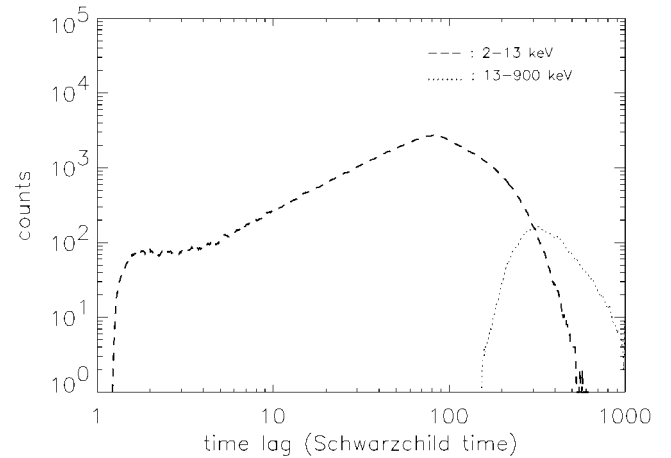


FIG. 4.—Time lag distributions for two energy bands. One can clearly see the area between  $150r_s/c$  and  $600r_s/c$ , where time lags of both signs can be present.

with a temperature stratification (a hot core and a relatively cold outer part), the thermal Comptonization can account for the positive and negative time lags as well as the observed colors (see R00).<sup>7</sup>

In the bulk motion Comptonization case, the soft-disk photons at first gain energy in the deep layers of the CI and then in their subsequent path toward the observer lose energy in the relatively cold outer layers. If the overall optical depth of the CI atmosphere (or the mass accretion rate) is near unity, we would detect only the positive lags as in the thermal Comptonization case, because relatively few photons would lose energy in escaping. But with an increase of the optical depth, the soft lags appear because more hard photons lose their energy in the cold outer layers.

In Figure 4, we present the calculations of the time lags for two energy bands: 2–13 and 13–900 keV. We first compute the time spent by the photon, drawn in a given direction, to cross the whole system without being scattered. Then, we compute the real time of flight of the photon, taking into account its scattering and its complete trajectory in the system. The general relativistic gravitational time dilatation was also taken into account in these computations. The time lag is then determined as a difference between these two times. In this time lag definition a photon that undergoes no scattering has a zero lag. Thus, the time lags between two energy bands can be defined as a difference of these two time lags, i.e.,  $\delta t = t_2 - t_1$ , where  $t_1$  and  $t_2$  are time lags for the 2–13 and 13–900 keV bands, respectively. The time lags for the 2–13 keV band are distributed over the interval between 1 and 600 Schwarzschild times,  $t_s = r_s/c$ , and the time lags for the 13–900 keV band are distributed over the interval between  $200t_s$  and  $10^3t_s$ . For a  $10 M_\odot$  BH,  $t_s = 0.1$  ms. Thus, for  $t_1 < 15$  ms, all time lags  $\delta t$  are positive; i.e., high-energy photons are produced later than the soft-energy photons. The  $t_2$  distribution has a broad peak at 30 ms, and the  $t_1$  distribution has a broad peak at 8 ms. Consequently, the positive lags  $\delta t$  are mostly higher than 20 ms, which is in good agreement with the time lag detection in GRS 1915+105 (R00). The values of the positive time lags for this source are consistent with the BH mass being around

<sup>7</sup> This Comptonization model with a hot core (for similar models, see also Skibo & Dermer 1995 and Lehr, Waggoner, & Wilms 2000) may reproduce the intrinsic spectral and timing properties of the CI.

$20 M_{\odot}$  (see BOR99 for the BH mass determination in GRS 1915+105). We show that the absolute value of the time (phase) lags get higher with the energy. In fact, Wijnands et al. (1999) for XTE J1550–564 (see also Remillard et al. 2001) and Tomsick & Kaaret (2001) for GRS 1915+105 show that the phase lags of both signs increase from 0 to 0.5 radians as the photon energy varies from 3 to 100 keV. These phase lag changes correspond to the time lag changes from 0 to 15 ms and from 0 to 50 ms for XTE J1550–564 and GRS 1915+105, respectively. These values are very close to what we obtain in our simulations.

For  $t_1 > 15$  ms, we get the time lags of both signs. Positive values of  $\delta t$  should be of order 30 ms and higher. Negative values should not be higher than 20 ms for a  $10 M_{\odot}$  BH. Our simulations demonstrate that for high accretion rates, time lags of both signs are present; i.e., the upscattering and downscattering are equally important in the formation of the CI spectrum, whereas for the low-mass accretion rates the upscattering process leads to the CI spectral formation and only the positive time lags are present. Our simulations are in good agreement with R00's values of  $\delta = 30$ –60 ms. The results for the simulated time lags can be understood using the simple upscattering model (see ETC). We assume that at any scattering event the relative mean energy change is constant,  $\eta$ ; i.e.,  $\eta = \langle \delta E \rangle / E$ . The number of scatterings  $k$  that are needed for the soft photon of energy  $E_0$  to gain energy  $E$  is  $k(E) = \ln(E/E_0)/\ln(1+\eta)$ . Then  $\delta t = kl(1-r_s/r)^{-1}/c$ , where  $l$  is the photon mean free path,  $l = [b(E)\sigma_T n]^{-1}$ ,  $1-r_s/r$  is the relativistic dilatation factor (e.g., Landau & Lifshitz 1971), and  $b(E)$  is an energy-dependent factor less than unity (e.g., Pozdnyakov, Sobol, & Sunyaev 1983). The free path  $l$  is estimated as  $l \sim 2(r/r_s)^{1.5} r_s/b(E)\dot{m}$  with an assumption that the number density  $n$  is calculated for the free-fall distribution (see eq. [2] in LT99). With  $r/r_s \approx 1.18$  (see Fig. 2, curve d),  $\dot{m} = 4$ , and  $b \approx 0.5$  for  $E = 100$  keV, we get  $l \approx 1.2r_s$ ;  $b(E) \approx 1$  for  $E = 10$  keV and  $r/r_s \gtrsim 2$ , and consequently  $l \gtrsim 1.5r_s$ . It is worth noting that the emergent high-energy photon gains its

energy being predominantly close to the horizon,  $r = (1-2)r_s$ , where the photon trajectories are close to circular (e.g., TZ98). Thus, our estimated values of the free path,  $l \sim (1-1.5)r_s$ , are consistent with the trajectory length. With  $\eta = 0.1$  extracted from our simulations for  $E < 100$  keV where the extended power law is seen in the spectrum (see also Papathanassiou & Psaltis 2001, Fig. 3) the time lags are  $\delta t = 7.6$  and 50 ms for  $E = 10$  and 100 keV, respectively.

## 5. SUMMARY AND CONCLUSIONS

Using Monte Carlo simulations, we have presented a detailed timing analysis of the X-radiation from a CI atmosphere and conclude the following: (1) We confirm TZ98's results that the high-energy photons are produced predominantly in the deep layers of the CI atmosphere from 1 to 2 Schwarzschild radii. (2) We also confirm that the 100 Hz phenomena should be seen in the high-energy tail of the spectrum rather than in the soft spectral component because the inner part of the CI is mostly fed by soft photons from the innermost part of the disk but the contribution of this disk area to the disk emission is small. (3) We find that the characteristic time lags in the CI are on the order of a few tens of milliseconds at 10 keV, and the hard (positive) time lags increase logarithmically with energy. (4) We demonstrate that soft (negative) along with hard (positive) lags are present in the X-ray emission from the CI for mass accretion higher than Eddington. In the end, we can also conclude that almost all of the X-ray timing and spectral properties of the high-soft state in BHs tends to indicate that the *high-energy tail of spectrum is produced within the CI region,  $(1-3)r_s$ , where the bulk inflow (gravitational attraction) is a dominant process*.

We acknowledge fruitful discussions with Chris Shrader and Paul Ray. We also acknowledge the useful suggestions and the valuable corrections by the referee, which improved the presentation of this Letter.

## REFERENCES

- Borozdin, K., Revnivtsev, M., Trudolyubov, S., Shrader, C., & Titarchuk, L. 1999, ApJ, 517, 367 (BOR99)  
 Chakrabarti, S. K., & Titarchuk, L. G. 1995, ApJ, 455, 623  
 Chandrasekhar, S. 1960, Radiative Transfer (New York: Dover)  
 Cui, W., Zhang, S. N., & Chen, W. 2000, ApJ, 531, L45  
 Di Salvo, T., et al. 2000, ApJ, 544, L119  
 Ebisawa, K., Titarchuk, L., & Chakrabarti, S. K. 1996, PASJ, 48, 59 (ETC)  
 Iaria, R., Burderi, L., Di Salvo, T., La Barbera, A., & Robba, N. R. 2001, ApJ, 547, 412  
 Landau, L. D., & Lifshitz, E. M. 1971, The Classical Theory of Fields (New York: Pergamon)  
 Laurent, P., & Titarchuk, L. 1999, ApJ, 511, 289 (LT99)  
 Lehr, D. E., Wagoner, R. V., & Wilms, J. 2000, preprint (astro-ph/0004211)  
 Nobili, L., Turolla, R., Zampieri, L., & Belloni, T. 2000, ApJ, 538, L137  
 Nowak, M. A., Wilms, J., Heindl, W. A., Pottschmidt, K., Dove, J. B., & Begelman, M. C. 2001, MNRAS, 320, 316  
 Papathanassiou, H., & Psaltis, D. 2001, MNRAS, in press (astro-ph/0011447)  
 Pozdnyakov, L. A., Sobol, I. M., & Sunyaev, R. A. 1983, Astrophys. Space Phys. Rev., 9, 1  
 Rees, M. 1978, Phys. Scr., 17, 193  
 Reig, P., Belloni, T., van der Klis, M., Méndez, M., Kylafis N. D., & Ford, E. C. 2000, ApJ, 541, 883 (R00)  
 Reig, P., Kylafis N. D., & Spruit, E. C. 2001, A&A, 375, 155  
 Remillard, R. A., Sobczak, G. J., Munro, M. P., & McClintock, J. E. 2001, ApJ, in press (astro-ph/0105508)  
 Shrader, C. R., & Titarchuk, L. G. 1998, ApJ, 499, L31  
 Skibo, J. G., & Dermer, C. D. 1995, ApJ, 455, L27  
 Strickman, M., & Barret, D. 1999, in AIP Conf. Proc. 510, Proc. Fifth Compton Symp., ed. M. L. McConnell & J. M. Ryan (New York: AIP), 222  
 Titarchuk, L., Mastichiadis, A., & Kylafis N. D. 1997, ApJ, 487, 834  
 Titarchuk, L., & Shrader, C. 2001, ApJ, in press (TS01)  
 Titarchuk, L., & Zannias, T. 1998, ApJ, 493, 863 (TZ98)  
 Tomsick, J. A., & Kaaret, P. 2001, ApJ, 548, 401  
 Wijnands, A. D., Homan, J., & van der Klis, M. 1999, ApJ, 526, L33

## EFFECTS OF DOWNSCATTERING ON THE CONTINUUM AND LINE SPECTRA IN A POWERFUL WIND ENVIRONMENT: MONTE CARLO SIMULATIONS, ANALYTICAL RESULTS, AND DATA ANALYSIS

PHILIPPE LAURENT<sup>1,2,3</sup> AND LEV TITARCHUK<sup>4,5</sup>

Received 2005 October 4; accepted 2006 November 2

### ABSTRACT

In an earlier paper, the general formulation and results for photon reprocessing (downscattering) that included recoil and Comptonization effects due to divergence of the flow were presented. In a second paper we showed the Monte Carlo (MC) simulated continuum and line spectra. We also provided an analytical description of the simulated continuum spectra using the diffusion approximation. We have simulated the propagation of monochromatic and continuum photons in a bulk outflow from a compact object. Electron scattering of the photons within the expanding flow leads to a decrease of their energy, which is of first order in  $V/c$  (where  $V$  is the outflow velocity). The downscattering effect of first order in  $V/c$  in the diverging flow is explained by semianalytical calculations and confirmed by MC simulations. We conclude that redshifted lines and downscattering bumps are intrinsic properties of the powerful outflows for which the Thomson optical depth is greater than 1. We fitted our model line profiles to the observations using four free parameters,  $\beta = V/c$ , the optical depth of the wind  $\tau$ , the wind temperature  $kT_e$ , and the original line photon energy  $E_0$ . We show how the primary spectrum emitted close to the black hole is modified by reprocessing in the warm wind. In the framework of our wind model, the fluorescent iron line  $K\alpha$  is formed in the partly ionized wind as a result of illumination by central source continuum photons. The demonstrated application of our outflow model to the *XMM-Newton* observations of MCG –6-30-15 and to the *ASCA* observations of GRO J1655–40 points out a potential powerful spectral diagnostic for probes of the outflow–central object connection in Galactic and extragalactic black hole sources.

*Subject headings:* accretion, accretion disks — radiation mechanisms: nonthermal

### 1. INTRODUCTION

Titarchuk & Shrader (2005, hereafter Paper I) have shown that downscattering modification of the primary photon spectrum by an outflowing plasma is a possible mechanism for producing the continuum excess in the  $\sim 10$  keV spectral region. This continuum excess can be formed only if the energy index of the primary photon spectrum is less than 1 (see also Sunyaev & Titarchuk 1980, hereafter ST80). This is usually attributed to Comptonization by a static reflector, such as a downwardly or obliquely illuminated accretion disk, although the overall continuum form differs from the basic Compton reflection form. Paper I thus suggests that in at least some cases, the outflow downscattering effect, rather than the standard Compton reflection mechanism, is responsible for the observed “excess” hard X-ray continuum.

To obtain a description of the X-ray photon spectrum, many authors (see, e.g., Gilfanov et al. 1999; Pottschmidt et al. 2003) used an empirical model in which each source spectrum is the sum of power-law spectrum with photon index  $\Gamma$  and a multi-temperature disk blackbody. To this continuum, a reflection spectrum adapted from Magdziarz & Zdziarski (1995) was added. However, Shaposhnikov & Titarchuk (2006, hereafter ST06) argue that these spectral features are results of reprocessing of the central source hard radiation in the outflow (warm wind) that surrounds the central black hole (BH). This claim is supported by

the observed power decay of quasi-periodic oscillations (QPOs) toward the softer states, which is presumably a result of reprocessing the time signal in the extended relatively warm wind (see Fig. 6 in ST06).

The basic idea is that electron scattering of photons from a central source entering the expanding outflow experience a decrease in energy (downscattering). The magnitude of this decrease is of first order in  $V/c$  and in  $E/m_e c^2$ , where  $V$  is the outflow speed,  $c$  is the speed of light,  $E$  is the initial photon energy, and  $m_e$  is the electron rest mass.

Paper I developed an analytic formulation for the emergent spectrum resulting from photon diffusion in a spherically expanding Comptonizing media, characterized by two model parameters: an average number of scatterings in the medium  $N_{av}$  and the efficiency of the energy loss in the divergent flow  $\varepsilon$ . In this formulation of the radiative transfer problem, the number of photons emitted in the wind shell equals the number that escape to the Earth observer (i.e., the photon number is conserved). Consequently, if the high-energy photons lose their energy on the way out, but the number of photons is conserved, it must result in the accumulation of photons at a particular lower energy band.

The basic idea of the wind photon downscattering is depicted in Figure 1, which presents a simple explanation of the diverging flow’s effect on photon propagation through the medium. A photon emitted outward near the inner boundary and then scattered at a certain point by an electron moving with velocity  $V_1$  is received by an electron moving with velocity  $V_2$ , as shown, with frequency  $\nu_2 = \nu_1 [1 + (\mathbf{V}_1 - \mathbf{V}_2) \cdot \mathbf{n}/c]$ , where  $\mathbf{n}$  is the unit vector along the path of the photon at the scattering point. In a diverging flow,  $(\mathbf{V}_1 - \mathbf{V}_2) \cdot \mathbf{n}/c < 0$ , and photons are successively redshifted until scattered to an observer at infinity. The color of the photon path (in Fig. 1) indicates the frequency shift in the rest frame of the receiver (electron or the Earth observer). On

<sup>1</sup> CEA/DSM/DAPNIA/SAp, CEA Saclay, Gif sur Yvette, France; plaurent@cea.fr.

<sup>2</sup> Fédération Astroparticule et Cosmologie, Collège de France, Paris, France.

<sup>3</sup> Current address: Astroparticule et Cosmologie, Paris, France.

<sup>4</sup> George Mason University, Center for Earth Observing and Space Research, Fairfax, VA.

<sup>5</sup> US Naval Research Laboratory, Washington, DC; ltitarchuk@ssd5.nrl.navy.mil.

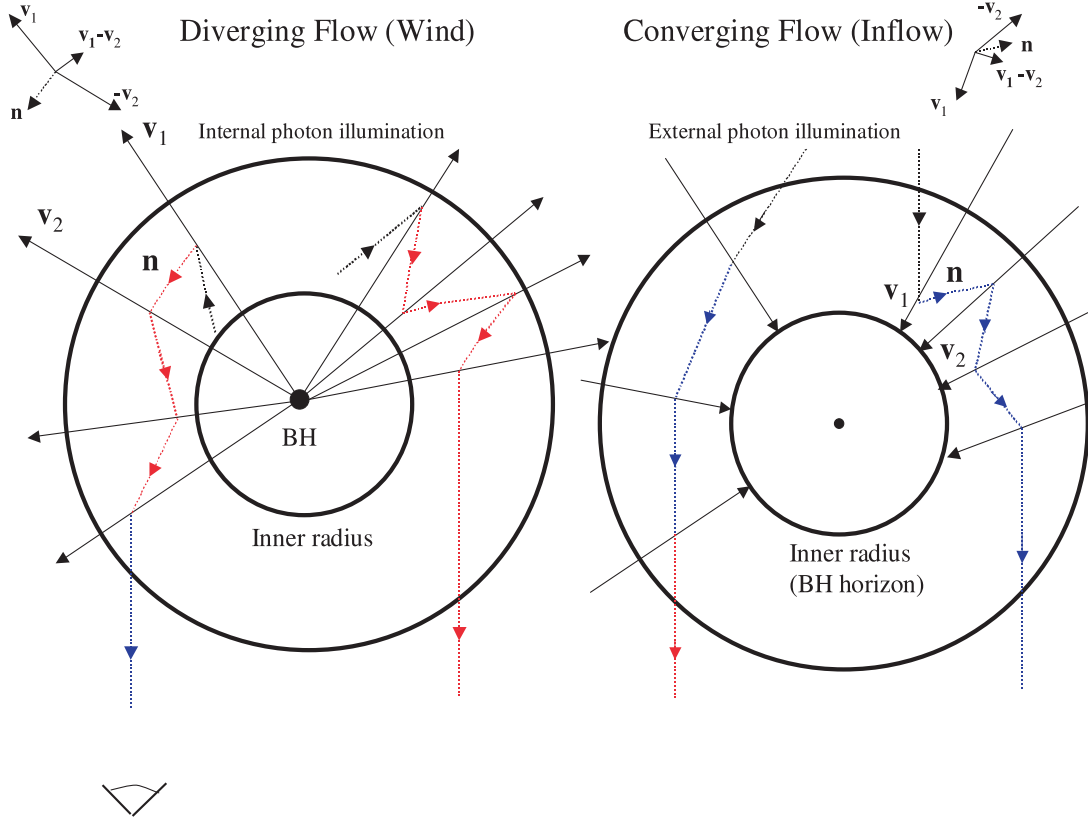


Fig. 1.—Left: Schematic diagram showing wind geometry. The relatively cold outflow (wind) originates at the inner radius. The optical depth of the wind in the Fe K continuum and the electron scattering optical depth of the wind are of order unity. A photon emitted near the inner boundary and subsequently scattered by an electron moving with velocity  $V_1$  is received by an electron moving with velocity  $V_2$ , as shown. The change in frequency is  $\nu_2 = \nu_1[1 + (\mathbf{V}_1 - \mathbf{V}_2) \cdot \mathbf{n}/c]$ , where  $\mathbf{n}$  is a unit vector along the path of the photon scattered at the next point. In a diverging flow,  $(\mathbf{V}_1 - \mathbf{V}_2) \cdot \mathbf{n}/c < 0$ , and photons are successively redshifted, until scattered to an observer at infinity. The color of the photon path indicates the frequency shift in the rest frame of the receiver (electron or the Earth observer). Right: In a converging flow,  $(\mathbf{V}_1 - \mathbf{V}_2) \cdot \mathbf{n}/c > 0$ , and photons are blueshifted.

the other hand, referring to the right-hand side of Figure 1 in a converging flow,  $(\mathbf{V}_1 - \mathbf{V}_2) \cdot \mathbf{n}/c > 0$ , and photons are blueshifted.

In this paper we present the results of extensive Monte Carlo (MC) simulations of the downscattering effects in the wind (diverging flow). In addition to the scattering, Doppler, and Compton effects, we include a photoabsorption effect in the diverging flow (wind). Any photon with energy of  $\sim 7$ – $8$  keV and higher interacting with the outflow plasma is more likely to be absorbed by the flow and be reemitted at energies  $\sim 6.4$ – $6.6$  keV, depending on the ionization stage of the flow (see Kallman et al. 2004). Laming & Titarchuk (2004, hereafter LT04) calculated the temperature and ionization balance in the outflow, determined by seeking the temperature at which the outflowing gas attains photoionization-recombination equilibrium. The gas is heated by Compton scattering and photoionization by photons from the central compact object and is cooled by radiation, ionization, and adiabatic expansion losses. The solution of this problem is general regarding the calculation of the temperature and ionization balance in the target illuminated by the hard radiation. It potentially has many applications beyond astrophysics (for example, in radiation safety physics). Our simulations allow us to reveal the spectral, timing, and absorption properties of the emergent radiation.

We update the analytical results of the downscattering modifications of the continuum obtained in Paper I (using the Fokker-Planck technique), and we verify them using the MC-simulated spectra. We demonstrate that the analytical formulas for the con-

tinuum spectra describe the MC spectra well for almost any  $\beta = V/c \lesssim 0.8$ .

Many authors (e.g., Tanaka et al. 1995; Nandra et al. 1997; Wilms et al. 2001; Uttley et al. 2004; Miller et al. 2004a, 2004b) have found unusual curvature (red-skewed features) at energies between 2 and 8 keV in the X-ray spectra of a number of Galactic and extragalactic BH sources. Significantly, the fluxes of these features remain nearly constant despite the large changes in the continuum flux, as shown in the observations of MCG –6-30-15, NGC 4051, and others (Markowitz et al. 2003). This lack of variability means that fast changes (which are almost certain to occur near the BH) are not obtained. These observations motivate us to make a detailed study of the spectral line formation in the outflows that possibly occur in BH sources. In this paper we demonstrate that red-skewed features can be a result of the scattering of iron line photons in the powerful outflow.

We offer a model in which the hard radiation of the central object illuminates and heats the outflow (wind) region that originated in the outskirts of the disk (well outside the innermost part of the accretion disk near the BH). The line photons are generated and scattered in the outflow. Our basic scenario is illustrated in Figure 1. The wind originates at a distance  $r_{in}$  from the central BH and is of a density so as to give a Thomson scattering optical depth  $\tau_T$  close to unity far from the BH. The optical depth in the Fe K continuum is about 1–3 times higher than that due to electron scattering (assuming a solar abundance of Fe and depending on charge state; see Kallman et al. 2004), and so Fe K $\alpha$  formed

by inner shell ionization of Fe ions in the outflow by the continuum from the central BH only comes from a smaller inner region. In fact, using the calculations of the ionization state of the outflow shell by LT04, we find that K $\alpha$  photon sources are exponentially distributed over a skin at the bottom of the outflow, the skin thickness being 4% of the optical depth of the wind shell. Furthermore, because the iron photoabsorption opacity  $\sigma_K$  is about a few times the Thomson opacity  $\sigma_T$ , any photon around the K-absorption edge energy must be absorbed. In fact, these edges are seen with the strong K $\alpha$  lines during X-ray superbursts detected from neutron star source 4U 1820–30 (see Figs. 5 and 9 in Strohmayer & Brown 2002).

A thorough analysis and review of the diffusion theory of photon propagation in an optically thick fluid in bulk outflow has been provided by Titarchuk et al. (2003, hereafter TKB03). They show that the iron line is produced in an effectively optically thick medium. Its red wing is the result of multiple scatterings, each scattering producing a first-order  $V/c$ -redshift. This process introduces a red wing to the line without any particular fine-tuned geometric arrangement.

The Paper I and TKB03 results are obtained using the Fokker-Planck equation (Blandford & Payne 1981; see also Lifshitz & Pitaevskii 1981 for a general treatment of the particle acceleration problem), which is valid for  $\beta = V/c \ll 1$  and  $\tau_{\text{eff}} > 1$ . The MC method does not have these limitations.

We show the results of MC simulations of scatterings of continuum and monochromatic photons for various values of plasma temperatures  $kT_e$ , outflow bulk velocity  $\beta$ , and Thomson optical depth  $\tau$ . The details of the MC method applied to the outflow model are given in § 2. We compare the results of the MC-simulated continuum with their analytical description and discuss the down-scattering modifications of the incident spectrum in §§ 3.1 and 3.2. The results of the simulated line formation in the outflow and its explanation using the analytical theory are shown in § 3.3. Examples of the model fits to the *XMM-Newton* data obtained for MCG –6-30-15 and to *Advanced Satellite for Cosmology and Astrophysics* (*ASCA*) archive data of Galactic BHs are shown in § 4. The results of the simulations of overall spectra including the scattering and photon absorption effects are presented in § 5. Discussion and conclusions follow in § 6.

## 2. DETAILS OF THE MONTE CARLO METHOD

Laurent & Titarchuk (1999) simulated the Comptonization of photons using a Monte Carlo (MC) method in the Schwarzschild metric. The geometry used in these simulations consists of a spherical shell harboring a BH in its center. Once given the cloud Thomson optical depth  $\tau$ ,  $N_e$  is the electron number density measured in the local rest frame of the flow that is

$$N_e = \tau(r_S/r)^2 / [r_S \sigma_T (r_S/r_{\text{in}} - r_S/r_{\text{out}})]. \quad (1)$$

Here  $\sigma_T$  is the Thomson cross section,  $r_{\text{in}}$  and  $r_{\text{out}}$  are the inner and outer radii of the shell, respectively, and  $r_S$  is the Schwarzschild radius. Simulations made for different values of  $r_{\text{in}}$  and  $r_{\text{out}}$  (that are much greater than the Schwarzschild radius) have shown no change of the line profile and continuum provided the shell optical depth remains the same. We have varied the shell electron temperature from 0.01 to 1 keV. Along with the thermal motion of the electrons in the cloud, we have also taken into account the bulk velocity of the outflow  $\beta = V/c$ . In these simulations, the spherical wind has a constant bulk velocity within the flow. It is worth noting that an increase of the shell temperature from 0.01 to 1 keV slightly increases the blue wing

of the observed line, but induces no change in the red wing that we are mostly interested in here.

For the timing studies described in § 3 we have also computed the path length that each photon in the simulations has covered before it escapes from the shell.

## 3. DOWNSCATTERING EFFECT IN AN OUTFLOW

The problem of photon propagation in a fluid in bulk motion has been studied in detail in a number of papers (see, e.g., Blandford & Payne 1981; Payne & Blandford 1981; Nobili et al. 1993; Titarchuk et al. 1997; TKB03; Paper I; Laurent & Titarchuk 1999, 2001). In particular, Paper I presented a general formulation and a solution of the spectral formation in the diverging outflow. They demonstrated that the resulting spectrum can be formed as a convolution of energy and spatial diffusion solutions.

To apply these radiative transfer results to observational data, Paper I developed a generic analytical formulation that leads to a simple analytic expression for modification of the emergent spectrum due to recoil and velocity divergence effects in the flow. For the recoil effect, Paper I extended the results by ST80, who showed that the downscattering feature, or “bump,” can appear superposed on power-law spectra with energy spectral indices  $\alpha < 1$  as a result of photon diffusion through a static cloud. From ST80 and calculations presented in Paper I, one might conclude that such bumps are not necessarily a feature of disk reflection, but they can be also formed as a result of photon reprocessing in a relatively cool, ambient plasma characterized by temperatures on the order of  $10^6$  K.

### 3.1. Time Distributions of Escape Photons

In order to understand and explain the shapes and the main features of the MC-simulated spectra, we have attempted to reproduce them using the analytical diffusion approximation. In the framework of the diffusion theory (Paper I), the resulting spectrum can be presented as a particular convolution of a primary photon spectrum  $\varphi(z)$  and a time distribution of escape photons  $\mathcal{P}(u)$  (see eq. [2] below). Here  $u = t/t_{\text{fp}}$ ,  $t$  and  $t_{\text{fp}} = l/c$  are the time for a photon to escape from the wind and the mean free path time between two consequent photon scatterings, respectively, and  $z = E/m_e c^2$  is the dimensionless photon energy. ST80 and Sunyaev & Titarchuk (1985, hereafter ST85) demonstrated that the photon escape distribution  $\mathcal{P}(u)$  exponentially decays with  $u$  as  $u > 1$  for any bounded configuration, namely,  $\mathcal{P}(u) \sim b \exp(-bu)$ .

In Figure 2 we present the simulated time distribution  $\mathcal{P}(t/t_{\text{fp}})$  for the optical depth of the wind  $\tau = 4$ . As was found by ST80 and ST85, the time distribution decays exponentially,  $\exp(-bt/t_{\text{fp}})$  for  $t > t_{\text{fp}}$ , when the photons propagate in any bounded medium. This result is used to derive the analytical spectra (see eq. [2]). It means that the best-fit  $b$ -parameters obtained by fitting  $\exp(-bt/t_{\text{fp}})$  to the time distributions and those  $b$ -parameters obtained by fitting the analytical spectra to the simulated spectra are identical within errors of  $b$ . We computed the  $b$ -values obtained by these ways, and we found that they are identical. This consistency check gives us more confidence in the accuracy of our simulations and their analytical description.

In Figure 3 we show the photon distribution for emergent photons over a range of deflecting angles with respect to the direction of the incident photons. The outflow shell is radially illuminated by the central source radiation. The simulations are presented for  $\tau = 1, 2$ , and  $4$  and  $\beta = 0.1$ . In fact, we find in our simulations that the distribution of the scattering component weakly depends on  $\tau$ . Practically, there is little difference between that related to

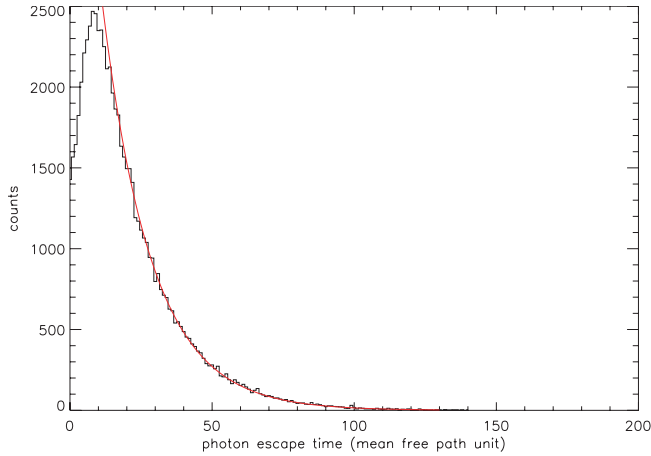


FIG. 2.—Timing properties of the outflow. The photon distribution over escape time  $\mathcal{P}(t/t_{fp})$ , where  $t_{fp} = l/c$  is a free path time. This simulation is made for the incident spectrum as a power law with exponential cutoff for  $kT_e = 0.1$  keV,  $\tau = 4$ , and  $\beta = 0.1$ . It is worth noting that the index  $b = 0.057$  of the exponential distribution  $\exp(-bt/t_{fp})$  (red line) is very close to the best-fit parameter values  $0.06 \pm 0.005$  for the energy spectrum. We find that in all cases the best-fit parameter  $b$  obtained from the photon distribution over escape time is very close to  $b$  obtained from the best-fit analytical spectrum.

$\tau = 4$  and  $\tau = 1$  or 2. There is only the difference in the normalization of the direct (nonscattering) component  $A_N$  for which the ratio of  $A_N(\tau = 4)/A_N(\tau) = \exp(-4 + \tau)$ . The distribution has a strong maximum about  $50^\circ$ . Thus, we expect that our results for the spherical wind can be applicable for the conical wind if the half-angle of the conical wind is about  $50^\circ$  or more (wide-open jet or wind).

As we demonstrate in Figure 2, the simulated escape time distribution in the wind has an exponential profile, which is a typical signature of photon diffusion propagation in any bounded configuration (ST85). This leads us to the conclusion that we can also treat the radiative transfer in the wind in the framework of the diffusion model (see Paper I).

### 3.2. MC-Simulated Spectra of the Continuum and Their Analytical Description

For the completeness of the present work we reproduce some necessary details of the analytical diffusion model in Paper I. Particularly, the downscattering modification of the incident spectrum  $\varphi(E)$  can be obtained using formula (24) in Paper I,

$$\mathcal{F}_\nu(z, \varepsilon) = \frac{1}{z} \int_0^{u_{\max, \varepsilon}(z)} e^{-4\varepsilon u/3} \psi^{(\varepsilon)}(z, u) \varphi[\psi^{(\varepsilon)}(z, u)] \mathcal{P}(u) du, \quad (2)$$

where  $\mathcal{P}(u)$  is the distribution of the photons over their dimensionless escape time  $u = t/t_{fp}$  and

$$u_{\max, \varepsilon}(z) = (3/\varepsilon) \ln(1 + \varepsilon/3z) \gg 1 \quad (3)$$

is the maximal number of scatterings related to the dimensionless energy  $z = E/m_e c^2$ . The dimensionless photon energy  $z_0 = E_0/m_e c^2$  at  $u = 0$  is

$$z_0 = \psi^{(\varepsilon)}(z, u) = \frac{(\varepsilon/3)}{(1 + \varepsilon/3z) \exp(-\varepsilon u/3) - 1}, \quad (4)$$

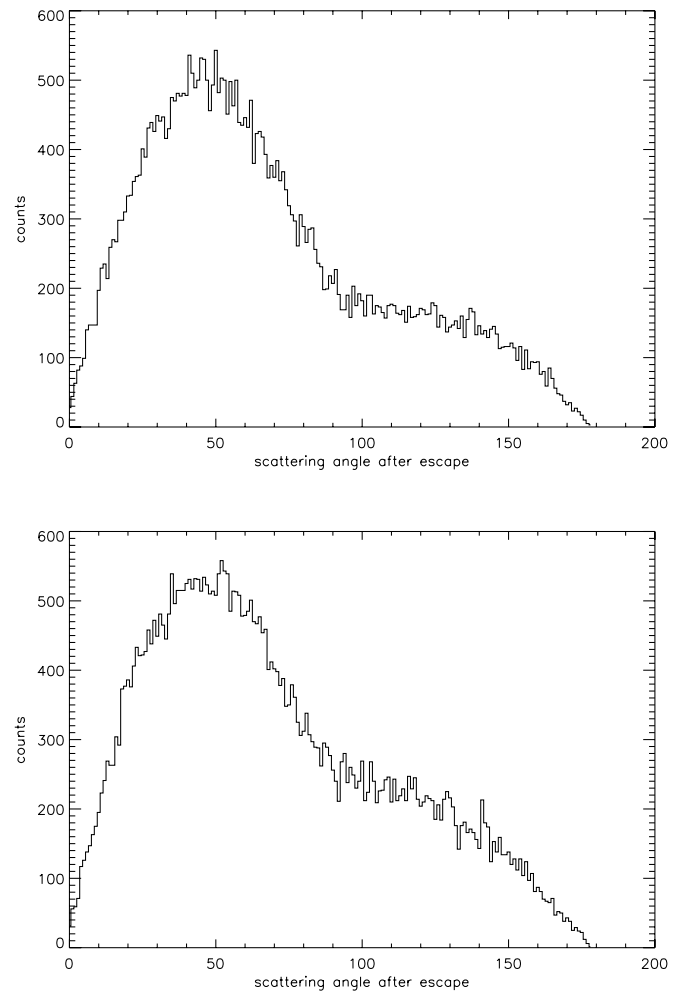
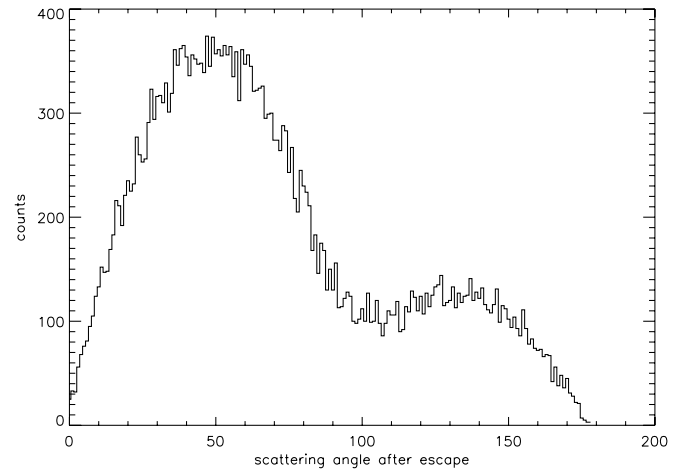


FIG. 3.—Photon distribution over deflecting angles. The outflow shell is radially illuminated by the central source radiation. Top:  $\tau = 1$ ; middle:  $\tau = 2$ ; bottom:  $\tau = 4$  and  $\beta = 0.1$ . In fact, we find in our simulations that the angle distribution of the scattering component weakly depends on  $\tau$ , but there is a big difference in the normalization of the direct (nonscattering) component  $A_N$  for which the ratio of  $A_N(\tau = 4)/A_N(\tau) = \exp(-4 + \tau)$ .

and  $\varepsilon \ll 1$  is a coefficient of the diverging term in the kinetic (Fokker-Planck) equation (see eqs. [16] and [17] in Paper I and related discussion). In fact,  $\varepsilon$  is an average relative energy redshift per scattering. Below (see eq. [12]), we evaluate these values and verify them using the results of our MC simulations. We

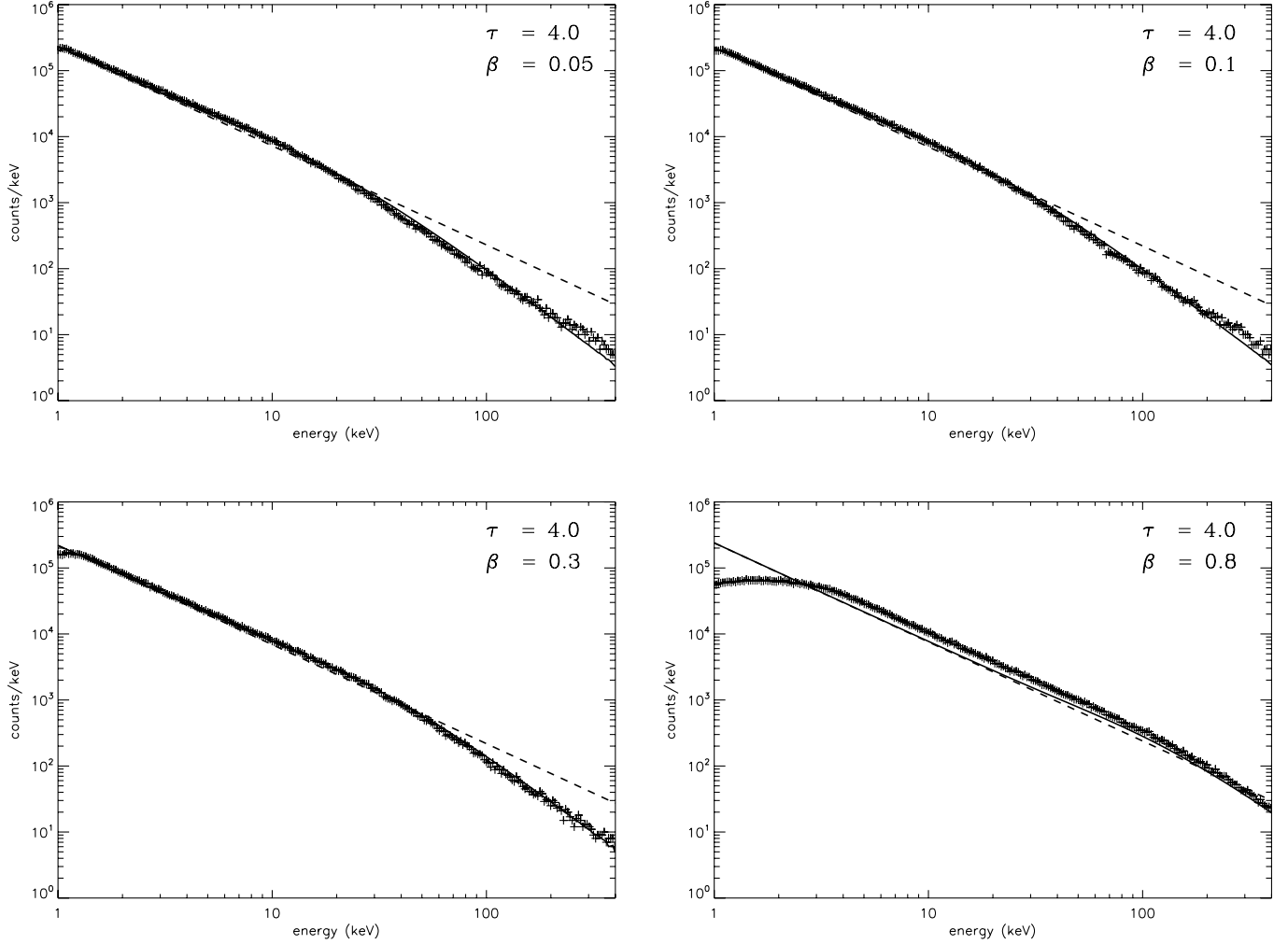


Fig. 4.—Emerging spectrum of a compact object through an outflowing plasma. The incident spectrum inside the outflowing plasma is taken to be a power law  $\varphi(E) \propto E^{-\alpha}$  for which the energy index  $\alpha = 0.5$ . Outflow parameters are  $kT_e = 0.1$  keV,  $\tau = 4$ , and  $\beta = 0.05, 0.1, 0.3$ , and  $0.8$ . The photon emerging spectrum (crosses) is compared to the incident spectrum (dashed line) and the analytical downscattering spectrum (solid line; see eq. [7]). For  $\beta = 0.05, 0.1, 0.3$ , and  $0.8$ , the best-fit parameters are  $b = 0.07, 0.07, 0.11$ , and  $0.45$ , respectively. For all cases we fix  $\varepsilon = 0$ . One can clearly see a bump in the MC-simulated and analytical spectra in the low-energy band around 10 keV for all  $\beta \lesssim 0.3$ . Indeed, in the purely diffusive case that is shown in this plot, the photon number is conserved, so the downscattered high-energy photons, which are removed from the high-energy part of the incident spectrum, are detected at lower energy.

find that  $\varepsilon \sim \beta/2\tau$  is on the order of  $10^{-2}$  for  $\beta \lesssim 0.1$  and for  $\tau$  of a few.

This result is a generalization of the ST80 and TKB03 results. ST80 derived the spectra when the downscattering effects due to the recoil were taken into account. It should be noted that the downscattering modification of the spectrum occurs when photons undergo multiple scatterings  $u$ . Thus, we can expand the integrand function  $W^{(\varepsilon)}(z, u) = e^{-4\varepsilon u/3} [\psi^{(\varepsilon)}(z, u)] \varphi[\psi^{(\varepsilon)}(z, u)]$  over  $u$  in formula (2),

$$W^{(\varepsilon)}(z, u) \approx W^{(\varepsilon)}(z, 0) + W_u^{(\varepsilon)'}(z, 0)u + \frac{W_u^{(\varepsilon)''}(z, 0)u^2}{2} + \frac{W_u^{(\varepsilon)'''}(z, 0)u^3}{3!} + \dots \quad (5)$$

For the simplest case of the power-law incident spectrum and neglecting the diverging term in the kinetic (Fokker-Planck) equation ( $\varepsilon = 0$ ), the resulting spectrum (eq. [2]) is

$$\mathcal{F}_E(z) = \frac{A}{z} \int_0^{1/z} \left( \frac{1}{z} - u \right)^{\alpha-1} \mathcal{P}(u) du. \quad (6)$$

Using equation (5), one can obtain (see Appendix A, eq. [A6])

$$\begin{aligned} \mathcal{F}_E(z) = Az^{-\alpha} & \left[ M_0(z^{-1}) + \frac{(1-\alpha)}{1!} z M_1 \right. \\ & + \frac{(1-\alpha)(2-\alpha)}{2!} z^2 M_2(z^{-1}) + \dots \\ & \left. + \frac{(1-\alpha)(2-\alpha)\dots(n-\alpha)}{n!} z^n M_n(z^{-1}) + \dots \right], \end{aligned} \quad (7)$$

where

$$M_n(z^{-1}) = b \int_0^{1/z} u^n \exp(-bu) du \quad \text{for } n = 0, 1, 2, \dots \quad (8)$$

Note that the first term in the parentheses of the right-hand side of equation (7)  $M_0(z^{-1}) = 1$  for  $z \ll 1$ , and the second term

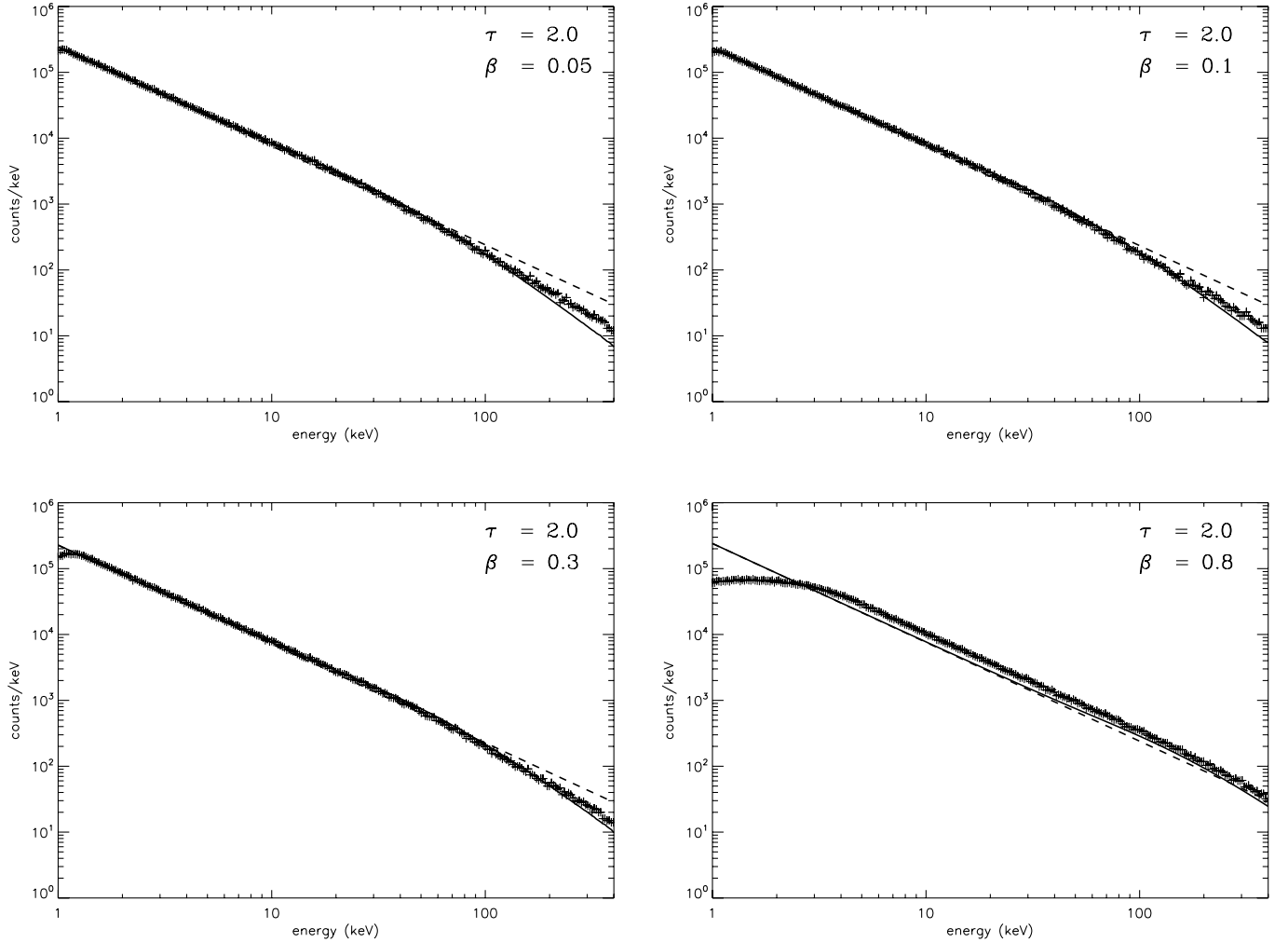


FIG. 5.—Same as Fig. 4, but for  $\tau = 2$ . For  $\beta = 0.05, 0.1, 0.3$ , and  $0.8$ , the best-fit parameters are  $b = 0.13, 0.15, 0.21$ , and  $0.62$ , respectively.

$(1 - \alpha)z M_1(z^{-1})$  is positive if the energy index of the primary photon spectrum  $\alpha < 1$ . Thus, one can expect the photon accumulation bump at low energies for the downscattered power-law spectra for which the primary photon spectrum is quite hard (the energy index  $\alpha < 1$ ). Indeed, in the pure scattering case the photon number is conserved, so if large numbers of the downscattered high-energy photons are removed from the high-energy part of the incident spectrum, then they should be seen at lower energies as a so-called downscattering bump.

In Figures 4 and 5 we present the MC-simulated spectra along with the analytical spectra (eq. [7]) for the power-law incident spectra for  $\tau = 4$  and  $2$ , respectively. The downscattering (accumulation) bump and softening of the spectrum at high energies are clearly seen in these spectra. As optical depth increases, more prominent bumps are formed in the outflow. The softening of the analytic spectra due to the downscattering effect is well described by exponential decay of moments of the time distribution  $M_i(1/z)$  ( $i = 0, 1, 2, \dots$ ) at higher energies (i.e., when  $b/z > 1$ ; see eqs. [8] and [A9]). The parameter  $b$  is only a free parameter we use to fit the analytical formula, we fix  $\varepsilon = 0$  for which  $u_{\max} = 1/z$  (see eq. [3]), namely,  $\lim_{\varepsilon \rightarrow 0} u_{\max, \varepsilon} = 1/z$ . For  $\tau = 4$  the analytical spectra in equation (7) perfectly represent the simulated spectra for a wide range of wind velocities  $V = \beta c \lesssim 0.8c$ . It is worth noting that we do not need more than six terms of the asymptotic series from equation (7) to achieve the highest accuracy of the analytical spectra calculations.

For  $\beta = 0.05, 0.1, 0.3$ , and  $0.8$ , the best-fit parameters are  $b = 0.07, 0.07, 0.11$ , and  $0.45$ , respectively. The inverse of the  $b$ -parameter  $N_{\text{av}} = 1/b$  is an average number of scatterings undergone by the photons in the wind. For a faster wind, the number of scatterings naturally decreases, because photons are effectively taken by the outflow and less photons are scattered off outflow electrons. ST85 calculated  $b$ -parameters (and the average number of scatterings  $N_{\text{av}}$ ) for spherical and plane (disk) geometry (Table 1 in ST85, where  $\beta$  corresponds to our value  $b$ ). ST85 presented their results for the static case, i.e., the zero bulk velocity case. Thus, we should compare their results with our results when  $\beta = 0.05$  and  $0.1$ . Moreover, our wind-extended envelope of optical depth  $\tau$  is equivalent to the disk of half optical depth  $\tau/2$ . For example, for  $\tau = 4$  our  $b = 0.07$  should be related to the  $0.101$  value in ST85 for  $\tau = 2$ . As expected our  $b$ -value is smaller (or  $1/b$  greater) than that in ST85, because the empty internal cavity of the wind envelope essentially amplifies the number of photon scatterings with respect to that in a plane disk of the same optical depth. The scattering effect of the cavity is suppressed when the wind velocity (or  $\beta$ ) increases. For  $\beta = 0.3$ , the cavity effect and the wind velocity effect on scattering compensate each other. Our value of  $b = 0.11$  is very close to that in ST85.

In Figure 5 we show the simulated spectra along with the analytical spectra for  $\tau = 2$ . One can note that the best-fit analytical spectra slightly deviate from the simulated spectra at high energies. For  $\beta = 0.05, 0.1, 0.3$ , and  $0.8$ , the best-fit parameters

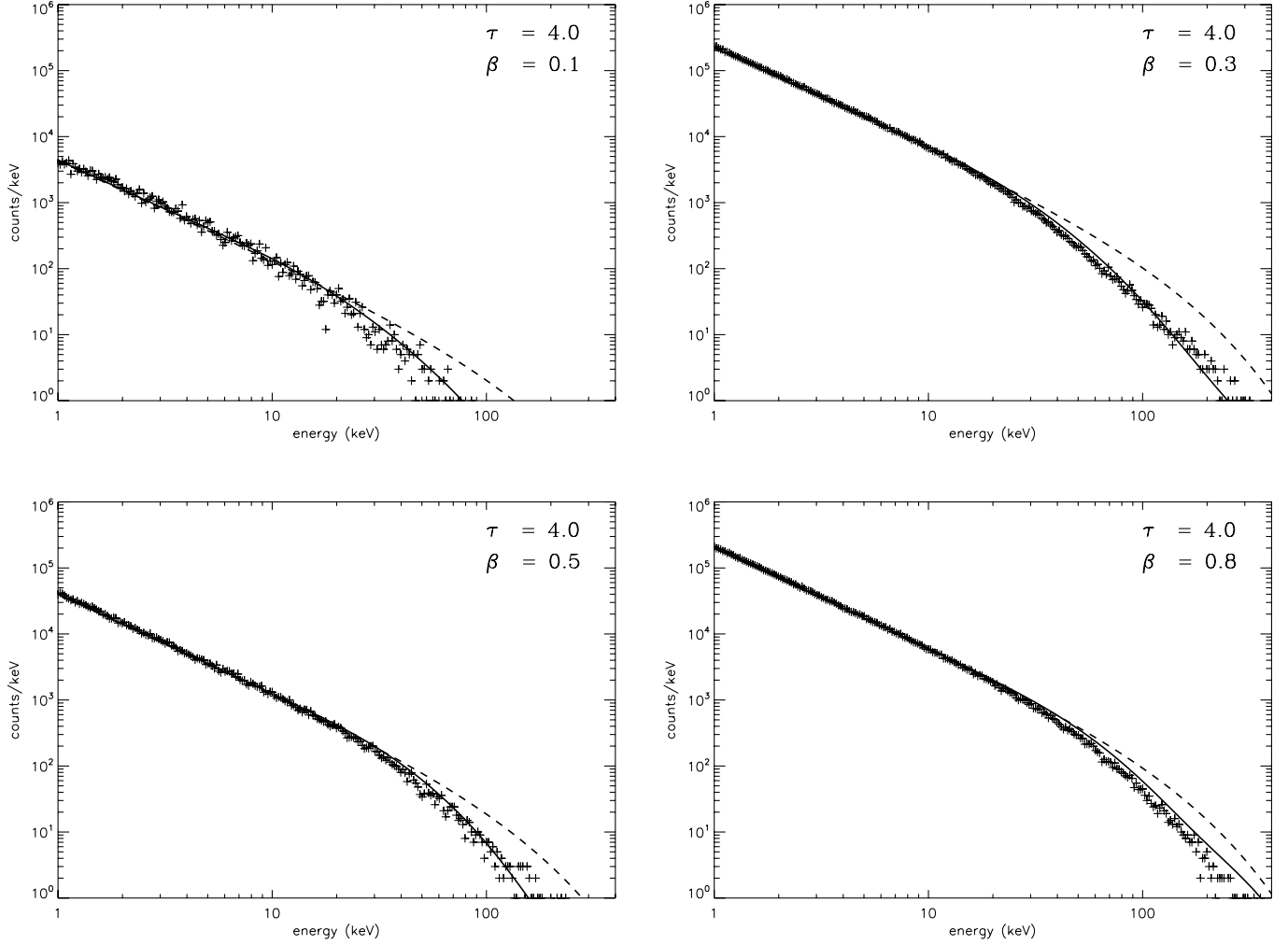


FIG. 6.—Emerging spectrum of a compact object through an outflowing plasma. The incident spectrum inside the outflowing plasma is taken to be  $\varphi_{\text{Comp}}(E) \propto E^{-\alpha} \exp(-E/E_*)$  (see eq. [9]) where energy index  $\alpha = 0.5$  and high-energy cutoff is at  $E = E_* = 130$  keV. Outflow parameters are  $kT_e = 0.1$  keV and  $\tau = 4$ . The photon emerging spectrum (crosses) is compared to the incident spectrum (dashed line) and the analytical downscattering spectrum (solid line; see eq. [A8]). For  $\beta = 0.1, 0.3, 0.5$ , and  $0.8$ , the best-fit parameters are  $b = 0.06, 0.10, 0.18$ , and  $0.38$ , respectively. The low-energy downscattering bump effect is not seen in the emergent spectra.

are  $b = 0.13, 0.15, 0.21$ , and  $0.62$ , respectively. ST85 give the corresponding value of  $b = 0.234$  (related to our  $b$ -parameter for  $\beta = 0.05$ ). From this comparison it is evident that the scattering effect of the cavity becomes stronger with the optical depth decrease. As expected, the analytical spectra as solutions of the diffusion problem in the Thomson regime may depart from the MC-simulated spectra for  $\tau \lesssim 2$  at high energies when the electron opacity is less than the Thomson opacity. The central source spectrum (Fig. 5, dashed line) is slightly less modified by the scattering in the wind (see the MC histogram for the simulated spectrum) than that using the diffusion spectrum (solid line).

Another interesting case is the downscattering modification of the Comptonization spectrum (see, e.g., ST80; Titarchuk 1994). The incident Comptonization spectrum can be well fitted by a power-law spectrum with an exponential cutoff, namely,

$$\varphi_{\text{Comp}}(z) \approx Az^{-\alpha} \exp(-z/z_*), \quad (9)$$

where  $z_* = E_*/m_ec^2$  is the dimensionless photon energy and the cutoff energy  $E_*$  is related to the Compton cloud electron temperature  $kT_e$ , namely,  $E_* \approx 2kT_e$ . The downscattering modification of the spectrum (see eq. [A8]) can be written using the

expansion from equation (5). It can be shown that for  $\varepsilon = 0$  and  $z_* \rightarrow \infty$ , equation (A8) is reduced to equation (7). In Figures 6 and 7 we present the MC-simulated spectra for the power law with exponential-cutoff incident spectra for  $\tau = 4$  and  $2$ , respectively, along with the analytically calculated spectra (see eqs. [A8] and [A20]–[A25]). The MC-simulated spectra are well described by the analytical model for all  $\beta \lesssim 0.8$ . It is worth noting that the downscattering bumps are seen in neither the simulated nor the model spectra.

For  $\tau = 4$  and  $\beta = 0.1, 0.3, 0.5$ , and  $0.8$ , the best-fit parameters are  $b = 0.06, 0.10, 0.18$ , and  $0.38$ , respectively. For  $\tau = 2$  and the same  $\beta$ , the best-fit parameters are  $b = 0.14, 0.21, 0.30$ , and  $0.59$ , respectively. It is worth noting that the values of the  $b$ -parameter for small  $\beta \lesssim 0.1$  are almost independent of the shape of the incident spectrum (within the error bar  $\delta b = \pm 0.005$ ) and depend on  $\tau$  only.

Comparison of the simulated and analytically calculated spectra leads us to conclude that the simulated spectra can be well described by the analytical model with only one free parameter  $b$  that is related to the mean number of photons scattering in the wind ( $N_{\text{av}} = 1/b$ ). It means that the continuum spectral formation in the pure scattering wind is dictated by the mean number of scatterings,  $N_{\text{av}}$ , only but that the value of  $N_{\text{av}}$  is determined by

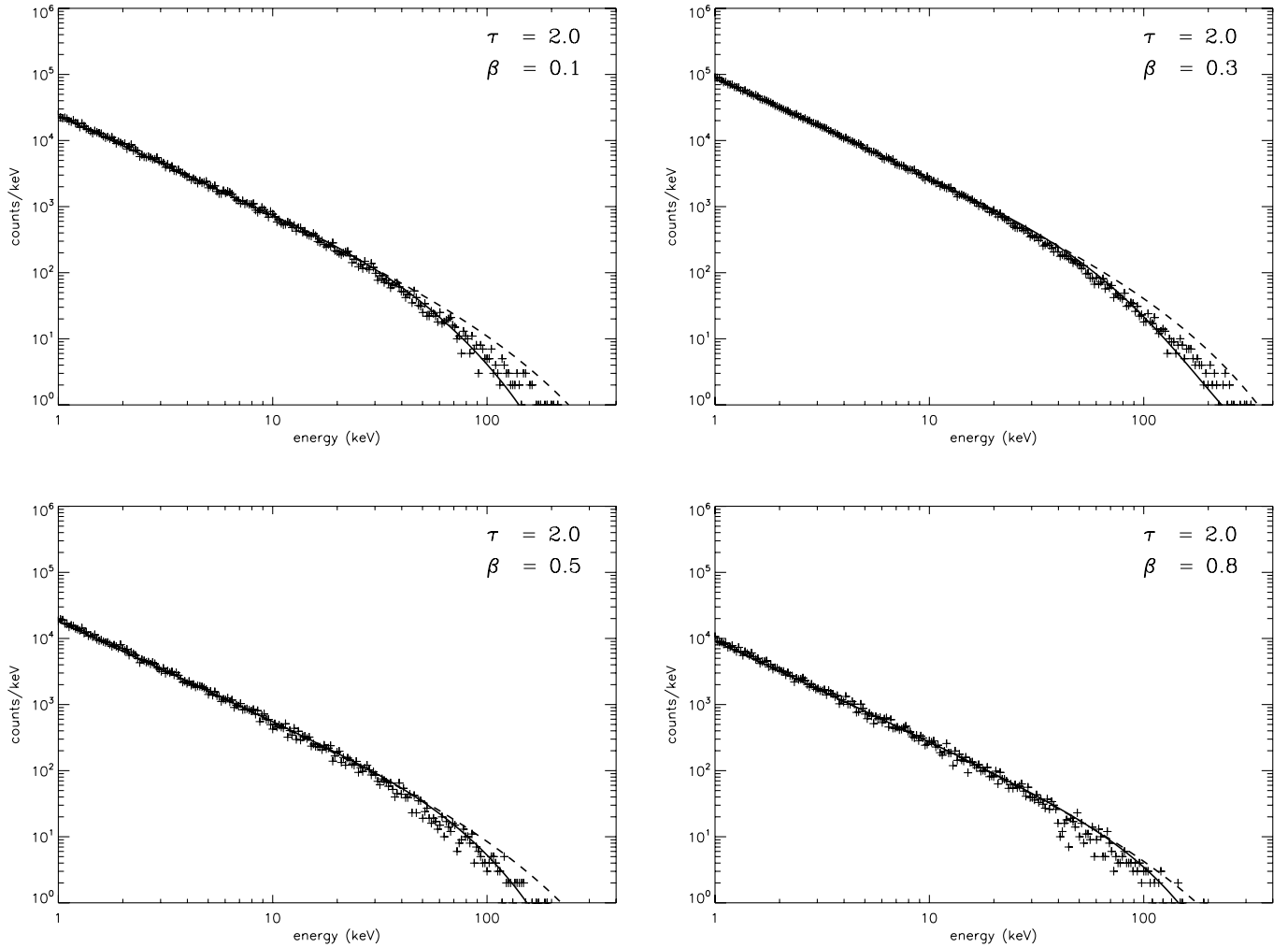


FIG. 7.— Same as Fig. 6, but for  $\tau = 2$ . For  $\beta = 0.1, 0.3, 0.5$ , and  $0.8$ , the best-fit parameters are  $b = 0.14, 0.21, 0.30$ , and  $0.59$ , respectively.

the combined effect of the wind optical depth  $\tau$  and the dimensionless wind velocity  $\beta$ .

### 3.3. K $\alpha$ Line Formation in the Outflow

Another observational feature of the wind is the strong broad feature of the K $\alpha$  line in the spectrum. Recently, Shaposhnikov & Titarchuk (2006) demonstrated that these strong iron lines are present in all spectral states of Cyg X-1. They also showed that the equivalent width (EW) of the K $\alpha$  line increases with the photon index  $\Gamma$  from about 150 eV in the low/hard state to about 1.3 keV in the high/soft and very soft states.

The X-ray photons of the central source illuminate the wind (see Fig. 1). The wind gas is heated by Compton scattering and photoionization by photons coming from the central object and is cooled by radiation, ionization, and adiabatic expansion losses (LT04). The photons above the K edge energy are absorbed and ionize iron atoms, which leads to the formation of the strong K $\alpha$  line. LT04 calculated ionization, temperature structure, and the EWs of Fe K $\alpha$  line formed in the wind. For the wide set of parameters for the wind (velocity, Thomson optical depth  $\tau$ ) and the incident Comptonization spectrum (index, Compton cloud electron temperature), they established that the EW of the line should be about 1 keV and less for the line to be observed. LT04 also predicted that in this case the inner radius of the wind should be situated at  $(10^3 - 10^4)/\tau$  Schwarzschild radii away from the central object.

#### 3.3.1. The Spectral Line Redshift in Outflow: Analytical Description

In Figure 1 we show the picture of the line photon propagation in the wind. At each consecutive scattering, the line photon on average loses its energy; in other words, it is redshifted. A photon emitted near the inner boundary and subsequently scattered by an electron moving with velocity  $V_1$  is received by an electron moving with velocity  $V_2$ , as shown in Figure 1. The change in frequency is

$$\nu_2 = \nu_1 [1 + (\mathbf{V}_1 - \mathbf{V}_2) \cdot \mathbf{n} / c], \quad (10)$$

where  $\mathbf{n}$  is a unit vector along the path of the photon scattered at the next point.

We remind the reader that in the static and spherically symmetric medium and where electrons experience a random (Brownian) motion only, the mean energy change per scattering,  $\langle \Delta E \rangle$ , for photons undergoing quite a few scatterings is proportional to the square of the electron velocity, namely,  $\langle \Delta E \rangle \propto (V/c)^2$  (see, e.g., Rybicki & Lightman 1979; ST80).

On the other hand, for photons undergoing numerous scatterings in the bulk flow,  $\langle \Delta E \rangle$  is just proportional to  $V/c$  (see Titarchuk et al. 1997, Appendix D; TKB03). In order to make an estimate of the loss per scattering, one has to find the response of the energy operator of the diffusion kinetic equation (see TKB03,

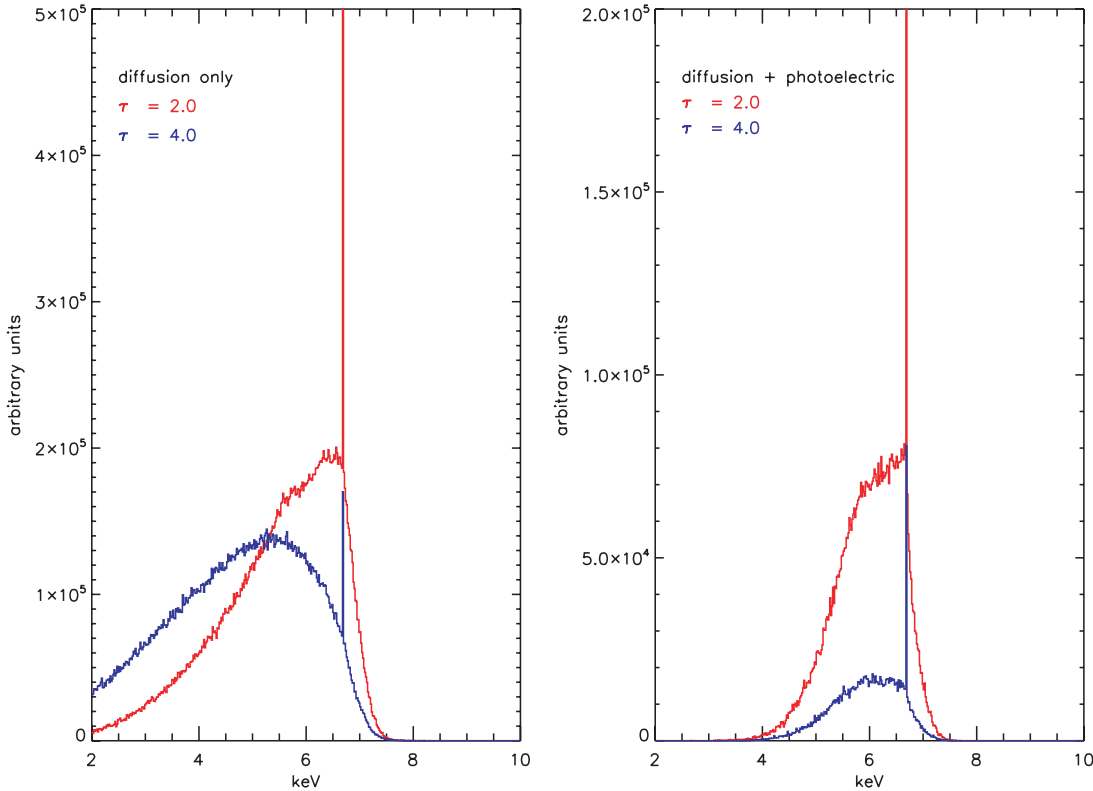


Fig. 8.—Line profiles as a function of  $\tau$  (for  $\beta = 0.1$ ). Primary photons are generated at the bottom of the outflow. *Left*: Line profiles for the pure scattering case; *right*: that for the scattering plus absorption case. In each case, the fixed parameters are  $E_0 = 6.6$  keV and  $kT_e = 0.1$  keV. The normalization of the direct nonscattering line component is suppressed for  $\tau = 2$ . The real normalizations are  $A_N = 1.35 \times 10^6$  and  $1.29 \times 10^6$  for the diffusion and diffusion + absorption cases, respectively.

eqs. [3] and [18]) to a delta-function injection. In Appendix B1 we show that in this standard diffusion approximation  $\langle \Delta E \rangle$  is proportional to the velocity divergence, namely,

$$\langle \Delta E \rangle \approx -\frac{4}{3} \frac{\nabla(V/c)}{\kappa} E_0 \sim \frac{8}{3} \frac{\beta}{\tau} E_0, \quad (11)$$

where  $\kappa$  is the scattering coefficient (or the inverse of the scattering mean free path). But this method provides a qualitative estimate of the redshift effect in the outflow rather than a quantitative one. The value of the numerical factor  $4/3$  in equation (11) is not precisely correct, which suggests that the factor  $4/3$  should be replaced by the right one; however, the form of the exact equation actually depends on  $\beta = V/c$  and  $\tau$  in a more complex way. Equation (11) should be then taken only as an estimate.

A useful result of the  $\langle \Delta E \rangle$  estimate is obtained using the scattering geometry method (see Appendix B2),

$$\langle \Delta E \rangle \approx -\beta f / (2\tau) \sqrt{1 - (f/2\tau)^2} E_0. \quad (12)$$

Below we utilize the MC simulations to show that the numerical factor  $f$  in equation (12) is about 1. Comparison of equations (11) and (12) leads us to conclude that  $\langle \Delta E \rangle$  is proportional to  $\beta$  but that it is overestimated in equation (11).

The average energy of photons escaping after  $N_{av} = 1/b$  scatterings is

$$\langle E \rangle_{sc} = (1 + \langle \Delta E \rangle)^{1/b} E_0. \quad (13)$$

From here, using equation (12) we obtain

$$\langle E \rangle_{sc} = \left[ 1 - \beta f / (2\tau) \sqrt{1 - (f/2\tau)^2} \right]^{1/b} E_0. \quad (14)$$

### 3.3.2. MC-Simulated Spectral Lines in Outflow: Evidence of the Strong Redshift Effect in the Outflow

We simulate line profiles for different optical depths of the wind. In Figure 8 (*left*) we present examples of the line profiles for simulations in which we take into account only the pure electron scattering in the flow, neglecting photoelectric absorption. In Figure 8 (*right*) we present the spectral profile of the line obtained as a result of the electron scattering in the flow along with photoelectric absorption. When the X-ray continuum spectrum of the central source illuminates the wind, the seed K $\alpha$  photons are formed in the innermost part of the wind. The photoabsorption profile as a function of energy, calculated by LT04, is related to the specific case of  $\beta = 0.1$ ,  $\alpha = 0.5$ , and  $kT_e = 50$  keV for which the inferred LT04 model parameter  $r_{in}\tau/L_{40} = 6 \times 10^{12}$  cm. The model and X-ray continuum parameters are the following:  $r_{in}$  is the outflow inner radius,  $L_{40}$  is the luminosity of the central source in units  $10^{40}$  ergs s $^{-1}$ ,  $\alpha$  is the energy spectral index, and  $kT_e$  is the electron temperature of the Comptonization spectrum (see details of the photoabsorption calculations in LT04). We find that the height scale of the source exponential distribution  $H$  is only a small fraction of the inner radius or in other words  $H/r_{in} \sim 0.04\tau$  is a small fraction of the optical thickness of the outflow. Thus, *the sources of K $\alpha$  are distributed in the innermost part of the flow*. We simulate the line profiles for  $\tau = 2$  and  $4$ ,  $kT_e = 0.1$  keV,  $\beta = 0.1$ , and for an initial seed photon energy  $E_0 = 6.6$  keV.

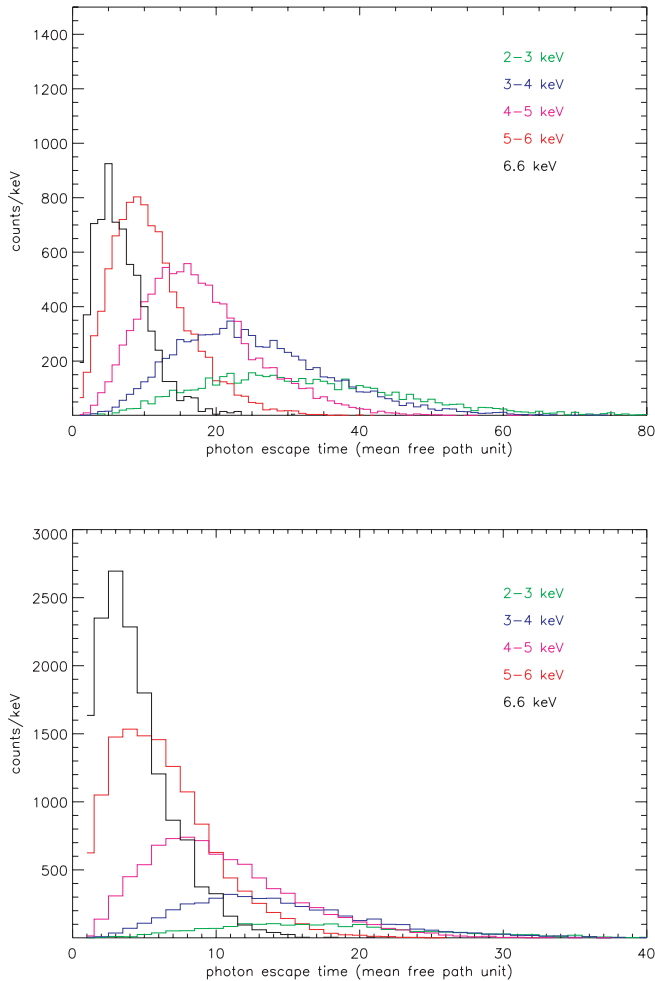


FIG. 9.—Timing properties of the line propagation in the outflow. A flash of monochromatic photons at 6.6 keV is simulated and propagated. Photons escaping from the bottom atmosphere without scattering are at 6.6 keV (see Fig. 1). The model parameters used here are  $kT_e = 0.1$  keV,  $\beta = 0.1$ , and  $\tau = 4$  (*top*) or 2 (*bottom*). We show the arrival time of photons at the top of the cloud for five energy bands, in free path time units  $t_{fp} = l/c$ . Soft lags, low-energy emission at later times, are clearly seen. The photon distribution over escape time integrated over energies can be fitted with an exponential law  $b \exp(-bt/t_{fp})$  (shown in Fig. 2). The values of  $b = 0.057$  and  $0.144$  for  $\tau = 4$  and 2, respectively (and consequently the average number of scatterings  $N_{av} = 1/b$ ), are very close to  $b$  (or  $N_{av}$ ) obtained from the best-fit analytical spectrum for the same values of  $\beta$  and  $\tau$ .

One can clearly see the red-skewed part of the spectrum formed by photons undergoing multiple scatterings, along with the primary peak formed by photons escaping directly to the observer. The normalization of the direct nonscattering line component is suppressed for  $\tau = 2$ . The real normalizations are  $A_N = 1.35 \times 10^6$  and  $1.29 \times 10^6$  for the diffusion and diffusion + absorption cases, respectively.

When the effect of the photon photoionization and absorption is taken into account, the red wing (for energies less than 4 keV) and blue wing (for energies higher than 8 keV) of the line have to be suppressed due to high photoelectric absorption opacities. Despite this photoabsorption suppression, the red-skewed shape of the line is retained. Thus, one can conclude that *the red-skewed line profiles are intrinsic signatures of outward propagation of K $\alpha$  photons generated at the bottom of the outflow due to the outflow illumination by the X-ray hard radiation of the central source*.

In Figure 9 we show timing properties of the line propagation in the outflow for five energy bands for the pure scattering case.

In the plot, the time is given in the free path time units  $t_{fp} = l/c$ . The iron line photons generated at the bottom of the atmosphere are emitted at 6.6 keV. The model parameters used here are  $kT_e = 0.1$  keV,  $\beta = 0.1$ , and  $\tau = 4$  (Fig. 9, *top*) and 2 (Fig. 9, *bottom*). We show the arrival time of photons at the top of the cloud for five energy bands, in free path time units  $t_{fp}$ . Soft lags, low-energy emission at later times, are clearly seen.

It is also worth noting that TKB03 predicted soft lags, namely, that a photon of initial energy  $E_0$  loses its energy with time, i.e.,  $E = \exp(-u_{TKB})E_0$  (compare with our eqs. [12] and [14]). The dimensionless time variable (we call it  $u_{TKB}$ ) used there is a mathematical variable for a convolution method (see their eq. [9]). It can be interpreted as a product of the number of scatterings  $t/t_{fp}$  multiplied by the mean photon inelasticity  $\langle \Delta E \rangle/E$  (eq. [12]), i.e.,  $u_{TKB} = ((\Delta E)/E)(t/t_{fp})$ .

The photon distribution with respect to escape time integrated over energies can be fitted with an exponential law  $b \exp(-bt/t_{fp})$  (shown in Fig. 2). The values of  $b = 0.057$  and  $0.144$  for  $\tau = 4$  and 2, respectively (and consequently the average number of scatterings  $N_{av} = 1/b$ ), are very close to the  $b$  (or  $N_{av}$ ) obtained from the best-fit analytical spectrum for the same values of  $\beta$  and  $\tau$ .

We also check the analytical estimate of the average redshift of the line energy using equation (14) and that obtained from our simulations with the values  $\langle E \rangle_{sc} = 4.56$  and  $5.27$  keV for  $\tau = 4$  and 2, respectively. On the other hand, keeping in mind the values of  $b$  related to a given  $\tau$  we can obtain the same values of  $\langle E \rangle_{sc}$  as the simulated ones using equation (14) with  $f = 1.3$  and  $1.7$  for  $\tau = 2$  and 4, respectively. These values of  $f > 1$  are expected in the framework of our analytical estimate of  $\langle E \rangle$ . (See details of the derivation in eq. [B11].) It is worth noting that now we can calculate  $\varepsilon = \langle \Delta E \rangle/E_0$ , which follows from equation (12) using the  $f$  inferred from our simulations. They are  $\varepsilon = 0.03$  and  $0.04$  for  $\tau = 2$  and 4, respectively, and  $\beta = 0.1$ .

In Figure 10 we present the emergent line profiles for different values of  $\tau$  and  $\beta$ . Spectral lines as a function of  $\tau$  are for  $\beta = 0.1$  and as a function of  $\beta$  are for  $\tau = 2$ . The source photons are generated at the bottom of the cloud, and the cloud temperature is kept fixed at  $kT_e = 0.1$  keV. The red wing of the line profile is insensitive to the temperature of the flow if  $kT_e < 1$  keV. On the other hand, the blue wing becomes broader with  $kT_e$ , but its relative width is still smaller than that of the red wing. In fact, the blue wing is affected for energies higher than K edge ( $> 8$  keV) if the photoabsorption is taken into account (see Fig. 10, *bottom left*). In general, the photoabsorption narrows the line profile (compare the lines profiles in the top and bottom panels of Fig. 10).

The line profiles depend quite strongly on  $\tau$  and  $\beta$ . The shape of the red wing below the broad peak (see Fig. 10) follows a power law with an index that is a strong function of  $\tau$  and  $\beta$ . Our calculated indices are in agreement with the TKB03 results for  $\beta < 0.5$  and  $\tau_{eff} = 3\beta\tau > 1$ . In TKB03, the photon indices are equal to  $\Gamma = 2 + \lambda_k^2$ , where  $\lambda_k^2$  are eigenvalues calculated using their equation (30).

When  $\beta \sim 1$  the spectrum of scattered photons becomes flat even for  $\tau = 2$ . The relativistic spherical outflow completely washes out the bump induced by scatterings (see Fig. 10, *right*). However, for relatively small  $\beta$ , the power-law tails remain steep (see Fig. 10, *left*). This is very similar to the results obtained by TKB03.

#### 4. COMPARISON OF MC-SIMULATED LINE PROFILES WITH THE DATA

In Figures 11 and 12 (*left*) we present the results of fitting our model to the *XMM-Newton* European Photon Imaging Camera (EPIC) data of Wilms et al. (2001) obtained during the observation

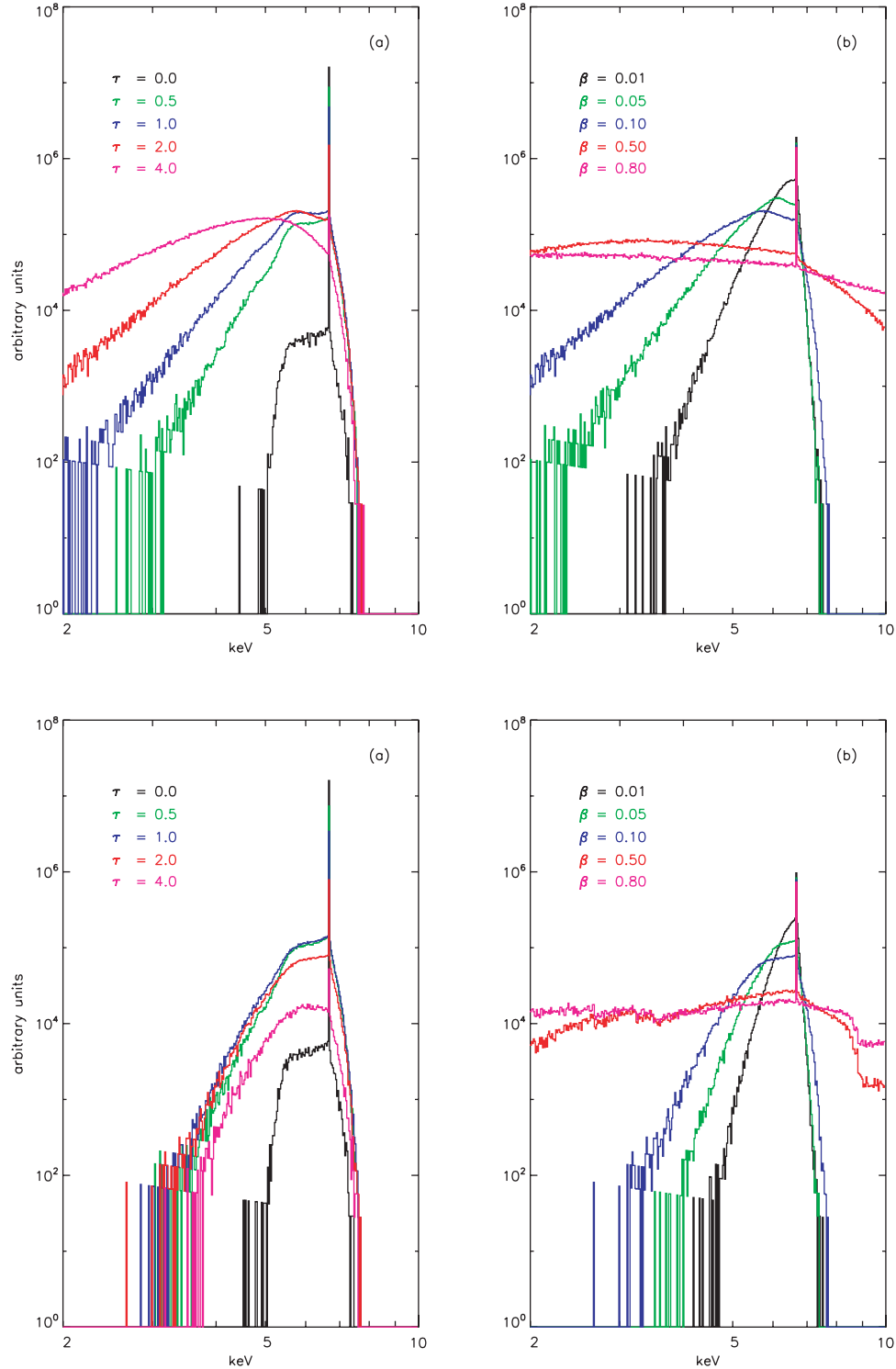


FIG. 10.—Line profiles as a function of  $\tau$  and  $\beta$  for the pure scattering case (top) and the scattering plus absorption case (bottom). Primary photons are generated in the bottom of the outflow. In each case, the fixed parameters are  $E_0 = 6.6$  keV and  $kT_e = 0.1$  keV. Spectral lines as a function of  $\tau$  are for  $\beta = 0.1$  and that as a function of  $\beta$  for  $\tau = 2$ . Note the case with notation  $\tau = 0.0$  (left panels) corresponds to  $\tau = 0.01$ .

of the bright Seyfert 1 galaxy MCG –6-30-15. These observations were focused on the broad Fe K $\alpha$  line at  $\sim 6.4$  keV. For MCG –6-30-15 we fit the continuum with a power law of index 1.8 and compare the residuals with our model. The best-fit parameters of the pure scattering model we found are  $E_0 = 6.51$  keV,  $kT_e = 0.1$  keV,  $\tau = 1.2$ , and  $\beta = 0.02$ . We generated the primary photons at the bottom of the outflow. If we take into account the LT04 model for the photoabsorption along with electron scatter-

ing, then the best-fit parameters become  $E_0 = 6.51$  keV,  $kT_e = 0.1$  keV,  $\tau = 1.7$ , and  $\beta = 0.02$ .

The best-fit model spectrum is very similar to the steep spectrum presented in Figure 10 for  $\beta = 0.01$  (bottom right, black line). The quality of the fits strongly depends on the outflow optical depth  $\tau$  and bulk velocity  $\beta$ . It is less sensitive to the outflow temperature  $kT_e$  unless  $kT_e \lesssim 0.1$  keV. It is important to note that using our diverging outflow model we confirm the finding

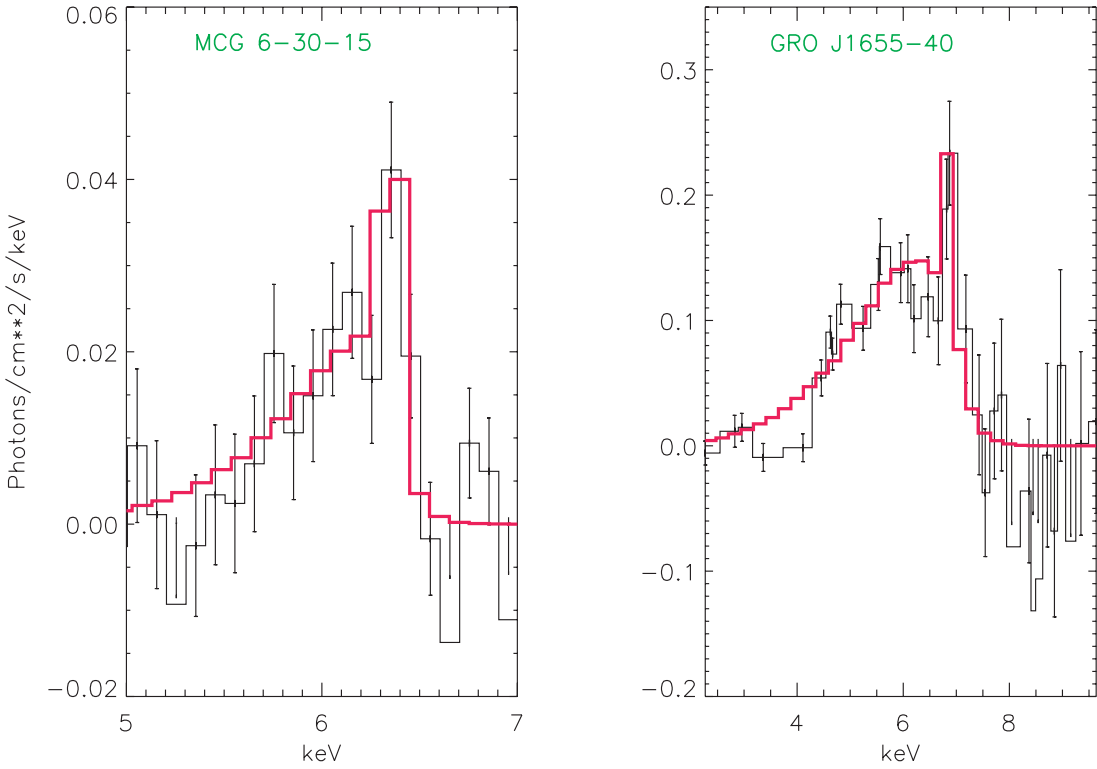


FIG. 11.—Fits of our model to the *XMM-Newton* observations of MCG –6-30-15 (Wilms et al. 2001) and to the *ASCA* observations of GRO J1655–40 (Miller et al. 2004a). For MCG –6-30-15, we fit the continuum with a power law of index 1.8 and compare the residuals with the pure scattering model. For this model the best-fit parameters that we found are  $E_0 = 6.51$  keV,  $kT_e = 0.1$  keV,  $\tau = 1.2$ , and  $\beta = 0.02$ . Primary photons are generated at the bottom of the outflow (illumination of outflow from inside). For GRO J1655–40 we found the best-fit parameters  $E_0 = 7.1$  keV,  $kT_e = 0.1$  keV,  $\tau = 2.0$ , and  $\beta = 0.1$ .

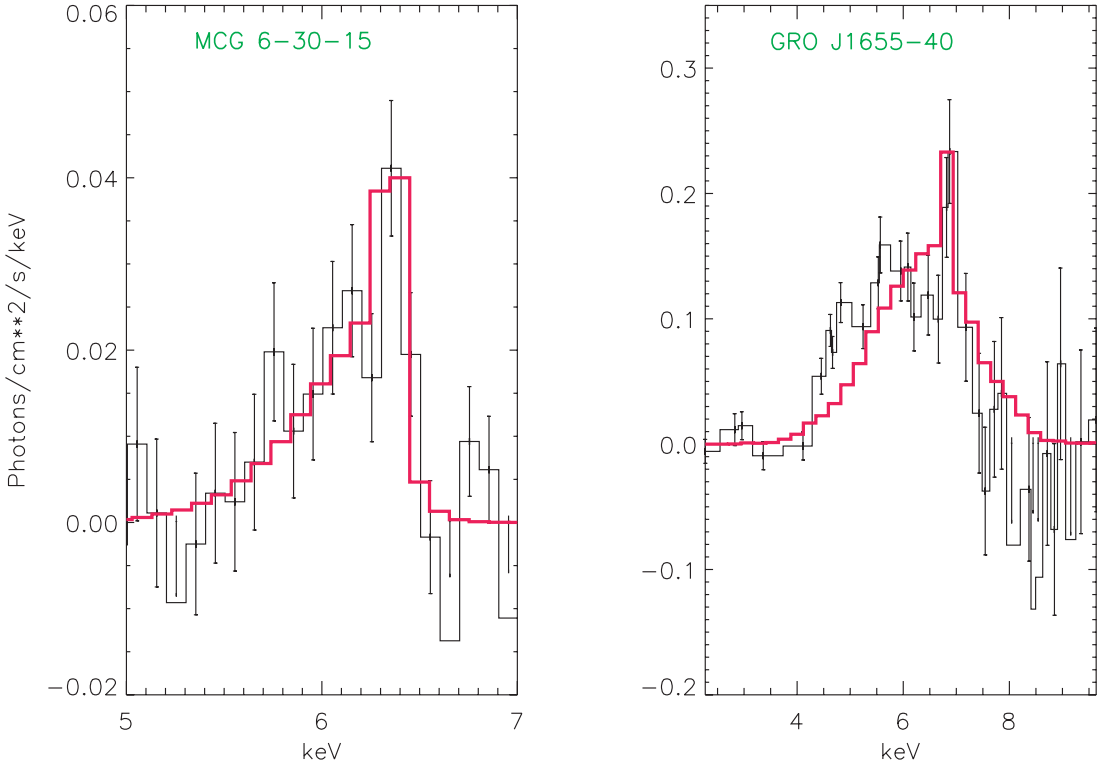


FIG. 12.—Fits of our model to the *XMM-Newton* observations of MCG –6-30-15 and to the *ASCA* observations of GRO J1655–40 using the model for which the photoabsorption along with scattering are included. For MCG –6-30-15, the best-fit model parameters that we found are  $E_0 = 6.51$  keV,  $kT_e = 0.1$  keV,  $\tau = 1.7$ , and  $\beta = 0.02$ . For GRO J1655–40, we found the best-fit parameters  $E_0 = 7.1$  keV,  $kT_e = 0.1$  keV,  $\tau = 3.3$ , and  $\beta = 0.25$ .

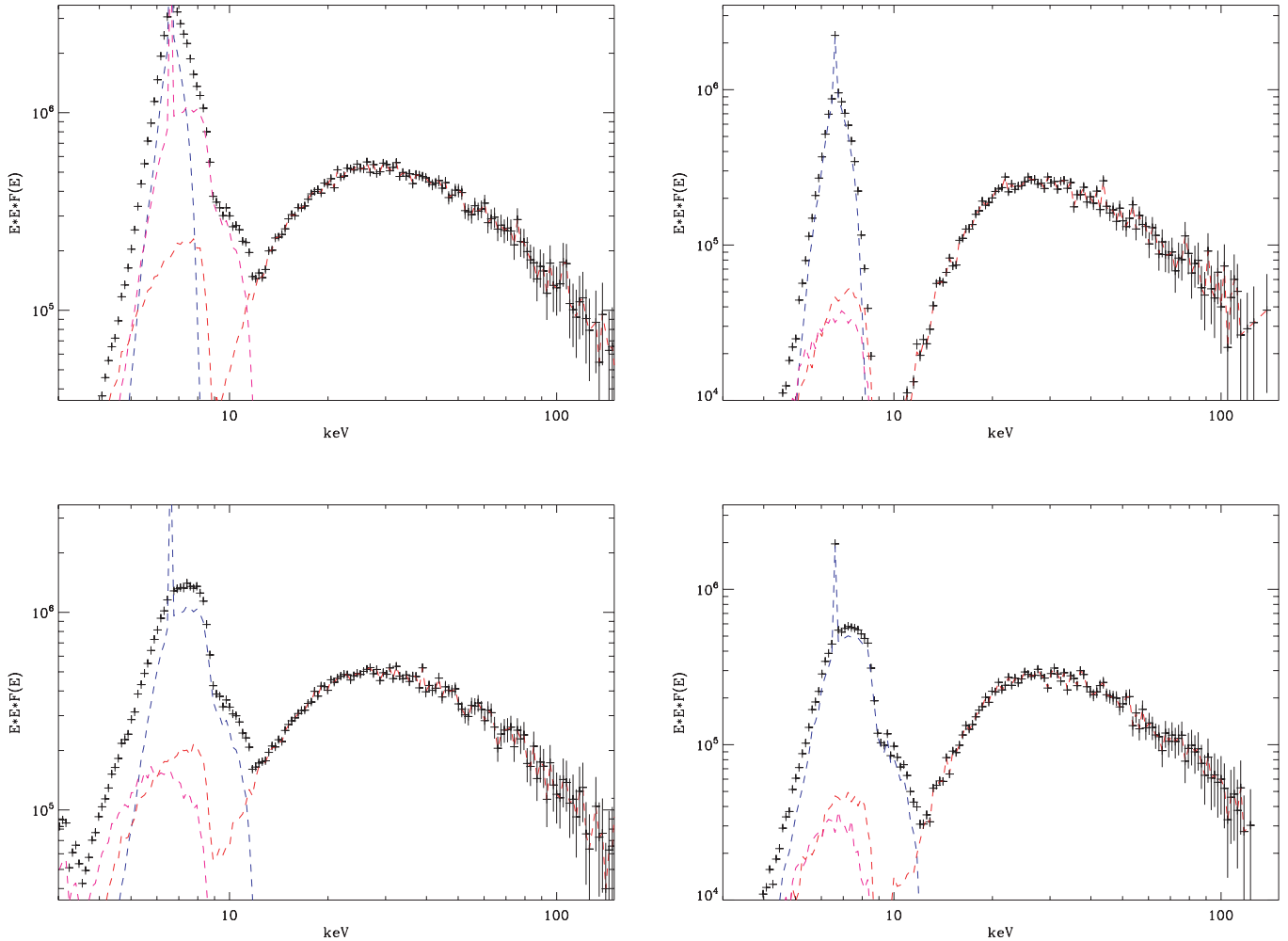


FIG. 13.—Central source spectrum reprocessed through the wind shell. *Top:*  $\beta = 0.1$  and  $\tau_0 = 2$  or 4. *Bottom:*  $\beta = 0.3$ . In the X-ray spectrum of the central source, the photon numbers are the same in the blackbody and hard components. In fact, the ratio of the photon numbers is arbitrary, and it depends on the illumination of the Compton cloud by the source of the blackbody radiation. In this simulation we assume the blackbody color temperature is 1.2 keV. The resulting spectrum is shown by the black histogram, whereas orange and pink lines present the hard and blackbody components of the central source reprocessed in the wind, respectively. A blue line is the K $\alpha$  line formed in the wind. One can clearly see the strong fluorescent K $\alpha$  line, K edge, formed in the wind and a prominent bump around 25 keV. The line consists of narrow and broad components (see narrow blue peak at 6.4 keV in all spectra).

from Fabian et al. (1994) that the velocity of the warm absorber outflow is about  $5000 \text{ km s}^{-1}$  in MCG –6-30-15.

We fitted the red-skewed iron line profiles for four Galactic sources XTE J1550–564, GRO J1655–40, Cyg X-1, and GRS 1915+105 obtained by Miller et al. (2004a). All of these data can be fitted by our model. In Figures 11 and 12 (*right*) we show an example of these fits to the data. For GRO J1655–40 for the pure scattering model we find that the optical depth is  $\tau = 2.0$ , the outflow velocity is  $\beta = 0.1$ , much higher than that for MCG –6-30-15, and  $E_0 = 7.1 \text{ keV}$ . If we take into account the photoabsorption along with scattering in our model, then the best-fit parameters are  $\tau = 3.3$ ,  $\beta = 0.25$ , and  $E_0 = 7.1 \text{ keV}$ . It is worth noting that the fit in this case is not as good as that in the case of the pure scattering model. It can mean that the iron abundance in GRO J1655–40 is less than the cosmic abundance. In fact, LT04 calculated the photoabsorption cross sections for the cosmic abundances.

As we have pointed out, the MC-simulated line profiles are independent of the outflow size and are determined by four parameters  $\tau$ ,  $\beta$ ,  $kT_e$ , and  $E_0$ . The size of the outflow shell can be determined by timing characteristics, such as variability time-scales and time lags. Our model predicts soft time lags, i.e., the

time lags become longer as energy decreases. Time lags are scaled with the light crossing time  $t_{\text{cross}}$  from 1 to a few  $t_{\text{cross}}$ . Unfortunately, time lag information is not yet available for all sources analyzed. The only available information at present is the lack of the iron line variability with respect to the continuum for a number of extragalactic sources (Markowitz et al. 2003). Thus, one can suggest that these line features are formed in a more extended configuration than the source of the continuum (which is presumably a Compton cloud close to the compact object). Here we demonstrate how our model can be used in the analysis of the line data. The detailed interpretation of the line data using our outflow model will be presented in a separate publication.

## 5. OUTFLOW REPROCESSING OF X-RAY CONTINUUM SPECTRA: MC-SIMULATED SPECTRA

We also study the modification of the central source X-ray spectrum in the warm outflow as a result of photoionization and downscattering. In Figure 13 we present the simulations for different values of  $\tau = 2$  and 4 and  $\beta = 0.1$  and 0.3. The results of simulations are shown as  $E^2F(E)$  diagrams, where  $F(E)$  is a photon spectrum. In these simulations, the incident (central source) spectrum is approximated by the sum of two components: a

blackbody-shaped radiation presumably coming from the inner part of the accretion disk and a power law with an exponential cutoff coming from the Compton cloud (corona). The parameters used for this input spectrum are the color temperature of the blackbody component  $kT_{bb} = 1.2$  keV, the power-law photon index  $\Gamma = 1.5$  (energy index  $\alpha = 0.5$ ), and the cutoff  $E_{cutoff} = 50$  keV. As shown in Comptonization theory (see, e.g., ST80; Titarchuk 1994), the exponential cutoff energy  $E_{cutoff}$  of the unsaturated Comptonization spectrum is approximately  $2kT_e$ , where  $kT_e$  is the plasma temperature of the Compton cloud. The temperature of spherically symmetric wind is  $kT_e = 0.1$  keV.

For the X-ray spectrum of the central source we assume that the photon numbers are the same for the blackbody and hard components. In fact, the ratio of the photon numbers depends on the illumination of the Compton cloud by the source of the blackbody radiation.

The photoelectric effect is taken into account in these simulations. When a photoelectric event occurred, we drew a random number to first determine if this event occurred in the K shell of iron. The probability of fluorescence is about 30%. The fluorescence photon is then propagated into the cloud in the same way as the input central object spectrum.

In the simulated spectra one can clearly see features of the strong fluorescent  $K\alpha$  line and the deep K edge formed in the wind. The prominent bump around 25 keV is a combined effect of photoionization and downscattering in the wind. The wind modification of the spectra is very sensitive to the optical depths of the wind  $\tau$  and  $\beta$ . For example, for a given  $\beta = 0.1$  (or wind velocity  $0.1c$ ) the depth of the K edge is broader and much deeper for  $\tau = 4$  than for  $\tau = 2$ . As expected, the width of the line increases with  $\beta$  (compare the spectrum for  $\beta = 0.1$  with that for  $\beta = 0.3$ ). It is important to emphasize that the shape of the  $K\alpha$  line consists of narrow and broad components. These narrow- and broad-line features of the line are in fact observed in Cyg X-1 (see the review of the  $K\alpha$  line observations in Cyg X-1 in § 1 of ST06).

The shape of the spectrum for  $\tau = 4$  and  $\beta = 0.3$  is very similar to the observed spectrum of Cyg X-3 (Paper I; S. P. Trudolyubov 2006, private communication). We will present the interpretation of Cyg X-3 data based on the results of our simulations elsewhere.

## 6. DISCUSSION AND CONCLUSIONS

It is important to point out that the Thomson optical depth of the outflow is on the order of unity when the mass outflow rate  $\dot{M}_{out}$  is on the order of the Eddington mass accretion rate  $\dot{M}_{Edd}$  and higher (see, e.g., eq. [4] in King & Pounds 2003; Titarchuk et al. 2007, hereafter TSA07).

Recent *XMM-Newton* observations of bright quasars (Pounds et al. 2003a, 2003b; Reeves et al. 2003) give strong evidence for powerful outflows from the nucleus with mass rates  $\dot{M}_{out} \sim \dot{M}_\odot \text{ yr}^{-1} \sim \dot{M}_{Edd}$  and velocity  $V \sim 0.1c$  (i.e.,  $\beta = 0.1$ ) in the form of blueshifted X-ray absorption lines. These outflows closely resemble those recently inferred in a set of ultraluminous X-ray sources with extremely soft spectral components (Mukai et al. 2003; Fabbiano et al. 2003). It is also worth noting the recent observations of the strong outflows from GRO J1655–40 (Miller et al. 2006) and the nucleus of the Seyfert 1 Galaxy NGC 3783 using an intensive *Hubble Space Telescope/Chandra/Far Ultraviolet Spectroscopic Explorer* monitoring (Crenshaw et al. 2004) and the recent *Chandra* observations of highly obscured active galactic nuclei (Levenson et al. 2004) reported in the AAS HEAD meeting in 2004. In particular, Levenson et al. analyze new *Chandra* observations of three Compton thick Seyfert 2 galaxies with obscuring column densities that exceed  $10^{24} \text{ cm}^{-2}$ . They report

that the  $Fe\ K\alpha$  line is very prominent in these examples, with  $EW > 1$  keV. Thus, one can conclude that powerful mass outflows from Eddington-limited accreting compact objects appear to be a very widespread phenomenon. King & Pounds (2003) and Begelman et al. (2006) argue that the powerful outflows may provide the high luminosity observed in quasars and ultraluminous X-ray sources and imply that such objects have a major effect on their surroundings. They further suggest that the powerful outflow phenomena have barely been explored, and the field promises to be fruitful.

It is outside the scope of this paper to study the consequences of the X-ray radiation for the hydrodynamics of these outflows. Our goal is to elaborate the spectroscopic tools for probing the outflow physical conditions, such as column density (the outflow optical depth), temperature, and iron ionization charge state. Moreover, the photoionization modeling of the outflow (see LT04) permits the determination of its distance from the central black hole (BH).

We have presented the Monte Carlo (MC) simulations of the radiative transfer of monochromatic photons and continuum photons within a diverging outflow, a problem that is also of observational interest, in view of the observations of broad, redshifted Fe lines and downscattering bumps (so-called reflection features) in extragalactic and Galactic BH candidate spectra. We also provide an analytic description of the simulated spectra, which allows us to understand, in detail, the effect of the downscattering modification of the central source spectrum. In the form presented, the derived formulae of the resulting spectra can be easily used as an efficient analytical tool for the spectral data analysis. We demonstrate that the strength of the downscattering bump is determined by the average number of scatterings that photons undergo in the wind. From our simulations of the pure scattering wind model we find that the average number of scatterings  $N_{av} = b^{-1}$  suffered by the photons in the wind of optical depth  $\tau \gtrsim 2$  is  $\gtrsim \tau^2$  for  $\beta \lesssim 0.1$  (see § 3 for details). On the other hand, the average number of scatterings  $N_{av}$  decreases when the velocity of the wind increases. A larger fraction of the photons are carried out by the flow rather than scattered there when velocities are higher than  $0.1c$ .

The outflow leads to a redshift of the photon energy producing a broad, red component (see Fig. 1 for illustration of this redshift effect) not unlike those of the  $Fe\ K\alpha$  lines observed. We demonstrate analytically and numerically (using MC simulations) that the mean photon energy change per scattering in the outflow,  $\langle \Delta E \rangle$ , is a first-order effect with respect of  $V/c$ , namely,  $\langle \Delta E \rangle \propto -V/c$ . We further emphasize that the red-skewed line features appear when the line photons are generated very close to the bottom of the outflow due to the outflow illumination by the hard X-ray radiation of the central source.

An important result of our simulations (see also the results from TKB03) is the natural suppression of a blue wing in the iron line feature without the need to invoke any specific geometric arrangement for the emission. The illumination of the outflow from inside by the X-ray radiation is natural for a compact source geometry in which the X-ray radiation originates from the innermost part of the source (a Compton cloud along with a disk). The powerful wind presumably starts in the outskirts of the source (see Everett & Ballantyne 2004 and TSA07 for the wind model). In our model, the red wing photons have undergone numerous scatterings in an (effectively) optically thick medium, with an associated first-order redshift in each scattering. It is not surprising that the blue wing, as a result of the second-order  $(V/c)^2$  effect, is weak for  $kT_e \lesssim 1$  keV and  $\beta = V/c \lesssim 0.1$ .

*This red-skewed line is a natural consequence of the first-order Doppler effect in the presence of multiple scattering and*

*photoabsorption events in the wind. It does not require any particularly fine-tuned geometric arrangement.*

LT04 find the self-consistent temperature and ionization structure of the wind shell as a function of the parameter (radius/luminosity,  $r_{\text{in}}\tau/L_{40}$ , where  $r_{\text{in}}$  is the inner outflow radius and  $L_{40}$  is the X-ray luminosity in units of  $10^{40} \text{ ergs s}^{-1}$ ) for a given Thomson optical depth of the shell. It is evident that the ionization parameter  $L_{40}/nr^2$  is constant throughout the shell (i.e., for  $r > r_{\text{in}}$ ) if the velocity of the wind is constant throughout the flow. Thus, the LT04 solution allows one to determine the size of the shell base for a given luminosity in which a red-skewed line is observed. LT04 derive the range of parameter  $r_{\text{in}}/L_{40}$  for which the outflow-produced stable solution exists. The allowed  $r_{\text{in}}/L_{40}$  values are concentrated around  $10^{12}\text{--}10^{13} \text{ cm}$ .

*Our model predicts the soft lags to be a function of  $E/E_0$ ,  $\beta$ , and  $\tau$ . The combination of the red-skewed features along with the soft time lags that strongly depend on  $\beta$ ,  $\tau$ , and  $kT_e$  are intrinsic signatures of any diverging outflow.*

The demonstrated application of our outflow model to data points out a potentially powerful spectral diagnostic for probes

of the outflow–central object connection in Galactic and extra-galactic BH sources. In particular, analyzing MCG –6-30-15 data (see § 4) we infer that bulk outflow velocity is about  $6000 \text{ km s}^{-1}$ . On the other hand, the O vii edge in the warm absorber of MCG –6-30-15 indicates that the flow along the line of sight is about  $5000 \pm 1000 \text{ km s}^{-1}$  (Fabian et al. 1994). Thus, using a new X-ray spectroscopic method (our diverging [outflow] model) we confirm the early finding (which used UV spectroscopy) that the velocity of the warm absorber outflow of MCG –6-30-15 is about  $5000 \text{ km s}^{-1}$ .

L. T. acknowledges the support of this work by the Center for Earth Observing and Space Research of George Mason University. L. T. also appreciates productive discussions with Ralph Fiorito, Stuart Wick, Phil Uttley, Martin Laming, and Chris Shrader. We also acknowledge discussion of the paper results with the referee and his/her constructive and interesting suggestions.

## APPENDIX A

### DOWNSCATTERING SPECTRUM: DERIVATION OF ANALYTICAL SPECTRA

#### A1. POWER LAW AS A SPECTRUM OF THE PRIMARY PHOTONS

Here we demonstrate how equation (2) can be analytically calculated using the steepest descent method. First, to illustrate the main idea of this derivation, we consider the simplest case in which  $\varepsilon = 0$  and  $\varphi(z) = z^{-\alpha}$  when

$$W^{(0)}(z, u) = (1/z - u)^{\alpha-1} \quad (\text{A1})$$

and integral (2) is given by equation (6), where  $\mathcal{P}(u) = b \exp(-bu)$ . If we change the variable  $v = (1/z - u)z$  under integral (6), then the integral can be rewritten as

$$\mathcal{F}_E(z) = \frac{Abz^{-\alpha}}{z} \exp\left(\frac{-b}{z}\right) \int_0^1 v^{\alpha-1} \exp\left(\frac{bv}{z}\right) dv. \quad (\text{A2})$$

Because the dimensionless frequency  $z = E/m_e c^2 \ll 1$  for the energy range of interest ( $E \ll 511 \text{ keV}$ ) and  $b \gtrsim 0.1$ , there is a wide energy range in which  $\lambda = b/z$  is a large parameter. Then the integral in equation (A2) can be calculated analytically using the steepest descent method. In order to do this, one should expand the integrand function  $v^{\alpha-1}$  in the Taylor series,

$$v^{\alpha-1} = 1 + \frac{(1-\alpha)}{1!}(1-v) + \frac{(1-\alpha)(2-\alpha)}{2!}(1-v)^2 + \dots + \frac{(1-\alpha)(2-\alpha)\dots(n-\alpha)}{n!}(1-v)^n + \dots, \quad (\text{A3})$$

near the point  $v = 1$ , where  $\exp(bv/z)$  has a sharp maximum. It is worth noting that the series in equation (A3) converges for all  $v < 1$ , and thus, the series presentation of the emergent spectrum in equation (A2) is exact for any  $\lambda = b/z$ ,

$$\mathcal{F}_E(z) = \frac{Abz^{-\alpha}}{z} \exp\left(\frac{-b}{z}\right) \left[ L_0(\lambda) + \frac{(1-\alpha)}{1!} L_1(\lambda) + \frac{(1-\alpha)(2-\alpha)}{2!} L_2(\lambda) + \dots + \frac{(1-\alpha)(2-\alpha)\dots(n-\alpha)}{n!} L_n(\lambda) + \dots \right], \quad (\text{A4})$$

where

$$L_n(\lambda) = \int_0^1 (1-v)^n \exp(\lambda v) dv \quad \text{for } n = 0, 1, 2, \dots \quad (\text{A5})$$

If we introduce the new variable  $u = (1-v)/z$  in the integral in equation (A5) then equation (A4) can be rewritten in the form

$$\begin{aligned} \mathcal{F}_E(z) = Az^{-\alpha} &\left[ M_0(z^{-1}) + \frac{(1-\alpha)}{1!} z M_1(z^{-1}) + \frac{(1-\alpha)(2-\alpha)}{2!} z^2 M_2(z^{-1}) \right. \\ &\left. + \dots + \frac{(1-\alpha)(2-\alpha)\dots(n-\alpha)}{n!} z^n M_n(z^{-1}) + \dots \right], \end{aligned} \quad (\text{A6})$$

where  $M_n(z^{-1})$  is defined by equation (8).

## A2. POWER LAW WITH EXPONENTIAL CUTOFF AS A SPECTRUM OF PRIMARY PHOTONS

In the general case of the incident spectra and  $\varepsilon > 0$ , equation (2) for the emergent spectrum can be rewritten as

$$\mathcal{F}_\nu(z, \varepsilon) = \frac{b}{z} \int_0^1 W^{(\varepsilon)}[z, vu_{\max, \varepsilon}(z)] \exp(-\lambda v) dv, \quad (\text{A7})$$

where  $\lambda = bu_{\max, \varepsilon}(z) \gtrsim 1$ ,  $W^{(\varepsilon)}(z, u) = e^{-4\varepsilon u/3} [\psi^{(\varepsilon)}(z, u)] \varphi[\psi^{(\varepsilon)}(z, u)]$ , and  $u = vu_{\max, \varepsilon}(z)$ . Because the integrand has a sharp exponential maximum at  $v = 0$  (or  $u = 0$ ), one can expand the nonexponential function  $W^{(\varepsilon)}(z, u)$  in series over  $v$  (or  $u$ ). That leads to the formula

$$\begin{aligned} \mathcal{F}_\nu(z, \varepsilon) = & \frac{A}{z} \left[ W^{(\varepsilon)}(z, 0) M_0(u_{\max, \varepsilon}) + W_u^{(\varepsilon)(1)}(z, 0) \frac{M_1(u_{\max, \varepsilon})}{1!} \right. \\ & \left. + W_u^{(\varepsilon)(2)}(z, 0) \frac{M_2(u_{\max, \varepsilon})}{2!} + \dots + W_u^{(\varepsilon)(n)}(z, 0) \frac{M_n(u_{\max, \varepsilon})}{n!} + \dots \right], \end{aligned} \quad (\text{A8})$$

where  $W_u^{(\varepsilon)(n)}(z, u)$  is  $n$ th partial derivative of  $W^{(\varepsilon)}(z, u)$  over  $u$  and the moments  $M_n(x)$  ( $x = u_{\max, \varepsilon}$ ) of  $\mathcal{P}(u)$  are written as

$$M_n(x) = -x^n \exp(-x) + nM_{n-1}(x)/b \quad \text{for } n = 1, 2, \dots \quad (\text{A9})$$

For example, for  $n = 0, 1$ , and  $2$  we obtain

$$M_0(x) = 1 - \exp(-bx), \quad (\text{A10})$$

$$M_1(x) = -x \exp(-bx) + (1/b)M_0(x), \quad (\text{A11})$$

$$M_2(x) = -x^2 \exp(-bx) + (2/b)M_1(x). \quad (\text{A12})$$

Because

$$W_u^{(\varepsilon)(n)}(z, 0) = W_u^{(\varepsilon)}(z, 0) \prod_{i=0}^{n-1} [\ln W_u^{(\varepsilon)(i)}(z, u)]'_u (u=0) \quad (\text{A13})$$

and

$$W^{(\varepsilon)}(z, 0) = z\varphi(z), \quad (\text{A14})$$

analytical equation (A8) for the emergent spectrum can be presented as

$$\mathcal{F}_\nu(z, \varepsilon) = \varphi(z) \left( M_0(u_{\max, \varepsilon}) + \sum_{n=1}^{\infty} \left\{ \prod_{i=0}^{n-1} [\ln W_u^{(\varepsilon)(i)}(z, u)]'_u (u=0) \right\} \frac{M_n(u_{\max, \varepsilon})}{n!} \right). \quad (\text{A15})$$

Thus, the resulting spectrum  $\mathcal{F}_\nu(z, \varepsilon)$  is a product of the incident spectrum  $\varphi(z)$  and the downscattering transformation function (the expression in the large parenthesis in eq. [A15]) that depends on the properties of the outflow: velocity and optical depth. In fact, the outflow optical depth is related to the parameter  $b$  for a given  $\varepsilon$ .

In fact, the more convenient way to calculate the resulting spectrum  $\mathcal{F}_\nu(z, \varepsilon)$  is to calculate the derivatives  $W_u^{(\varepsilon)(n)}(z, u)$  explicitly using the factorized form of  $W_u^{(\varepsilon)(1)}(z, u)$ , namely,

$$W_u^{(\varepsilon)(1)}(z, u) = W_u^{(\varepsilon)}(z, u)\Phi(z, u), \quad (\text{A16})$$

where

$$\Phi(z, u) = [\ln z_0 \varphi(z_0)]_u, \quad (\text{A17})$$

$$\varphi(z_0) = z_0^{-\alpha} \exp(-z_0/z_*). \quad (\text{A18})$$

Using equations (A17) and (A18), we obtain a formula for  $\Phi(z, u)$ ,

$$\Phi(z, u) = [\ln z_0 \varphi(z_0)]_u = -\frac{4\varepsilon}{3} + \frac{1-\alpha}{z_0} \frac{\partial z_0}{\partial u} - \frac{1}{z_*} \frac{\partial z_0}{\partial u}. \quad (\text{A19})$$

Then one can calculate  $W_u^{(\varepsilon)(n)}(z, u)$  as

$$W_u^{(n)} = \sum_{i=0}^{n-1} C_{n-1}^i W_u^{(n-1-i)} \Phi_u^{(i)} \quad \text{for } n = 2, 3, \dots, \quad (\text{A20})$$

where  $C_n^k = n(n-1)\dots(n-k-1)/k!$  and  $W_u^{(0)} = W$ . Here and below we omit the superscript  $\varepsilon$  in order to simplify the notation for  $W_u^{(\varepsilon)(n)}(z, u)$  and its derivatives. We also introduce new notations  $W_u^{(i)} = W^{(i)}(z, u)_u$  and  $\Phi_u^{(i)} = \Phi^{(i)}(z, u)_u$ .

Because

$$\frac{\partial z_0}{\partial u} = \left(\frac{\varepsilon}{3}\right) z_0 + z_0^2, \quad (\text{A21})$$

we can write equation (A19) as

$$\Phi(z, u) = \frac{-4\varepsilon}{3} + (1 - \alpha) \left(\frac{\varepsilon}{3} + z_0\right) - \frac{1}{z_*} \frac{\partial z_0}{\partial u} \quad (\text{A22})$$

and find the derivatives of  $\Phi(z, u)$  as

$$\Phi_u^{(n)}(z, u) = (1 - \alpha) \frac{\partial^n z_0}{\partial u^n} - \frac{1}{z_*} \frac{\partial^{n+1} z_0}{\partial u^{n+1}} \quad \text{for } n = 1, 2, 3, \dots \quad (\text{A23})$$

The second and higher derivatives of  $z_0$  over  $u$  are

$$\frac{\partial^2 z_0}{\partial u^2} = \left(\frac{\varepsilon}{3}\right) \frac{\partial z_0}{\partial u} + 2z_0 \frac{\partial z_0}{\partial u}, \quad (\text{A24})$$

$$\frac{\partial^n z_0}{\partial u^n} = \left(\frac{\varepsilon}{3}\right) \frac{\partial^{n-1} z_0}{\partial u^{n-1}} + 2 \sum_{i=0}^{n-2} C_{n-2}^i \frac{\partial^i z_0}{\partial u^i} \frac{\partial^{n-1-i} z_0}{\partial u^{n-1-i}} \quad \text{for } n = 3, 4, \dots \quad (\text{A25})$$

Now all derivatives  $W_u^{(n)}$  in equation (A20) can be calculated very easily, because  $z_0 = z$  at  $u = 0$  by definition.

## APPENDIX B

### THE MEAN PHOTON ENERGY CHANGE IN THE BULK OUTFLOW: ANALYTICAL EVALUATIONS

#### B1. DIFFUSION METHOD

There is a standard procedure to estimate the energy gain and loss per scattering using diffusion approximation (Prasad et al. 1988; Titarchuk et al. 1997, Appendix D). Let us assume that at the initial moment  $t = 0$  the monochromatic line of energy  $E_0$  emits at any point in the scattering medium (outflow). The energy change of the line  $\langle \Delta E \rangle$  due to scattering can be found using the time-dependent diffusion kinetic equation,

$$\frac{\partial n}{\partial u} = L_r n + L_\nu n, \quad (\text{B1})$$

where  $n(r, \nu)$  is the photon occupation number,  $L_r$  and  $L_\nu$  are the space and energy operators, respectively (see TKB03, eq. [3]), and  $u = \kappa c t$  is the time measured in units of the mean time between scatterings (see Rybicki & Lightman 1979; ST80). Our goal is to find a small change of the radiation field background, which at the initial moment is

$$z^3 n|_{u=0} = z^3 n_0 = z \delta(z - z_0). \quad (\text{B2})$$

The energy change per scattering  $\langle \Delta z \rangle = \langle \Delta E \rangle / m_e c^2$  can be found by multiplication of the kinetic equation (B1) by  $z^3$ , substitution of equation (B2) in the right-hand side, and integration over  $z$ . Thus, we have

$$\frac{\delta z}{\delta u} = \langle \Delta z \rangle = \int_0^\infty \frac{1}{3} \frac{\nabla(V/c)}{\kappa} z^4 \frac{\partial n}{\partial z} dz, \quad (\text{B3})$$

where  $\delta z/\delta u$  is a photon energy change per scattering.

Integration by parts gives

$$\langle \Delta z \rangle = -\frac{4}{3} \frac{\nabla(V/c)}{\kappa} \int_0^\infty z^3 n_0 dz. \quad (\text{B4})$$

Substituting  $z^3 n_0 = z\delta(z - z_0)$  (see eq. [B2]) in this equation, we obtain

$$\langle \Delta E \rangle = -\frac{4}{3} \frac{\nabla(V/c)}{\kappa} E_0. \quad (\text{B5})$$

Because

$$\nabla\left(\frac{V}{c}\right) = \frac{2\beta}{r} \quad (\text{B6})$$

and  $\kappa r = \sigma_T n_e r \approx \tau$  for the electron number density of the constant velocity wind, we can rewrite equation (B5) in the form

$$\langle \Delta E \rangle \approx -\frac{8}{3} \frac{\beta}{\tau} E_0. \quad (\text{B7})$$

## B2. GEOMETRY OF PHOTON SCATTERING IN THE OUTFLOW

In this section we evaluate  $\langle \Delta E \rangle$  using equation (10) and the geometry of photon scattering in the outflow. Ultimately, we should calculate the mean of the scalar product of  $(V_1 - V_2) \cdot \mathbf{n}/c$  ( $\mathbf{n}$  is a unit vector along the path of the photon scattered at the next point; see Fig. 1).

The length of the vector

$$|\Delta V| = |V_1 - V_2| = 2V \sin \theta/2 \approx v \sin \theta \quad \text{for } \theta < 1, \quad (\text{B8})$$

where  $\theta$  is the angle between  $V_1$  and  $V_2$ . Let  $l$  be the mean free path between two consecutive scatterings at  $r_1$  and  $r_2$  (see Fig. 1); then

$$\cos \theta = \frac{r_1^2 + r_2^2 - l^2}{2r_1 r_2}. \quad (\text{B9})$$

If  $|r_1 - r_2|/r_1 = \Delta r/r < 1$  ( $r_1 \approx r_2 = r$ ) and  $\Delta r < l^2/2r$ , then we can estimate  $1 - \cos \theta$  as

$$1 - \cos \theta \approx \frac{(l/r)^2}{2}. \quad (\text{B10})$$

Thus, we can find that

$$\sin \theta \approx l/r = 1/(N_e \sigma_T r) = r/(r_{\text{in}} \tau) \sim f/\tau \quad (\text{B11})$$

when  $l/r < 1$  and where the numerical factor  $f \gtrsim 1$ . The precise value of the factor  $f$  can be evaluated using our MC simulations. To derive equation (B11), we use the electron number distribution of the constant velocity wind (see eq. [1]).

The cosine of the angle  $\gamma$  between  $\Delta V = (V_1 - V_2)$  and  $\mathbf{n}$  is

$$\cos \gamma = \cos \psi \cos(\pi - \theta/2) + \sin \psi \sin(\pi - \theta/2) \cos(\varphi - \varphi_0), \quad (\text{B12})$$

where  $\psi$  is a zenith angle between the vector  $\mathbf{n}$  and the normal to vector  $V_1$  directed toward vector  $V_2$  and  $\varphi$  and  $\varphi_0$  are meridian (longitudinal) angles of  $\mathbf{n}$  and  $\Delta V$ , respectively. Then the mean value of  $\cos \gamma$  over the half of the sphere located to the left of the vector  $V_1$  is calculated as

$$\langle \cos \gamma \rangle = \frac{1}{2\pi} \int_0^{2\pi} d\varphi \int_0^{\pi/2} \cos \gamma \sin \psi d\psi = -\frac{1}{2} \cos\left(\frac{\theta}{2}\right). \quad (\text{B13})$$

Thus, using equation (10) and equations (B8)–(B13), one can relate the mean energy change per scattering,  $\langle \Delta E \rangle$ , for photons undergoing quite a few scatterings in the flow with  $\beta$  as

$$\langle \Delta E \rangle \approx -\beta f/(2\tau) \sqrt{1 - (f/2\tau)^2} E_0. \quad (\text{B14})$$

## REFERENCES

- Begelman, M. C., King, A. R., & Pringle, J. E. 2006, MNRAS, 370, 399
- Blandford, R. D., & Payne, D. G. 1981, MNRAS, 194, 1033
- Crenshaw, D. M., et al. 2004, BAAS, 8, 3202
- Everett, J. E., & Ballantyne, D. R. 2004, ApJ, 615, L13
- Fabbiano, G., King, A. R., Zelas, A., Ponman, T. J., Rots, A., & Schweizer, F. 2003, ApJ, 591, 843
- Fabian, A. C., et al. 1994, PASJ, 46, L59
- Gilfanov, M., Churazov, E., & Revnivtsev, M. 1999, A&A, 352, 182
- Kallman, T. R., Palmeri, P., Bautista, M. A., Mendoza, C., & Krolik, J. H. 2004, ApJS, 155, 675
- King, A. R., & Pounds, K. A. 2003, MNRAS, 345, 657
- Laming, J. M., & Titarchuk, L. 2004, ApJ, 615, L121 (LT04)
- Laurent, P., & Titarchuk, L. 1999, ApJ, 511, 289
- . 2001, ApJ, 562, L67
- Levenson, N. A., Weaver, K. A., Heckman, T. M., Krolik, J. H., & Zycki, P. T. 2004, BAAS, 8, 3204
- Lifshitz, E. M., & Pitaevskii, L. P. 1981, Physical Kinetics (Oxford: Pergamon)
- Magdziarz, P., & Zdziarski, A. A. 1995, MNRAS, 273, 837
- Markowitz, A., Edelson, R., & Vaughan, S. 2003, ApJ, 598, 935
- Miller, J., Fabian, A. C., Nowak, M. A., & Lewin, W. H. G. 2004a, in Proc. 10th Marcel Grossmann Meeting, ed. M. Novello, S. Perez Bergliaffa, & R. Ruffini (Singapore: World Scientific), 1296
- Miller, J., Raymond, J., Fabian, A., Steeghs, D., Homan, J., Reynolds, C., van der Klis, M., & Wijnands, R. 2006, Nature, 441, 953
- Miller, J., et al. 2004b, ApJ, 601, 450
- Mukai, K., Pence, W. D., Snowden, S. L., & Kuntz, K. D. 2003, ApJ, 582, 184
- Nandra, K., George, I. M., Mushotzky, R. F., Turner, T. J., & Yaqoob, T. 1997, ApJ, 477, 602
- Nobili, L., Turolla, R., & Zampieri, L. 1993, ApJ, 404, 686
- Payne, D. G., & Blandford, R. D. 1981, MNRAS, 196, 781 (PB81)
- Pottschmidt, K., et al. 2003, A&A, 407, 1039
- Pounds, K. A., Reeves, J. N., King, A. R., Page, K. L., & O'Brien, P. T. 2003a, MNRAS, 346, 1025
- Pounds, K. A., Reeves, J. N., King, A. R., Page, K. L., O'Brien, P. T., & Turner, M. J. L. 2003b, MNRAS, 345, 705
- Prasad, M. K., Shestakov, A. V., Kershaw, D. S., & Zimmerman, G. B. 1988, J. Quant. Spectrosc. Radiat. Transfer, 40, 29
- Reeves, J. N., O'Brien, P. T., & Ward, M. J. 2003, ApJ, 593, L65
- Rybicki, G. B., & Lightman, A. P. 1979, Radiative Processes in Astrophysics (New York: Wiley)
- Shaposhnikov, N., & Titarchuk, L. 2006, ApJ, 643, 1098 (ST06)
- Strohmayer, T. E., & Brown, E. F. 2002, ApJ, 566, 1045
- Sunyaev, R. A., & Titarchuk, L. G. 1980, A&A, 86, 121 (ST80)
- . 1985, A&A, 143, 374 (ST85)
- Tanaka, Y., et al. 1995, Nature, 375, 659
- Titarchuk, L. G. 1994, ApJ, 434, 570
- Titarchuk, L., Kazanas, D., & Becker, P. A. 2003, ApJ, 598, 411 (TKB03)
- Titarchuk, L., Mastichiadis, A., & Kylafis, N. D. 1997, ApJ, 487, 834
- Titarchuk, L., Shaposhnikov, N., & Arefiev, A. 2007, ApJ, in press (astro-ph/0612675) (TSA07)
- Titarchuk, L., & Shrader, C. R. 2005, ApJ, 623, 362 (Paper I)
- Uttley, P., Taylor, R. D., McHardy, I. M., Page, M. J., Mason, K. O., Lamer, G., & Fruscione, A. 2004, MNRAS, 347, 1345
- Wilms, J., Reynolds, C. S., Begelman, M. C., Reeves, J., Molendi, S., Staubert, R., & Kendziorra, E. 2001, MNRAS, 328, L27



## **5. PROJET DE RECHERCHE ET PERSPECTIVES**

### ***Les perspectives instrumentales***

#### **Le projet Simbol-X**

Je compte continuer ma participation au projet spatial *Simbol-X*, actuellement sur le point de passer en phase B. Je devrais gérer, en collaboration avec le chef de projet, la conception et la réalisation de l'anticoïncidence, afin d'en assurer les meilleures performances. Je continuerai aussi à assurer la coordination du groupe « simulation et bruit de fond» afin d'optimiser le plan détecteur.

#### **Le projet IXO**

Notre expérience sur Simbol-X pourrait aussi servir, de manière plus générale, de support aux développements de futures missions X et gamma. Dans cet optique, nous avons commencé, début 2008, une collaboration à l'intérieur de l'« Instrument Working Group », en vue de l'optimisation du système de rejet de bruit de fond du projet XEUS. Au sein de l'IWG, nous avons participé à un groupe de travail, transverse sur tous les instruments, d'étude du bruit de fond et de sa réduction. Cet été, la mission ESA « Cosmic Vision » XEUS a évolué vers une mission réunissant l'Europe, les USA, et le Japon, appelée IXO. La mission IXO est encore en cours de définition, mais elle embarquera probablement, comme XEUS, une charge utile complexe équipée de multiples instruments, principalement le NFI (Narrow Field Imager), le HTRS (High Timing Resolution Spectrometer) et le WFI/HXI (Assemblage d'un Wide Field Imager et d'un Hard X-ray Imager).

Un concept de bouclier d'anti-coïncidence a été présenté, avec l'accord du CNES, lors de l'IWG, dans le cadre du HXI, le détecteur à haute énergie proposé pour XEUS par l'agence spatiale Japonaise (JAXA). Nous avons aussi pris des contacts avec le groupe Japonais (université de Tokyo et JAXA/ISAS). Le principe d'une collaboration a été bien accueilli et doit faire l'objet d'une définition détaillée incluant le partage des tâches. Il a été convenu que l'équipe Japonaise, sous la responsabilité du Pr. Takahashi, proposait son concept pour IXO, et qu'une collaboration avec la France était souhaitable, notamment sur trois volets potentiels et distincts :

- les détecteurs CdTe et leur électronique frontale bas bruit, ultra basse consommation, tolérante aux radiations, un point développé par le labo CdTe du SAp.
- la simulation de bruit de fond et l'optimisation de l'instrument,
- et enfin l'étude du système d'anticoïncidence.

Je participerai à ces deux derniers points à l'APC, L'étude du système d'anticoïncidence se fera aussi dans le cadre d'une demande spécifique de R&T CNES.

## D'autres projets en perspectives ...

Nous avons aussi le projet de définir pour un avenir assez lointain un télescope utilisant l'effet Compton pour imager le ciel au-delà du MeV, avec une bonne résolution angulaire, ce qui n'a jamais été fait. Les progrès actuels des détecteurs semi-conducteurs ou des cristaux, en spectroscopie comme en imagerie, nous permettraient d'atteindre des performances très prometteuses pour des projets futurs. Ce projet a fait l'objet d'une demande de financement pour l'APC dans le cadre européen du FP7.

## *Les perspectives observationnelles*

### **Observations jusqu'à plusieurs MeV de Cygnus X-1 grâce à Integral**

Les nombreuses observations Integral que nous pouvons maintenant cumulées en provenance du système le plus brillant, Cygnus X-1, vont nous permettre de connaître, dans un futur proche, l'émission d'un système à trou noir jusqu'à plusieurs MeV. Nous pourrons voir si l'état dur, où la source passe 90% de son temps, est toujours décrit par un modèle ST, ou si une composante supplémentaire est nécessaire. Nous pourrons aussi mesurer l'éventuelle coupure en énergie du spectre dans l'état mou, si nous avons la chance d'observer suffisamment longtemps cette source dans cet état. Nous pourrons aussi commencer à avoir ces informations pour des systèmes moins brillants.

### **Observation de la polarisation en provenance des systèmes à trous noirs**

Le développement des logiciels du mode Compton m'a amené à rechercher une éventuelle polarisation des sources Integral au delà de 200 keV. Il n'y a actuellement pas de résultats obtenus dans ce domaine pour les binaires X à trou noir, mais il est clair qu'une détection positive serait une première mondiale et permettrait d'ouvrir une nouvelle fenêtre sur ces systèmes. On peut, par exemple, imaginer qu'une mesure de polarisation pourrait nous permettre de déterminer de manière indépendante la vitesse de rotation du trou noir, un paramètre encore mal connu actuellement.

## *Les perspectives théoriques*

### **Etude de l'état « ultrasoft »**

Comme je l'ai noté précédemment, l'état « ultrasoft » des trous noirs où on observe très peu d'émission à haute énergie n'est pas vraiment expliqué. L'idée reste à confirmer mais il pourrait s'agir de la signature d'une sorte de cocon entourant le système lorsque le taux d'accrétion est très fort. Mon code de simulation pourra me servir à vérifier ou infirmer cette hypothèse.

## **Création de paires au voisinage d'un trou noir**

La simulation de la comptonisation sur les électrons en chute libre (« bulk motion comptonisation » ou BMC) a montré que l'on pouvait reproduire de manière satisfaisante le spectre observé dans l'état mou. Néanmoins, le spectre BMC simulé a une coupure en énergie aux alentours de 300 keV, coupure qui n'est pas observée dans certains systèmes. Nous sommes donc en train de réfléchir à un mécanisme qui pourrait étendre notre spectre simulé à de plus hautes énergies. Une possibilité est de créer des paires au voisinage du trou noir. En effet, un photon du disque peut subir un effet Compton inverse sur un électron tombant dans le trou noir et acquérir beaucoup d'énergie. Il a ensuite toutes les chances de tomber dans le trou noir, mais il y a une probabilité non nulle qu'il rencontre un autre photon X dans sa chute. Il pourrait alors créer une paire électron – positron par effet photon – photon :

$$\gamma + \gamma \rightarrow e^+ + e^-$$

J'ai donc modifié mon code pour prendre cet effet en compte. Les premiers résultats préliminaires montrent que beaucoup de paires sont créées très près du trou noir, ce qui devrait avoir une influence sur l'accrétion et le rayonnement résultant. J'ai donc le projet d'étudier quelles seraient toutes ces conséquences. D'autres particules pourraient aussi être créées selon ce principe, dont il faudrait en étudier les conséquences.

## **Les trous noirs de Kerr : accélérateur de particules ?**

Un projet plus « futuriste » serait de faire une simulation de particules en rotation autour d'un trou noir de Kerr, c'est-à-dire un trou noir en rotation. En effet, il existe naturellement deux sortes de trajectoires autour de ces trous noirs : des trajectoires progrades alignées avec la rotation du trou noir et des trajectoires rétrogrades où les particules vont dans le sens inverse. Un trou noir de Kerr est donc un système qui naturellement accélère des particules à de très hautes énergies dans des directions opposées. Comme dans les accélérateurs terrestres, il serait intéressant d'étudier ce qui se passe lorsque ces particules collisionnent. On pourrait peut-être ainsi expliquer les sources non identifiées détectées au GeV par GRO/Egret et *GLAST*.



## **ANNEXE : LISTE COMPLETE DES PUBLICATIONS**

### **1. Publications à comité de lecture**

1. Polarization of the Crab pulsar and nebula as observed by the Integral/IBIS telescope  
Forot, M., Laurent, P., Grenier, I., Gouiffes, C., & Lebrun, F.,  
2008, Submitted to ApJ Letters
2. An unusually bright and long outburst of Cygnus X-1 observed with INTEGRAL  
Malzac, J., Lubinski, P., Zdziarski, A.A., Cadolle Bel, M., Turler, M., & Laurent, P.  
2008, Accepted for publication in ApJ
3. Compton Telescope with a Coded Aperture Mask: Imaging with the INTEGRAL/IBIS Compton Mode  
Forot, M., Laurent, P., Lebrun, F., & Limousin, O.  
2007, ApJ, 668, 1259
4. Simultaneous Multiwavelength Observations of the Low/Hard State of the X-Ray Transient Source SWIFT J1753.5-0127  
Cadolle Bel, M., et al.  
2007, ApJ, 659, 549
5. Effects of Downscattering on the Continuum and Line Spectra in a Powerful Wind Environment: Monte Carlo Simulations, Analytical Results, and Data Analysis  
Laurent, P., & Titarchuk, L.  
2007, ApJ, 656, 1056
6. High-Energy Particles in the Wind Nebula of Pulsar B1509-58 as Seen by INTEGRAL  
Forot, M., Hermsen, W., Renaud, M., Laurent, P., Grenier, I., Goret, P., Khelifi, B., & Kuiper, L.  
2006, ApJ, 651, L45
7. GRB 030406 - an extremely hard burst outside of the INTEGRAL field of view  
Marcinkowski, R., Denis, M., Bulik, T., Goldoni, P., Laurent, P., & Rau, A.  
2006, A&A, 452, 113
8. Bimodal spectral variability of Cygnus X-1 in an intermediate state  
Malzac, J., et al.  
2006, A&A, 448, 1125
9. The broad-band spectrum of Cygnus X-1 measured by INTEGRAL  
Cadolle Bel, M., et al.  
2006, A&A, 446, 591
10. INTEGRAL IBIS Extragalactic Survey: Active Galactic Nuclei Selected at 20-100 keV  
Bassani, L., et al.  
2006, ApJ, 636, L65

11. The high-energy spectrum of Cygnus X-1 as measured by INTEGRAL  
Cadolle Bel, M., et al.  
2006, Advances in Space Research, 38, 1354
12. Gamma-ray burst detection and localization capabilities of the IBIS/INTEGRAL telescope Compton mode  
Marcinkowski, R., Laurent, P., Denis, M., Goldoni, P., Bulik, T., & Rau, A.  
2005, Nuovo Cimento C Geophysics Space Physics C, 28, 845
13. IBIS preliminary results on Cygnus X-1 spectral and temporal characteristics  
Bazzano, A., et al.  
2003, A&A, 411, L389
14. First results from the IBIS/ISGRI data obtained during the Galactic Plane Scan. II. The Vela region  
Rodriguez, J., et al.  
2003, A&A, 411, L373
15. The INTEGRAL/IBIS scientific data analysis  
Goldwurm, A., et al.  
2003, A&A, 411, L223
16. Status of the Integral/IBIS telescope modeling and of the response matrices generation  
Laurent, P., et al.  
2003, A&A, 411, L185
17. In-flight calibrations of IBIS/PICsIT  
Malaguti, G., et al.  
2003, A&A, 411, L173
18. In-flight calibration of the ISGRI camera  
Terrier, R., et al.  
2003, A&A, 411, L167
19. IBIS ground calibration  
Bird, A.J., et al.  
2003, A&A, 411, L159
20. ISGRI: The INTEGRAL Soft Gamma-Ray Imager  
Lebrun, F., et al.  
2003, A&A, 411, L141
21. IBIS: The Imager on-board INTEGRAL  
Ubertini, P., et al.  
2003, A&A, 411, L131

22. INTEGRAL/SPI ground calibration  
 Attié, D., et al.  
 2003, A&A, 411, L71
23. Timing and Spectral Properties of X-Ray Emission from the Converging Flows onto a Black Hole: Monte Carlo Simulations  
 Laurent, P., & Titarchuk, L.  
 2001, ApJ, 562, L67
24. CLAIRE - towards the first light for a gamma-ray lens.  
 Laporte, P., et al.  
 2000, Nuclear Instruments and Methods in Physics Research A, 442, 438
25. The ISGRI CdTe gamma-ray camera: first steps.  
 Limousin, O., et al.  
 2000, Nuclear Instruments and Methods in Physics Research A, 442, 244
26. Long-term variability of the hard X-ray source GRS 1758-258: GRANAT/SIGMA observations  
 Kuznetsov, S.I., et al.  
 1999, Astronomy Letters, 25, 351
27. Spring, 1997 it GRANAT/SIGMA observations of the Galactic Center: discovery of the X-ray nova GRS 1737-31  
 Trudolyubov, S., et al.  
 1999, A&A, 342, 496
28. The Converging Inflow Spectrum Is an Intrinsic Signature for a Black Hole: Monte Carlo Simulations of Comptonization on Free-falling Electrons  
 Laurent, P., & Titarchuk, L.  
 1999, ApJ, 511, 289
29. Towards the First Light for a Gamma-Ray Lens  
 Laporte, P., et al.  
 1999, Astrophysical Letters Communications, 39, 453
30. The Gamma-Ray Imager on Board Integral  
 Ubertini, P., et al.  
 1999, Astrophysical Letters Communications, 39, 331
31. Nature of the Galactic Soft gamma-ray Emission  
 Lebrun, F., Goldoni, P., Goldwurm, A., Laurent, P., Limousin, O., & Paul, J.  
 1999, Astrophysical Letters Communications, 38, 457

32. Imaging Simulations of the Galactic Nucleus with the Ibis Gamma-Ray Telescope on Board Integral  
 Goldwurm, A., Goldoni, P., Laurent, P., & Lebrun, F.  
 1999, *Astrophysical Letters Communications*, 38, 333
33. Spring, 1997 GRANAT/SIGMA Observations of the Galactic Centre: Discovery of X-Ray Nova GRS 1737-31  
 Trudolyubov, S., et al.  
 1999, *Astrophysical Letters Communications*, 38, 313
34. Monte-Carlo Simulations of Comptonization on Free-Falling Electrons  
 Laurent, P., & Titarchuk, L.  
 1999, *Astrophysical Letters Communications*, 38, 173
35. Hard X-ray observations of GX 339-4 with GRANAT/SIGMA  
 Trudolyubov, S., et al.  
 1998, *A&A*, 334, 895
36. The SIGMA pulse profiles of GX 1+4: four years of monitoring  
 David, P., et al.  
 1998, *A&A*, 332, 165
37. Hard X-ray observations of X-ray Nova Ophiuchi 1993 (GRS 1716-249) with GRANAT/SIGMA  
 Revnivtsev, M., et al.  
 1998, *A&A*, 331, 557
38. SIGMA observations of X-ray Nova Velorum 1993 (GRS 1009-45)  
 Goldoni, P., et al.  
 1998, *A&A*, 329, 186
39. Long-term variability of the hard X-ray source GRS 1758-258  
 Kuznetsov, S., et al.  
 1998, *Physica Scripta Volume T*, 77, 84
40. Properties of the hard X-ray radiation from Cygnus X-1 and 1E1740.7-2942  
 Kuznetsov, S., et al.  
 1997, *MNRAS*, 292, 651
41. ASCA X-ray observations of the Galactic bulge source SLX 1735-269.  
 David, P., Goldwurm, A., Murakami, T., Paul, J., Laurent, P., & Goldoni, P.  
 1997, *A&A*, 322, 229
42. Spectral distinction between black holes and neutron stars: the contribution of the sigma telescope  
 Laurent, P., & Denis, M.  
 1997, *Advances in Space Research*, 19, 45

43. GRANAT/SIGMA observations of X-ray nova persei 1992  
Finogenov, A., et al.  
1997, Advances in Space Research, 19, 35
44. SIGMA/GRANAT Discovery of GRS 1739-278, a Hard X-Ray Transient in the Galactic Bulge  
Vargas, M., et al.  
1997, ApJ, 476, L23
45. SIGMA/GRANAT Observations of the X-Ray Nova Persei 1992  
Finoguenov, A.V., et al.  
1996, Astronomy Letters, 22, 721
46. A CdTe gamma-camera for the space observatory INTEGRAL: software charge-loss corrections.  
Lebrun, F., Leray, J.-P., Laurent, P., de Antoni, P., & Blondel, C.  
1996, Nuclear Instruments and Methods in Physics Research A, 380, 414
47. SIGMA/GRANAT observations of the X-ray Nova Persei 1992.  
Finogenov, A.V., et al.  
1996, Pisma Astronomicheskii Zhurnal, 22, 803
48. Observations of the binary accreting pulsar VELA X-1 with the SIGMA telescope  
Laurent, P., et al.  
1995, A&A, 300, 399
49. SIGMA/GRANAT observations of the bright nearby millisecond pulsar PSR J0437-4715  
Barret, D., et al.  
1994, A&A, 288, 472
50. Spectral characteristics of gamma-ray bursts observed by the anticoincidence shield of the SIGMA telescope aboard GRANAT  
Pelaez, F., et al.  
1994, ApJS, 92, 651
51. Noise variability of the hard X-ray transient Nova Persei  
Denis, M., et al.  
1994, ApJS, 92, 459
52. Review of GRANAT/SIGMA observations of the Galactic center region  
Churazov, E., et al.  
1994, ApJS, 92, 381
53. Is the Galactic center annihilator 1E 1740.7-2942 a source of MeV Gamma-ray continuum emission?  
Laurent, P., & Paul, J.  
1994, ApJS, 92, 375

54. Observations of the pulsar PSR 1509-58 with the SIGMA telescope  
 Laurent, P., et al.  
 1994, A&A, 286, 838
55. Discovery of a low-frequency broad quasi-periodic oscillation peak in the power density spectrum of Cygnus X-1 with Granat/SIGMA  
 Vikhlinin, A., et al.  
 1994, ApJ, 424, 395
56. Sidelobes of the SIGMA telescope  
 Claret, A., Lebrun, F., Laurent, P., & Leray, J.P.  
 1994, A&A, 282, 1034
57. Three Years of Monitoring GRS 1758-258: an Extremely Hard X-Ray Source near GX 5-1  
 Gilfanov, M., et al.  
 1993, ApJ, 418, 844
58. SIGMA observations of hard X-ray and soft gamma-ray emission from X-ray binaries.  
 Laurent, P., et al.  
 1993, Advances in Space Research, 13, 139
59. SIGMA observations of the soft gamma-ray source GRS 1758-258  
 Laurent, P., et al.  
 1993, Advances in Space Research, 13, 751
60. SIGMA hard X-ray observations of GX339-4  
 Bouchet, L., et al.  
 1993, Advances in Space Research, 13, 743
61. SIGMA/GRANAT observations of hard X-ray emission from type I X-ray bursters  
 Barret, D., et al.  
 1993, Advances in Space Research, 13, 719
62. The observations of AGNs in the 40-1300 keV energy range by the SIGMA telescope  
 Jourdain, E., et al.  
 1993, Advances in Space Research, 13, 705
63. Sigma observations of hard X-ray and soft gamma-ray emission from X-ray binaries  
 Laurent, P., et al.  
 1993, Advances in Space Research, 13, 139
64. Photon spectrum and period evolution of GX 1+4 as observed at hard X-ray energies by SIGMA  
 Laurent, P., et al.  
 1993, A&A, 278, 444

65. On the hard X-ray variability of Centaurus A  
 Jourdain, E., et al.  
 1993, ApJ, 412, 586
66. X-ray observations of 4U 1700-377/HD 153919 at 35-1300 keV by the SIGMA telescope of the Granat observatory  
 Sittikov, A.F., et al.  
 1993, Astronomy Letters, 19, 188
67. SIGMA Soft Gamma-Ray Observations of 1E:1740.7-2942 in the Spring of 1992 - Discovery of a Sub-Luminous State of Emission and Precise Gamma-Ray Position Measurement  
 Cordier, B., et al.  
 1993, A&A, 272, 277
68. SIGMA hard X-ray observations of GX 339-4 during the hard state and a transition to the soft state  
 Bouchet, L., et al.  
 1993, ApJ, 407, 739
69. Hard x-ray observations of the Large Magellanic Cloud. Upper limits for flux of Supernova 1987A  
 Finogenov, A.V., et al. 1993, Astronomy Letters, 19, 69
70. Sigma upper limits to the hard X-ray/soft gamma-ray emission from the millisecond pulsars of the nearby globular cluster 47 Tucunae  
 Barret, D., et al.  
 1993, ApJ, 405, L59
71. The spectra of Nova MUSCAE 1991 between 3 keV and 1 MeV observed with GRANAT  
 Gilfanov, M., et al.  
 1993, A&AS, 97, 303
72. Sigma observations of the X-ray nova in Musca  
 Goldwurm, A., et al.  
 1993, A&AS, 97, 293
73. Observations of black hole candidates with GRANAT  
 Grebenev, S., et al.  
 1993, A&AS, 97, 281
74. SIGMA observations of two X-ray transients - KS1731-260 and TrA X-1  
 Barret, D., et al.  
 1993, A&AS, 97, 241

75. SIGMA observations of bright X-ray binaries  
 Laurent, P., et al.  
 1993, A&AS, 97, 225
76. SIGMA observations of the Virgo cluster  
 Lebrun, F., et al.  
 1992, A&A, 264, 22
77. Sigma observation of two quasars - 3C 273 and 0241 + 62  
 Bassani, L., et al.  
 1992, ApJ, 396, 504
78. Sigma detection of hard X-ray emission from the soft transient type I X-ray burster KS 1731 - 260  
 Barret, D., et al.  
 1992, ApJ, 394, 615
79. Observation of 4U 1700-377 with the SIGMA telescope  
 Laurent, P., et al.  
 1992, A&A, 260, 237
80. SIGMA observation of hard X-ray emission from the ultrasoft X-ray transient Triangulum Austral X-1 (A1524 - 62)  
 Barret, D., et al.  
 1992, ApJ, 392, L19
81. SIGMA observation of a steep spectral shape in NGC 4151 above 35 keV  
 Jourdain, E., et al.  
 1992, A&A, 256, L38
82. Discovery with the Sigma telescope of hard X-rays from the globular cluster Terzan 2  
 Barret, D., et al.  
 1991, ApJ, 379, L21
83. Two hard X-ray sources in 100 square degrees around the Galactic Center  
 Sunyaev, R., et al.  
 1991, A&A, 247, L29
84. Two Hard X-Ray Sources Near the Galactic Center - the Known Source 1E:1740.7-2942 and the Newly Discovered Source GRS:1758-258  
 Syunyaev, R., et al.  
 1991, Soviet Astronomy Letters, 17, 50
85. The first soft gamma-ray image of the Galactic centre with arc-min accuracy  
 Cordier, B., et al.  
 1991, Advances in Space Research, 11, 169

86. X/gamma-ray observation of the Crab pulsar with the Sigma telescope  
Natalucci, L., et al.  
1991, Advances in Space Research, 11, 79

## **2. Publications dans des comptes rendus de conférence**

1. Status of the Simbol-X detector background simulation activities.  
Chipaux, R., et al.  
2008, Memorie della Societa Astronomica Italiana, 79, 234
2. Science with Simbol-X.  
Fiore, F., et al.  
2008, Memorie della Societa Astronomica Italiana, 79, 38
3. The Simbol-X focal plane.  
Laurent, P., et al.  
2008, Memorie della Societa Astronomica Italiana, 79, 32
4. The Simbol-X mission  
Ferrando, P., et al.  
2008, Memorie della Societa Astronomica Italiana, 79, 19
5. GRB Observed by IBIS/PiCsIT in the MeV Energy Range  
Bianchin, V., di Cocco, G., Foschini, L., Gianotti, F., Laurent, P., Malaguti, G., & Schiavone, F.  
2008, 37th COSPAR Scientific Assembly. 13-20 July 2008, in Montréal, Canada., p.286, 37, 286
6. IBIS/PICsIT Status  
di Cocco, G., Bianchin, V., Foschini, L., Gianotti, F., Laurent, P., Malaguti, G., Natalucci, L., & Schiavone, F.  
2007, ESA Special Publication, 622, 619
7. GRB spectra in the MeV range: hints from INTEGRAL  
Bulik, T., Denis, M., Marcinkowski, R., Goldoni, P., Laurent, P., & Osuch, L.  
2007, The First GLAST Symposium, 921, 277
8. The focal plane of the Simbol-X space mission  
Dirks, B.P.F., et al.  
2006, Proceedings of the SPIE conference, 6276, 38
9. Monte Carlo simulations of stacked x-ray detectors as designed for SIMBOL-X  
Tenzer, C., Kendziorra, E., Santangelo, A., Kuster, M., Ferrando, P., Laurent, P., Claret, A., & Chipaux, R.  
2006, Proceedings of the SPIE conference, 6266, 78
10. Simbol-X: mission overview  
Ferrando, P., et al.  
2006, Proceedings of the SPIE conference, 6266, 11

11. Hybrid modelization of the high-energy broad-band spectra of Cygnus X-1 observed by INTEGRAL  
 Cadolle Bel, M., et al. 2006,  
 SF2A-2006: Semaine de l'Astrophysique Française, 119
12. Spectral Variability of Cygnus X-1 during an Intermediate State  
 Malzac, J., et al.  
 2006, The X-ray Universe 2005, 604, 223
13. GRB 061126: a GRB detected off-axis by INTEGRAL.  
 Denis, M., Marcinkowski, R., Bulik, T., Goldoni, P. & Laurent, P.  
 2006, GRB Coordinates Network, 5908, 1
14. Localization and spectra of the Integral Compton mode gamma-ray bursts  
 Marcinkowski, R., Denis, M., Bulik, T., Laurent, P., Goldoni, P., & Rau, A.  
 2005, Astrophysical Sources of High Energy Particles and Radiation, 801, 133
15. First catalogue of the INTEGRAL off-axis gamma-ray bursts  
 Marcinkowski, R., Denis, M., Bulik, T., Laurent, P., Goldoni, P., & Rau, A.  
 2005, Astrophysical Sources of High Energy Particles and Radiation, 801, 131
16. SIMBOL-X: a formation-flying mission for hard-x-ray astrophysics  
 Ferrando, P., et al. 2005, Proceeding of the SPIE, 5900, 195
17. Redshifted iron lines as spectral signatures of Compton-thick outflow near accreting (galactic and extragalactic) black holes: Self-consistent calculations of ionization and temperature structures and spectral formation in the outflow.  
 Titarchuk, L., Laming, J.~M., & Laurent, P. 2004,  
 Bulletin of the American Astronomical Society, 36, 1421
18. The MAX Mission: Focusing on High-Sensitivity Gamma-Ray Spectroscopy  
 von Ballmoos, P., et al.  
 2004, 5th INTEGRAL Workshop on the INTEGRAL Universe, 552, 747
19. Observations of PSR B1509-58 using INTEGRAL Core Program Data  
 Sturner, S.J., Forot, M., & Laurent, P.  
 2004, 5th INTEGRAL Workshop on the INTEGRAL Universe, 552, 479
20. Study of the Crab Pulsar with the IBIS Compton Mode Data  
 Forot, M., Laurent, P., Marcinkowski, R., & Denis, M.  
 2004, 5th INTEGRAL Workshop on the INTEGRAL Universe, 552, 463
21. ISGRI Observation of the Crab Pulsar  
 di Cocco, G., et al.  
 2004, 5th INTEGRAL Workshop on the INTEGRAL Universe, 552, 459

22. INTEGRAL Observations of the Accreting Pulsar OAO 1657- 415  
 Denis, M., Marcinkowski, R., Bulik, R., Laurent, P., Goldoni, P., & Santangelo, A.  
 2004, 5th INTEGRAL Workshop on the INTEGRAL Universe, 552, 453
23. Extensive INTEGRAL Observations of the HMXB 4U 1700-377  
 Orr, A., Falanga, M., Cocchi, M., Laurent, P., & Goldwurm, A.  
 2004, 5th INTEGRAL Workshop on the INTEGRAL Universe, 552, 357
24. INTEGRAL Observation of Cyg X-1 in an Intermediate State  
 Malzac, J., et al.  
 2004, 5th INTEGRAL Workshop on the INTEGRAL Universe, 552, 341
25. INTEGRAL Observations of the Accreting Pulsar 4U 1626-67  
 Denis, M., Grygorczuk, J., Bulik, R., Laurent, P., Goldoni, P., & Santangelo, A.  
 2004, 5th INTEGRAL Workshop on the INTEGRAL Universe, 552, 295
26. The Sky Behind Our Galaxy as Seen by IBIS on INTEGRAL  
 Bassani, L., et al.  
 2004, 5th INTEGRAL Workshop on the INTEGRAL Universe, 552, 139
27. MAX: a gamma-ray lens for nuclear astrophysics  
 von Ballmoos, P., et al.  
 2004, Proceedings of the SPIE conference, 5168, 482
28. Calibration of the spectrometer aboard the INTEGRAL satellite  
 Schanne, S., et al.  
 2003, Proceedings of the SPIE conference, 4851, 1132
29. Design and flight performance of a crystal diffraction telescope  
 Halloin, H., et al.  
 2003, Proceedings of the SPIE conference, 4851, 895
30. Photon Bending Effects near Black Hole Horizons: Spectral and Timing Signatures  
 Titarchuk, L., & Laurent, P.  
 2003, Bulletin of the American Astronomical Society, 35, 615
31. First results of IBIS observations of Compact Accreting Objects  
 Goldoni, P., Goldwurm, A., Laurent, P., Lebrun, F., & Bazzano, A.  
 2003, SF2A: Semaine de l'Astrophysique Française, 417
32. Monte-Carlo simulations of Comptonization on free-falling electrons  
 Laurent, P., & Titarchuk, L. 2002,  
 The Ninth Marcel Grossmann Meeting, 2327

33. IBIS/INTEGRAL galactic plane observations: X-ray Novae  
 Goldoni, P., Goldwurm, A., Laurent, P., & Lebrun, F.  
 2001, X-ray Astronomy: Stellar Endpoints, AGN, and the Diffuse X-ray Background,  
 599, 630
34. Timing and Spectral Properties of X-ray Emission from the Converging Flows onto  
 Black hole: Monte-Carlo Simulations  
 Titarchuk, L.G., & Laurent, P.  
 2001, Bulletin of the American Astronomical Society, 33, 1473
35. The first flight of a gamma-ray lens  
 von Ballmoos, P., et al. 2001,  
 Exploring the Gamma-Ray Universe, 459, 649
36. ISGRI: The CdTe gamma-ray camera onboard INTEGRAL  
 Lebrun, F., Leray, J.-P., Limousin, O., Blondel, C., Laurent, P., Goldoni, P.,  
 Goldwurm, A., & Sauvageon, A.  
 2001, Exploring the Gamma-Ray Universe, 459, 591
37. The INTEGRAL/IBIS telescope modeling  
 Laurent, P., Limousin, O., Malaguti, G., Caroli, E., de Cesare, G., Bird, A.J.,  
 Grygorczuk, J., & Torrejon, J.M.  
 2001, Exploring the Gamma-Ray Universe, 459, 587
38. Observation of a black-hole X-ray nova in outburst with INTEGRAL  
 Goldoni, P., Goldwurm, A., Laurent, P., Lebrun, F., & Cordier, B.  
 2001, Exploring the Gamma-Ray Universe, 459, 573
39. INTEGRAL/IBIS observations of persistent black hole spectral states during the Core  
 Program  
 Laurent, P., Goldoni, P., Goldwurm, A., & Lebrun, F.  
 2001, Exploring the Gamma-Ray Universe, 459, 505
40. Monte-Carlo simulations of bulk motion Comptonization  
 Laurent, P., & Titarchuk, L. 2001,  
 Exploring the Gamma-Ray Universe, 459, 313
41. INTEGRAL observations of galaxy clusters  
 Goldoni, P., Goldwurm, A., Laurent, P., Cassé, M., Paul, J., & Sarazin, C.  
 2001, Exploring the Gamma-Ray Universe, 459, 165
42. The first flight of a gamma-ray lens  
 von Ballmoos, P., et al.  
 2001, European Rocket and Balloon Programmes and Related Research, 471, 453

43. In-flight Calibration Sources Simulations for the IBIS Telescope  
 del Santo, M., Bazzano, A., Bird, A.~J., de Cesare, G., Laurent, P., Malaguti, G., & Natalucci, L.  
 2001, Gamma 2001: Gamma-Ray Astrophysics, 587, 826
44. Evaluation of the INTEGRAL/IBIS Photons Detectors Efficiencies by Monte-Carlo Simulation  
 de Cesare, G., et al.  
 2001, Gamma 2001: Gamma-Ray Astrophysics, 587, 821
45. A Black Hole Spectral Signature  
 Titarchuk, L., & Laurent, P.  
 2000, Nuclear Physics B Proceedings Supplements, 80, 173
46. Hard X-rays from the galactic nucleus: present and future observations  
 Goldwurm, A., Goldoni, P., Laurent, P., Lebrun, F., & Paul, J.  
 2000, Nuclear Physics B Proceedings Supplements, 80, 1511
47. Observation of X-Ray Novae with INTEGRAL  
 Goldwurm, A., Goldoni, P., Laurent, P., & Lebrun, F.  
 2000, American Institute of Physics Conference Series, 510, 703
48. The IBIS Gamma-Ray Telescope on INTEGRAL  
 Ubertini, R., et al. 2000,  
 American Institute of Physics Conference Series, 510, 684
49. IBIS: the gamma-ray imaging telescope on board INTEGRAL  
 Lebrun, F., et al.  
 1999, Memorie della Societa Astronomica Italiana, 70, 1299
50. SIGMA observations of galactic black holes.  
 Laurent, P.  
 1999, Memorie della Societa Astronomica Italiana, 70, 1127
51. Hard X-rays From the Galactic Nucleus: Present and Future Observations  
 Goldwurm, A., Goldoni, P., Laurent, P., Lebrun, F., & Paul, J.  
 1998, 19th Texas Symposium on Relativistic Astrophysics and Cosmology,
52. Hard X-ray Observations of GRS 1009-45 with the SIGMA Telescope  
 Goldoni, P., et al.  
 1997, Proceedings of the Fourth Compton Symposium, 410, 957
53. Two Distinct Modes in the Low (hard) State of Cygnus X-1  
 Ballet, J., Laurent, P., Bouchet, L., Roques, J.-P., Kuznetsov, S., Gilfanov, M., Churazou, E., & Sunyaev, R.  
 1997, X-Ray Imaging and Spectroscopy of Cosmic Hot Plasmas, 453

54. GRANAT/SIGMA observations of 4U1705-44 and 4U1608-52 and spectral states of X-ray bursters  
 Revnivtsev, M., et al.  
 1997, Joint European and National Astronomical Meeting,
55. SIGMA Observations of Pulsars  
 Laurent, P., & David, P.  
 1997, The Transparent Universe, 382, 279
56. Detection of the Hard X-Ray Emission from X-Ray Burster 4U1705-44 with GRANAT/SIGMA  
 Revnivtsev, M., et al.  
 1997, The Transparent Universe, 382, 277
57. Hard X-Ray Observations of X-Ray Nova Ophiuchi 1993 (GRS 1716-249) with GRANAT/SIGMA  
 Revnivtsev, M., et al.  
 1997, The Transparent Universe, 382, 273
58. Properties of the Hard X-Ray Emission from the Black Hole Candidates: Cygnus X-1 and 1E1740. 7-2942  
 Kuznetsov, S., et al.  
 1997, The Transparent Universe, 382, 213
59. Sigma Observations of High Energy Steady Sources and Transients in the Milky Way  
 Vargas, M., et al.  
 1997, The Transparent Universe, 382, 129
60. IBIS: the Imager on-Board the INTEGRAL Satellite.  
 di Cocco, G., et al.  
 1997, Cosmic Physics in the Year 2000, 61
61. The IBIS View of the Galactic Centre: INTEGRAL's Imager Observations Simulations  
 Goldoni, P., Goldwurm, A., Laurent, P., & Lebrun, F.  
 1997, Proceedings of the Fourth Compton Symposium, 410, 1549
62. ISGRI: a CdTe array imager for INTEGRAL  
 Lebrun, F., Blondel, C., Fondeur, I., Goldwurm, A., Laurent, P., & Leray, J.P.  
 1996, Proceedings of the SPIE conference, 2806, 258
63. Imager onboard INTEGRAL  
 Ubertini, P., et al.  
 1996, Proceedings of the SPIE conference, 2806, 246

64. Hard X-ray observations of X-ray Nova Ophiuchi 1993 (GRS 1716-249) with GRANAT/SIGMA.  
 Revnivtsev, M., et al. 1996,  
*Roentgenstrahlung from the Universe*, 185
65. Two distinct modes in the low (hard) state of Cygnus X-1 and 1E 1740.7-2942.  
 Kuznetsov, S., et al.  
 1996, *Roentgenstrahlung from the Universe*, 157
66. Hard X-Ray Observations of Black Holes and Neutron Stars  
 Laurent, P.  
 1996, Proceedings of the Seventh Marcel Grossman Meeting on recent developments in theoretical and experimental general relativity, gravitation, and relativistic field theories, 1314
67. The Cosmological Diffuse y-Ray Background Myth or Reality?  
 Laurent, P.  
 1996, *Examining the Big Bang and Diffuse Background Radiations*, 168, 271
68. SIGMA Observations of Pulsars  
 Laurent, P.  
 1995, *The Lives of the Neutron Stars*, 405
69. Hard X-ray Observations of Black-Hole Candidates  
 Gilfanov, M., et al.  
 1995, *The Lives of the Neutron Stars*, 331
70. Averaged Picture of the GC Region in Hard X-rays  
 Churazov, E., et al.  
 1994, *New Horizon of X-Ray Astronomy.~First Results from ASCA*, 491
71. Spectral and Temporal Properties of Black Hole Candidates  
 Gilfanov, M., et al.  
 1994, *New Horizon of X-Ray Astronomy.~First Results from ASCA*, 433
72. Review of GRANAT observations of AGNs.  
 Churazov, E.~M., et al.  
 1994, *Multi-Wavelength Continuum Emission of AGN*, 159, 63
73. Galactic Hard X-Ray Sources Viewed by Sigma  
 Ballet, J., et al.  
 1994, *Frontiers of Space and Ground-Based Astronomy*, 187, 23
74. Black Holes vs Neutron Stars Among Sigma Sources  
 Ballet, J., et al.  
 1994, *The Evolution of X-ray Binaries*, 308, 131

75. Highlights of Sigma Observations  
Laurent, P.  
1992, Towards a Major Atmospheric Cerenkov Detector for TeV Astro/particle Physics, 115
76. Detection and period measurements of GX1+4 at hard X ray energies with the SIGMA telescope  
Laurent, P., et al.  
1992, The Compton Observatory Science Workshop, 209
77. Observations of 4U1700-377 with the Sigma Telescope  
Laurent, P., & et al.  
1991, International Cosmic Ray Conference, 1, 29
78. Observations of 4U1700 - 377 with the Sigma telescope  
Laurent, P., et al.  
1991, Gamma-Ray Line Astrophysics, 232, 346
79. High energy observations of GX1 + 4 with the Sigma imaging telescope  
Barret, D., et al.  
1991, Gamma-Ray Line Astrophysics, 232, 42
80. Granat images of the Galactic center region in 4-1300 keV band - Localization of the possible candidate for 511 keV source  
Siuniaev, R., et al.  
1991, Gamma-Ray Line Astrophysics, 232, 29

### **3. Télégrammes ou circulaires à l'IAU**

1. Bright flare of Cyg X-1 in hard X-ray band  
Neronov, A., et al. 2008, The Astronomer's Telegram, 1533, 1
2. INTEGRAL observation of Cyg X-1 at a historic hard X-ray maximum  
Türler, M., et al. 2006, The Astronomer's Telegram, 911, 1
3. INTEGRAL serendipitous hard X-ray detection of the millisecond pulsar HETE J1900.1-2455  
Goldoni, P., Soldi, S., Shaw, S.~E., Bel, M.~C., Laurent, P., Falanga, M., Goldwurm, A., & Ubertini, P., 2005, The Astronomer's Telegram, 590, 1
4. INTEGRAL High-Energy Detection of SWIFT J1753.5-0127  
Cadolle Bel, M., Rodriguez, J., Goldwurm, A., Goldoni, P., Laurent, P., Ubertini, P., & Mereghetti, S., 2005, The Astronomer's Telegram, 574, 1
5. Candidate AGN in the 2nd IBIS/ISGRI survey catalogue  
Bassani, L., et al. 2005, The Astronomer's Telegram, 537, 1
6. Cygnus X-1  
Vikhlinin, A., et al. 1992, Circulaire l'UAI, 5576, 1
7. Nova MUSCAE 1991  
Sunyaev, R., Jourdain, E., & Laurent, P. 1991, Circulaire l'UAI, 5176, 1

## Résumé

Mes recherches ont eu pour but principal de trouver des signatures astrophysiques des trous noirs dans les systèmes binaires d'étoiles. Comme je le montre dans ce mémoire, les astronomies X et  $\gamma$  semblent bien adaptées pour ces recherches. J'ai donc participé à la définition d'instruments X et  $\gamma$ , tout d'abord dans le cadre de la mission franco-russe Granat/Sigma puis dans celui de la mission de l'Agence Spatiale Européenne Integral. Mon rôle y a été de modéliser aussi précisément que possible la réponse des instruments, grâce à des simulations Monte-Carlo. Dans le cadre de la mission Integral, j'ai aussi contribué à définir et à réaliser les étalonnages au sol du satellite complet (étalonnage « end to end »), et à réaliser avec mon étudiant, Michaël Forot, le logiciel pour traiter les données dites « Compton » du télescope Integral/Ibis. Ces études nous ont permis, mon collègue Olivier Limousin et moi, de déposer un brevet sur une nouvelle  $\gamma$ -caméra permettant l'imagerie 3D de sources radioactives.

Grâce aux données  $\gamma$  récoltées par Sigma et Integral, j'ai étudié, avec Marion Cadolle-Bel, les systèmes binaires contenant un trou noir de masse stellaire. Celui-ci accrète la matière de l'étoile compagnon donnant lieu à une émission X et  $\gamma$ , dont le processus d'émission, lié principalement à l'effet Compton sur les électrons chauds du plasma entourant le trou noir, est décrit dans le mémoire. Le résultat majeur de ce travail fut l'observation avec l'observatoire Integral du candidat trou noir, Cygnus X-1, en particulier lors d'un changement d'état en juin 2003 et lors de son éruption de septembre 2006.

Enfin, j'ai modélisé la signature X/ $\gamma$  de trous noirs, comme il est décrit au chapitre 4. Cette modélisation s'est faite grâce à un modèle que j'ai développé avec Lev Titarchuk, modèle qui montre que le spectre observé de candidat trou noir peut être expliqué en considérant des photons X faisant un effet Compton inverse sur les électrons tombant en chute libre dans le trou noir. Ce modèle original, basé sur des simulations Monte-Carlo en Relativité Générale, a fait l'objet de plusieurs publications. Nous avons aussi étudié l'élargissement de la raie du fer, une autre signature très connue des trous noirs dans le domaine des X mous. Nous avons montré que cet élargissement pourrait être plutôt dû à la propagation des photons de fluorescence dans un vent, ce qui ne nécessiterait pas la présence d'un trou noir. Cet élargissement pourrait donc être une signature de trous noirs controversée.

Dans les années à venir, je continuerai la définition de télescopes nouveaux, en particulier en optimisant les performances du projet d'astronomie spatiale Simbol-X. Ce projet prévoit, par le moyen de deux satellites en formation, d'étendre la technique de focalisation par incidence rasante aux rayons X durs afin d'étudier les phénomènes non thermiques de notre Univers. Je superviserai aussi la conception et la réalisation de l'anticoïncidence de Simbol-X, afin d'obtenir un bruit de fond sur les détecteurs aussi faible que possible. Notre expérience sur Simbol-X pourra aussi nous servir, de manière plus générale, de support aux développements de futures missions X et  $\gamma$ , comme par exemple l'observatoire IXO prévu par la NASA et l'ESA. Les futures observations Integral, d'un autre côté, me permettront d'observer les trous noirs accrétants au MeV, et potentiellement, grâce au mode Compton, de mesurer leur état de polarisation, ce qui n'a encore jamais été fait dans cette gamme d'énergie. Enfin, nous développons avec L. Titarchuk un modèle de création de paires électrons-positrons au voisinage d'un trou noir, qui aura de nombreuses conséquences observationnelles qu'il nous faudra étudier.